U.PORTO

FMUP FACULDADE DE MEDICINA
UNIVERSIDADE DO PORTO

THE ROLES OF BRANCHED MICROTUBULE NUCLEATION AND KINETOCHORE ARCHITECTURE IN CHROMOSOME CONGRESSION AND SEGREGATION

ANA ISABEL COELHO DE ALMEIDA

TESE DE DOUTORAMENTO APRESENTADA À
FACULDADE DE MEDICINA DA UNIVERSIDADE DE PORTO EM
BIOMEDICINA

PORTO, PORTUGAL

2022

TÍTULO: The roles of branched microtubule nucleation and kinetochore architecture in chromosome congression and segregation

Orientador: Prof. Doutor Helder José Martins Maiato

Chromosome Instability and Dynamics, i3S -Instituto de Investigação e Inovacão em Saúde, Universidade do Porto, Rua Alfredo Allen 208, 4200-135 Porto, Portugal.

Departamento de Biomedicina,
Faculdade de Medicina, Universidade do Porto,
Alameda Prof. Hernâni Monteiro, 4200-319 Porto, Portugal.

Dissertação de candidatura ao grau de Doutor em Biomedicina submetida à Faculdade de Medicina da Universidade do Porto

Porto, Janeiro de 2022

JÚRI

Presidente:

Doutor José Carlos Lemos Machado, Professor Catedrático da Faculdade de Medicina da Universidade do Porto

Vogais:

- Doutor Tom Maresca, Professor Associado da University of Massachusetts Amherst, USA;
- Doutor Alexey Khodjakov, Investigador Principal do Wadsworth Center, USA;
- Doutor Reto Gassmann, Investigador Principal do i3S - Instituto de Investigação e Inovação em Saúde;
- Doutor Helder José Martins Maiato, Professor Catedrático Convidado da Faculdade de Medicina da Universidade do Porto;
- Doutor Henrique Manuel Nunes de Almeida, Professor Associado da Faculdade de Medicina da Universidade do Porto;
- Doutora Filipa Abreu Gomes de Carvalho, Professora Auxiliar com Agregação da Faculdade de Medicina da Universidade do Porto**.**

CORPO DOCENTE CATEDRÁTICO DA FMUP

- Patrício Manuel Vieira Araújo Soares Silva
- Alberto Manuel Barros Da Silva
- Jose Henrique Dias Pinto De Barros
- Maria Fátima Machado Henriques Carneiro
- Maria Dulce Cordeiro Madeira
- Altamiro Manuel Rodrigues Costa Pereira
- Manuel Jesus Falcao Pestana Vasconcelos
- João Francisco Montenegro Andrade Lima Bernardes
- Maria Leonor Martins Soares David
- Rui Manuel Lopes Nunes
- Jose Manuel Pereira Dias De Castro Lopes
- Joaquim Adelino Correia Ferreira Leite Moreira
- Raquel Ângela Silva Soares Lino
- Fernando Manuel Mendes Falcão Dos Reis
- Francisco José Miranda Rodrigues Cruz
- José Paulo Alves Vieira De Andrade
- Jorge Manuel Silva Junqueira Polónia
- José Luís Dias Delgado
- Isaura Ferreira Tavares
- Fernando Carlos De Landér Schmitt
- Acácio Agostinho Gonçalves Rodrigues
- Maria De Fátima Moreira Martel
- João Tiago De Sousa Pinto Guimarães
- José Carlos Lemos Machado
- José Carlos De Magalhães Silva Cardoso

NOTA EXPLICATIVA

A presente dissertação foi escrita em inglês devido ao facto de os trabalhos terem sido realizados com colaboração internacional e envolvendo um Júri composto por membros estrangeiros.

ACKOWLEDGEMENTS

The work behind this PhD thesis would not be possible without the collaboration and help of several people to whom I dedicate this space to express my gratitude.

First, I would like to thank my supervisor Helder Maiato, who has been very supportive of my work and helped me to grow over the years of my PhD. You always challenged me to dare and make a difference in developing alternative and novel assays/experimental setups. It was a great privilege to be introduce to the field of cell division and microscopy, alongside someone with such exceptional scientific knowledge and passion for the subject.

A huge thanks to the CID lab members who have helped me along the way, in particular to António for the guidance and training in the different microscopes (STED, our favorite!!), Danica for the mentoring and good vibes, and the Muntjac team (Joana O., Naoyuki, Liam & Alex) for the good energy and companionship. It has been a pleasure to share with you the unique opportunity to work with such a cool model system. Thanks to my 'Miaus' Joana M., Margarida D., and Joana O. for the amazing friendship, help inside and outside the lab, the shared coffees and all the sweets. Thanks to Carolina and Bernardo for the great laughs, support, and advice. Thanks to all my other colleagues with whom I had the privilege to work since I joined the lab: Margarida G., Danilo, Marco, Hugo, Luísa, Ariana, Jorge, Vanessa and Joana L.. It was such a pleasure to work with you; we have grown together as persons and as scientists.

A big thanks to Paulo Aguiar, Helder Rocha and Reto Gassmann for the guidance and help in our collaborative projects. Finally, thanks to all the members of ANA's lab for everyday support and nice environment.

I would like to thank to the incredible people who crashed into my life over the last couple of years: GBL's friends for all the chats, FCP games and after-work beers; the Clusps group for the constant laughs, all the music and good moments and the GoGym crew for the 'circuito' classes that helped me stress-busting. Finally, to my besties Bárbara and Ana, your friendship and dinners have been fundamental in my life, and I am definitely very lucky to have you! My apologies to all those both that I have missed out and who have supported me in their own ways.

Filipe, thank you for all the dedication, support, and partnership. The unlimited pep talks, constant encouraging, and all the overly long chats were crucial during this journey. Thanks for making all the travelling so much fun and showing me that good things happen to those who wait. It has been worthwhile!

Last but not least, I would like to express my gratitude to my family: my mum and dad for all the love and patience; and a special thanks to my sister who was always ready to give me an extra

hand and to listen to my daily life struggles. They are my biggest pride, and all my achievements are a reflect of their support.

The work of this thesis was generously founded by Fundação para a Ciência e Tecnologia during the last four years.

ABSTRACT

Accurate spindle assembly and chromosome congression during mitosis are essential for life and rely on the activity of several proteins. However, due to technical constraints or limitations of the available model organisms, some of their roles might have been overlooked. The Indian muntjac is the mammal with the lowest known chromosome number (2N=6), and due to chromosome fusions during evolution it has a large kinetochore (~ 2 μm in length) that can bind up to 60 microtubules. Its unique cytological features confer a great advantage for micromanipulation and high-resolution live-cell studies. Here, we proposed to identify the key players and principles underlying chromosome congression and segregation, as well as to elucidate the mechanism by which kinetochore (k)-fibers mature in mammalian cells.

As such, the main goals of this work were (1) to establish the Indian muntjac as a model system for the comprehensive study of mitosis; (2) to investigate how spindle assembly occurs in mammalian cells and dissect the players implicated in k-fiber maturation; and lastly (3) to evaluate the importance of kinetochore size for chromosome bi-orientation/congression and error formation.

Following on the recent genome sequencing efforts, we screened the role of 63 conserved mitotic genes in spindle assembly and chromosome segregation in Indian muntjac fibroblasts. Among the analyzed proteins, perturbation of the Augmin complex emerged as the most deleterious condition for mitosis. By combining functional perturbations, with fixed- and subsecond live-cell super-resolution CH-STED nanoscopy, we uncovered a key role for Augmin in kinetochore microtubule self-organization and maturation, regardless of pioneer centrosomal microtubules. Augmin promoted kinetochore microtubule turnover by sustaining microtubule formation from kinetochores, while assisting poleward flux. Tracking of microtubule growth events within individual k-fibers revealed a wide angular dispersion, consistent with Augmin-mediated branched microtubule nucleation. Moreover, Augmin depletion reduced the frequency of such events and hampered normal repair after acute k-fiber injury by laser microsurgery. Together, these findings underscore the contribution of Augmin-mediated microtubule amplification for k-fiber self-organization and maturation in mammals.

Next, we sought to investigate the implication of kinetochore size for chromosome congression and segregation fidelity. Measurement of intra-kinetochore distances, serial-section electron microscopy, and RNAi against key kinetochore proteins confirmed a standard structural and functional organization of the Indian muntjac kinetochores and revealed that microtubule binding capacity scales with kinetochore size. Surprisingly, we found that chromosome congression in this specie is not random, and that chromosomes with larger kinetochores bi-orient more efficiently, displaying a bias to congress to the equator in a motor-independent manner. On the other hand, despite the robust correction mechanisms, when experimentally challenged,

chromosomes with larger kinetochores were also strongly biased to establish erroneous merotelic attachments and missegregate during anaphase. This bias was impervious to the experimental attenuation of polar ejection forces on chromosome arms by RNAi against the chromokinesin Kif4a. Thus, kinetochore size is decisive of chromosome segregation fidelity.

Lastly, following on our observations that chromosomes with larger kinetochores rely less on motor CENP-E-dependent pathway to congress to the spindle equator, and the fact that multiple metazoans with holocentric kinetochores (that extends to the entire chromosome length) congress their chromosomes in the absence of a CENP-E ortholog, we hypothesized that there is a relationship between kinetochore size and CENP-E-mediated transport dependency. We engineered a *C. elegans* model expressing human CENP-E docked to a kinetochore protein and prevented chromosome direct congression due to rapid bi-orientation by knocking-down chromokinesin klp-19. We found that CENP-E expression partially rescues chromosome congression imposed by defective kinetochore-microtubule attachments, which suggests that CENP-E may represent an advantage when 'direct' congression pathway is compromised. Taken together, these results propose that both kinetochore and arm-mediated motor activities are important for successful chromosome congression.

RESUMO

A formação correta do fuso mitótico e o alinhamento dos cromossomas na placa metafásica durante a mitose são essenciais para a manutenção da vida e dependem da atividade de várias proteínas. Devido a constrangimentos técnicos e limitações dos sistemas modelo usados até à data, algumas das suas funções podem ter sido subestimadas. O Indian muntjac é o mamífero conhecido com o menor número de cromossomas (2N=6) que, como consequência de múltiplas rondas de fusão, contêm um cinetocoro com cerca de 2 μm de comprimento que pode ligar até 60 microtúbulos. Estas características únicas constituem uma grande vantagem para estudos de micromanipulação e microscopia de fluorescência de células vivas. Assim, propusemo-nos a identificar quais os principais intervenientes e princípios associados com os processos de bi-orientação, alinhamento e segregação dos cromossomas, enquanto dissecamos qual o mecanismo responsável pela maturação das fibras mitóticas que se ligam aos cinetocoros (*'k-fibers'*) em células mamíferas.

Os principais objetivos deste trabalho foram (1) estabelecer e validar o Indian muntjac como um sistema modelo para o estudo dos processos associados à divisão celular; (2) investigar qual o modo de formação do fuso mitótico em mamíferos e quais os intervenientes na maturação das *k-fibers;* e (3) determinar qual a relevância do tamanho do cinetocoro para o processo de bi-orientação/alinhamento de cromossomas e ocorrência de erros.

Tendo em conta os últimos desenvolvimentos na sequenciação do genoma do Indian muntjac, monitorizou-se a depleção e analisou-se quais as funções na formação do fuso mitótico e segregação de cromossomas de 63 proteínas conservadas. De entre as proteínas em estudo, a depleção do complexo Augmin surgiu como uma das condições mais prejudiciais para a mitose neste sistema. Ao combinar ensaios de perda de função com microscopia de super-resolução (*'CH-STED'*) de células fixadas e células vivas, determinou-se o papel desempenhado pela Augmin na auto-organização e maturação de microtúbulos nucleados nas imediações dos cinetocoros, independentemente de microtúbulos provenientes dos centrossomas. O complexo Augmin participa no '*turnover'* de microtúbulos através da formação de novos microtúbulos, enquanto assiste simultaneamente o fluxo em direção aos polos. A análise dos eventos de crescimento de microtúbulos nas *k-fibers* revelou uma ampla distribuição angular, consistente com a nucleação ramificada dependente de Augmin. Adicionalmente, a depleção de Augmin reduziu a frequência destes eventos e comprometeu a recuperação normal das fibras após um corte por um laser de microcirurgia. Em suma, estes resultados reforçam a contribuição da amplificação de microtúbulos dependente de Augmin para a auto-organização e maturação das *k-fibers* em células mamíferas.

Em seguida, procurou-se investigar qual o papel do tamanho do cinetocóro para o alinhamento e separação corretos dos cromossomas. Através da determinação das distâncias intra-cinetocoros,

microscopia eletrónica e ARN de interferência contra proteínas chave, foi possível confirmar que a arquitetura e organização funcional dos cinetocoros do Indian muntjac é conservada, e que a capacidade de ligar microtúbulos é proporcional ao tamanho do cinetocoro. Surpreendentemente, verificou-se que o alinhamento dos cromossomas não é um fenómeno aleatório. Este é enviesado pelo tamanho do cinetocoro, sendo que os maiores bi-orientam mais rápido e dependem menos da atividade de proteínas motoras para o seu transporte para o equador da célula. Por outro lado, apesar dos mecanismos de correção existentes durante uma mitose normal, cromossomas com o cinetocoro maior também mostraram uma propensão superior para estabelecer ligações erradas com os microtúbulos, culminando em erros durante a anáfase. Esta tendência manteve-se após a atenuação das forças de ejeção polar nos braços dos cromossomas induzida pela depleção da cromocinesina Kif4a. Assim, conclui-se que o tamanho do cinetocoro é um fator determinante para a segregação correta dos cromossomas.

Por último, partindo das observações anteriores de que os cromossomas com o cinetocoro maior são menos dependentes de CENP-E para o seu transporte para o equador, e do facto de vários metazoários com cinetocoros holocêntricos (que se estendem por todo o comprimento do cromossoma) conseguirem alinhar na ausência de um ortólogo de CENP-E, foi colocada a hipótese de que pode haver uma relação entre o tamanho do cinetocoro e a dependência da atividade de CENP-E. Para testar esta hipótese, criou-se uma estirpe de *C. elegans* que expressa a sequência humana do CENP-E fundida com uma proteína do cinetocoro e interferiu-se com o alinhamento direto dos cromossomas devido à rápida bi-orientação através da depleção da cromocinesina klp-19. Verificou-se que a expressão do CENP-E é suficiente para atenuar os problemas de alinhamento dos cromossomas. Isto pode ser indicativo de que a presença de CENP-E pode conferir uma vantagem, no caso de a via direta de alinhamento estar comprometida. Em conclusão, estes resultados sugerem que as atividades motoras, quer no cinetocoro, quer mediadas pelos braços dos cromossomas, são importantes para o seu alinhamento correto.

TABLE OF CONTENTS

LIST OF ORIGINAL ARTICLES

The results and few sections of the introduction included in this thesis constitute research work of scientific articles published in international journals. In accordance with article 8º do Decreto-Lei nº 388/70, the author of this thesis declares that was involved in the conception and execution of the experimental work, in the interpretation of the results and in the redaction of the published/submitted manuscripts under the name of **Almeida AC**:

Almeida AC, Soares-de-Oliveira J, Drpic D, Cheeseman LP, Damas J, Lewin HA, Larkin D, Aguiar P, Pereira AJ, and Maiato H. Augmin-dependent microtubule self-organization drives kinetochore fiber maturation in mammals. Cell Reports. 2022 Apr 5; 39, 110610. DOI: 10.1016/j.celrep.2022.110610

Barisic M, **Almeida AC**, Maiato H. The Mitotic Spindle. (in Encyclopedia of Cell Biology, Academic Press, second ed. *to be published in 2023*)

Almeida AC, Drpic D, Okada N, Bravo J, Madureira M, Maiato H. Functional Dissection of Mitosis Using Immortalized Fibroblasts from the Indian Muntjac, a Placental Mammal with Only Three Chromosomes. Methods Mol Biol. 2020; 2101:247-266. DOI: 10.1007/978-1-0716-0219-5_16. PMID: 31879909.

Pereira A, Sousa M, **Almeida AC**, Ferreira LT, Costa AR, Novais-Cruz M, Ferrás C, Sousa MM, Sampaio P, Belsley M, Maiato H. Coherent-hybrid STED: high contrast sub-diffraction imaging using a bi-vortex depletion beam. Opt Express. 2019 Mar 18; 27(6):8092-8111. DOI: 10.1364/OE.27.008092. Epub 2019 Mar 5. PMID: 30894786; PMCID: PMC6420153.

Almeida AC, Maiato H. Chromokinesins. Curr Biol. 2018 Oct 8; 28(19):R1131-R1135. DOI: 10.1016/j.cub.2018.07.017. PMID:30300593; PMCID: PMC6402541.

Drpic D*, **Almeida AC***, Aguiar P, Renda F, Damas J, Lewin HA, Larkin DM, Khodjakov A, Maiato H. Chromosome SegregationIs Biased by Kinetochore Size. Curr Biol. 2018 May 7; 28(9):1344-1356.e5. DOI: 10.1016/j.cub.2018.03.023. **equal contribution*

LIST OF ABBREVIATIONS

ACA - Anti-Centromere Antiserum

APC/C - Anaphase Promoting Complex/Cyclossome

ATP - Adenosine Triphosphate

BAC - Bacterial Artificial Clones

BUB1/3 - Budding Uninhibited by Benzimidazoles 1/3

BUBR1 - BUB1-Related Protein 1

C. elegans - *Caenorhabditis elegans*

CCAN - Constitutive Centromere Associated Protein Network

Cdks - Cyclin-dependent kinases

CH-STED - Coherent-Hybrid Stimulated Emission Depletion

CIN - Chromosomal Instability

CLASP - CLIP-Associated Protein

CLIP-170 - Cytoplasmic Linker Protein 170

CREST - Calcinosis, Raynaud's Phenomenon, Esophageal Dysmotility, Sclerodactyly, and Telangiectasia

DNA - Deoxyribonucleic Acid

EM - Electron Microscopy

EML3 - Echinoderm Microtubule-associated protein-Like 3

FISH - Fluorescence *In Situ* Hybridization

FSM - Fluorescence Speckle Microscopy

GDP - Guanosine Diphosphate

GTP - Guanosine Triphosphate

HCC - Hepatocellular Carcinoma

HhH - Helix-hairpin-Helix

Hi-C - High-throughput Chromosome Conformation Capture

INCENP - INner CENntromere Protein

KMN - KNL-1, Mis12 complex, and Ndc80 complex

LECA - Last Eukaryotic Common Ancestor

MAD1/2 - Mitotic Arrest Deficiency 1/2

MAPs - Microtubule Associated proteins

MCAK - Mitotic centromere-associated kinesin

MCC - Mitotic Checkpoint Complex

MPF - M-phase Promoting Factor

MTOCs - Microtubule Organizing Centers

NEBD - Nuclear Envelope Breakdown

NEDD1 - Neural precursor cell expressed, Developmentally Down-regulated 1

Nod - No distributive disjunction

PCM - Pericentriolar Material

PEF - Polar Ejection Force

Plks - Polo-like Kinases

PP1 - Protein Phosphatase 1

PRC1- Protein Regulator of Cytokinesis 1

PtK1 - *Potorous tridactylus* Kidney Epithelial Cells

PTMs - Post-translational modifications

RAN - RAs-related Nuclear Protein

RCC1 - Regulator Of Chromosome Condensation 1

RNA - Ribonucleic Acid

RNAi - RNA interference

ROD - Rough-deal

RPE-1 - Retinal Pigment Epithelial-1

RZZ - Rod-ZW10-Zwilch

SAC - Spindle Assembly Checkpoint

SAS-6 - Spindle Assembly Abnormal protein 6

Ska1 - Spindle and kinetochore associated 1

STED - Stimulated Emission Depletion

STMN1 - Stathmin 1

TOG - Tumor Overexpressed Gene

TPX2 - Targeting Protein for Xklp2

β - Beta

α - Alpha

γ - Gamma

γ-TuRC - γ-Tubulin Ring Complex

LIST OF FIGURES

CHAPTER 1.

CHAPTER 2.

CHAPTER 2.1.

CHAPTER 2.2.

CHAPTER 2.3.

LIST OF TABLES

THESIS OUTLINE

Chapter 1 provides a broad overview of mitosis, that highlights its key components and regulatory elements required for faithful chromosome segregation. Additionally, it summarizes the current knowledge on mitotic spindle assembly and k-fiber formation models, chromosome congression and how this is regulated by multiple proteins, while emphasizing Augmin and CENP-E roles in these processes. Chapter 1 ends with the introduction of the model organism used throughout most of this work.

Chapter 2 describes the experimental work and the main results obtained in this thesis:

- Section 2.1. reflects the establishment of Indian muntjac as a model organism for the comprehensive study of mitosis. We knocked-down more than 60 conserved mitotic genes and investigated their roles for spindle assembly and chromosome segregation in Indian muntjac fibroblasts. This work underscores the added value of Indian muntjac cells as a model system, while offering an open access resource for the cell division community. Among the analyzed proteins, perturbation of the Augmin complex emerged as one of the most deleterious conditions for mitosis in this system. The remaining section 2.1. focuses on its in-depth characterization. Overall, we unveiled the contribution of Augmin-mediated microtubule amplification for k-fiber maturation and spindle assembly in mammals.
- Section 2.2. focuses on how kinetochore size impacts chromosome congression and segregation. By taking advantage of Indian muntjac fibroblasts, which we showed to be amenable for pharmacological inhibition and genetic manipulation, and high-resolution fixed/live-cell microscopy, we demonstrated that both chromosome congression and segregation are not random, instead are strongly biased by kinetochore size. The implications for chromosome segregation fidelity in metazoans are further discussed in section 2.2..
- Section 2.3. describes a side-project where we explored the relationship between CENP-E-mediated transport dependency and kinetochore size. Following on our previous observations that chromosomes with larger kinetochores rely less on the CENP-E-dependent pathway to congress to the spindle equator (described in section 2.2.), and the fact that various metazoans with holocentric kinetochores congress their chromosomes in the absence of a CENP-E ortholog, we engineered a *C. elegans* model expressing human CENP-E fused to a kinetochore protein. CENP-E expression partially rescued congression defects associated defective kinetochore microtubule attachments. The advantages of having two alternative pathways for chromosome congression are discussed in section 2.3..

Chapter 3 summarizes the main findings and conclusions of this thesis, while opening questions for future works.

CHAPTER 1.

STATE OF THE ART

'The gifts of microscopes to our understanding of cells and organisms are so profound that one has to ask: What are the gifts of the microscopist?' ...

(Daniel Mazia)

CHAPTER 1. STATE OF THE ART

1.1. The Cell Cycle

The cell cycle has been a field of interest for more than a century, since Robert Remak in 1852 proposed that all cells derive from pre-existing ones (Remak, 1855). Three years later, Rudolf Virchow reinforced this theory, culminating in what we recognize today as the modern 'cell theory' (reviewed in (Wilson, 1925)). The cell cycle can be generally described as a coordinated series of events that lead to DNA duplication and propagation into two genetically identical daughter cells. The sequence of events is characterized by its tight regulation and precision that ensure the control of each stage to preserve the chromosome number of the progenitors.

During the cell cycle of eukaryotic cells two major sequential phases guarantee the inheritance of the genetic material: interphase and M phase (also known as mitosis). During interphase the genome is replicated (synthesis phase or S phase), the cell grows and doubles its mass of proteins and organelles in preparation for mitosis. Typically, this process takes up to 23 hours of a 24-hour cycle, with the remaining time dedicated to mitosis. The 'gap' between mitosis and the onset of DNA duplication is known as G_1, and the 'gap' between S and M phases is called G_2. In the absence of specific mitogenic signals, cells can remain in a reversible quiescent state where proliferation is stopped, known as G_0 (Figure 1.1.) (reviewed in (Alberts et al., 2017)).

1.1.1. Cell cycle regulation

Cell cycle progression is monitored by specific proteins that are expressed and/or degraded at critical transitions, coordinating the unidirectionality and the switch-like behavior of the four cell cycle stages (G_1, S, G_2, M phase) (Figure 1.1.). These protein complexes have regulatory subunits called Cyclins, which fluctuate in phase with the cell cycle, and catalytic subunits named Cyclin-dependent kinases (Cdks) required for the phosphorylation of many substrates involved in cell cycle progression (Nurse, 1975). The activity of Cdks vary as cell cycle progresses due to the oscillations of the interacting cyclins. Each Cyclin-Cdk complex ensures the next stage in sequence, promoting the ordered transition between cell cycle stages (reviewed in (Nurse, 2000)). In metazoans it has been identified three Cdks that regulate interphase (Cdk2, Cdk4 and Cdk6), one mitotic Cdk (Cdk1) and a few Cyclins which play critical roles in the cell cycle (Cyclins -A, -B, -C, -D and -E) (reviewed in (Martinez-Alonso and Malumbres, 2020)). While C- and D-Cyclins monitor cell cycle entry from quiescence and progression throughout G_1 phase, Cyclin D promotes the activation of Cdk4 and Cdk6 in preparation for DNA replication. Entry into S phase is determined by Cyclin E-dependent Cdk2 activation and is regulated by Cyclin A-dependent Cdk2 and Cdk1 activities which control DNA synthesis and mediate progression through G_2 phase (Pagano et al., 1992; Roy et al., 1991). Moreover, Cyclin A is responsible for the activation of Cyclin B-Cdk1 complex, the major regulator of mitotic entry and chromosome segregation.

During late G_2/early M-phase, Cyclin B binds to Cdk1 and phosphorylates multiple substrates required for the structural and regulatory re-organization that accompany cell division (reviewed in (Alvarez-Fernandez and Malumbres, 2014)). After nuclear envelope breakdown (NEDB), Cyclin A-Cdk1 levels decrease to facilitate the initial stabilization of the attachments between chromosomes and the mitotic spindle (Kabeche and Compton, 2013). This complex is ultimately degraded before metaphase by the Anaphase-Promoting Complex/Cyclossome (APC/C), a multiprotein E3 ubiquitin ligase that targets proteins for proteasomal degradation (den Elzen and Pines, 2001; Geley et al., 2001; Minshull et al., 1990). Cyclin B-Cdk1, also known as M-phase Promoting Factor (MPF) (Nurse, 1990), directly regulates mitosis until all chromosomes are correctly attached to spindle microtubules. At this point, APC/C targets Cyclin B for degradation, which consequently decreases Cdk1 activity, thus triggering anaphase onset (reviewed in (Alfieri et al., 2016; Dick and Gerlich, 2013; Holder et al., 2019; Pines, 2011)) (Figure 1.1.).

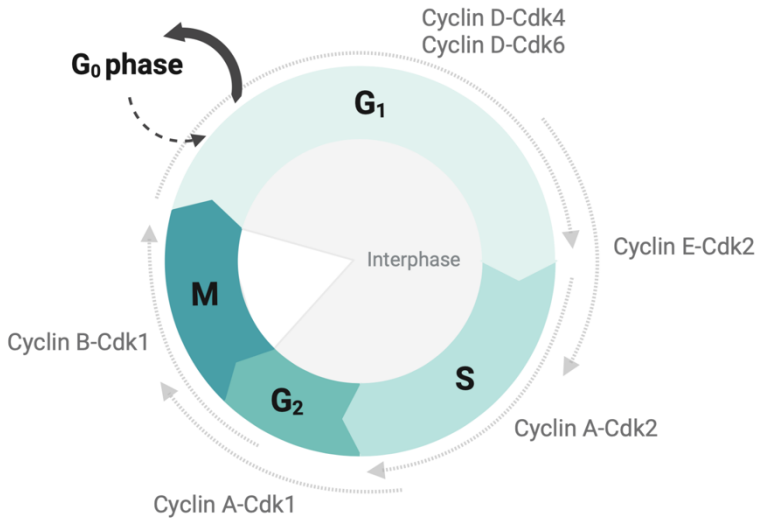

Figure 1.1. Schematic representation of the cell cycle regulation in eukaryotic cells.

The cell cycle is composed by four highly regulated phases, G_1- Gap_1, S- Synthesis phase, G_2- Gap_2 phase and M-Mitosis. Cyclins D and C (not shown) mediate cell cycle entry and exit from the quiescent state (G_0 phase). At G_1, Cyclin D-Cdk4 and -Cdk6 levels increase in preparation for the DNA replication. S-phase is initiated by the rising levels of Cyclin E-Cdk2 and maintained by Cyclin A-Cdk2 activity. Cyclin A-Cdk1 activity controls protein synthesis during G_2 and mitotic entry. Cyclin B-Cdk1 is the master regulator of mitotic progression and chromosome segregation.

The unidirectionality of the cell cycle is additionally ensured by the existence of several checkpoints that monitor and promote correct cell cycle progression (Hartwell and Weinert, 1989). In the presence of stress stimuli or errors, checkpoints induce a cell cycle delay to facilitate the repair and/or damage resolution. Two of these checkpoints delay cells in interphase (before entering mitosis), offering protection against DNA damage and replication errors. If the repair is unsuccessful, cells may enter senescence, undergo apoptosis or DNA may accumulate alterations

which ultimately leads to genomic instability and cell transformation (reviewed in (Barnum and O'Connell, 2014)). A third checkpoint that ensures the quality of cell cycle progression is the Spindle Assembly Checkpoint (SAC) (reviewed in (Musacchio, 2015)). The SAC monitors the attachment status between a specialized structured at the chromosomes composed by more than one hundred of proteins, named kinetochore, and the fibrous polymers that form the mitotic spindle, known as microtubules (reviewed in (Lara-Gonzalez et al., 2021)) (see section 1.2.2.1. for details).

1.2. Mitosis

Mitosis was first described in the early 1880's by Walther Flemming, a German geneticist who captured with remarkable precision the sequence of events and cellular transformations that occur during cell division, based on the observation of Salamander cells by light microscopy (Flemming, 1882). At a time, when no good histological methods existed, Flemming formulated a fine mixture of osmic, glacial, and chromic acetic acids that preserved cells' structures (*'Flemming's solution'*). Together with haematein and haematoxylin dyes he observed that the nuclear 'chromatin' (stainable material) of the mother cell rearranged into threads (chromosomes) that migrated to the center of the cell and were then separated into two groups, giving rise to two daughter nuclei. Hereafter, he termed this process 'mitosis' (from the Greek '*mitos'*, thread and modern Latin '*osis'*, process).

Despite all the descriptive groundwork, the mitotic spindle was regarded as artefactual for many years (reviewed in (Inoue, 2008; Paweletz, 2001)), until two optical breakthroughs changed the paradigm. The invention of polarized light microscopy (Schmidt, 1937; Schmitt, 1939) allowed for the first time the observation of a birefringent fibrous structure that enclosed the chromosomes during mitosis (the mitotic spindle) (Inoue, 1953). Furthermore, the incorporation of a camera into the microscope, together with the invention of phase contrast microscopy granted time-lapse recordings of the entire process of mitosis (Bajer, 1957; Hughes, 1952; Inoue and Bajer, 1961; Zernike, 1955). Combined efforts of many discoveries allowed the division of mitosis into five successive stages: prophase, prometaphase, metaphase, anaphase, and telophase (Figure 1.2.).

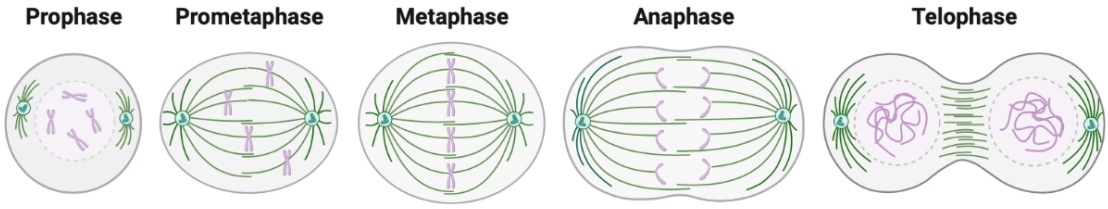

(figure legend on the next page)

Figure 1.2. Schematic representation of the mitotic stages.

At prophase, chromosomes become highly condensed, and centrosomes start to migrate to opposite poles. After NEBD, spindle microtubules interact and attach to kinetochores (prometaphase), such that chromosomes can bi-orient and align at the spindle equator (metaphase). As soon as all kinetochores are correctly attached to microtubules, the poleward movement of chromosomes is initiated (anaphase). The nuclear envelope begins to reform around the two daughter cells, and the DNA begins to decondense (telophase). Finally, the physically separation of the cytoplasm allows the segregation of the two daughter nuclei into individual cells (cytokinesis, not represented).

1.2.1. Brief overview of mitosis

Prophase initiates with the condensation of the previously duplicated DNA into the form of chromosomes, and with the coordinated migration to opposite directions of the replicated centrosomes, the main microtubule organizing centers (MTOCs) in metazoans. Centrosomes consist of a pair of centrioles embedded in a pericentriolar material (PCM) where multiple copies of γ-tubulin ring complexes (γ-TuRCs) are clustered together to mediate nucleation of new microtubules (Conduit et al., 2015; Snyder and McIntosh, 1975). Prometaphase begins with the disruption of the nuclear envelope, forcing the invasion of the nuclear space by microtubules (reviewed in (Ferreira and Maiato, 2021)). Hereafter, the chromosomes congress and align at the spindle equator, forming a metaphase plate (reviewed in (Kapoor, 2017; Maiato et al., 2017)). When all sister chromatids are correctly attached to microtubules, they are pulled and separated synchronously towards opposite poles. During the first moments of anaphase, sister chromatids lose cohesion and kinetochore-microtubules shorten (anaphase A), pulling the chromosomes poleward. The spindle elongates while the two poles move further apart, bringing the chromosomes with them into what will become two daughter cells (anaphase B) (reviewed in (McIntosh, 2021)). The two sets of daughter chromatids start to decondense, and the nuclear envelope reassembles around each nucleus (telophase). From mid anaphase, a contractile ring of actin and myosin II filaments is shaped, dividing the cytoplasm in two halves, each with an identical copy of the genome (cytokinesis) (reviewed in (McIntosh and Hays, 2016)).

1.2.2. Mitosis regulation

First attempt to characterize how mitotic entry is regulated remounts to 1950 when an ‘antephase’ was proposed to precede mitosis, during which the commitment to division could be reverted (Bullough and Johnson, 1951). In the presence of stress signals during G_2 phase, p38 protein kinase becomes activated and phosphorylates Cdc25B phosphatase, thus inducing its exclusion to the cytoplasm (Mikhailov et al., 2005). Here, Cyclin A-Cdk2 and Cyclin B-Cdk1 inhibitory signals dictate a delay in G_2 phase (Mikhailov et al., 2005). Furthermore, in the presence of DNA replication stress it was shown that Emi1, a mitotic inhibitory protein, accounts for the premature activation of APC/C, consequently blocking mitotic entry (Feringa et al., 2016; Hornsveld et al., 2021). On the contrary, some years later a ‘point of no return’, in which cells had to continue

division without reverting their fate, was described. In fact, Rieder and Cole described a G_2/M checkpoint from where early prophase could be reversible but not late prophase (Rieder and Cole, 1998). At this stage, Cyclin B-Cdk1 is rapidly activated, and the cell is no longer capable of its inactivation, being committed to mitosis. Likewise, polo-like kinases (Plks) and Aurora-B kinase assume an important role phosphorylating several substrates required for further Cyclin B-Cdk1 activation, centrosome maturation and chromosome condensation, respectively (reviewed in (Bruinsma et al., 2012; Colicino and Hehnly, 2018; Giet and Glover, 2001)).

1.2.2.1. Mitotic checkpoints

Once at mitosis, the SAC provides a universal safety mechanism that promotes chromosome segregation fidelity by monitoring the kinetochore-microtubule attachments status. First studies in 1991 identified several genes that conferred the ability to arrest in mitosis in the presence of spindle poisons. By performing a screen in *Saccharomyces cerevisiae*, the authors characterized MAD (mitotic-arrest deficient) genes MAD1, MAD2 and MAD3 (BUBR1 in humans) and BUB (budding uninhibited by benzimidazole) genes BUB1, BUB2 and BUB3 (Hoyt et al., 1991; Li and Murray, 1991). Several of these genes are conserved in eukaryotes, and collectively constitute the checkpoint that induces a mitotic delay to avoid the precocious loss of cohesion and separation of sister chromatids. In the presence of unattached kinetochores (i.e., at prometaphase), SAC catalyzes the formation of the mitotic checkpoint complex (MCC), a heterotetramer composed by Cdc20, MAD2, BUBR1 and BUB3. This complex, known as the SAC effector, binds to the APC/C and inhibits its ubiquitin-ligase activity, thus preventing anaphase onset. Once all chromosomes align and bi-orient at the spindle equator, tension between kinetochores and microtubules stabilizes the attachments, thus promoting SAC satisfaction. SAC proteins are then stripped from the kinetochores along microtubules by Dynein-mediated motor activity (Howell et al., 2001; Wojcik et al., 2001). Removal of SAC proteins from kinetochores dictates the full activation of APC/C, which targets Securin and Cyclin B for proteasomal degradation, ultimately leading to the hallmark changes of anaphase (reviewed in (Lara-Gonzalez et al., 2021; Lara-Gonzalez et al., 2012)).

Recent evidence proposed the existence of a regulatory element during anaphase-telophase transition that ensures proper chromosome separation and promotes anaphase error correction during cell division. This ‘Chromosome Separation Checkpoint’ is centered on a constitutive midzone-based Aurora-B phosphorylation gradient, that monitors and delays nuclear envelope reformation and chromosome decondensation until efficient separation of sister chromatids during anaphase is achieved (Afonso et al., 2014; Maiato et al., 2015). More recently, Aurora-B kinase has been suggested to stabilize kinetochore-microtubule attachments and assist spindle forces during early anaphase to promote rapid correction of lagging chromosomes. This surveillance mechanism prevents micronuclei (chromosome fragments or whole chromosomes

that lag behind in anaphase and are excluded from the main nuclei) formation from frequent chromosome segregation errors (Orr et al., 2021; Sen et al., 2021).

1.3. The Mitotic Apparatus

Experimental research carried over several years had shown that faithful chromosome segregation during cell division, relies on the assembly and regulation of a highly complex molecular 'machine' - the mitotic apparatus. Its main function is to equally distribute the chromosomes into two daughter cells during mitosis, thus preserving genomic stability. Accurate spindle assembly is an absolute requirement for normal tissue development and relies on the action of hundreds of proteins that contribute to chromosome capture and subsequent movement during mitosis.

1.3.1. Centrosomes

The centrosomes were first spotted and studied by Edouard Van Beneden towards the end of the nineteenth century. A few years later, Theodor Boveri and Walther Fleming coined the terms 'centrosome' (due to its localization at the center of the cell) and 'centriole', respectively (Beneden, 1876; Boveri, 1900; Wilson, 1925). 'Canonical' centrosomes consist of a pair of cylindrical microtubule-based structures termed centrioles, embedded in PCM where γ-tubulin ring shaped multiprotein complexes (γ-TuRCs) localize to nucleate microtubules (reviewed in (Conduit et al., 2015)). The lattice of the cylinders is formed of nine triplets of microtubules, which confer a symmetric organization to centrioles (cartwheel shape) (reviewed in (Nigg and Holland, 2018)) (Figure 1.3. A). Each centrosome has one older centriole (mother) and a newly assembled one (daughter), that normally organize orthogonally to each other. Centrosomes are involved in diverse cellular processes such as cell migration, regulation of cell shape and cell division. Accurate control over centrosome number is vital, as both increased and decreased centrosome numbers can cause severe errors in cell division, leading to aneuploidy and tumor development. In addition, supernumerary centrosomes may contribute to tumor cell invasiveness and can deregulate centrosome-based signaling pathways (Ben-David and Amon, 2020; Godinho and Pellman, 2014; Nigg and Holland, 2018; Wilhelm et al., 2019).

Interestingly, the fact that spindle formation occurs in cells that are naturally devoid of centrosomes, such as female oocytes or land plants (Bonaccorsi et al., 1998; Megraw et al., 2001; Wadsworth and Khodjakov, 2004), or after experimental centrosome inactivation in animal somatic cells (Hinchcliffe, 2011; Hinchcliffe et al., 2001; Khodjakov et al., 2000), suggests the existence of redundant MTOCs that contribute to spindle assembly. In support of this theory, microtubules have been found to nucleate at non-centrosomal sites, even in cells containing centrosomes (De Brabander et al., 1981; Nicklas and Gordon, 1985; Witt et al., 1980) (see section 1.4.2. for in-depth characterization).

1.3.1.1. The centrosome cycle

In proliferating cells, centrosomes are duplicated in interphase and separated at the onset of mitosis (Figure 1.3. B). Centriole doubling initiates at the G_1-S transition where one procentriole (a short immature centriole) is formed adjacently to the pre-existing parental ones. This event is under the control of Plk4 and activation of the centriolar protein SAS-6 (Puklowski et al., 2011; Strnad et al., 2007). Once formed, procentrioles elongate and mature throughout S- and G_2-phases and each centrosome initiates PCM recruitment. Once at late interphase, the two centrosomes separate and migrate towards opposite poles of the cell. Mitotic centrosomes are highly enriched in PCM, allowing them to organize the mitotic spindle by promoting microtubule polymerization and focusing the spindle poles. After mitosis, each daughter cell inherits one centrosome, with a pair of centrioles (reviewed in (Bettencourt-Dias and Glover, 2007)).

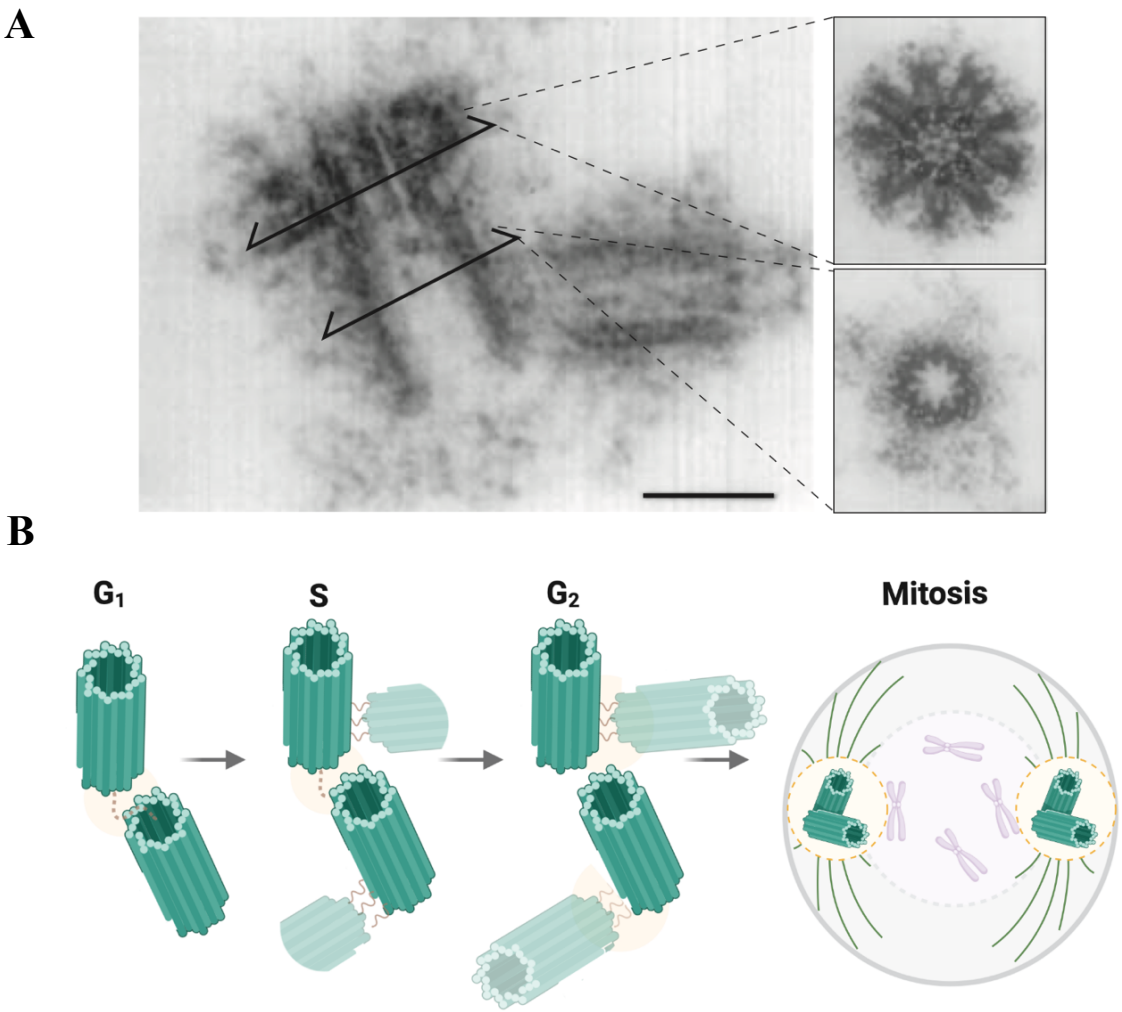

(figure legend on the next page)

Figure 1.3. Representation of a 'canonical' centrosome and its replication cycle within animal cells.

A, Electron micrograph of the centrosome. The top inset indicates a cross-section of subdistal appendages; the bottom inset indicates a cross-section of the proximal part of the centriole. Scale bar: 0.2 μm. Adapted from (Bettencourt-Dias and Glover, 2007). **B,** Diagram representing the centriole replication cycle. At mitotic exit–early G_1 phase, the centrioles disengage and lose the orthogonal configuration Daughter centrioles start to originate from the mother centrioles at G_1-S phase, originating 2 pairs of procentrioles (light green). During G_2, the linkage between centrosomes is disrupted and the maturation/elongation process initiates giving rise to two mature centrosomes. At G_2-M transition, centrosomes further migrate apart from each other, recruit PCM and begin to behave as MTOCs (centrosomes highlighted in the yellow circle).

1.3.2. Kinetochore

Early drawings of mitosis revealed that the interaction between chromosomes and spindle microtubules was mediated by a proteinaceous structure at the centromeric region of chromosomes (reviewed in (Cheeseman and Desai, 2008; Kops and Gassmann, 2020; Monda and Cheeseman, 2018)). Due to its ability to move chromosomes, it was named kinetochore (from the Greek '*kinetos'*, movement and '*chore'*, place) in the early 1930's by Lester Sharp (following the suggestion of J.A. Moore) (Sharp, 1934). Electron Microscopy (EM) studies were used to characterize a kinetochore as a three-layered disk structure, composed of two electron dense regions: an inner and outer plate separated by a 20-30 nm low contrast gap. An electron-dense plate called the fibrous corona, lies at the periphery of the outer kinetochore, and extends up to 250-1000 nm (Bielek, 1978; Brinkley and Stubblefield, 1966; Cleveland et al., 2003; Rieder and Alexander, 1990; Roos, 1973) (Figure 1.4. A, C). Once microtubules occupy the kinetochores, the last compacts and the corona can no longer be distinguished (Figure 1.4. B-C). Interestingly, mammalian kinetochores change from a 'ball and cup' ('spheric ball' of fibrillar material inserted into a dense 'cup') before prophase to a plate-like structure covered with fibrillar material in mitosis (Rieder, 1982).

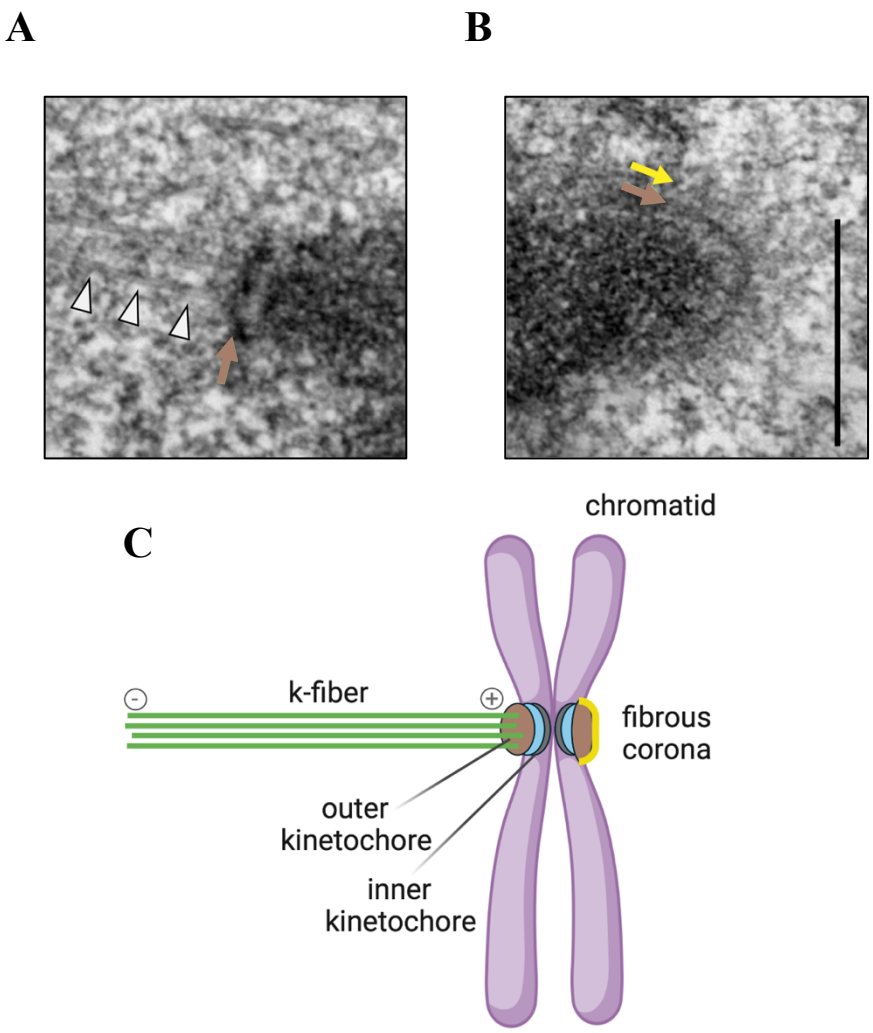

Figure 1.4. Kinetochore structure.

EM images of human RPE-1 cells show the distinct kinetochore morphology when (**A**) attached to the plus ends of spindle microtubules (k-fibers) and (**B**) treated with a microtubule poison (3 μM nocodazole) for 10 minutes. At metaphase, microtubules (white arrowheads) are embedded end-on at the outer kinetochore plate (brown arrow) and fibrous corona material is not visible. In the absence of microtubules, the fibrous nature of the corona material (yellow arrow) is visible, and the outer kinetochore plate (brown arrow) is enlarged. Scale bars: 0.5 μm. Adapted from (Kops and Gassmann, 2020). **C**, schematic representation of a prometaphase mitotic chromosome in which one sister kinetochore is attached to microtubules (k-fiber) and the other sister kinetochore is in an unattached state characterized by formation of an expanded outermost domain, the fibrous corona.

1.3.2.1. Structure and composition

Kinetochore inner plate is closely associated with centromeric DNA and it is composed by a constitutive centromere associated protein network (CCAN), a sixteen-component (CENP-S/T/X/W; -C/N/L; -H/I/K/M; -O/P/Q/U/R) that recognizes centromeric nucleosomes and establishes the link between the inner kinetochore and outer kinetochore proteins (reviewed in (Cheeseman and Desai, 2008; McKinley and Cheeseman, 2016; Suzuki et al., 2014)). Conversely to the constitutive localization of inner proteins throughout the cell cycle, outer components are

loaded in the beginning of prophase and leave the kinetochore at anaphase onset or when they disassemble at the end of mitosis. The CCAN components CENP-C and CENP-T recruit multiple copies of the ten-subunit KMN network to the kinetochore which includes KNL1, Zwint, Mis12 complex (Mis12, Nnf1, Nsl1, and Dsn1), and the Ndc80 complex (Ndc80, Nuf2, Spc24, and Spc25) (reviewed in (McKinley and Cheeseman, 2016)). The assembly of the KMN network provides the core microtubule attachment sites via Ndc80 complex, and works as docking site for SAC proteins, plus-end-tracking microtubule proteins and motor proteins (reviewed in (Cheeseman and Desai, 2008; Kops and Gassmann, 2020; Santaguida and Musacchio, 2009)).

1.3.3. Microtubules

The most abundant component of mitotic spindles are microtubules, cytoskeleton straw-shaped structures that organize in different populations inside the cell. In a series of experiments, it was revealed that spindle 'threads', which we now know to be microtubules, disappeared by lowering the temperature, by adding microtubule disassembling agent colchicine or by increasing hydrostatic pressure (reviewed in (Inoue, 2008)). This process was reversible by increasing the temperature, washing-out colchicine from the medium, or after pressure release, suggesting a dynamic and polymeric nature of microtubules. Later, by isolating and identifying the target of colchicine, it was confirmed that microtubules are indeed polymers, and tubulin is their main building unit (Borisy and Taylor, 1967; Mohri, 1968).

1.3.3.1. Structure

Research over the following decades revealed that each microtubule is a hollow cylindrical structure assembled from α- and β-tubulin dimers, that associate longitudinally with γ-TuRCs (reviewed in (Kollman et al., 2011; Nogales, 2001)). These cone-shaped proteins work as template for the assembly of a ring of thirteen protofilaments that form a growing microtubule in eukaryotic cells (Tilney et al., 1973). γ-TuRC makes microtubule minus ends less dynamic by working as a microtubule cap, while providing the template for microtubule growth and defining their polarity (Kollman et al., 2011). The head-to-tail arrangement of α- and β-tubulin heterodimers generates the intrinsic polarity of microtubules, with α-tubulin at the so-called minus-end (slow addition of new subunits) and β-tubulin at the plus end, where most tubulin subunits are added.

1.3.3.2. Spindle Microtubules

The mitotic spindle is a hallmark of mitosis, composed of three broad categories of microtubules: kinetochore microtubules, astral microtubules, and interpolar microtubules (Figure 1.5.). In mammals, kinetochore microtubules organize into bundles that attach at the kinetochore region on each chromosome, termed kinetochore (k)-fibers (Begley et al., 2021; Godek et al., 2015; Rieder, 1982). These structures are essential to maintain chromosome position at the metaphase

plate, kinetochore oscillations, as well as for operating the forces required to separate chromosomes during anaphase (Cai et al., 2009; Nicklas et al., 1982) (see sections 1.7. and 1.7.1 for further discussion). Astral microtubules radiate from centrosomes at the spindle poles and interact with the cell cortex to ensure correct spindle positioning, whereas interpolar microtubules assist the separation of the spindle poles during anaphase and provide key structural modules that account for spindle mechanical and dynamic properties (Dumont and Mitchison, 2009; Elting et al., 2018; Vukusic and Tolic, 2021).

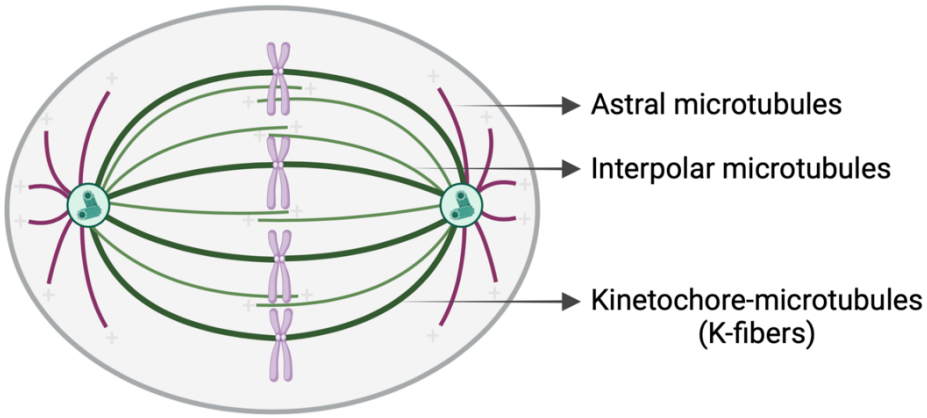

Figure 1.5. Different microtubule populations form the mitotic spindle.

Emerging from the spindle poles towards the cortex, astral microtubules (shown in magenta) are involved in spindle positioning and spindle length control. In dark green are represented the k-fibers, the most stable population of microtubules, required to bind chromosomes (light pink). In light green are shown interpolar-microtubules, important for maintaining spindle bi-polarity and stability. Centrosomes at both spindle poles are represented as green cylinders.

1.3.3.3. Dynamics

Tubulins use guanosine triphosphate (GTP) hydrolysis to regulate microtubule assembly. Although they belong to the GTP-binding proteins family, only β- subunit acts as a GTPase once a new heterodimer is added (Linse and Mandelkow, 1988). After GTP hydrolyzation into guanosine diphosphate (GDP), tubulin heterodimers tend to bend, which destabilizes the linear array and results in microtubule plus-end depolymerization. This, however, happens with a delay that is long enough to allow the accumulation of GTP-bound β-tubulin at the plus ends and the formation of a GTP-cap, which keeps the heterodimers straight and, consequently, stabilizes the protofilaments (Figure 1.6. A). Even though GTP starts being hydrolyzed, lateral interactions between the tubulin protofilaments prevents previously integrated heterodimers from bending and contributes to energy storage along the microtubule lattice (reviewed in (Howard and Hyman, 2009; Prosser and Pelletier, 2017)). Sudden loss of the GTP-cap causes curving of tubulin heterodimers and rapid depolymerization of microtubule plus-ends (Figure 1.6. B) accompanied

by the release of stored energy on the lattice of microtubules. This can be harvested to facilitate cell division, e.g., to promote the movement of chromosomes bound to depolymerizing microtubules (Chretien et al., 1995; Mandelkow et al., 1991). The transition from growth to shrinkage is termed 'catastrophe', whereas regrowth of shrinking microtubules upon the recovery of their GTP-cap is called 'rescue'. The ability of microtubules to rapidly switch between these two states is termed 'dynamic instability' (Mitchison and Kirschner, 1984) (Figure 1.6. C). Microtubules become more dynamic at mitotic entry, when the interphase cytoskeleton rapidly remodels to form the mitotic spindle (reviewed in (Ferreira and Maiato, 2021)).

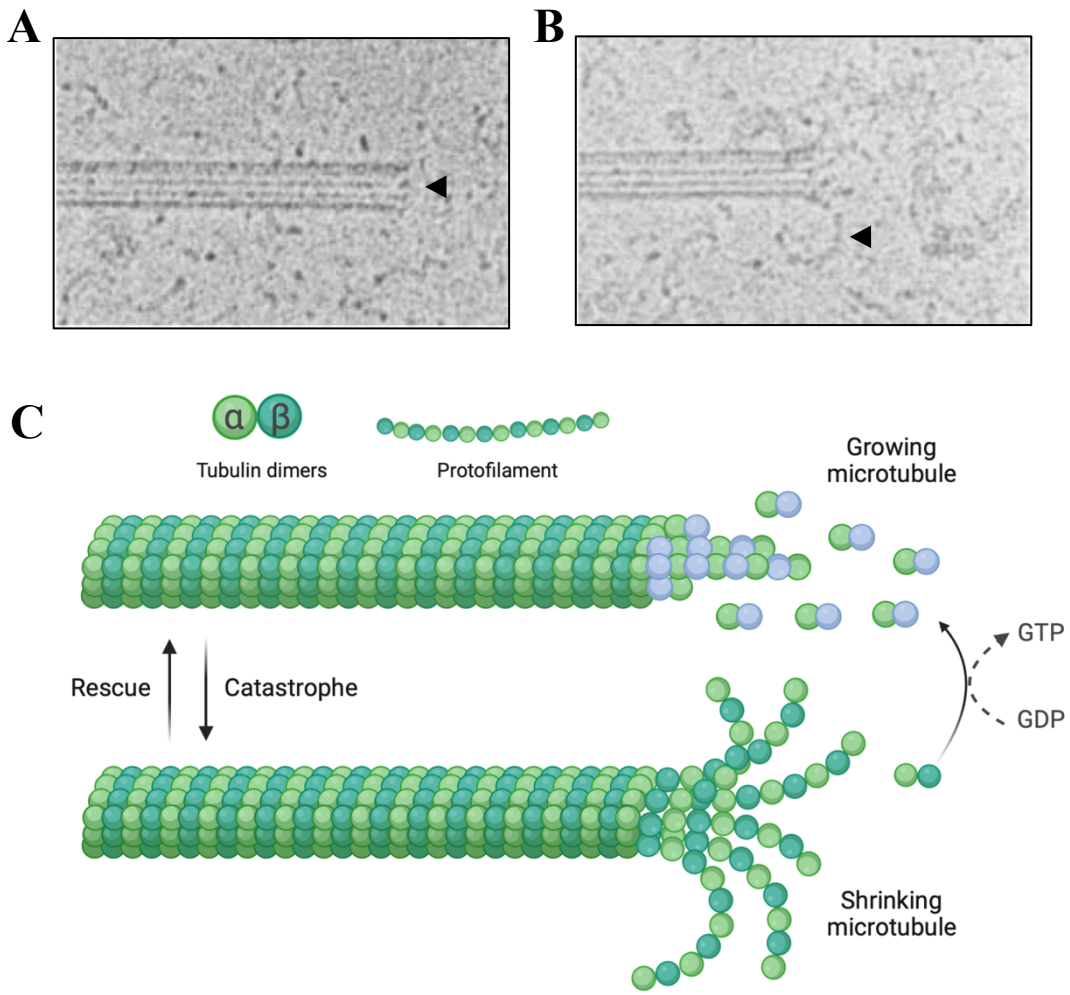

Figure 1.6. Microtubule structure and dynamic instability.

Electron micrographs of (**A**) growing microtubules (exhibit blunt ends, black arrowhead) and (**B**) shrinking microtubules (shown bent protofilaments, black arrowhead). Adapted from (Mandelkow et al., 1991). **C,** Schematic representation of microtubule structure and dynamic instability at the plus ends. Microtubules are polymers of α- and β-tubulin, arranged in a head-to-tail fashion and typically composed of 13 protofilaments. Microtubules possess a dynamic plus end and a less dynamic minus end. The mechanism of microtubules polymerization (growing) and depolymerization (shrinking) is mediated by the exchange of a GTP (blue subunit) on the β-tubulin monomer. GTP-tubulin subunits are incorporated at the plus tip, thus allowing the microtubule to grow (rescue). The transition from a period of growth to shrinkage is called a catastrophe.

1.3.3.3.1. Microtubule Turnover

The development of microscopy techniques such as photo-bleaching, photo-activation and photo-conversion revealed that spindle microtubules turnover rapidly, exhibiting typical half-times of several seconds to several minutes (reviewed in (Girao and Maiato, 2020)). This led to the identification of at least two spindle microtubule populations with distinct turnover dynamics that have been attributed to less stable non-kinetochore microtubules and more stable kinetochore microtubules, respectively (Zhai et al., 1995). Moreover, microtubule turnover also varies within the same microtubule population depending on the mitotic stage. For instance, kinetochore microtubules become more stable throughout mitosis, with their turnover rate decreasing from prometaphase to metaphase and finally to anaphase (Girao and Maiato, 2020; Gorbsky and Borisy, 1989; Warren et al., 2020; Zhai et al., 1995). This appears to be dependent on inter-kinetochore tension (Nicklas and Koch, 1969) and on Cdk1 kinase activity. Perturbation of microtubule turnover interferes with SAC signaling which leads to mitotic arrest (high microtubule turnover) or compromises chromosome segregation fidelity (low microtubule turnover) (Godek et al., 2015).

1.3.3.3.2. Microtubule Flux

In metaphase, although spindle size and shape are at steady-state, microtubules remain highly dynamic. This translates into another dynamic property, called microtubule poleward flux (Mitchison, 1989). Flux is defined by the translocation of tubulin dimers added at the microtubule plus ends and their simultaneous removal at the minus-ends of microtubules, generating a continuous poleward motion of tubulin subunits (or treadmilling). Although undetectable in yeast, this feature is highly conserved in higher eukaryotes and significant advances in the investigation of this cellular phenomenon were achieved using Fluorescence Speckle Microscopy (FSM), which offer higher sensitive than photoconversion and photoactivation techniques (reviewed in (Barisic et al., 2012)). FSM-based studies revealed that different classes of microtubules display different flux rates; for instance, that astral microtubules do not flux (LaFountain et al., 2004; Maddox et al., 2003). Current models of spindle microtubule flux are mainly based on one of the two force-generating mechanisms: the ‘treadmilling-like’ model (i.e. via microtubule depolymerization at the spindle pole coupled with polymerization at the kinetochore) and the kinesins-mediated microtubule-sliding model (reviewed in (Barisic et al., 2021a)). The first debates that flux is driven by kinesin-13 mediated depolymerization at microtubule minus ends coupled with CLASPs-mediated plus-ends polymerization at kinetochores (Ganem et al., 2005; Maiato et al., 2003a; Maiato et al., 2005). The second argues that microtubule flux relies on the coupling of microtubules within the spindle (Itabashi et al., 2009; Shimamoto et al., 2011), likely through the action of microtubule crosslinking proteins. In this model, microtubule crosslinkers

transduce the force generated by motor-driven sliding of interpolar microtubules (Brust-Mascher and Scholey, 2002; Matos et al., 2009; Pereira and Maiato, 2012; Vukusic et al., 2017). Remarkably, this function has been recently attributed to the coordinated action of four kinesis in human cells. The collaborative interpolar microtubule-sliding activity of Eg5 and Kif15 is sequentially supported by CENP-E at kinetochores during prometaphase, and Kif4a on chromosome arms during metaphase. The resulting outward sliding force of interpolar microtubules is then transmitted to k-fibers via microtubule crosslinking proteins like NuMA and HSET, licensing k-fibers to flux and facilitating the uniform distribution of spindle forces on metaphase chromosomes. These flux-promoting sliding activities are counteracted by Kif2a microtubule depolymerizing activity at spindle poles.

Poleward pulling forces generated by the activity of the four kinesins promote the maintenance of steady-state mitotic spindle length, by suppressing MCAK-mediated microtubule-depolymerizing activity at kinetochores and by promoting CLAPs-dependent polymerization of kinetochore-microtubules (Barisic and Rajendraprasad, 2021; Steblyanko et al., 2020).

Perturbation of poleward microtubule flux by co-depletion of kinesin-13 proteins Kif2a and MCAK results in attenuated flux velocity, accompanied by a significant increase of lagging chromosomes frequency during anaphase. Noteworthy, the error rates were higher in non-fluxing cells, highlighting the importance of flux *per se* to the correction of erroneous kinetochore-microtubule attachments (Ganem et al., 2005). One alternative explanation is that microtubule flux drives microtubule slippage at kinetochores, which facilitates error correction and equal distribution of spindle forces along the metaphase chromosomes (King and Nicklas, 2000; Matos et al., 2009; Pereira and Maiato, 2012). More specifically, experimental attenuation of microtubule flux in Drosophila S2 cells significantly impaired anaphase synchrony, resulting in more than twice the number of cells with merotelic chromosome attachments (one kinetochore is attached to microtubules from opposite spindle poles; see section 1.7.2.) (Matos et al., 2009).

1.3.3.4. Tubulin Code

At the resolution of optical microscopes, all microtubules look similar, but this is deceptive. Microtubules are composed of multiple tubulin isoforms and functionalized with diverse post-translational modifications (PTMs). This microtubule diversity has been named as the ‘tubulin code’ (Janke and Bulinski, 2011; Verhey and Gaertig, 2007; Yu et al., 2015). Most of tubulin PTMs such as, phosphorylation, acetylation, polyglutamylation and detyrosination, label distinct α- and β-tubulin isotypes to program these microtubules for specific physiological functions in diverse cellular processes (reviewed in (Janke and Magiera, 2020; Roll-Mecak, 2020)). How cells read and write the tubulin code is poorly understood. However, new advances and tools

for *in vitro* and *in vivo* tubulin manipulation, and the identification of a list of tubulin-modifying enzymes are now encouraging the study of this fundamental problem.

In mitosis, due to their intrinsic dynamic nature, spindle microtubules are vastly tyrosinated (most gene-encoded α-tubulin isoforms carry a last-tyrosine residue at their C-terminal tail). Spindle microtubules become gradually stabilized due to the establishment of end-on attachments with kinetochores, as well as, by interacting with interpolar microtubules, and become increasingly detyrosinated (enzymatic removal of the last tyrosine residue from the α-tubulin C-terminal tail) These modifications have been shown to have different physiological roles, while conferring higher or lower affinities for certain motor-proteins to transport their cargos, and to perform their functions (reviewed in (Janke and Magiera, 2020; Roll-Mecak, 2020)) (see section 1.6.). For instance, tyrosinated astral microtubules are essential for spindle orientation/position, as kinesin-13 depolymerases that regulate astral microtubule length, and Dynein at the cell cortex are regulated by this PTM (Janke and Magiera, 2020). Additionally, centriolar microtubules have high levels of polyglutamylation (binding of polyglutamate to specific glutamate residues in the C-terminal tail of both α- and β-tubulin), which is essential for centrosome integrity throughout mitosis.

Importantly, several works have reported an emerging link between alterations of tubulin PTMs and/or associated modifying enzymes with certain cancers. These alterations often correlate with specific cancer properties, including poor prognosis, metastasis, and resistance to chemotherapeutic drugs, supporting the potential use of cancer tubulin isotypes and/or PTM signatures for therapeutic purposes (reviewed in (Lopes and Maiato, 2020)).

1.3.4. Microtubule associated proteins and Motor proteins

Microtubules in living cells exhibit a more dynamic behavior compared to microtubules reconstituted *in vitro*, which suggests the existence of additional stabilizing and destabilizing factors in living cells (Desai and Mitchison, 1997). Many microtubule-associated proteins (MAPs) and motor proteins that affect microtubule stability were found through biochemical and proteomic approaches, as well as genetic and genome-wide RNA interference (RNAi)-based screens (Bodakuntla et al., 2019; Bonner et al., 2011; Gache et al., 2010; Maiato et al., 2004c). While MAPs directly influence microtubule stability through the interaction with the microtubule lattice and/or ends, motor proteins use ATP hydrolysis to provide the energy either to cross-link and slide microtubules relative to adjacent microtubules or other structures; or to destabilize the microtubule lattice and to transport different cargos along the surface of microtubules which equally impacts the efficiency of mitotic spindle assembly (reviewed in (Bodakuntla et al., 2019)).

1.3.4.1. Microtubule cross-linkers

Several MAPs and motors that participate in spindle assembly and integrity are able to cross-link microtubules. One of the most studied microtubule cross-linkers is Eg5, a member of the kinesin-5 protein family. Eg5 is a microtubule plus-end directed motor, which assembles into homo-tetramers with two motor domains located on each of the opposite sides of the complex (Cole et al., 1994). This allows it to bind two different microtubules and, due to its preference for antiparallel microtubules, to slide their minus-ends away from each other (van den Wildenberg et al., 2008). Eg5 inhibition prevents bipolar spindle assembly by preventing centrosome separation (reviewed in (Mann and Wadsworth, 2019)). However, once spindle bipolarity is achieved, Eg5 may be dispensable to maintain it, due to the cooperative activity of another homo-tetramer microtubule cross-linker, Kif15, which has been proposed to share this ability to slide antiparallel microtubules (Mann and Wadsworth, 2019; Tanenbaum et al., 2009; Vanneste et al., 2009).

An additional cross-linker of antiparallel microtubules is PRC1, which is enriched along overlapping interpolar microtubules that are in close contact with sister kinetochores (also known as bridging fibers) (Kajtez et al., 2016). During early mitosis, PRC1 remains mostly inactive due to the phosphorylation by Cdk1 and Plk1 (Hu et al., 2012; Zhu et al., 2006). At metaphase, PRC1-mediated cross-linking of microtubules, together with the recruitment of plus-end directed motor proteins Kif4a and Kif18a to interpolar microtubules, promotes chromosome alignment by generating overlap length-dependent forces that are transmitted to the associated k-fibers (Jagric et al., 2021). Moreover, PRC1 promotes lateral and longitudinal reinforcement that allows k-fibers to resist to transient movement/force near chromosomes (Suresh et al., 2020). At anaphase onset, PRC1 is transported to the spindle midzone by Kif4a, which in turn is regulated by Aurora-B activity (Nunes Bastos et al., 2013; Zhu and Jiang, 2005). There, it interacts with antiparallel microtubules' plus ends and is essential for stable microtubule organization and successful completion of cytokinesis (Kurasawa et al., 2004; Subramanian et al., 2010).

Two minus-end directed motor proteins also contribute to efficient mitotic spindle assembly due to its activity to crosslink microtubules: Dynein, a multisubunit protein complex (Verde et al., 1991) and HSET/kinesin-14 (Mountain et al., 1999). These proteins slide antiparallel microtubules generating an inward force within the spindle that assists spindle pole focusing and antagonizes the effect on outward microtubule sliding forces generated by Eg5 (Allan, 2011; Ferenz et al., 2009; Fink et al., 2009; Hepperla et al., 2014; Hueschen et al., 2017; Tanenbaum et al., 2013).

1.3.4.2. Microtubule polymerization-promoting proteins

A significant fraction of MAPs belongs to the microtubule plus-end-tracking protein family or +TIPs, including members of the CLIP, CLASP and TOG protein families (reviewed in (Ferreira

et al., 2014)), which contribute to spindle assembly and maintenance through their stabilizing effect on microtubules. CLIP-170 stabilizes microtubules by promoting rescue events (Arnal et al., 2004; Komarova et al., 2002), while facilitates spindle bipolarity maintenance by counteracting outward microtubule sliding through interaction with Dynein (Tanenbaum et al., 2008). Likewise, proteins from the CLASP family (CLASP1 and CLASP2 in mammals) promote microtubule rescue events (Akhmanova et al., 2001; Al-Bassam et al., 2010) and stabilize kinetochore-microtubule attachments, both required for normal chromosome alignment and segregation (Girao et al., 2020; Maiato et al., 2003a; Maiato et al., 2003b). CLASPs mediate polymerization at microtubule plus-ends (Girao et al., 2020; Logarinho et al., 2012; Maiato et al., 2005) and are important for bipolar spindle organization (Logarinho et al., 2012; Mimori-Kiyosue et al., 2006; Pereira et al., 2006). Similarly, the *Xenopus* member of the TOG protein family, XMAP215, promotes microtubule polymerization at microtubule plus-ends (Brouhard et al., 2008; Gard and Kirschner, 1987) and its depletion prevents bipolar spindle assembly, resulting in short spindles (Tournebize et al., 2000). RNAi-mediated depletion of its mammalian homologue, chTOG, also affected mitotic spindle assembly resulting in disorganized and multipolar spindles (Gergely et al., 2003). In addition to its growth promoting function, chTOG contributes to microtubule stabilization by protecting kinetochore-microtubules from depolymerization by MCAK (Barr and Gergely, 2008). Further stabilization of kinetochore-microtubule attachments is thought to be mediated by the activity of HURP, which decorates the kinetochore-proximal end of k-fibers in a Ran (Ras-related nuclear protein)-GTP dependent manner (Silljé et al., 2006) and promotes chromatin-induced microtubule assembly (Casanova et al., 2008). HURP depletion impairs k-fiber stability and leads to chromosome congression problems, whereas its overexpression increases microtubule stability (Silljé et al., 2006; Wong and Fang, 2006).

1.3.4.3. Microtubule depolymerization-promoting proteins

Unlike conventional kinesins, members of the kinesin-13 subfamily do not move directionally along microtubules but, instead, induce a conformational change at the protofilament end that leads to microtubule depolymerization (Desai et al., 1999). The best studied member of the kinesin-13 motor protein family is MCAK, which localizes to the spindle poles, centromeres, kinetochores and microtubule plus-ends, where it uses the energy from ATP hydrolysis to depolymerize microtubules from both ends (reviewed in (Ems-McClung and Walczak, 2010)). *In vitro* reconstitution experiments with MCAK and Kif2a, another member of the kinesin-13 protein family, directly demonstrated their microtubule destabilizing activity by being able to completely depolymerize chemically stabilized microtubules (Desai et al., 1999). MCAK orthologue in *Xenopus*, XKCM1, was shown to negatively regulate microtubule growth, since its depletion in egg extracts interfered with spindle assembly, giving rise to abnormally long microtubules (Walczak et al., 1996). In mammalian cells, spindle length is less affected after

MCAK depletion but it strongly increased by simultaneous knocked-down of Kif2a, emphasizing a conserved role of kinesins-13 in mitotic spindle assembly (reviewed in (Ems-McClung and Walczak, 2010)).

In contrast, Kinesin-8 family proteins are highly processive motors, which accumulate at microtubule-plus ends and, once saturated, initiate microtubule-disassembly in a length-dependent manner. One of the human orthologues, Kif18a, regulates microtubule-growth and its depletion results in elongated spindle microtubules (reviewed in (Shrestha et al., 2018)).

Finally, microtubule-severing proteins that include Katanin, Spastin and Fidgetin use ATP hydrolysis to promote microtubule disassembly by severing microtubules into short fragments. These proteins bind to tubulin C-terminal tails at the surface of the microtubule lattice and initiate microtubule depolymerization by removing tubulin subunits (reviewed in (McNally and Roll-Mecak, 2018)). Loss of katanin in *Xenopus* egg extracts resulted in abnormally long spindles, whereas in mammals this phenotype was less penetrant, possibly due to the presence of centrosomes that might compensate its loss by increasing microtubule nucleation activity (Kuo and Howard, 2021). In Drosophila S2 cells, microtubule severing proteins additionally contribute to the poleward chromosomal movements during anaphase A by inducing depolymerization of kinetochore microtubule plus- and minus-ends (Zhang et al., 2007). Surprisingly, recent works showed that both Katanin and Spastin are powerful promoters of microtubule growth by increasing the frequency of rescue events (conversion of shrinking microtubules to growing ones) with the intent that microtubule fragments generated by severing act as seeds for new microtubules (reviewed in (Kuo and Howard, 2021)).

1.3.4.4. Chromokinesins

Chromokinesins are distinct from conventional kinesins due to their ability to associate with chromosomes during mitosis. Their localization on chromatin was originally reported for *chk* (a kinesin-4 family member) in chicken, and verified across different species: *Xenopus* (Xklp1), humans (Kif4a and Kif4b) and *C. elegans* (Klp-19) (Sekine et al., 1994; Vernos et al., 1995; Wang and Adler, 1995; Williams et al., 1995). The putative kinesin-10 ‘No distributive disjunction’ (Nod) in Drosophila female meiosis also associates with DNA, which was subsequently confirmed in other kinesin-10 family members, including Kid in mammals and XKid in *Xenopus* (Antonio et al., 2000; Funabiki and Murray, 2000; Theurkauf and Hawley, 1992). Kinesin-12 Kif15/Hklp2 was also shown to localize to the chromosome arms in human cells, thereby qualifying as a chromokinesin (Vanneste et al., 2011; Vanneste et al., 2009) (Table 1).

All chromokinesins share the same structural features of most kinesins: an N-terminal motor domain, an α-helical coiled-coil stalk domain and a C-terminal tail region, which contains a chromatin-interacting domain. The presence of the motor domain is consistent with the plus-end-

directed motility demonstrated for several chromokinesins, such as Kid, XKid, Kif4a and Xklp1, but they appear to be weak processive motors under load (reviewed in (Almeida and Maiato, 2018). On the contrary, Kif15 is a highly processive motor and was shown to target to chromosomes through the interaction with Ki67, a peri-chromosomal layer protein that decorates the chromosome arms during mitosis (Vanneste et al., 2011).

Table 1. Mitotic properties of the chromokinesin families.

Family	Name	Species	Location	Chromosome targeting	Motility	Oligomeric structure	Main mitotic function
Kinesin-4	hKif4a hKif4b	Hs	Xq13.1 5q33.1	ZBZ domains and C-R motifs	N.A.	Dimer	Spindle bipolarity; Chromosome condensation and alignment at the metaphase; MTs dynamics.
	Xklp1	Xl	NM_00108 7550	C2H2 zinc finger domain at C-terminus	Yes	N.A.	Affects spindle MTs density/polymerization; With PRC1 controls anaphase midzone MT overlap.
	Kif4a	Mm	X C3; X 43.72 cM	-	Yes	N.A.	Spindle assembly, chromosome alignment and cytokinesis.
	Klp-3B	Dm	3A6-3A6; 19.0 cM	-	N.A.	N.A.	Drives spindle pole separation and facilitates chromosome movement.
	Klp-19	Ce	mum-3-unc 49	CPC during meiosis	N.A.	N.A.	Polar ejection forces, important for chromosome segregation.
	chk	Gg (chicken)	Chromoso me 4	Leucine zipper DNA-binding domain	Yes	N.A.	
Kinesin-10	KID/Kif 22	Hs	16p11.2	HhH motifs at C-terminal	Yes	Monomer*	Polar ejection force; chromosome arms oscillation and orientation; MT bundling.
	Xkid	Xl	NM_203914	HhH motifs at C-terminal	Yes	N.A.	Chromosome alignment.
	Kid	Mm	7 F3; 7 69.29cM	-	Yes	N.A.	
	Nod	Dm	10C7 - 10C8; 1 - 36 cM	-	Yes	Dimer**	Brake while chromosomes move along the spindle.
Kinesin-12	Kif15/ Hklp2	Hs	3p21.31	Ki67 interaction	Yes	Tetramer***	Bipolar spindle assembly/spindle pole separation

Abbreviations used: *Ce, Caenorhabditis elegans; CPC, chromosomal passenger complex; C-R, cysteine-rich; Dm, Drosophila melanogaster; Gg, Gallus gallus; HhH, helix/hairpin/helix; HMG, high mobility group; Hs, Homo sapiens; Mm, Mus musculus; Xl, Xenopus laevis; ZBZ, zip/basic/leucine zip; NA, not available; MT, microtubule. ∗At low concentrations in solution. ∗∗Processive only after artificial dimerization, but monomeric at low concentrations in solution. ∗∗∗At physiological ionic strength but dimer at high ionic strength. Adapted from (Almeida and Maiato, 2018).*

Chromokinesins perform non-redundant functions during mitosis, despite the similarities in protein organization and chromosomal localization. During congression to the metaphase plate, chromosomes experience pushing forces along the chromosome arms and away from spindle poles, hence named ‘polar ejection forces’ (PEFs) (Cassimeris et al., 1994; Rieder et al., 1986;

Rieder and Salmon, 1994). Chromokinesins have emerged as excellent candidates for powering chromosome mobility by promoting PEFs. *In vitro* reconstitutions and *in vivo* measurements have predicted that PEFs can produce between 0.5–1 pN per microtubule and around 100 pN when microtubule density is higher, and that those could be generated either by the action of single kinesin motors or by individual polymerizing microtubules pushing on chromosome arms (Brouhard and Hunt, 2005; Cane et al., 2013).

Kinesin-10 was found to bind more strongly to microtubules, overruling kinesin-4 during cooperative movement associated with chromatin. Functional perturbation of both chromokinesins in *Drosophila* and human cells suggested a combined role during chromosome congression, with kinesin-10 providing the major PEF required for arm orientation and oscillation and kinesin-4 mainly regulating microtubule dynamics (Ke et al., 2009; Marshall et al., 2001). Similarly, XKid in *Xenopus*, was found to push chromosome arms towards the spindle equator, playing an important role on chromosome alignment (Antonio et al., 2000; Levesque and Compton, 2001; Tokai-Nishizumi et al., 2005; Wandke et al., 2012). Together, these two chromokinesins are sufficient to promote the random ejection of chromosomes away from the pole (reviewed in (Almeida and Maiato, 2018)) (Table 1).

1.4. Spindle Assembly Models

Mitotic spindle assembly is a conserved and redundant process among metazoans, which is thought to comprise multiple pathways (McIntosh et al., 2012; O'Connell et al., 2009; Prosser and Pelletier, 2017). In the late nineteenth century, centrosomes were identified at the center of astral microtubules arrays where spindle poles localized, and the relationship with spindle assembly seemed obvious. However, one hundred years later, it has been shown that there are concurrent microtubule nucleation sources in animal cells, independent of the centrosomes (reviewed in (Khodjakov et al., 2000)). All pathways are at least partially redundant and share some common elements. First, they all require γ-TuRC to initiate microtubule nucleation; second, they rely on microtubule-associated motors to organize microtubules into a bipolar array; third, the newly formed microtubules are stabilized by the chromosomes (Gaglio et al., 1996; Goshima et al., 2005; Goshima and Vale, 2003; Luders et al., 2006; Walczak et al., 1998). Centrosomal- and non-centrosomal microtubule nucleation pathways provide an intricate balance of microtubule nucleation that ensures the timely completion of mitosis and chromosome segregation fidelity. In the absence of one of the pathways spindle assembly still occurs, though mitosis takes longer and this may lead to genome instability (Bazzi and Anderson, 2014; Hayward et al., 2014; Khodjakov and Rieder, 2001; Prosser and Pelletier, 2017; Sir et al., 2013).

1.4.1. Search-and-capture model

As a result of centrosome maturation at mitotic entry and more frequent switches between microtubule growth and shrinkage due to dynamic instability, astral microtubules highly increase their chances to interact with chromosomes. Such random exploration of the cell space by dynamic astral microtubules in their search for chromosomes is known as 'search-and-capture' (Kirschner and Mitchison, 1986) (Figure 1.7. A). If a microtubule is 'captured' by a chromosome, its dynamic instability is suppressed, the plus end is stabilized, and the chromosome is incorporated in the assembling spindle. High resolution time-lapse imaging, followed by 3-D reconstructions, revealed that chromosome positioning during prometaphase significantly facilitates 'search-and-capture' and chromosome congression (Magidson et al., 2011). In this context, PEFs generated by the plus-end directed motor proteins chromokinesins during mitosis promote a toroid, ring-like arrangement of chromosomes that are laterally attached to the surface of the forming spindle. This promotes kinetochore exposure to a microtubule dense area, while preventing kinetochores from being shielded by other chromosomes. Nevertheless, computational studies have shown that spindle assembly could not rely exclusively on dynamic instability, since 'search-and-capture' of all kinetochores would require several hours, in contrast to the observed time of spindle assembly in living mitotic cells in the range of minutes (Paul et al., 2009; Wollman et al., 2005). Likewise, the fact that spindle formation occurs in cells that are naturally devoid of centrosomes, such as female oocytes and land plants (Wadsworth and Khodjakov, 2004), or after experimental centrosome inactivation in animal somatic cells (Khodjakov et al., 2000), suggests the existence of alternative pathways of spindle assembly.

1.4.2. Acentrosomal microtubule nucleation

Three main mechanisms drive acentrosomal microtubule formation in dividing cells: one is triggered by the chromosomes (dependent on the Ran-GTP gradient and on the Chromosomal Passenger Complex (CPC)); the second one relies on kinetochore-mediated microtubule growth; and the last drives microtubule amplification via Augmin-dependent microtubule nucleation (reviewed in (Meunier and Vernos, 2016; Prosser and Pelletier, 2017)) (Figure 1.7. B, C, D).

1.4.2.1. Chromatin-mediated microtubule nucleation

The 'self-organizing' properties of spindles were directly demonstrated using *Xenopus* egg extracts. In this system, spindles successfully formed in the absence of centrosomes, just by adding whole chromosomes or chromatin-coated beads to the cell extracts (Heald et al., 1996). Microtubule polymerization around chromosomes is driven by the stabilizing effect of GTP-bound Ran molecules (Carazo-Salas et al., 2001; Carazo-Salas et al., 1999) and the CPC (Maresca et al., 2009; O'Connell et al., 2009; Sampath et al., 2004). The Ran-GTP molecules are generated near chromatin by a guanine nucleotide exchange factor, RCC1, that establishes a concentration

gradient throughout the cytoplasm (Kalab and Heald, 2008). The Ran-GTP gradient is thought to release spindle assembly factors from the inhibitory effect of Importin. Such factors include TPX2, which targets Aurora-A kinase to the spindle, where it interacts and phosphorylates the γ-TuRC adaptor protein NEDD1 and thereby favors microtubule nucleation and microtubule growth towards chromatin (reviewed in (Meunier and Vernos, 2016)). However, despite a well-documented role of the Ran-GTP gradient in acentrosomal spindle assembly in *Xenopus* egg extracts, in somatic animal cells it does not seem to play an essential role (Moutinho-Pereira et al., 2013; O'Connell et al., 2009). In these systems, chromosomes regulate microtubule nucleation and dynamics regardless of a Ran-GTP gradient, via the CPC complex. This complex consists of INner CEntromere Protein (INCENP), Survivin, Borealin and Aurora-B kinase (reviewed in (van der Horst and Lens, 2014)). The CPC complex is recruited to centromeres through the binding of Survivin to phosphorylate chromatin histone H3. This phosphorylation drives Aurora-B accumulation and activation on centromeres, which spatially inactivates microtubule-destabilizing proteins such as MCAK and Stathmin 1 (STMN1), thus promoting microtubule stabilization at kinetochores (reviewed in (Meunier and Vernos, 2016; Prosser and Pelletier, 2017)).

1.4.2.2. Kinetochore-mediated microtubule nucleation

The observed ability of spindle assembly around chromatin-coated beads initially excluded an essential role of kinetochores in this process (Heald et al., 1996). However, in somatic cells, kinetochores can organize their own k-fibers (Khodjakov et al., 2003; Maiato et al., 2004b; O'Connell et al., 2009; Snyder and McIntosh, 1975; Witt et al., 1980). Detailed analysis of EM serial sections revealed that microtubule polymerization is initiated in close proximity of kinetochores (Witt et al., 1980). In fact, microtubule nucleation by the kinetochores themselves has been detected in animal somatic cells during monastrol (Eg5 inhibitor) treatment and subsequent removal, after microtubule regrowth assays, as well as under physiological conditions (Khodjakov et al., 2003; Maiato et al., 2004b; Tulu et al., 2006). Chromatin-mediated microtubule nucleation increases the density of microtubules around kinetochores, which facilitates their capture. Kinetochores then capture, orient and stably attach those short growing microtubule plus-ends, allowing their subsequent growth with microtubule plus-ends facing the kinetochore and the minus-ends oriented towards the pole (Maiato et al., 2004b). Interestingly, the correct orientation of microtubule plus-ends towards the kinetochore has been attributed to CENP-E motor activity, and the subsequent incorporation of pre-formed k-fibers into the spindle to Dynein-mediated interaction with non-kinetochore microtubules (Elting et al., 2014; Hueschen et al., 2017; Khodjakov et al., 2003; Maiato et al., 2004b; Sikirzhytski et al., 2018).

1.4.2.3. Microtubule-mediated microtubule nucleation

Efficient and rapid assembly of the mitotic spindle additionally relies on microtubule nucleation initiated by Augmin. Augmin is a Y-shaped protein, composed of eight subunits, that recruits γ-TuRC to the outer lattice of pre-existing microtubules, initiating branching of new microtubules within the spindle (Goshima et al., 2008; Hsia et al., 2014; Kamasaki et al., 2013; Petry et al., 2011; Uehara et al., 2009b; Verma and Maresca, 2019). First evidence implicating this complex in mitotic spindle assembly came from a genome-wide RNAi-based screen in Drosophila cells, that identified five genes (dgt2–dgt6), which encoded proteins required for γ-TuRC localization to the spindle microtubules, but not to the centrosomes (Goshima et al., 2007). In human cells, depletion of Augmin significantly reduces γ-TuRC within the mitotic spindle which compromises overall spindle integrity and k-fiber formation (David et al., 2019; Goshima et al., 2008; Lawo et al., 2009; Uehara et al., 2009b; Zhu et al., 2008). Of note, plants also contain Augmin orthologues, which highlights the importance of this pathway in cells naturally devoid of centrosomes, where microtubule formation within the spindle is essential (Hofmann, 2012; Wainman et al., 2009) (see the following section for Augmin's functions in-depth description).

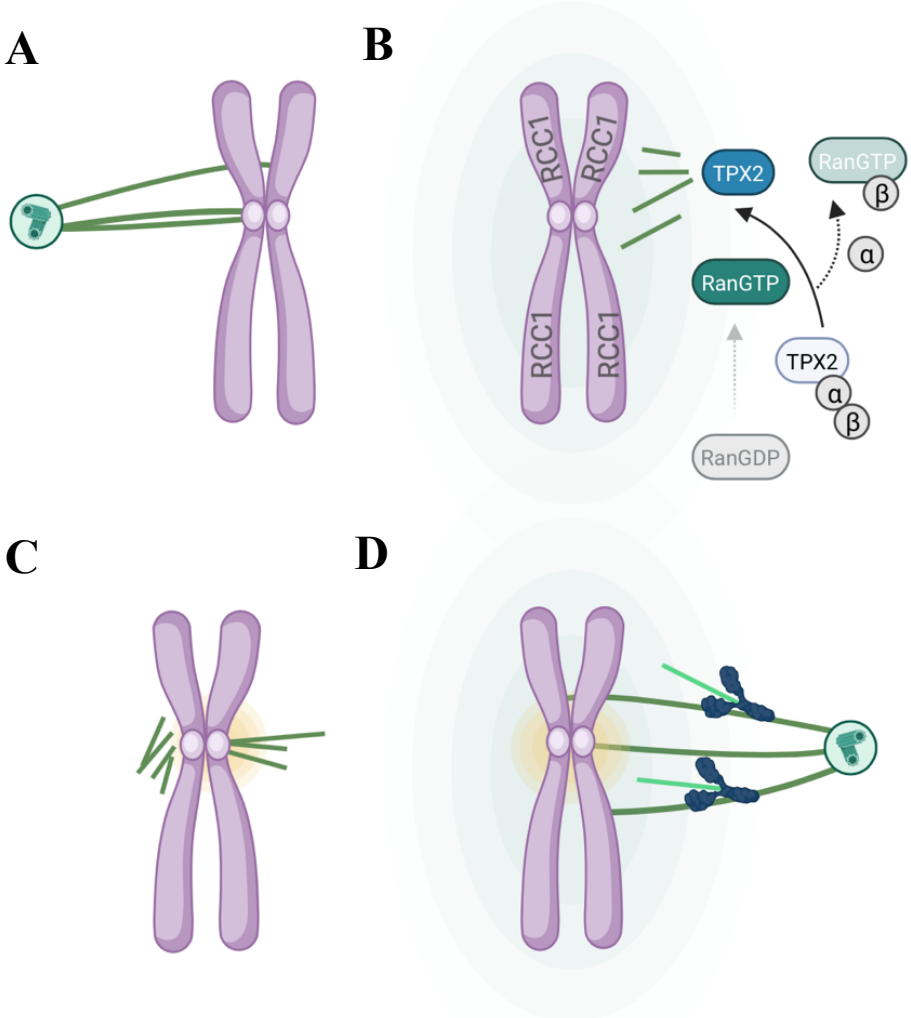

(figure legend on the next page)

Figure 1.7. Models of mitotic spindle assembly.

A, centrosomal microtubules search the cellular space as they growth and shrink. As soon as a microtubule encounter a kinetochore, its dynamic instability is suppressed, and its plus ends becomes stabilized. **B,** RCC1 binds to chromosomes and induces a local high concentration of Ran-GTP around chromatin. The Ran-GTP gradient (light green) promotes the local dissociation of spindle assembly factors, such as TPX2, from their inhibitory binding to importins (α- and β-importins shown in grey). Here, TPX2 together with γ–TuRC mediate local nucleation of acentrosomal microtubules around chromosomes. **C,** short growing microtubule plus-ends attach to kinetochores and are further stabilized by the CPC activity. Aurora-B at kinetochores phosphorylates microtubule-destabilizing proteins (e.g MCAK) creating a local environment (yellow) around the kinetochore that acts as a hotspot for microtubule stabilization. **D,** the Augmin complex (dark blue) is recruited to pre-existing microtubules and promotes microtubule amplification. The newly nucleated microtubules are then stabilized through the CPC and the Ran-GTP pathways (yellow and light green, respectively).

1.5. Augmin-dependent Microtubule Nucleation

In most eukaryotes, Augmin is a conserved protein complex composed by the following subunits: Ccdc5 (HAUS1), Cep27 (HAUS2), hDgt3 (HAUS3), C14orf94 (HAUS4), hDgt5 (HAUS5), hDgt6 (HAUS6), UCHL5IP (HAUS7), and Hice1 (HAUS8) (Hsia et al., 2014; Lawo et al., 2009; Meireles et al., 2009; Uehara et al., 2009b). All eight subunits were demonstrated to contribute for microtubule nucleation. The tetramer composed by HAUS2, HAUS6, HAUS7 and HAUS8 subunits binds directly to microtubules, whereas HAUS1, HAUS3, HAUS4, HAUS5 (and possibly HAUS6) interacts with γ-TuRC protein adaptor NEDD1 (Chen et al., 2017; Haren et al., 2006; Luders et al., 2006; Song et al., 2018; Uehara et al., 2009b; Zhu et al., 2008). Augmin activity is regulated by the action of two kinases: Cdk1 and Plk1. Cdk1 phosphorylation of γ-TuRC protein adaptor NEDD1 facilitates the phosphorylation of HAUS8 by Plk1 and leads to Augmin association with microtubules (Johmura et al., 2011).

Initial predictions that Augmin was able to link γ-TuRC-capped microtubule ends to a neighboring microtubule wall (Goshima et al., 2008; Uehara and Goshima, 2010) were supported by (1) the visualization of Augmin-γ-TuRC-dependent microtubule nucleation events that led to microtubule branching in *Xenopus* egg extracts (Alfaro-Aco et al., 2020; Petry et al., 2013; Petry and Vale, 2015); and (2) by mapping microtubules ends within the mitotic spindle using electron tomography (Kamasaki et al., 2013). Strikingly, the authors observed that newly formed microtubules were positioned mostly at shallow angles (<30°) relative to the existing microtubule, both *in vitro* (Alfaro-Aco et al., 2020; Petry et al., 2013), as well as, in fixed cells (Kamasaki et al., 2013). In turn, there is a discrepancy between the measured microtubule branched angles across systems. Higher plants exhibit larger microtubule branching angles (~40º) (Murata and Hasebe, 2007; Murata et al., 2005), along with nucleation events detected in Drosophila S2 anaphase cells and in *in vitro* reconstitution assays (~35º) (Tariq et al., 2020; Verma and Maresca,

2019). These observations are somewhat reminiscent of the 'fir-tree'/'tree-like' microtubule patterns observed in Haemanthus endosperm, onion root spindles, and green plants (Bajer and Mole-Bajer, 1986; Palevitz, 1988; Wasteneys and Williamson, 1989). The first observation predicts that newly formed microtubules have the same polarity (and shallow angles) as the existing microtubules, such that they can interact to assemble the spindle body and to sustain kinetochore-microtubule attachments (David et al., 2019; Kamasaki et al., 2013; Sanchez-Huertas and Luders, 2015). This is consistent with the idea that nearly parallel microtubule nucleation would function more efficiently to maintain k-fiber bundle formation/architecture. Furthermore, the fact that Augmin is required for anaphase central spindle and phragmoplasts formation in animals and plants, respectively, also favors the rapid polarized microtubule arrays' formation premise (Hotta et al., 2012; Nakaoka et al., 2012; Uehara and Goshima, 2010; Uehara et al., 2009b). In contrast, the second observation debates the existence of a wider branched microtubule nucleation mediated by Augmin, which may provide an advantage to capture scattered chromosomes and to build a bipolar spindle framework (Kirschner and Mitchison, 1986). Although the significance of this wide angular dispersion remains unclear, it implies that additional factors may be involved either on bundling or stabilizing newly nucleated kinetochore microtubules into a cohesive fiber. In fact, *in vitro* studies also suggested that branched microtubules are frequently pulled apart by Dynein, indicating the newly formed branched microtubules might be rapidly sorted by motor proteins (Alfaro-Aco et al., 2020; Petry et al., 2013). The physiological role of Augmin-mediated branched- *vs* parallel-microtubule nucleation within the mitotic spindle is still under investigation.

Previous reports localized Augmin in mitotic spindles, being preferentially accumulated near the spindle poles, where long-lived microtubules (more stable) are concentrated (David et al., 2019; Goshima et al., 2008; Zhu et al., 2008). Interestingly, a pool of Augmin (HAUS6) associated with γ-TuRC was also found at the centriole lumen, where it does not seem to perform its canonical function, but instead, it preserves centriole-scaffold integrity (Schweizer et al., 2021). Further experiments are required to fully understand how these opposite HAUS6 roles are regulated.

Moreover, it remains unclear if Augmin interacts directly with spindle microtubules or if requires other protein adaptors to perform its functions. *In vitro* reconstitution assays have proposed TPX2 as such adaptor (Alfaro-Aco et al., 2020; Petry et al., 2013), while others suggested that Augmin directly interacts with microtubules (Tariq et al., 2020; Verma and Maresca, 2019). Recent efforts hinted EML3 (Echinoderm Microtubule-associated protein-Like 3) as the responsible MAP for Augmin recruitment to spindle microtubules in human HeLa cells (Luo et al., 2019).

1.6. Chromosome Bi-orientation and Congression

Chromosome congression in humans can essentially be explained by two alternative mechanisms that operate parallelly (reviewed in (Maiato et al., 2017)). After NEBD, chromosomes that are in between the spindle poles rapidly bi-orient using a 'direct congression' pathway, in which chromosomes align after bi-orientation and the establishment of end-on kinetochore-microtubule attachments. This promotes the balance action of opposite kinetochore-pulling forces, resulting from the tight regulation of kinetochore microtubule dynamics, and PEFs along chromosome arms, which accounts for chromosome oscillatory movements during and after congression (Auckland and McAinsh, 2015). The second pathway is independent of end-on microtubule-attachments and relies on the coordinated action of the kinetochore motors Dynein and CENP-E, which laterally transport peripheral chromosomes along microtubules, first towards the poles and subsequently towards the spindle equator (Barisic et al., 2014) (Figure 1.8.). These motor proteins are regulated by position-dependent phosphorylation and by spindle microtubule diversity through tubulin PTMs (Barisic et al., 2015). Kinetochores become laterally attached by centrosomal microtubules, and chromosomes are then transported closer to the pole by the minus-end directed action of Dynein (Li et al., 2007; Rieder and Alexander, 1990; Vorozhko et al., 2008; Yang et al., 2007), which travels along tyrosinated astral microtubules (Figure 1.8. A-B). Once at the poles, CENP-E travels along detyrosinated microtubules, favoring chromosome congression to the metaphase plate where the chances of bi-orientation are maximal (Barisic et al., 2015; Kapoor et al., 2006) (Figures 1.8. C-D). Microtubule nucleation in the vicinity of kinetochores and chromosomes may additionally favor rapid chromosome congression and bi-orientation (Sikirzhytski et al., 2014; Sikirzhytski et al., 2018).

Once at the spindle equator, chromokinesins promote the conversion from lateral to end-on attachments, which further removes CENP-E and Dynein from kinetochores, thereby ensuring the maintenance of chromosome position and the stabilization of end-on kinetochore-microtubule attachments (Almeida and Maiato, 2018; Cane et al., 2013; Drpic et al., 2015; Wandke et al., 2012). This transition from lateral to end-on attachments relies on alternative factors. The localization of Dynein motor complex to the outer kinetochore layer is very dynamic and depends on Spindly, which is loaded on kinetochores through interaction with the RZZ complex (Rod-ZW10-Zwilch) (reviewed in (Barisic and Geley, 2011)). Here, the role of the RZZ complex is to support lateral contacts by decreasing the binding affinity of the Ndc80 complex for microtubules, which is in turn regulated by Spindly and Dynein. When Dynein removes this whole complex through its poleward motor activity, inhibition of Ndc80 is relieved, allowing the formation of stable end-on attachments (Barisic et al., 2010; Cheerambathur et al., 2013; Gassmann et al., 2010). This process is facilitated by CENP-E, that tethers the kinetochore to the microtubule lattice while MCAK corrects these interactions in a subsequent conversion step (Shrestha and

Draviam, 2013). In addition, Aurora B counteracting activity of protein phosphatase 1 and 2A (PP1 and PP2A) also participate in the end-on attachments conversion, together with the Astrin/SKAP complex (Shrestha et al., 2017b).

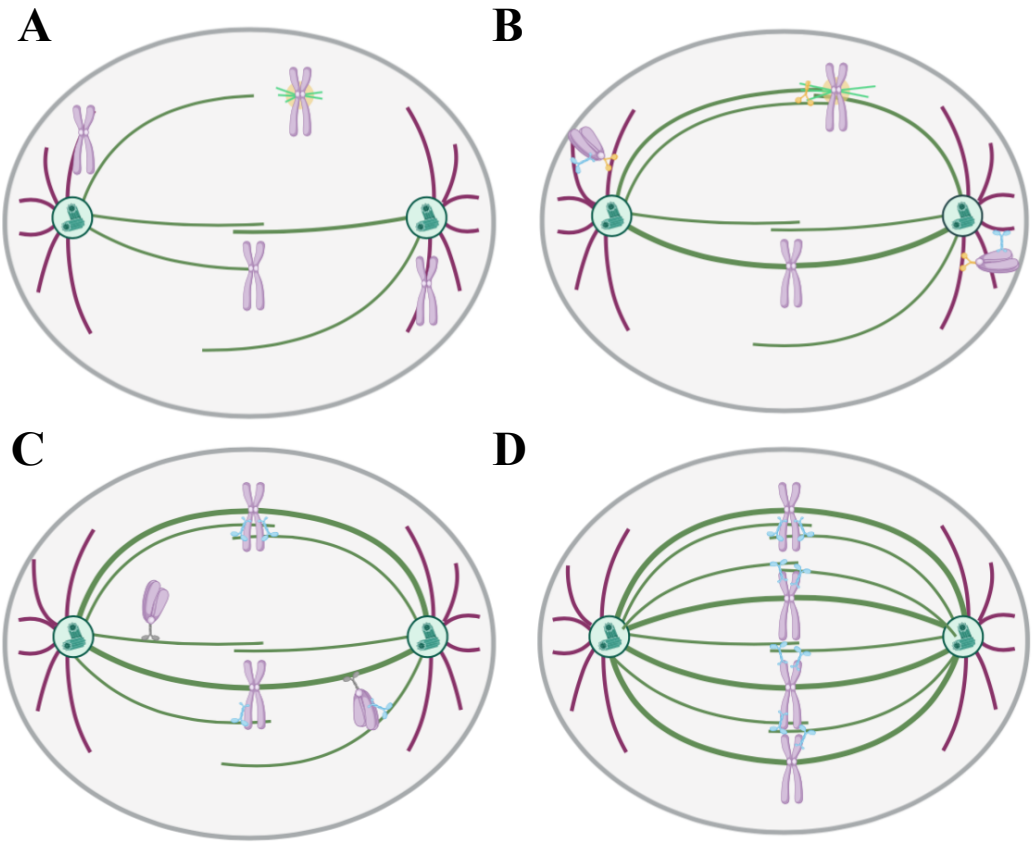

Figure 1.8. Mechanisms of chromosome congression.

A, initial positioning of chromosomes after NEBD affects chromosome congression. Peripheral chromosomes depend more on motor proteins to congress to the metaphase plate than the centrally localized chromosomes, which can easily be reached from both poles. Kinetochore-derived microtubules are formed in the initial stages of spindle assembly and increase the probability of lateral interaction with non-kinetochore microtubules. **B,** centrally localized chromosomes then become bi-oriented and align via changes in microtubule polymerization dynamics in coordination with PEFs along chromosome arms ('direct congression'). Dynein (yellow) motor activity at the newly nucleated kinetochore microtubules drives the incorporation of pre-formed k-fibers into the spindle by interacting with astral and interpolar microtubules. Peripheral chromosomes are carried to the spindle poles by the minus-end directed motion of Dynein (yellow) along tyrosinated microtubules. **C,** after reaching the pole chromosomes continue to congress towards the metaphase plate mainly via activity of a plus-end directed motor protein - CENP-E (grey) - along more stable detyrosinated microtubules. **D,** coordination of different motor protein activities and microtubule dynamics results in successful alignment of all chromosomes at the metaphase plate. Here, chromokinesins (blue) facilitate the conversion from lateral to end-on attachments, which downregulates Dynein and CENP-E, thus promoting chromosome position maintenance at the mitotic spindle equator.

1.7. Kinetochore-microtubule Attachments

Mammalian kinetochores have multiple microtubules plus end attachment sites, typically 15-25 within the kinetochore outer plate (Khodjakov et al., 1997; McEwen et al., 2001; Rieder, 1982; Wendell et al., 1993). These numbers are variable across different species (Table 2) and appear to be proportional to the surface area of the kinetochore rather than the size of the chromosome (Campbell et al., 2019; Cherry and Johnston, 1987; McEwen et al., 1998; Nicklas et al., 1982) .

Several studies have proposed the Ndc80/Hec1 complex as the core of the kinetochore force-transducing microtubule binding activity (reviewed in (Wimbish and DeLuca, 2020)). Injection of PtK1 cells (derived from female rat kangaroo kidney epithelium) with an N-terminal Hec1 antibody shed light on how kinetochores stabilize the attached microtubules (DeLuca et al., 2006). Consequently, kinetochore-microtubule attachments became hyper-stable, centromeres stretched, and kinetochore oscillations were dampened. These phenotypes were in part attributed to the loss of the Hec1-tail domain (the extreme N-terminal region), and were corroborated across species to be phospho-regulated by Aurora-B kinase (Cheerambathur et al., 2013; Cheeseman et al., 2006; DeLuca et al., 2011; Guimaraes et al., 2008; Maiato et al., 2004a; Zaytsev et al., 2014). In fact, the prevailing models comprehend that phosphorylation of Hec1, which decreases Ndc80 complex affinity for microtubules, is the major regulator of the kinetochore-microtubule stability (reviewed in (Wimbish and DeLuca, 2020).

Upon attachment, kinetochore-microtubules are more stable and become more resistant to depolymerization induced by cold treatment, calcium shock or by high hydrostatic pressure, compared with microtubules that have unattached plus ends (Brinkley and Cartwright, 1975; Mitchison et al., 1986; Salmon et al., 1976). However, the temporal longevity of k-fibers, and how its dynamic behavior is regulated remains unclear (reviewed in (Elting et al., 2018)). A handful of MAPs, such as Kif15 (Begley et al., 2021; Sturgill et al., 2014) and its regulator TPX2 (Bird and Hyman, 2008; Mann et al., 2017), the clathrin/chTOG/TACC3 complex (Booth et al., 2011; Cheeseman et al., 2013; Nixon et al., 2015; Royle et al., 2005), HURP (Dudka et al., 2019; Sillje et al., 2006; Tsuchiya et al., 2021), and kinesin Kif18a (Mayr et al., 2007; Ye et al., 2011) have been described to preferentially localize to k-fibers and/or to stabilize them, thereby promoting efficient mitotic progression and segregation. Though, their precise contributions to k-fiber mechanics and force production are still under investigation.

Table 2. Comparison of microtubule numbers within a single k-fiber in different species/cell types.

Specie/Cell type	Microtubule number/K-fiber	References
Saccharomyces cerevisiae	1	(Peterson and Ris, 1976)
Schizosaccharomyces pombe	2-4	(Ding et al., 1993)
Caenorhabditis elegans	6-50	(Redemann et al., 2017)
Drosophila S2 cells	6-15	(Maiato et al., 2006)
HeLa cells	9-22	(McEwen et al., 2001) (Wendell et al., 1993) (Kiewisz et al., 2021)
RPE-1 cells	13	(O'Toole et al., 2020)
Rat Kangaroo Kidney Epithelial Cells (PtK1 cells)	21-30	(McEwen et al., 1997) (Brinkley and Cartwright, 1971) (McIntosh et al., 1975)
Indian muntjac fibroblasts (chromosome 3+X)	60-100	(Brinkley et al., 1984; Drpic et al., 2018)

1.7.1. K-fiber Formation and Maturation

Two opposing models have emerged regarding how k-fibers are organized within a bundle of microtubules. The first suggests that there is a direct connection between kinetochores and spindle poles, which implies that all kinetochore-microtubules within a k-fiber have approximately the same length and are rigidly connected (Rieder, 1981; Witt et al., 1981). The formation of such a competent/mature k-fiber is compatible with consecutive rounds of 'search-and-capture' by centrosomal microtubules (Kirschner and Mitchison, 1986). First examination of this process, known as k-fiber maturation, was performed in PtK1 cells where the authors correlated the number of attached microtubules per kinetochore with the duration of these attachments, and the respective stage of mitosis (McEwen et al., 1997). However, the relatively slow rate of initial microtubule acquisition (~1.9 kinetochore-microtubule/min) revealed not to be compatible with a simple model of association/dissociation of kinetochore-microtubules from independent binding sites at the kinetochore (Brinkley and Cartwright, 1971; McEwen et al., 1997; McIntosh and Landis, 1971). As for the length of the kinetochore-microtubules, EM analyses, both in RPE-1 and PtK1 cells, have shown short microtubules associated with kinetochores (McDonald et al., 1992; Sikirzhytski et al., 2018), thus implying that not all kinetochore-microtubules are associated with the spindle poles. The second model considers that there is an indirect connection between kinetochore-microtubules and spindle-poles via interaction with interpolar and/or astral microtubules within the spindle (Sikirzhytski et al., 2014; Sikirzhytski et al., 2018). Recent

evidence suggests a semi-direct pattern of connection, in which some of the kinetochore-microtubules of each k-fiber are associated with spindle poles, while others are indirectly linked to non-kinetochore microtubules (Conway et al., 2021; Kiewisz et al., 2021; Redemann et al., 2017). These hypotheses are consistent with a role of acentrosomal-microtubule nucleation in k-fiber formation. In fact, Augmin protein complex has been described to interact with Ndc80 and to be required for kinetochore-dependent microtubule formation in Drosophila (Bucciarelli et al., 2009). On the other hand, Augmin-driven microtubule amplification was proposed to be the predominant source of spindle microtubules in human somatic cells and to account for the directional bias of microtubule growth towards the kinetochores after initial capture of pioneer centrosomal microtubules (David et al., 2019; Kamasaki et al., 2013). However, due to intrinsic limitations imposed by the high chromosome number and the sub-diffraction size of human kinetochores and associated k-fibers, how these models reconcile is yet to be explored.

1.7.2. Error Correction

Proper chromosome segregation during mitosis demands that each sister kinetochore is attached to spindle microtubules from opposite spindle poles - amphitelic attachment (Nicklas 1997; Rieder and Salmon, 1998) (Figure 1.9. B). Yet, erroneous configurations can often occur: (1) mono-oriented/monotelic chromosomes that can either be attached to a single spindle pole or be laterally attached to a microtubule; (2) syntelic attachments, where both sister kinetochores are oriented to the same spindle pole; and (3) a single kinetochore is attached to microtubules extending from both spindle poles, in a merotelic configuration (Figure 1.9. C-E). The latter is particularly dangerous for the cell because it is undetected by the SAC surveillance mechanism. In contrast, syntelic attachments are highly unstable and are often corrected before chromosome bi-orientation (reviewed in (Monda and Cheeseman, 2018)). Failure to correct erroneous kinetochore-microtubule attachments may result in chromosome segregation errors. Despite the stochasticity, chromosome segregation is remarkably accurate, which implies the presence of molecular mechanism(s) dedicated to error correction before and after anaphase onset.

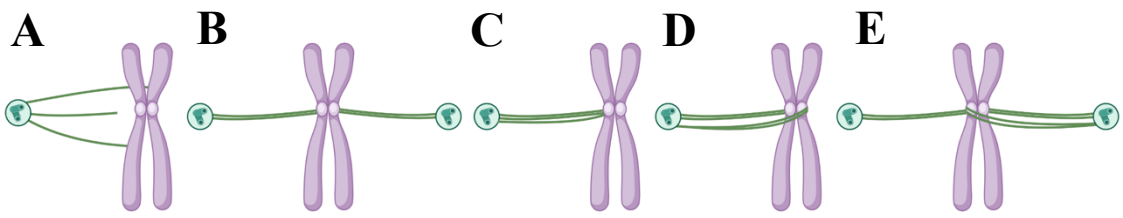

Figure 1.8. Kinetochore-microtubule types of attachments.

Representation of the different configurations of the kinetochore-microtubule attachments: **A**, unattached, **B**, amphitelic, **C**, monotelic/mono-oriented, **D**, syntelic and **E**, merothelic.

Tension between sister chromatids has been described as the main regulator of kinetochore microtubule attachment stability (Biggins and Murray, 2001; Krenn and Musacchio, 2015; Liu et al., 2009). This hypothesis was first explored in the late 1960's by Bruce Nicklas' experiments in grasshopper spermatocytes. Artificial tension generated by pulling a synthelically attached bivalent towards the opposite one, resulted in the stabilization of microtubule attachments (Nicklas and Koch, 1969). Upon chromosome bi-orientation, tension is applied along the centromeric region, resulting in increased inter-kinetochore distances, as well as alterations in kinetochore architecture (reviewed in (Maresca and Salmon, 2010)). This leads to the physical separation of Aurora-B kinase, which is at the heart of error correction, from Hec1, causing its dephosphorylation and the rise affinity for microtubules, ultimately contributing to a stronger interaction between kinetochores and spindle microtubules (DeLuca et al., 2011; Wimbish and DeLuca, 2020). Disruption of its activity by small molecule inhibitors significantly increases the frequencies of both merotelic and syntelic errors (Lampson and Cheeseman, 2011). Finally, Aurora-B activity is counteracted by PP1 and PP2A, that localize at the outer kinetochore plate where it dephosphorylates Aurora-B substrates at the kinetochore (Lampson and Cheeseman, 2011; Liu et al., 2010).

The microtubule-depolymerizing kinesin-13s play a role in destabilizing erroneous kinetochore-microtubule attachments during both prometaphase and metaphase (reviewed in (Bakhoum and Compton, 2012)). These kinesin-like proteins use their catalytic activity to alter microtubule dynamics (reviewed in (Manning et al., 2007; Walczak et al., 2013). The positively charged neck domain, flanked by the N-terminal (required for sub-cellular targeting) and the catalytical domain (required for ATP binding and interaction with microtubules), is crucial for the catalytic activity (microtubule depolymerization), as well as to target microtubule ends (Maney et al., 2001; Wordeman and Mitchison, 1995). Phosphorylation of the neck domain by Aurora-B kinase reduces the overall affinity of MCAK for its substrate, thus controlling its depolymerizing activity. In contrast, Plk1 has been reported to stimulate kinesin-13s activity (Jang et al., 2009; Zhang et al., 2011). Once bound to microtubules, kinesin-13s can diffuse in both directions. At microtubule ends, MCAK changes into a closed conformation, allowing tighter binding to the substrate and removal of tubulin dimers. On the other hand, kinesin-13 Kif2b localizes at kinetochores during prometaphase and facilitates the rapid turnover of kinetochore-microtubules (Bakhoum et al., 2009b). During metaphase, Kif2b is displaced from kinetochores and has no effect on kinetochore-microtubule turnover rates (Bakhoum et al., 2009b; Manning et al., 2010). Knock-down of MCAK or Kif2b prevents correction of erroneous attachments after monastrol washout, an experimental treatment that increases the number of aberrant attachments (Bakhoum et al., 2009a; Bakhoum et al., 2009b; Lampson et al., 2004). On the other hand, overexpression of MCAK or Kif2b prevents not only erroneous attachments, but also abolishes

chromosomal instability (CIN) in already aneuploid cancer cells (Bakhoum et al., 2009b). In fact, potentiation of MCAK activity suppressed chromosome mis-segregation in CIN cancer cells and elderly cells, concomitantly reduced cellular senescence (Barroso-Vilares et al., 2020; Orr et al., 2016). Additional pathways for error correction have been recently proposed. The first is based on kinesins' differential affinity for tubulin PTMs (in specific α-tubulin tyrosination/detyrosination), which allows microtubule depolymerases localized at the centromere/kinetochore to distinguish incorrect *vs* correct kinetochore-microtubule attachments. Consequently, less stable syntelic or merotelic attachments are destabilized by MCAK, whose activity is favored by microtubule tyrosination (Ferreira et al., 2020). The second proposes that chTOG activity at the kinetochore drives microtubule destabilization at low-tension kinetochore-microtubule attachments, independently of Aurora-B kinase phosphorylation (Herman et al., 2020).

1.8. Chromosome Separation

During metaphase-to-anaphase transition, a network of antiparallel microtubules assembles between the segregating sister chromosomes. This structure, referred to as the spindle midzone, is required for overall spindle architecture, spindle elongation, and cleavage furrow positioning (D'Avino et al., 2005; Eggert et al., 2006; Euteneuer and McIntosh, 1980). Among several key proteins, Augmin, which promotes microtubule amplification, plays a critical role in the assembly and maintenance of a spindle midzone and a functional cleavage furrow (Uehara and Goshima, 2010; Uehara et al., 2016; Uehara et al., 2009b; Verma and Maresca, 2019). Along with the physical changes, anaphase onset is under the control of SAC activity (reviewed in (Khodjakov and Pines, 2010)) (see section 1.2.2.1.). When cohesion between sister chromatids is lost, chromosomes are pulled apart by spindle forces (reviewed in (Lara-Gonzalez et al., 2021; Musacchio, 2011)). These movements are initially spawned by k-fiber shortening during anaphase A, which is thought to be driven by microtubule depolymerization at the kinetochore (known as the 'Pacman' activity), as well as via microtubule depolymerization near the spindle poles (reviewed in (McIntosh, 2021)) (Figure 1.10. A). This mechanism implicates that k-fibers preserve their attachment with the kinetochore even when microtubules are depolymerizing and that microtubule depolymerization produces pulling forces on kinetochores. However, how these contrasting features work and are finely tuned is still poorly understood. Subsequently, motor protein-mediated microtubule sliding drives spindle elongation, further contributing to chromosome segregation (anaphase B, Figure 1.10. B) (reviewed in (Vukusic et al., 2021)). Finally, chromosomes decondense, and a cleavage furrow is formed by contraction of an actin–myosin ring surrounding the central spindle, preparing the cell for the abscission in cytokinesis (reviewed in (Leite et al., 2019)) (Figure 1.10. C).

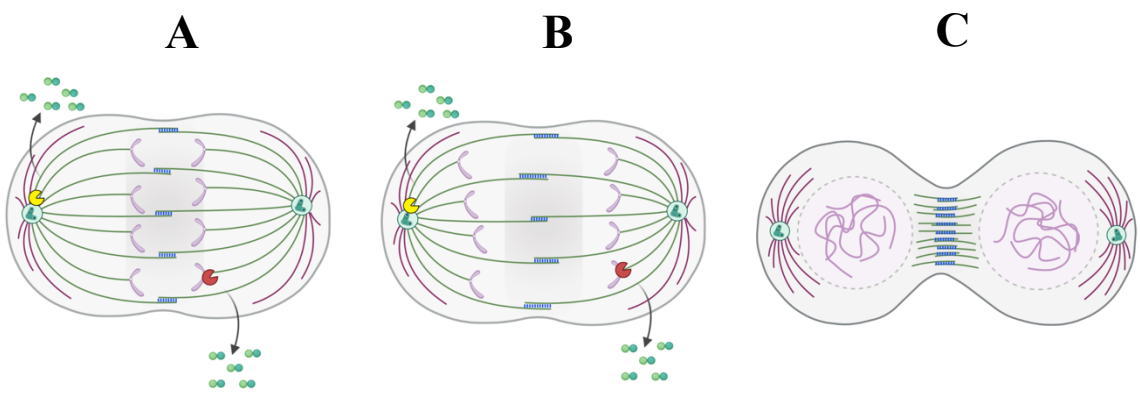

Figure 1.9. Mechanisms of chromosome segregation.

Once the last chromosome becomes bi-oriented and aligned, the cell is ready to enter anaphase. At anaphase onset, the CPC localizes to the centromeres and interacts with the motor protein Mklp2, which drives the re-localization of the CPC to the spindle midzone (grey gradient). **A,** chromosome separation in anaphase A starts with the shortening of kinetochore microtubules that is driven by microtubule depolymerization at the kinetochores ('Pacman') and near the spindle poles. **B**, in anaphase B sister chromatids further separate due to spindle elongation caused by motor protein-driven microtubule sliding. **C**, chromatids decondense, and a cleavage furrow is formed surrounding the central spindle and preparing the cell for cytokinesis.

1.9. Indian Muntjac

Diploid chromosome number among mammalian species is normally well established, typically ranging from 36 to 60 (Hartmann and Scherthan, 2004; Matthey, 1973; Scherthan et al., 1994). However, extreme cases are observed such as the red viscaha rat (*T. barrerae*) with 102 chromosomes (Contreras et al., 1990), and the small deer Indian muntjac (*M. muntjak)* whose females have the lowest known diploid chromosome number in mammals (2N=6) (Wurster and Benirschke, 1970). The genus *Muntiacus* experienced the greatest karyotype diversification within related species, spreading from the thought common ancestor of all Cervidae with 2N=70 (Bogenberger et al., 1987), to 2N=46 (*M. reveesi*) (Yang et al., 1997), 2N=13♀/14♂ (*M. feae*) (Soma et al., 1983), 2N=8♀/9♂ *(M. crinifrons*) (Ma, 1990) and finally the extreme case of Indian Muntjac (2N=6♀/7♂, *M. muntjak*) (Wurster and Benirschke, 1970). The latter is believed to result from repeated series of tandem and centric fusions (Chi et al., 2005b; Hsu et al., 1975; Liming et al., 1980), giving rise to large and morphologically distinct chromosomes, with one pair of acrocentric chromosomes (chromosome 3+X) containing an unusually large compound kinetochore (~2 μm linear length) (Drpic et al., 2018; Rattner and Bazett-Jones, 1989). The female karyotype consists of two pairs of autosomes, chromosome 1 and chromosome 2, which are metacentric (centromere is in the centre of the chromosome) and acrocentric (centromere is off-centred), respectively. Chromosome 3 carries an X-autosome translocation (long arm) and the actual X (short arm). The X chromosome is dividable in two portions, the distal section (acrocentric), and the proximal section that is the long and centromeric 'neck'. The male

karyotype contains a complementary small metacentric which corresponds to the Y sex chromosome (Figure 1.11.).

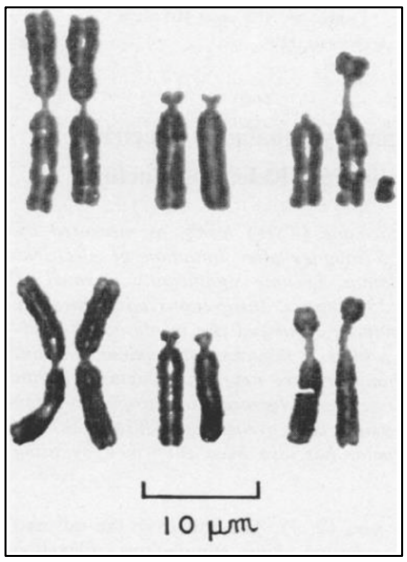

Figure 1.10. Karyotype of Indian muntjac cells.

Top row, male karyotype. Bottom row, female karyotype. The X chromosome is the upper portion of pair 3 (unpaired in the male) and the Y chromosome is the small metacentric. Adapted from (Wurster and Benirschke, 1970).

Since the discovery of the *M. muntjak* karyotype, cytogeneticists have been interested in exploring the mechanism of chromosome variation in this lineage. First studies suggested a reduction of chromosome number from a related deer, the Chinese muntjac, whose karyotype resembles those of cattle and other ancestral deer and is composed by 46 small acrocentric chromosomes (Wurster and Benirschke, 1967; Yang et al., 1997; Yingxiang and Longhui, 1986). Following this growing body of evidence, Brinkley *et al* used a specific antiserum derived from human patients with autoimmune disease scleroderma CREST (Brenner et al., 1981), as an immunofluorescence probe to follow Indian and Chinese muntjac kinetochores throughout the cell cycle (Brinkley et al., 1984). Surprisingly, a similar bead like pattern was found in both species, as well as a similar total fluorescence intensity of 'pre-kinetochores' in interphase nuclei. After comparing the morphology of the metaphase kinetochores with the 'pre-kinetochores' at interphase in both species, non-random aggregation of pre-kinetochores was suggested to originate the compound large kinetochores of Indian muntjac. The most popular mechanism suggested that centromeric heterochromatin targeted by clastogenic agents (mutagenic agents that disturb normal DNA, leading to chromosome rearrangements) allowed the fusion of chromosomes at telomeres and/or centromeres. The association of chromosomes, either centromere-centromere ('Robertsonian fusion'), centromere-telomere ('head-to-tail') or telomere-telomere generated a larger chromosome without extensive loss of DNA. In agreement, deletion of portions or entire blocks of centromeric heterochromatin during fusions is consistent

with the DNA sequence data available at the time (Schmidtke et al., 1981). Furthermore, the maintenance of the chromosome arms is supported by the G-banding patterns observed in the chromosomes of the two related muntjacs (Liming and Pathak, 1981). In contrast, random centric and lateral chromosome fusions followed by breaks and annealing at the centromeric heterochromatin were also considered as an plausible explanation for Indian muntjac compound kinetochores' evolution (Brinkley et al., 1984).

The chromosome 'head-to-tail fusion' theory was firstly supported by evidence showing that hybridization probes isolated from the DNA of Chinese muntjac cells targeted Indian muntjac centromeres and chromosome arms (Lin et al., 1991). Likewise, *M. reevesi* interstitial centromeric satellites and telomeric sequences were found in *M. muntjak* chromosomes (Lee et al., 1993; Lin et al., 1991; Scherthan, 1990). Few years later, by combining Fluorescence *In Situ* Hybridization (FISH), draft sequences of bacterial artificial clones (BAC) and chromosome painting techniques, the chromosome fusion theory was directly confirmed (Fronicke et al., 1997; Fronicke and Scherthan, 1997; Yang et al., 1995; Zhou et al., 2006). Nonetheless, some independent fusions not shared between the two related deer were found, suggesting that multiple tandem and centric fusions must have occurred independently in the *M. muntjak* and *M. reevesi* lineages (Wang and Lan, 2000; Yang et al., 1997). Building on these pioneering cytogenetic efforts, recent examination of their karyotype evolution using genome sequence comparisons, elucidated that there is an extensive collinearity (the same set of loci are located on the same chromosome and in the same order in each one of the considered species) between the two genomes and when compared with other deer and cattle genomes (Mudd et al., 2020). Moreover, chromosome-scale genome assemblies and high-throughput chromosome conformation capture (Hi-C) analyses revealed that, despite some chromosomal structure differences due to chromosome fission and fusion events, chromatin structure between the two muntjacs is largely conserved (Mudd et al., 2020).

The rate of chromosome changes on the muntjac lineage is estimated to be ten-fold higher relative to the observed average in other mammalian. However, what is the driver of this increased rate is still unknown. Previous studies estimated a ~3.2-4.9 million years divergence between the *M. muntjak* and *M. reevesi* (Chen et al., 2019b; Chi et al., 2005a; Hartmann and Scherthan, 2004; Mudd et al., 2020; Tsipouri et al., 2008; Zhou et al., 2006). Interestingly, despite the karyotype disparity between the two species, they are morphologically similar and can mate and produce viable, albeit sterile, offspring (Liming and Pathak, 1981). Regardless, the genome content of the two species is largely conserved, although packed into a different number and size of chromosomes. This provides an excellent setup to dissect potential roles and advantages regarding chromosome/kinetochore number and size (Brinkley et al., 1984; Chi et al., 2005a; Lin et al., 1991; Murmann et al., 2008; Wurster and Benirschke, 1967; Yang et al., 1997). Interestingly, the

Indian muntjac genome size is relatively small compared to other mammals. Estimation of haploid C-content (amount of DNA in a haploid genome) is approximately ~2.5 Gb for the *Cervidae*, whereas other families such as *Primates* (e.g. human) and *Rodentia* (e.g. rat) have genomes of roughly ~3.0 Gb and ~2.75 Gb, respectively (Chen et al., 2019b; Johnston et al., 1982). This difference might be due to differences on the intron dynamics, since Indian muntjac genes have a significant reduction in intron size compared to other mammals (Britten and Kohne, 1968; Zhou et al., 2006).

In the past, primary Indian muntjac fibroblasts were extensively used to study centromere morphogenesis and organization (Brinkley et al., 1984; Brinkley et al., 1988; Brown and Loughman, 1980; Comings and Okada, 1971; Rattner and Bazett-Jones, 1989), chromosomal structure (Hsu et al., 1975), as well as telomere biology (Zou et al., 2002). Nonetheless, their use for the study of mitosis has been limited by the demanding culture conditions of primary Indian muntjac fibroblasts and the tendency for replicative senescence, precluding the establishment of stable lines expressing useful fluorescent markers. Moreover, the lack of a sequenced genome until very recently, hampered the molecular studies in this system. Indian muntjac unique cytological features, combined with microscopy techniques may provide the ideal setup to dissect the underlying mechanisms of mitotic spindle assembly and chromosome segregation in mammalian cells. Nevertheless, more definitive proof of Indian muntjac advantages as a valuable model system are lacking in the field.

CHAPTER 2.

EXPERIMENTAL WORK

... 'The gift of the great microscopist is the ability to Think with the eyes and see with the brain. Deep revelations into the nature of living things continue to travel on beams of light'.

(Daniel Mazia)

CHAPTER 2.1.

‘Augmin-dependent microtubule self-organization drives kinetochore fiber maturation in mammals’

(Published in Cell Reports, 2022 https://doi.org.10.1016/j.celrep.2022.110610)

Abstract

Chromosome segregation in mammals relies on the maturation of a thick bundle of kinetochore-attached microtubules known as k-fiber. How k-fibers mature from initial kinetochore-microtubule attachments remains a fundamental question. By combining molecular perturbations and phenotypic analyses in Indian muntjac fibroblasts containing the lowest known diploid chromosome number in mammals (2N=6) and distinctively large kinetochores, with fixed/live-cell super-resolution coherent-hybrid stimulated emission depletion (CH-STED) nanoscopy and laser microsurgery, we demonstrate a key role for Augmin in kinetochore microtubule self-organization and maturation, regardless of pioneer centrosomal microtubules. In doing so, Augmin promotes kinetochore and interpolar microtubule turnover and poleward flux. Tracking of microtubule growth events within individual k-fibers reveals a wide angular dispersion, consistent with Augmin-mediated branched microtubule nucleation. Augmin depletion reduces the frequency of kinetochore microtubule growth events and hampers efficient repair after acute k-fiber injury by laser microsurgery. Together, these findings underscore the contribution of Augmin-mediated microtubule amplification for k-fiber self-organization and maturation in mammals.

CHAPTER 2.1. Augmin-dependent microtubule self-organization drives kinetochore fiber maturation in mammals

2.1.1. Introduction

Accurate chromosome segregation during mitosis relies on the formation of a thick bundle of microtubules that attach at the kinetochore region of each chromosome to form kinetochore fibers (k-fibers) (Rieder, 1982). While the molecular basis of end-on kinetochore-microtubule attachments has been elucidated in recent years and was shown to involve the conserved Ndc80 complex (Musacchio and Desai, 2017), the mechanism by which mammalian kinetochores attach up to dozens of microtubules within a matter of minutes remains poorly understood. For years, this process, known as k-fiber maturation, was thought to rely on consecutive rounds of 'search-and-capture' by centrosomal microtubules (Kirschner and Mitchison, 1986). However, this proved to be highly inefficient (Wollman et al., 2005) and inconsistent with the rapid acceleration of k-fiber maturation after a relatively slow initial microtubule capture rate at kinetochores (McEwen et al., 1997). Moreover, 'search-and-capture' by centrosomal microtubules cannot explain k-fiber formation and maturation in cells that are naturally devoid of centrosomes, such as in land plants or female oocytes (Wadsworth and Khodjakov, 2004), or after experimental centrosome inactivation in animal somatic cells (Khodjakov et al., 2000; Moutinho-Pereira et al., 2013).

Short non-centrosomal microtubules can be nucleated in the vicinity of chromosomes and kinetochores due to the microtubule stabilizing activity promoted by a Ran-GTP gradient and/or the chromosomal passenger complex (Maiato et al., 2004b; Maresca et al., 2009; O'Connell et al., 2009; Sampath et al., 2004; Tulu et al., 2006; Witt et al., 1980). These short microtubules are then captured and oriented with their plus-ends towards the kinetochore by CENP-E/kinesin-7 motors, and pre-formed kinetochore microtubules subsequently incorporated into the spindle by a Dynein-mediated interaction with non-kinetochore microtubules (Elting et al., 2014; Hueschen et al., 2017; Khodjakov et al., 2003; Maiato et al., 2004b; Sikirzhytski et al., 2014; Sikirzhytski et al., 2018). Augmin, an octameric Y-shaped complex that recruits γ-tubulin to pre-existing microtubules, triggers branched microtubule nucleation, thereby contributing to rapid microtubule amplification in the spindle (Goshima et al., 2008; Goshima et al., 2007; Hsia et al., 2014; Kamasaki et al., 2013; Lawo et al., 2009; Petry et al., 2013; Petry et al., 2011; Uehara et al., 2009b; Verma and Maresca, 2019; Wainman et al., 2009). In particular, the Augmin complex has been previously implicated in k-fiber formation (Goshima et al., 2008; Lawo et al., 2009; Uehara et al., 2009a; Zhu et al., 2008), but the underlying mechanism remains unclear. On one

hand, in *Drosophila* and human cells, Augmin subunits were shown to interact with the Ndc80 complex (Bucciarelli et al., 2009; Wu et al., 2009), which is required for the stabilization of end-on kinetochore-microtubule attachments, offering an alternative mechanistic explanation that is independent of Augmin's roles in microtubule amplification from pre-existing microtubules. On the other hand, Augmin-mediated microtubule amplification was recently shown to be the predominant source of spindle microtubules in human somatic cells and was proposed to account for the directional bias of microtubule growth towards the kinetochores after initial capture of pioneer centrosomal microtubules (David et al., 2019). However, due to intrinsic limitations imposed by the high chromosome number and the sub-diffraction size of human kinetochores and associated k-fibers, Augmin's role in k-fiber maturation has not been directly assessed. Moreover, the recent finding that most kinetochores in human cells develop their own k-fibers by 'sorting' short randomly oriented non-centrosomal microtubules that appear in the immediate vicinity of the kinetochores (Sikirzhytski et al., 2018), calls into question the requirement of pioneer centrosomal microtubules for k-fiber maturation.

The Indian muntjac (*Muntiacus muntjak)*, commonly known as 'barking deer', is a placental mammal whose females have the lowest known diploid chromosome number of their class (2N=6) (Wurster and Benirschke, 1970). As a result of repeated cycles of tandem and centric fusions (Chi et al., 2005b; Mudd et al., 2020), Indian muntjac cells have long and morphologically distinct chromosomes with unusually large kinetochores (up to 2 μm linear length) that bind up to 60 microtubules (Comings and Okada, 1971; Drpic et al., 2018; Rattner and Bazett-Jones, 1989). These unique cytological features, combined with recent large-scale ruminant genome sequencing efforts (Chen et al., 2019a), create the ideal conditions to directly dissect the molecular mechanism underlying k-fiber maturation in mammals. Here we used RNAi and high-resolution live-cell microscopy to investigate the role of more than 60 conserved mitotic proteins in mitotic spindle assembly and chromosome segregation in Indian muntjac fibroblasts. Assisted by sub-second live-cell super-resolution CH-STED nanoscopy analysis (Pereira et al., 2019) of microtubule growth within individual k-fibers and direct perturbation of k-fiber structure by laser microsurgery, we identified Augmin as the main driver of k-fiber self-organization and maturation.

2.1.2. Results

2.1.2.1. A live-cell RNAi screen in Indian muntjac fibroblasts identifies Augmin as a critical spindle assembly factor required for chromosome segregation

We used high-resolution live-cell microscopy combined with RNAi in hTERT-immortalized Indian muntjac fibroblasts (Zou et al., 2002) stably expressing histone H2B-GFP (to visualize chromosomes) and labelled spindle microtubules with 50 nM of SiR-tubulin (Drpic et al., 2018; Lukinavicius et al., 2014) to screen the roles of 63 conserved mitotic genes in spindle assembly and chromosome segregation in this system (Figure 2.1.1. A, B). Control cells took 25 ± 8 min (mean ± standard deviation (S.D.)) from nuclear envelope breakdown (NEBD) until the completion of chromosome alignment (metaphase), or 37 ± 7 (mean ± S.D.) min until anaphase onset (AO) (Figure 2.1.2. A', B and Figure 2.1.3). Upon RNAi, phenotypical fingerprints were generated for each protein based on the fraction of cells that exhibited one or more of the following defects: A) incomplete congression and faster mitosis (NEBD-AO<23 min); B) incomplete congression and normal mitotic duration (23≤NEBD-AO<52 min); C) incomplete congression and prolonged mitosis (NEBD-AO≥52 min); D) congression delay (NEBD-metaphase≥41 min); E) metaphase delay (metaphase-AO≥28 min); F) anaphase lagging chromosomes; G) mitotic death and H) cytokinesis failure (Figure 2.1.1. A, Figure 2.1.2. A' and Figure 2.1.3.).

To facilitate the visualization of the observed phenotypes, we set up a public repository where time-lapse movies, phenotypical fingerprints, siRNA sequences and western blotting analysis for each depletion can be conveniently browsed, and is freely available as a community resource (http://indianmuntjac.i3s.up.pt). An unbiased systematic cluster analysis defined ten distinct clusters and few 'orphan' proteins that highlight hierarchical relationships based on phenotypic similarities and respective frequencies (Figure 2.1.1. B). Among others, depletion of the Ndc80 complex (Nuf2, Ndc80 and Spc24), Aurora A, chTOG or the chromosomal passenger complex (INCENP, Survivin and Aurora B) was highly detrimental for spindle assembly and/or chromosome segregation (Figure 2.1.1. B, Figure 2.1.2. A, A', C and Figure 2.1.3.). Interestingly, co-depletion of VASH1 and VASH2, two recently identified carboxypeptidases involved in α-tubulin detyrosination (Aillaud et al., 2017; Nieuwenhuis et al., 2017), clustered together with CENP-E/kinesin-7 (Figure 2.1.1. B, Figure 2.1.2. A, A', C and Figure 2.1.3.), providing genetic evidence for the recently proposed role of microtubule detyrosination in the regulation of CENP-E-dependent congression of pole-proximal chromosomes (Barisic et al., 2015). Surprisingly, depletion of HURP and TPX2, two proteins previously implicated in Ran-GTP-dependent acentrosomal k-fiber formation (Katayama et al., 2008; Silljé et al., 2006; Torosantucci et al., 2008; Tulu et al., 2006; Wong and Fang, 2006) resulted only in very mild mitotic defects (Figure

2.1.1. B, Figure 2.1.2. A, A', C and Figure 2.1.3.). In contrast, depletion of Eg5/kinesin-5 or the Augmin complex subunit HAUS6 emerged as the most deleterious conditions for mitosis in Indian muntjac fibroblasts (Figure 2.1.1. B, Figure 2.1.2. A, A', C and Figure 2.1.3.). Because the critical role of Eg5/kinesin-5 motor activity in centrosome separation and bipolar spindle assembly is well established (Mann and Wadsworth, 2019), we focused on dissecting the mechanism by which Augmin impacts spindle assembly and chromosome segregation.

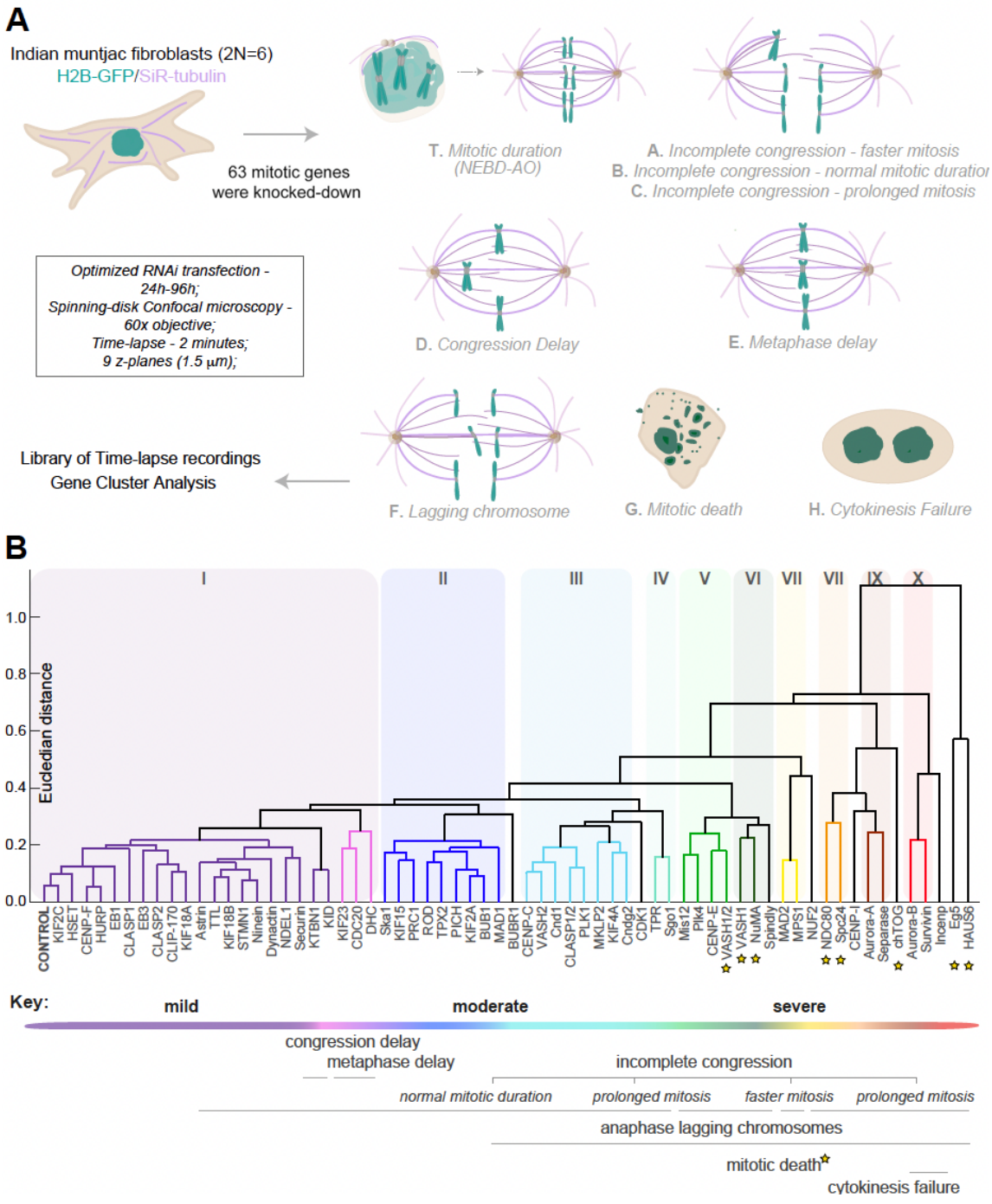

(figure legend on the next page)

Figure 2.1.1. A live-cell RNAi screen in Indian muntjac fibroblasts identifies Augmin as a critical spindle assembly factor required for chromosome segregation.

A, schematic representation of the mitotic screen performed in Indian muntjac fibroblasts. Mitotic timings (T. NEBD-AO) were determined and genes blindly clustered based on the probability of occurrence of eight binary features: A) incomplete congression and faster mitosis; B) incomplete chromosome and normal mitotic duration; C) incomplete congression and prolonged mitosis; D) congression delay; E) metaphase delay; F) anaphase lagging chromosomes; G) mitotic death and H) cytokinesis failure. **B,** dendrogram highlighting the hierarchical relationships between ten distinct clusters (I-X) and few 'orphan' proteins based on phenotypic similarities and respective frequencies. The severity of the defects increases from left to right. Euclidean distance was used as the distance metric to compare the phenotypical fingerprints.

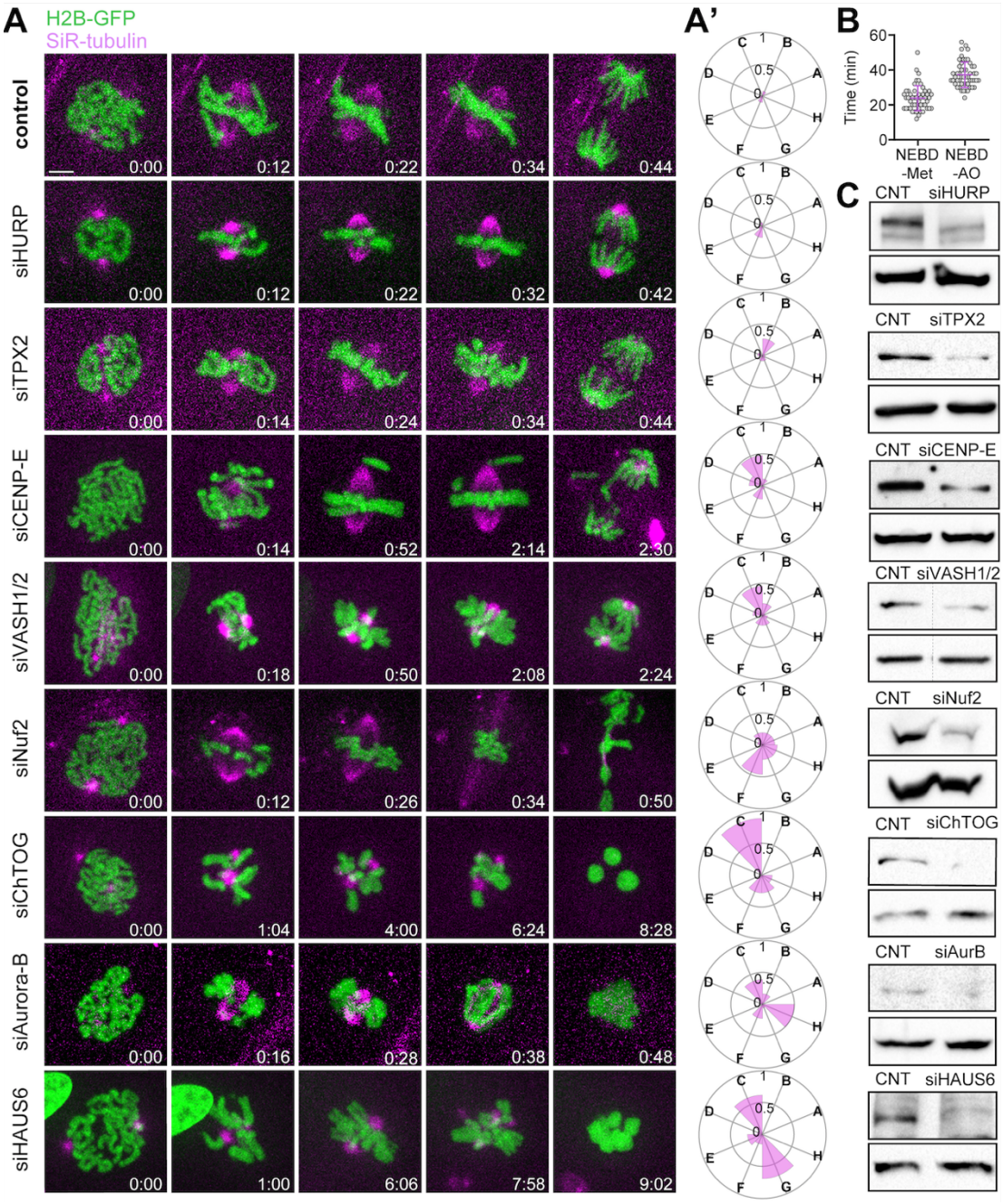

Figure 2.1.2. Augmin depletion is one of the most deleterious conditions for mitosis in Indian muntjac fibroblasts.

A, examples of the phenotypic analysis performed by live-cell spinning-disk confocal microscopy in Indian muntjac fibroblasts: siHURP (n=17 cells), siTPX2 (n=26 cells), siCENP-E (n=25 cells), siVASH1/2 (n=26 cells), siNuf2 (n=26 cells), siChTOG (n=18 cells), siAurora B (n=18 cells) and siHAUS6 (n=13 cells). Mock transfection (lipofectamine only) was used as control (n=52 cells). Scale bar: 5 µm. Time: h:min. **A'**, radar plots illustrating the phenotypic fingerprints reflecting the probability of occurrence of the 8 analyzed features (A-G) for the depletions shown in Figure 2.1.1. A.. Zero corresponds to a null-event and 1 to all cells displaying a certain event. **B,** mitotic timings from NEBD-Metaphase and NEBD-AO in control cells. Data pooled from 3 independent experiments. **C,** validation of RNAi efficiency by immunoblotting with specific antibodies against each target protein (upper band), except for VASH1/2, where only anti-VASH1 was used, and Nuf2, where anti-Hec1 was used. The bottom band corresponds to anti-GAPDH (siTPX2, siMad2, siVASH1/2, siNuf2 and siHAUS6), anti-α-tubulin (siHURP, siCENP-E and siAuroraB) or anti-vinculin (siChTOG), which were used as loading controls. CNT=control.

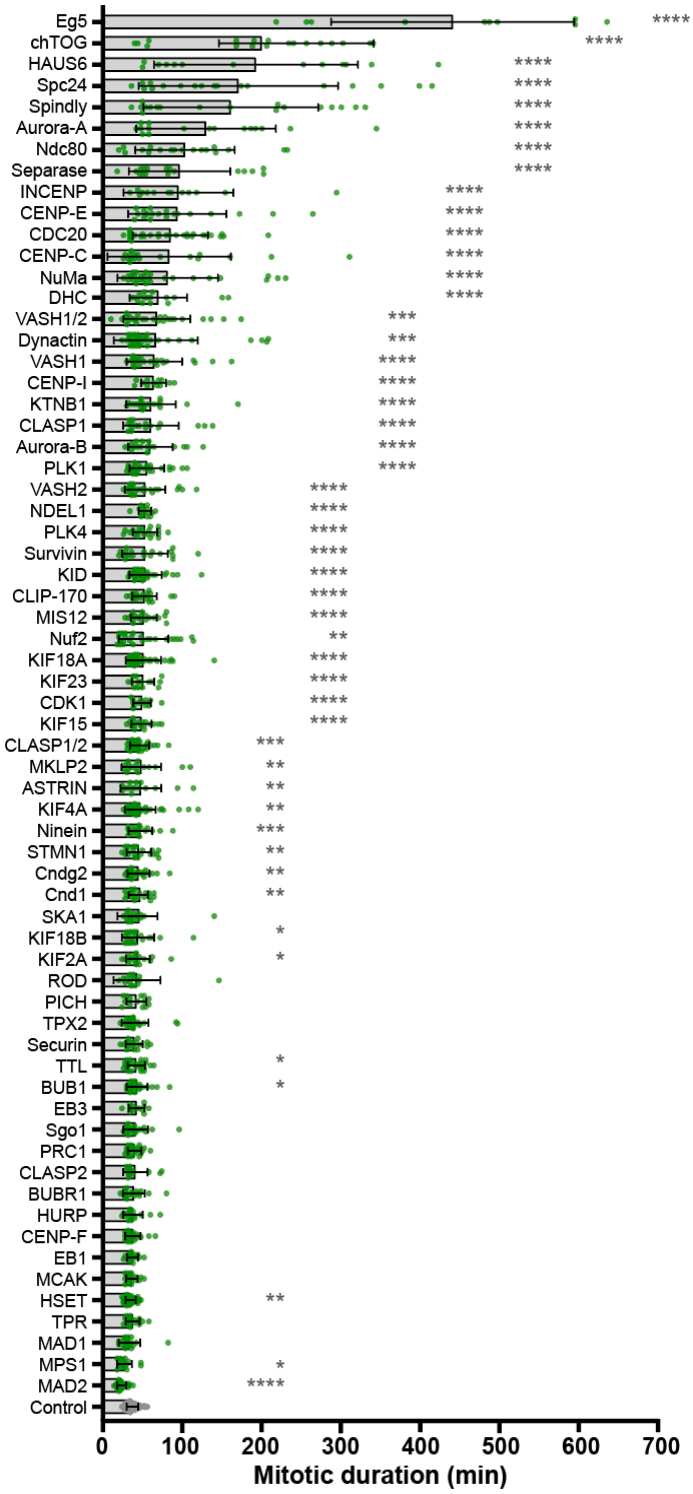

Figure 2.1.3. Mitotic timings of Indian muntjac fibroblasts upon gene-specific RNAi-mediated depletion.

Indian muntjac fibroblasts stably expressing H2B-GFP and labelled with 50 nM SiR-tubulin were acquired by confocal spinning-disk microscopy every 2 minutes. Mitotic duration was determined by measuring the time between NEBD to AO; shown in minutes. Each data point corresponds to one cell; data pooled from at least 3 independent experiments, except for siBubR1, siMPS1, siCdc20, siCENP-I, siCENP-F, siSurvivin, siAstrin, siEB1, siCLASP2, siCLASP1/2, siCLIP-170, siKTNB1, siAuroraA, siKif18B, siKID, siDHC, siNuMA, siNDEL1, siSpindly, siCnd1, siSgo1, siPlk1, siPRC1, siSeparase, siCDK1 where 2 experiments were performed; unpaired t-test; mean ± S.D.; *p≤0.05, **p≤0.01, ***p≤0.001, ****p≤0.0001, no asterisk corresponds to not significantly different from controls.

2.1.2.2. Augmin recruits γ-tubulin to the spindle region and promotes robust k-fiber and interpolar microtubule formation in Indian muntjac fibroblasts

We started by using conventional fluorescence microscopy in fixed cells to validate whether Augmin's requirement for k-fiber formation was conserved in Indian muntjac fibroblasts. To standardize conditions and allow enough time for spindle assembly, both control and HAUS6-depleted cells were arrested in mitosis for 1.5 hours with the proteasome inhibitor MG-132. In agreement with our live-cell data, mitotic spindle length after HAUS6 depletion was reduced almost 50% relative to controls (Figure 2.1.2. A, A', Figure 2.1.4. A, A'). In line with previous findings in *Drosophila* and human cells (Goshima et al., 2008; Goshima et al., 2007; Uehara et al., 2009a; Wainman et al., 2009), Indian muntjac HAUS6 (~80% similarity with human HAUS6 protein) was found associated with spindle microtubules (Figure 2.1.5. A), and its depletion drastically reduced γ-tubulin accumulation in the spindle region (Figure 2.1.4. B, B'). These phenotypes were the specific result of Augmin perturbation since RNAi-mediated depletion of another Augmin subunit (HAUS1) was indistinguishable from HAUS6 depletion (Figure 2.1.5. B). Immunofluorescence analysis with antibodies against the spindle assembly checkpoint protein Mad2, which accumulates at unattached kinetochores (Chen et al., 1996), and HURP, which decorates the kinetochore-proximal ends of k-fibers (Silljé et al., 2006), revealed that robust k-fiber formation was significantly compromised in HAUS6-depleted cells (Figure 2.1.4. C, C', D, D'). Indeed, cold treatment at 4°C for 5 minutesto selectively destabilize non-kinetochore microtubules in the spindle, as well as additional immunofluorescence analysis with antibodies against detyrosinated and acetylated α-tubulin, two post-translational modifications associated with stable microtubules (Khawaja et al., 1988; Piperno et al., 1987; Webster et al., 1990), confirmed that k-fibers were nearly absent after HAUS6 depletion (Figure 2.1.4. E, E', 2.1.6. A, A', B, B'). Depletion of Ndc80, an outer kinetochore protein required for the stabilization of end-on microtubule attachments (Musacchio and Desai, 2017) was used as a positive control, with the noticeable exception of acetylated α-tubulin that remained close to control levels (likely due to the preservation of interpolar microtubules), suggesting that detyrosinated α-tubulin has higher selectivity for more stable kinetochore-microtubules (Figure 2.1.4. D, D', E, E', Figure 2.1.5. C-D, 2.1.6. A, A', B, B').

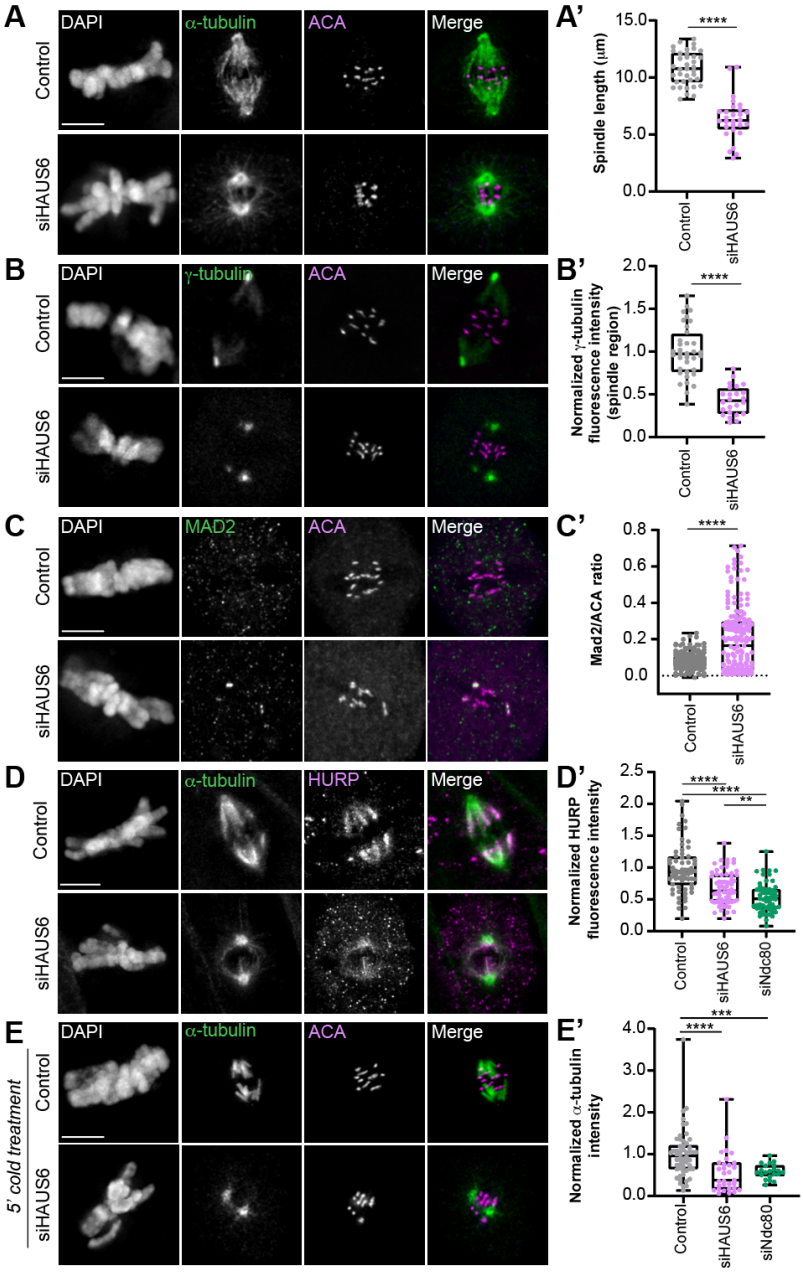

Figure 2.1.4. Augmin recruits γ-tubulin to the spindle region and is required for the formation of robust k-fibers in Indian muntjac fibroblasts

Immunofluorescence images of control and HAUS6-depleted Indian muntjac fibroblasts labelled for α-tubulin (green, **A**), γ-tubulin (green, **B**), Mad2 (green, **C**), HURP (magenta, **D**), anti-centromere antiserum (ACA, magenta, A-C) and DAPI (white). Spindle length was calculated in **A'** (n=37 Control cells; n=28 siHAUS6 cells); overall γ-tubulin fluorescence intensity was measured and normalized to the average control levels in **B'** (n=36 Control cells; n=24 siHAUS6 cells); ratio between Mad2 positive KTs and ACA fluorescence values was determined in **C'** (n=252 Control KTs; n=176 siHAUS6 KTs) and HURP signal in the spindle of HAUS6- and Ndc80-depleted cells was normalized to the average control levels in **D'** (n=65 Control cells; n=67 siHAUS6 cells; n=57 siNdc80 cells). **E,** cold treatment at 4°C for 5 min was performed to selectively destabilize non-kinetochore-microtubule. α-tubulin (green) signal was normalized to the average control levels in **E'** (n=54 Control cells; n=31 siHAUS6 cells; n=17 siNdc80 cells). Depletion of Ndc80 was used as a positive control (see Figure 2.1.5. C, D). The box plot determines the interquartile range; the line inside the box represents the median; data were pooled from 3 (A', C', D') or 2 (B', E') independent experiments; unpaired t-test (A', B') or Mann-Whitney test (C', D', E'); **p≤0.01, *** p≤0.001, ****p≤0.0001. Scale bars: 5 μm.

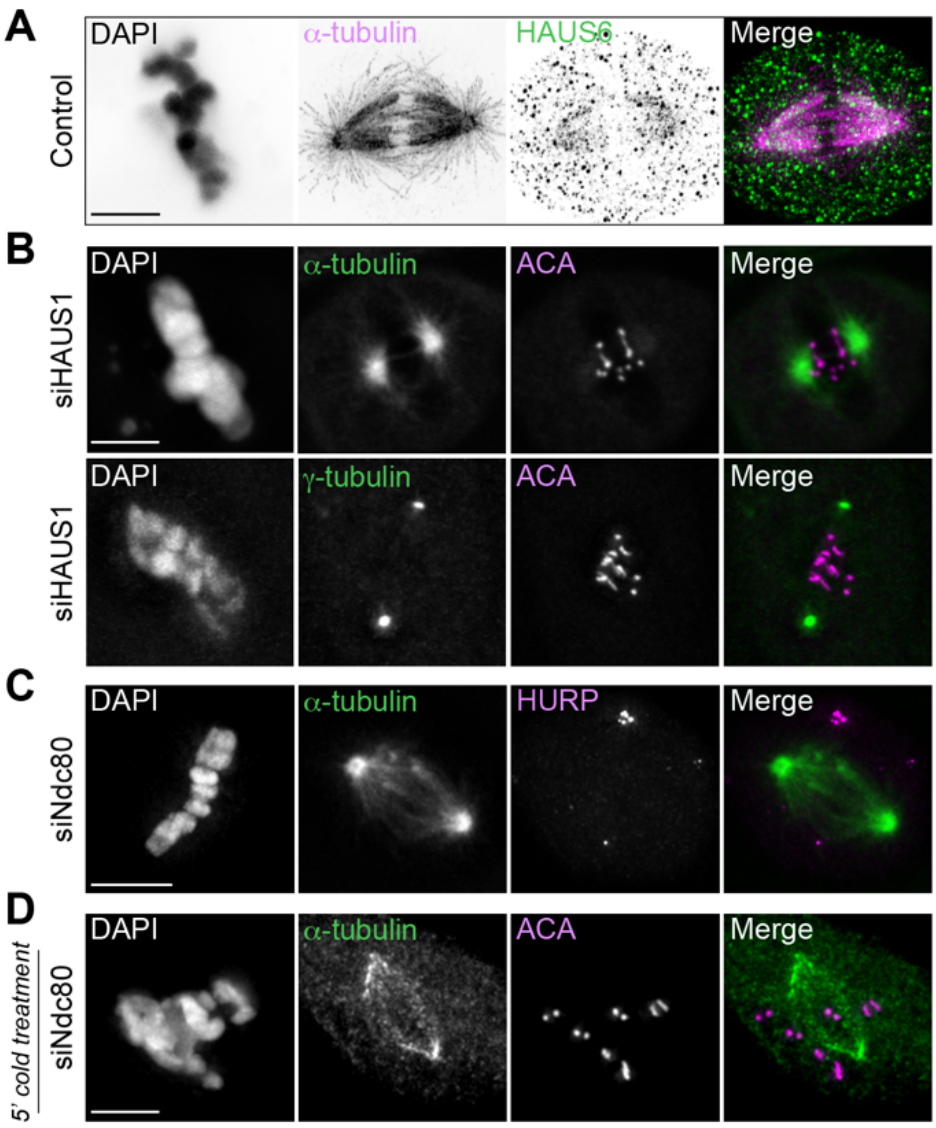

Figure 2.1.5. Depletion of a different Augmin subunit (HAUS1) resulted in short spindles and loss of γ-tubulin recruitment to the spindle region.

A, representative CH-STED image of HAUS6 localization in Indian muntjac mitotic spindle. DAPI (inverted grayscale), α-tubulin (magenta), HAUS6 (green). **B,** immunofluorescence of HAUS1-depleted cells. DAPI (white), α-tubulin/γ-tubulin (green) and ACA (magenta). Ndc80-depleted cell incubated with MG-132 for 1.5 hours and stained with anti-HURP (magenta), anti-α-tubulin (green) and DAPI (white) is shown in **C. D,** a cold treatment at 4°C for 5 min was performed to selectively destabilize non-kinetochore-microtubule. α-tubulin (green), ACA (magenta) and DAPI (white). For quantifications see Figure 2.1.4. C', D'. Scale bars: 5 μm.

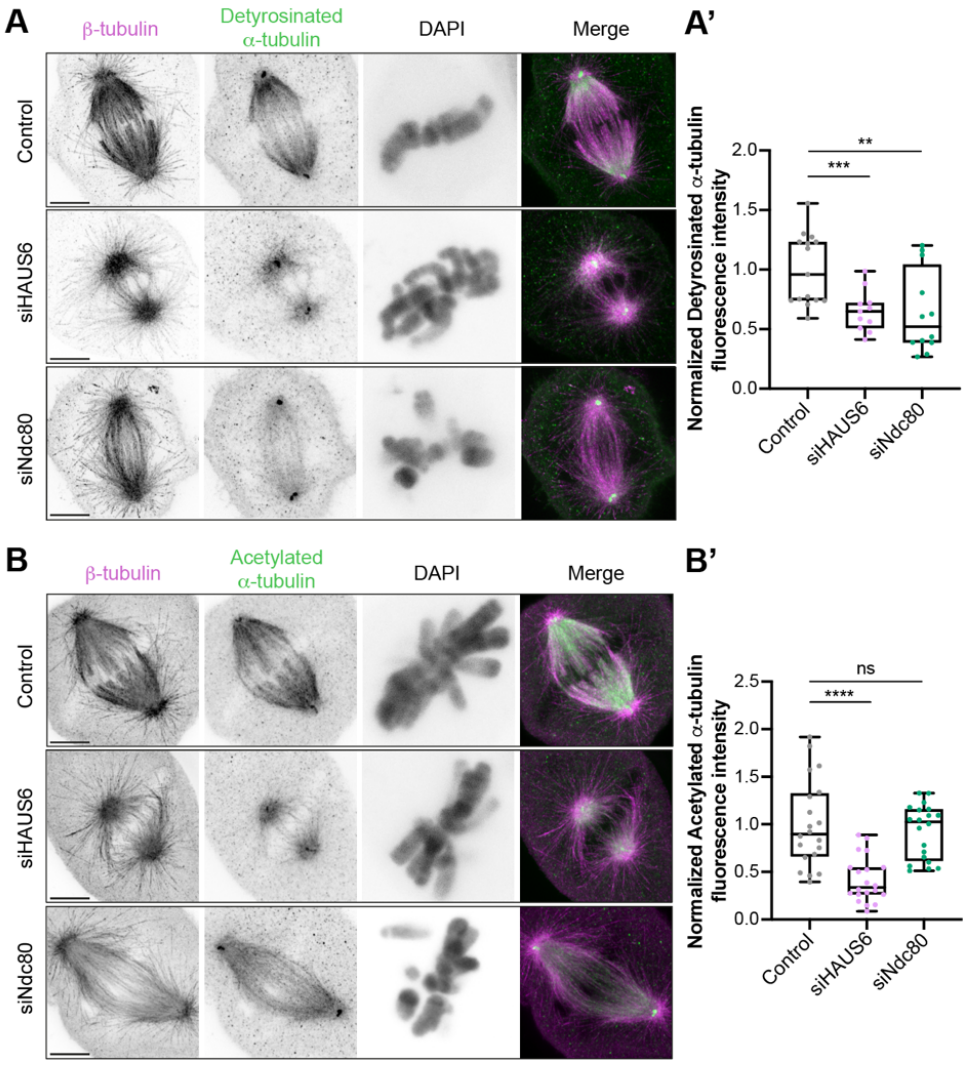

Figure 2.1.6. Levels of detyrosinated and acetylated α-tubulin are reduced after Augmin depletion.

Immunofluorescence of parental Indian muntjac fibroblasts treated with 3 μM MG-132 for 1 h stained with antibodies against detyrosinated (**A**) and acetylated α-tubulin (**B**). β-tubulin (magenta); detyrosinated/acetylated α-tubulin (green); DAPI (inverted grayscale). Quantification of detyrosinated and acetylated α-tubulin fluorescence intensity normalized to the average control levels is shown in **A'** and **B'**, respectively. The box plot determines the interquartile range and the line inside the box represents the median. Data pooled from 2 independent experiments and analyzed using a Mann-Whitney (A') or an unpaired t-test (B'); ns: not significant, **p≤0.01, ***p≤0.001, ****p≤0.0001 relative to controls. Scale bars: 5 μm.

To gain additional insight into the role of Augmin in k-fiber formation, we optimized fixation conditions to preserve microtubule structure (see Materials and Methods) and inspected HAUS6-depleted cells by super-resolution coherent-hybrid stimulated emission depletion (CH-STED) nanoscopy, which improves contrast in complex 3D objects like the mitotic spindle relative to conventional 2D-STED (Pereira et al., 2019). This analysis confirmed the absence of robust k-fibers after Augmin perturbation (Figure 2.1.7. A). In addition, we found that HAUS6-depleted cells exhibited overly elongated astral microtubules (Figure 2.1.7. A-B).

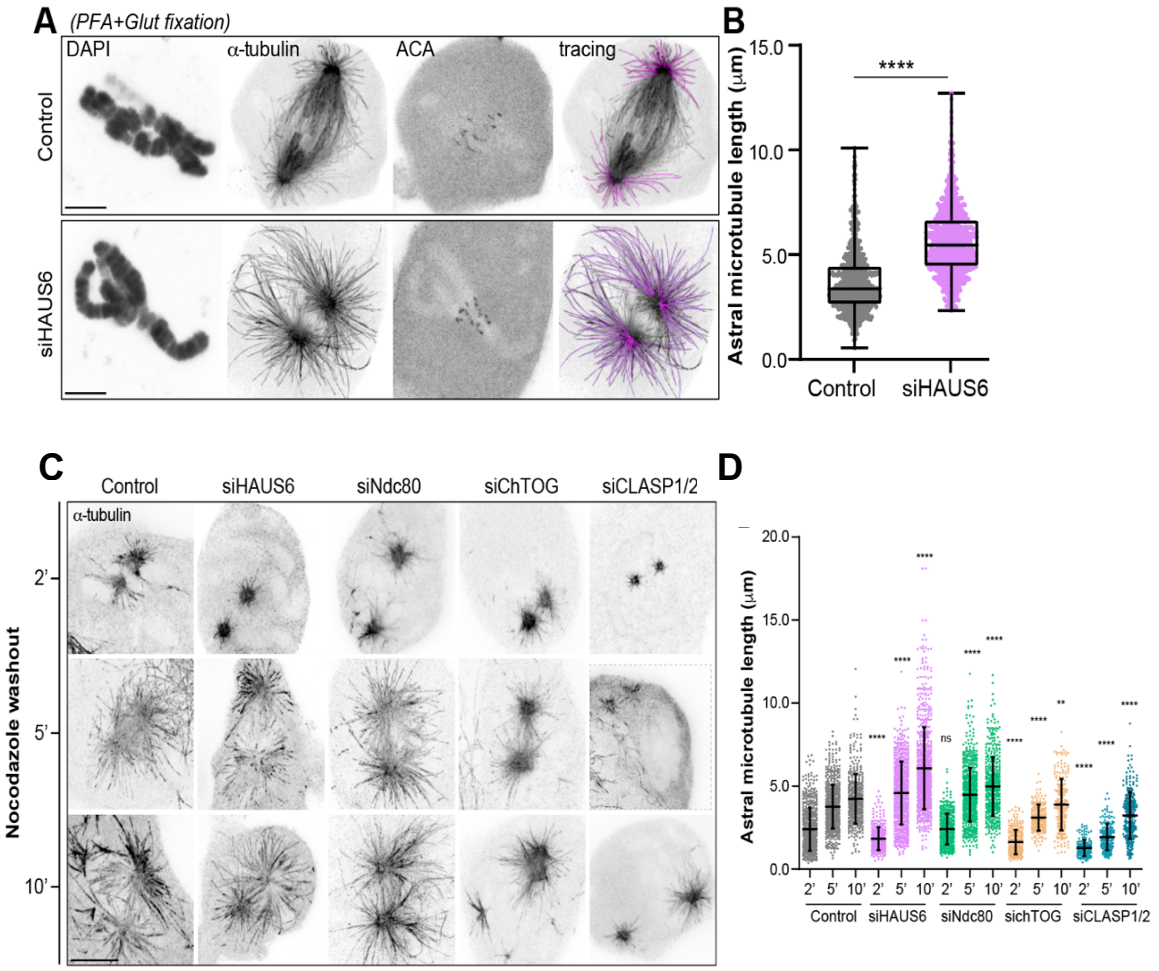

Figure 2.1.7. Perturbation of k-fiber formation in Indian muntjac cells is sufficient to bias tubulin polymerization towards astral microtubules.

Images of control and HAUS6-depleted cells acquired by CH-STED nanoscopy. **A**, immunofluorescence of Indian muntjac fibroblasts using paraformaldehyde and glutaraldehyde fixation. DAPI, α-tubulin and ACA are shown in inverted grayscale. Astral microtubule tracks are represented in magenta (tracing). **B,** quantification of astral microtubule length (n=665 Control astral microtubules/10 cells; n=750 siHAUS6 astral microtubules/11 cells). The box plot determines the interquartile range; the line inside the box represents the median; data pooled from 3 independent experiments and analyzed using an unpaired t-test. **C**, representative CH-STED images of control, HAUS6-, Ndc80-, chTOG- and CLASP1/2-depleted cells incubated with 1 μM nocodazole for 2 h, washed-out into warm medium and fixed after 2-, 5- and 10-minutes. Cells were then stained for α-tubulin (inverted grayscale). Astral microtubule length was determined in **D** (Control: 2' n=567, 5' n=650, 10' n=434 astral microtubules; siHAUS6: 2'= 376, 5' n=633, 10' n=754 astral microtubules; siNdc80: 2' n=425, 5' n=704; 10' n=469 astral microtubules; siChTOG: 2' n=261, 5' n=194, 10' n=217 astral microtubules; siCLASP1/2: n=161, 5' n=183, 10' n=284 astral microtubules). Acquisition ROI for siCLASP1/2 nocodazole washout 2' image is represented in grey-dashed line. All data were pooled from 3 independent experiments and analyzed using an unpaired t-test; mean ± S.D.; ns: not significant, **p≤0.01, ****p≤0.0001 relative to controls. Scale bar: 5 μm

To rule out a possible role for the Augmin complex in centrosome-dependent microtubule nucleation (Wu et al., 2009), we performed a microtubule regrowth assay after treatment with the microtubule-depolymerizing drug nocodazole for 2 hours, a condition that completely depolymerized all microtubules without compromising cell viability, followed by nocodazole washout and fixation after 2, 5 and 10 min, in the presence or absence of HAUS6 (Figure 2.1.7. C and Figure 2.1.10. A-B). We found that after HAUS6 depletion, centrosome-nucleated astral microtubules grew significantly longer than controls, 5 and 10 minutes after nocodazole washout, despite being slightly shorter at 2 minutes (Figure 2.1.7. C-D). By comparison, depletion of Ndc80, led to a similar, yet less pronounced, outcome (Figure 2.1.7. C-D). In contrast, perturbation of the TOG-domain proteins chTOG and CLASPs, which promote microtubule polymerization (Al-Bassam and Chang, 2011), significantly compromised microtubule regrowth from centrosomes after nocodazole treatment/washout in all time points (Figure 2.1.7. C-D). These results strongly suggest that, regardless of the underlying molecular nature, experimental perturbation of k-fiber formation in Indian muntjac cells is sufficient to bias tubulin polymerization towards astral microtubules.

To obtain a quantitative picture of Augmin's contribution to k-fiber and interpolar microtubule formation, we processed Indian muntjac fibroblasts for immunofluorescence with antibodies against PRC1 and β-tubulin. PRC1 detection was only preserved upon cold methanol fixation and was found enriched along overlapping interpolar microtubules (also known as bridging fibers) (Kajtez et al., 2016) in control metaphase cells (Figure 2.1.8. A). Surprisingly, HAUS6 depletion caused the dispersion of PRC1 to both parallel and anti-parallel microtubules (Figure 2.1.8. A). For this reason, we implemented a quantitative assay relying exclusively on the β-tubulin signal to determine the proportion of kinetochore and non-kinetochore microtubules (Figure 2.1.8. B; see Materials and Methods). This analysis revealed that HAUS6 depletion caused ~60% reduction in the total spindle microtubule population, affecting both kinetochore and interpolar microtubules (Figure 2.1.8. C). Taken together, these data demonstrate that Augmin recruits γ-tubulin to the spindle and is required for k-fiber and interpolar microtubule formation in Indian muntjac fibroblasts.

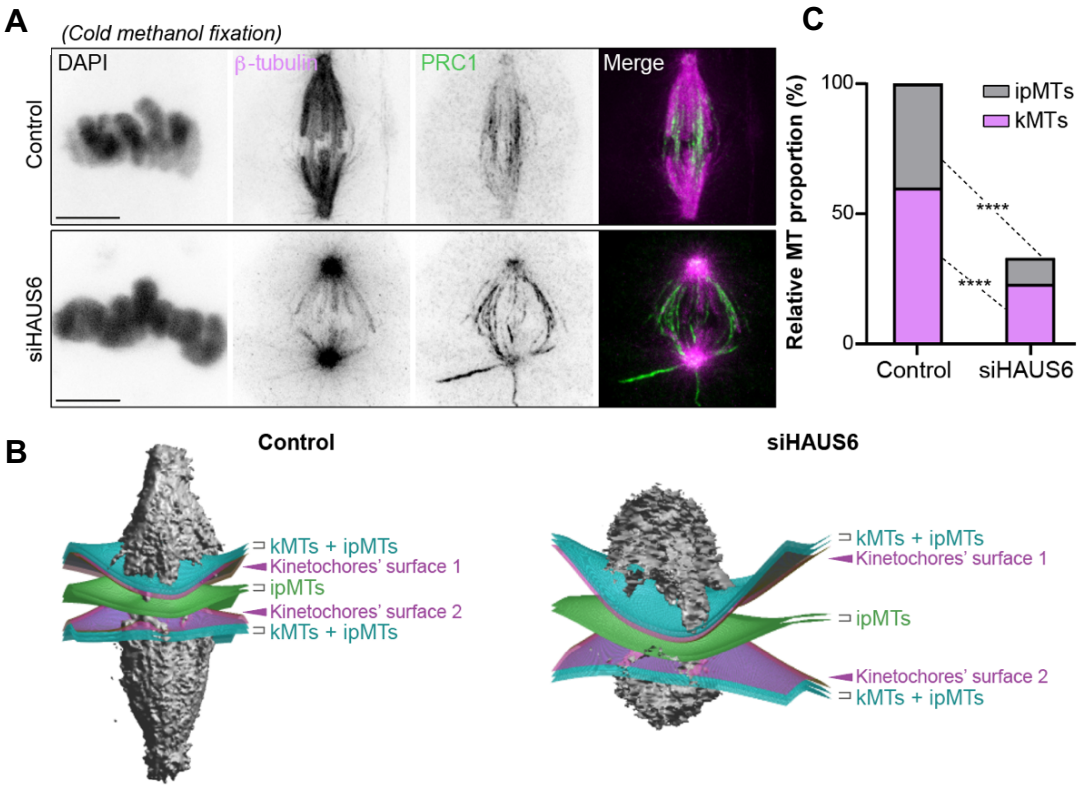

Figure 2.1.8. Augmin contributes to k-fiber and interpolar microtubule formation.

A, immunofluorescence of Indian muntjac fibroblasts using cold methanol fixation. β-tubulin (magenta) and PRC1 (green). **B**, 3D representations of mitotic spindles in control and HAUS6-depleted cells, illustrating KT surfaces' 1 and 2 (magenta), as well as the plates that define the measurement volumes, corresponding to interpolar microtubules (ipMTs, green) and k-fibers (kMTs) plus ipMTs (cyan). **C**, quantification of ipMTs and kMTs in control and HAUS6-depleted cells. Proportion relative to control levels is represented for HAUS6-depleted cells (n=14 Control cells; n=12 siHAUS6 cells). Data pooled from 2 independent experiments and analyzed using an unpaired t-test; ****p≤0.0001. Scale bar: 5 µm.

2.1.2.3. Augmin sustains centrosome-independent microtubule self-organization from kinetochores

Recent correlative light and electron microscopy studies in early prometaphase in human cells revealed that most k-fibers form by capturing short randomly oriented non-centrosomal microtubules that appear in the immediate vicinity of the kinetochores (Sikirzhytski et al., 2018). To investigate the role of Augmin in centrosome-independent k-fiber self-organization, we followed microtubule regrowth from Indian muntjac kinetochores (labeled with 2xGFP-CENP-A) after nocodazole treatment/washout, which recapitulates microtubule self-organization from kinetochores under physiological conditions (Sikirzhytski et al., 2018; Tulu et al., 2006; Witt et

al., 1980), in cells treated with centrinone, a Plk4 inhibitor that prevents centriole duplication (Wong et al., 2015) (Figure 2.1.9. A, A'). Successful elimination of centrioles was confirmed by the loss of GFP-Centrin-1 signal (which is brighter than 2xGFP-CENP-A) and by counting the number of kinetochores by CH-STED microscopy (Figure 2.1.10. C). We found that short microtubule stubs appeared virtually in all kinetochores in control, HAUS6- and Ndc80-depleted cells (Figure 2.1.9. A-C, Figure 2.1.10. D-E), suggesting that the Augmin and Ndc80 complexes are dispensable for the initial step of microtubule nucleation in the vicinity of kinetochores in mammals. However, both HAUS6- and Ndc80-depleted cells showed a significant decrease in the fraction of kinetochores that remained associated with microtubules over time (Figure 2.1.9. A-B, Figure 2.1.10. D-F). Importantly, whereas HAUS6 depletion prevented kinetochore-microtubules from growing to the same extent as in controls and caused an overall reduction in the microtubule polymer that was initially associated with kinetochores, Ndc80 depletion led to longer microtubules that appeared to associate laterally with kinetochores (Figure 2.1.9. A, C, D, Figure 2.1.10. D-F). These results suggest that, while Ndc80 is necessary to stabilize end-on microtubule attachments after nucleation in the vicinity of kinetochores, Augmin is required to amplify and sustain the growth of small microtubules after their initial capture by kinetochores.

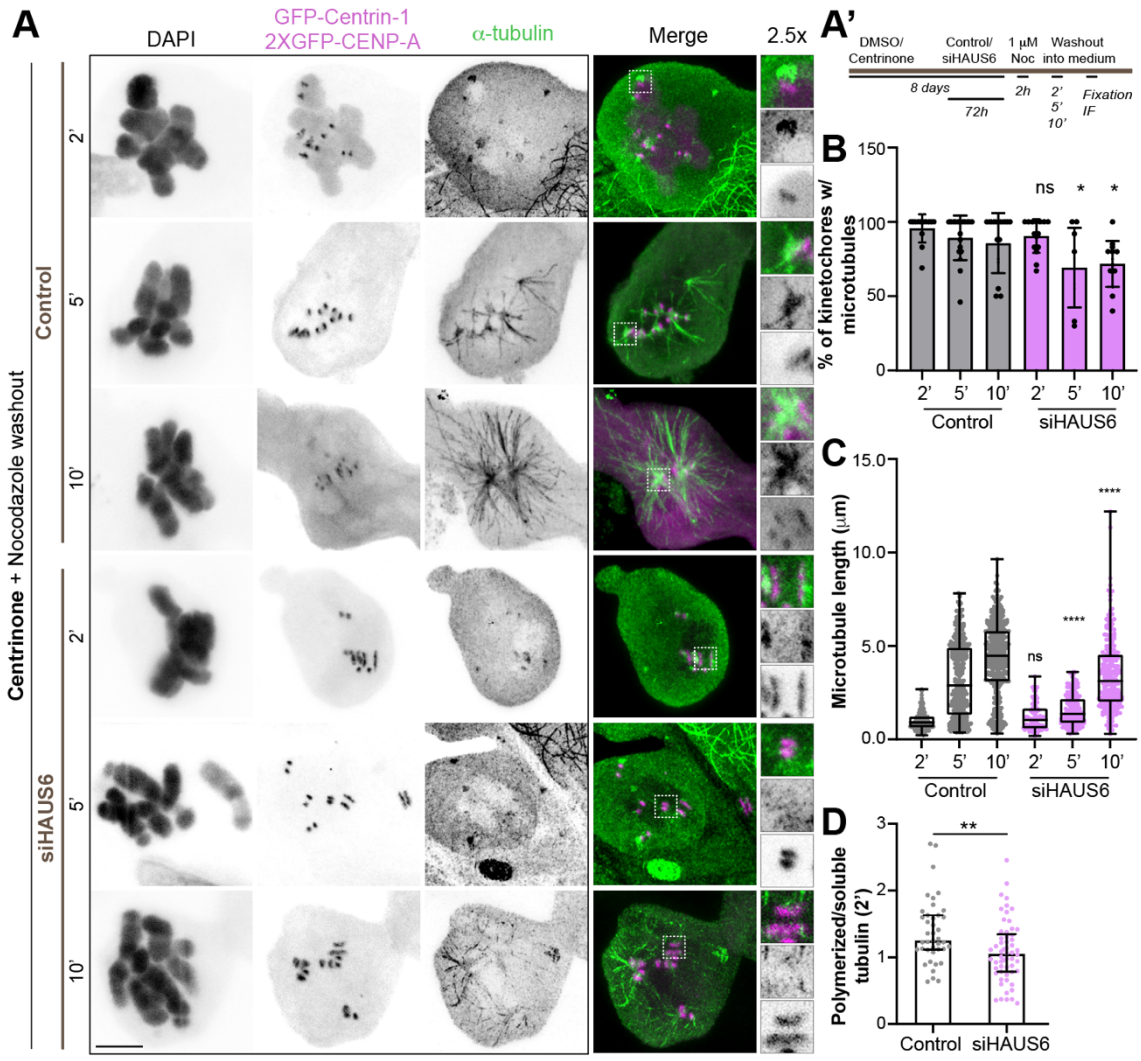

Figure 2.1.9. Augmin sustains centrosome-independent microtubule self-organization from kinetochores.

A, CH-STED images of Indian muntjac cells stably expressing GFP-Centrin-1 (magenta) and 2xGFP-CENP-A (magenta) treated with centrinone for 8 days with or without HAUS6 RNAi for 72 h. Cells were treated with the microtubule-depolymerizing drug nocodazole for 2 h, followed by drug washout and fixation after 2, 5 and 10 minutes. α-tubulin (green) and DAPI (inverted grey scale). Insets show 2.5x magnification of selected regions with KT and nucleated microtubules (grayscale for single channels of 2xGFP-CENP-A and α-tubulin). The experimental setup is described in **A'**. The percentage of KTs with microtubules and overall microtubule length are represented in **B** and **C**, respectively (Control 2': n=13 cells/154 microtubules, Control 5': n=20 cells/350 microtubules, Control 10': n=19 cells/402 microtubules; siHAUS6 2': n=16 cells/91 microtubules; siHAUS6 5': n=14 cells/176 microtubules; siHAUS6 10': n=14 cells/254 microtubules). The ratio of polymerized tubulin at KTs relative to the overall cytoplasmatic pool 2 min after nocodazole washout is shown in **D** (Control 2': n=41 KTs; siHAUS6 2': n=53 KTs). Data pooled from 3 independent experiments, analyzed using a Mann-Whitney test; the box plot determines the interquartile range and the line inside the box represents the median (C); mean ± S.D. (B, D); ns: not significant, *p≤0.05, **p≤0.01, ****p≤0.0001. Scale bars: 5 μm.

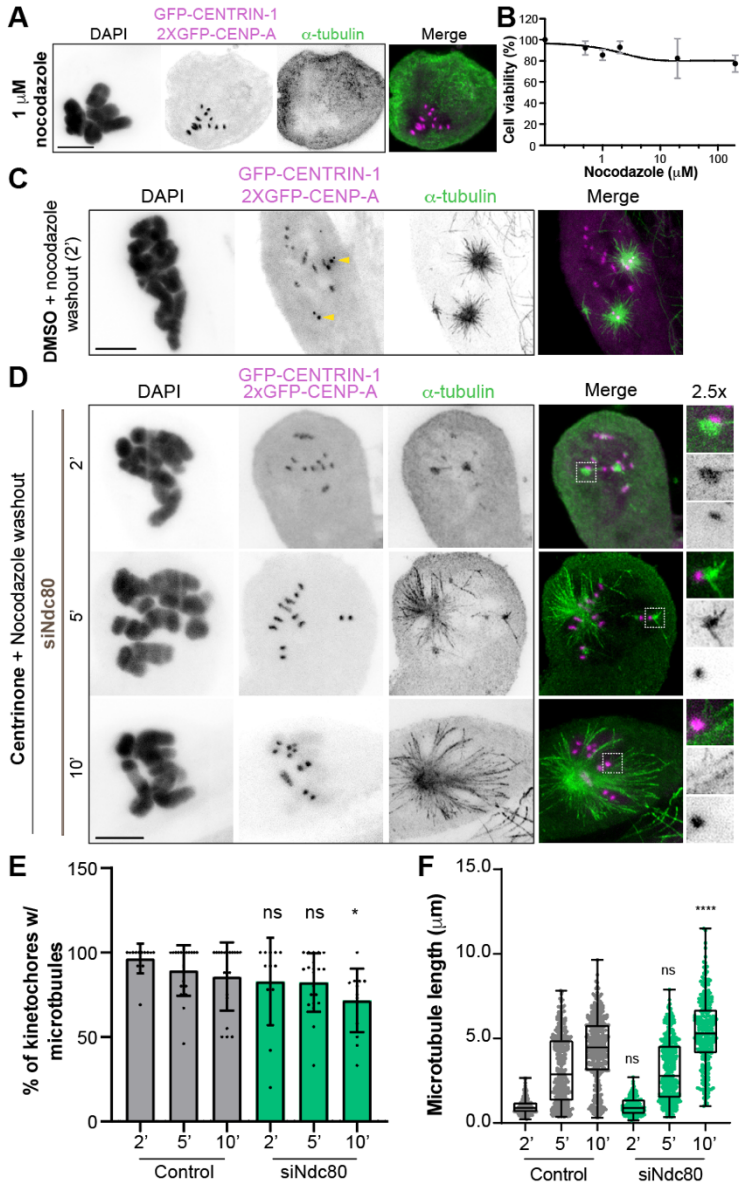

Figure 2.1.10. Ndc80 depletion does not affect microtubule re-growth in acentrosomal spindles.

A, representative CH-STED image of an Indian muntjac cell stably expressing GFP-Centrin-1 (magenta) and 2xGFP-CENP-A (magenta), treated with 1 μm nocodazole for 2 h. No microtubules were detected (α-tubulin, green). **B**, cell viability assay of Indian muntjac cells treated with increasing concentrations of Nocodazole (0.5, 1, 2, 20 and 200 μm) for two h. Each point represents the average of three replicates. Mean ± S.D. **C,** representative CH-STED image of an Indian muntjac cell stably expressing GFP-Centrin-1 (magenta) and 2xGFP-CENP-A (magenta), 2 min after washout from nocodazole, upon 8-days DMSO treatment. Yellow arrowheads indicate the centrioles. **D**, microtubule regrowth assay after 2, 5 and 10 min nocodazole washout in warm medium, upon 8-days centrinone treatment and Ndc80 RNAi transfection for 24 h. Cells were fixed and immunostained with α-tubulin antibody (green) and DAPI (inverted grayscale). Insets show 2.5X magnification of selected regions with KT and nucleated microtubules (grayscale for single channels of CENP-A and α-tubulin). The percentage of KTs with microtubules, **E**, and overall microtubule length, **F**, at each time point is shown (siNdc80 2' n=12 cells/154 microtubules; 5' n=21 cells/400 microtubules; 10' n=14 cells/337 microtubules). Each data point represents one cell (E) or one microtubule (F); data were collected from 2 (F) or at least 3 (E) independent experiments and analyzed using a Mann-Whitney test; the box plot determines the interquartile range and the line inside the box represents the median (F); mean ± S.D. (E); ns: not significant, ****p≤0.0001. Scale bars: 5 μm.

2.1.2.4. Augmin promotes kinetochore microtubule turnover and poleward flux

To investigate how Augmin sustains microtubule growth from kinetochores we started by implementing a live-cell CH-STED nanoscopy assay in Indian muntjac fibroblasts stably expressing 2xGFP-CENP-A to visualize kinetochores, and Halo-tagged EB3 conjugated with the bright, photostable, far-red ligand JF646 (Erdmann et al., 2019; Grimm et al., 2015) to track growing microtubule plus ends for 2 minutes at 8 seconds and ~100 nm resolution (Figure 2.1.11. A-A', Figure 2.1.14. A-B). Quantitative analyses revealed that the velocity of poleward and anti-poleward chromosome movement, chromosome oscillation amplitude, but not oscillation period, were severely reduced upon HAUS6 or Ndc80 depletion (Figure 2.1.11. B-E). Moreover, while in control cells EB3 accumulated at kinetochores for one half period of chromosome oscillations corresponding to anti-poleward movement, EB3 only rarely associated with kinetochores after HAUS6 or Ndc80 depletion (Figure 2.1.11. F). Importantly, HAUS6, but not Ndc80, depletion led to a shorter kinetochore-to-pole distance (Figure 2.1.11. G), suggesting a distinct mode of action by which these proteins contribute to k-fiber formation.

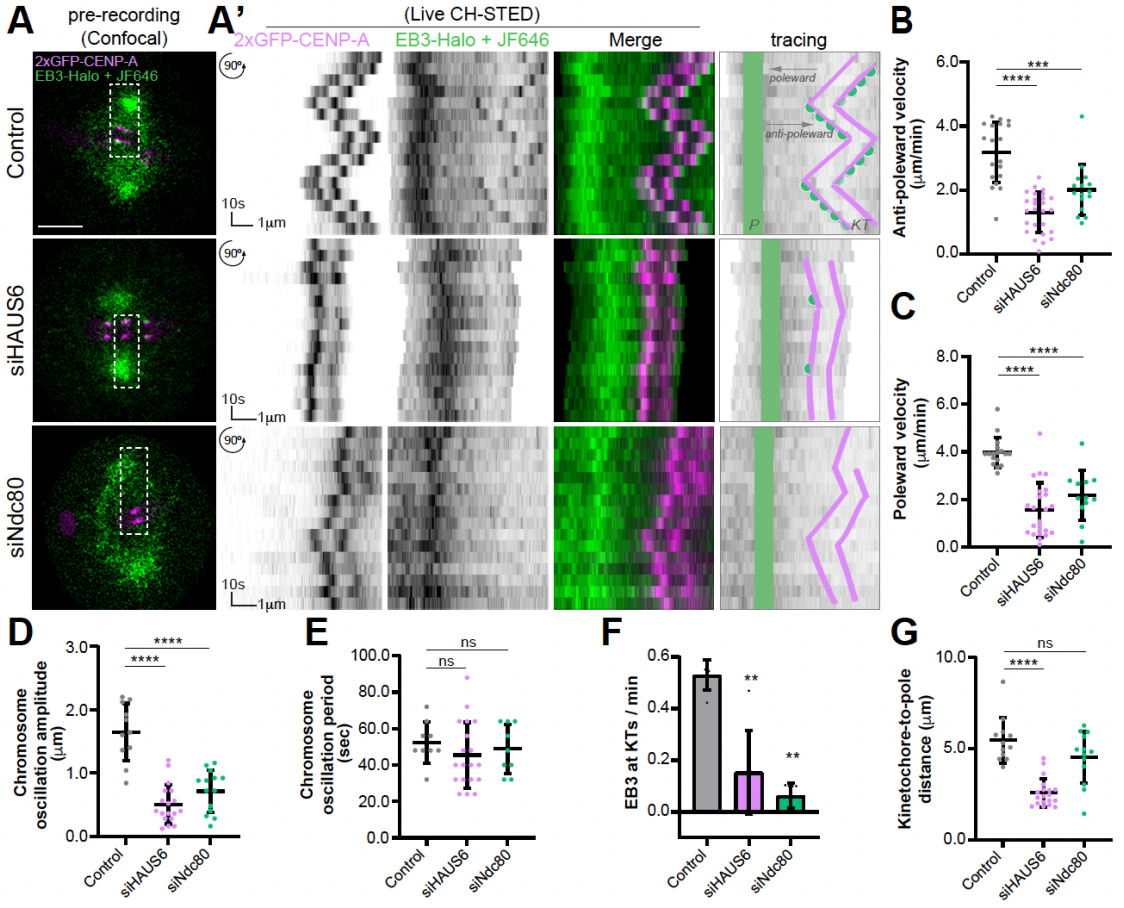

(figure legend on the next page)

Figure 2.1.11. Augmin is required to maintain kinetochore dynamics and oscillations.

A, pre-recording snapshots of control, HAUS6- and Ndc80-depleted Indian muntjac fibroblasts stably expressing 2xGFP-CENP-A (magenta) and EB3-Halo tag conjugated with JF646 (green), imaged by confocal microscopy. **A',** collapsed kymographs of live CH-STED recordings (time-lapse: 8 sec; pixel size: 40 nm). Graphical sketches on the right highlight chromosome movement over time (tracing); P- pole (green); KT- kinetochore (magenta); EB3 accumulation at KT is shown in green. Quantitative analysis of chromosome anti-poleward, **B**, and poleward, **C,** velocities, chromosome oscillatory amplitude, **D**, and period, **E**. Fraction of EB3 accumulation at KT per minute (approximately one period) was measured from track data in **F**, and KT-to-pole distance determined in **G**. Horizontal bar: 1 µm; vertical bar: 10 sec; (n=8 Control cells, n=9 siHAUS6 cells and n=8 siNdc80 cells). Each data point represents one measurement; data pooled from at least 3 independent experiments and analyzed using a Mann-Whitney test (B, C, F, G) or an unpaired t-test (D). ns: not significant, **p≤0.01, ***p<0.001, ****p≤0.0001. Scale bar: 5 µm.

To determine whether Augmin is required to promote kinetochore-microtubule turnover we used fluorescence dissipation after photoactivation (FDAPA) of PA-GFP-α-tubulin (Girao and Maiato, 2020) (Figure 2.1.12. A). By fitting the fluorescence decay over time to a double exponential curve (R^2>0.98), we differentiated two spindle microtubule populations with fast and slow fluorescence decay (Figure 2.1.12. B) that have been attributed to less stable non-kinetochore microtubules (non-kMTs) and more stable microtubules (kMTs), respectively (Conway et al., 2021; Girao and Maiato, 2020; Zhai et al., 1995). We found that partial HAUS6 depletion by RNAi over 36 hours (note that optimal HAUS6 depletion over 72 hours completely disrupts k-fiber formation) significantly increased the half-life of both kinetochore and non-kMTs (Figure 2.1.12. C). In parallel, by measuring the velocity by which the photoactivation mark on spindle microtubules moved relative to the metaphase plate (i.e. underwent poleward flux) (Barisic et al., 2021b), we found that it was reduced by ~40% after partial HAUS6 depletion (Figure 2.1.12. D). Overall, these data indicate that Augmin promotes kMTs and non-kMTs turnover, while assisting poleward flux in metaphase cells.

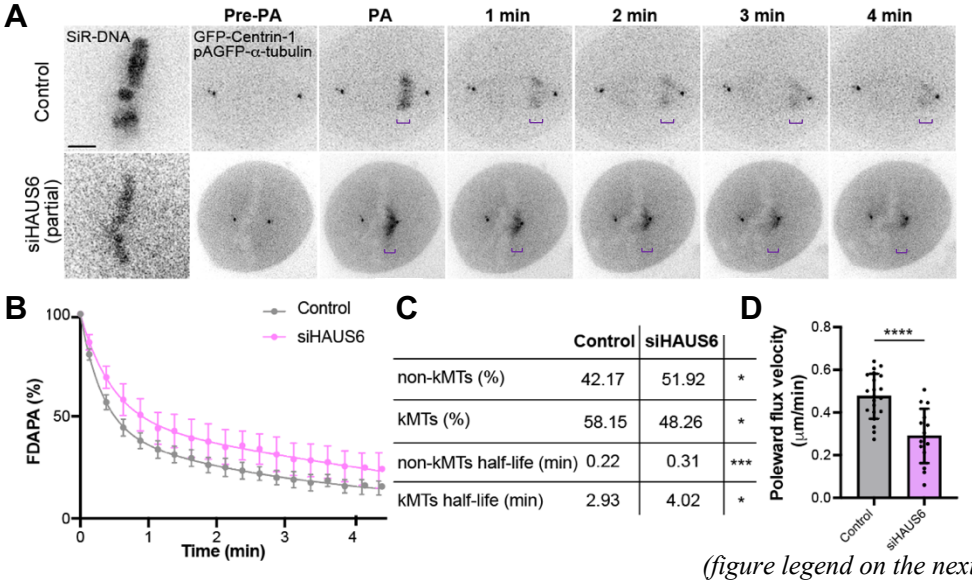

(figure legend on the next page)

Figure 2.1.12. Augmin promotes kinetochore microtubule turnover and poleward flux.

A, examples of control and partial HAUS6-depleted metaphase cells displaying photoactivatable PA-GFP-α-tubulin (inverted grayscale), GFP-Centrin-1 (inverted grayscale) and labeled with 50 nM SiR-DNA to visualize chromosomes (inverted grayscale). 'Pre-PA': frame immediately before photoactivation; 'PA': frame immediately after photoactivation; purple brackets: photoactivation mark. **B**, normalized fluorescence dissipation after photoactivation (FDAPA) curves of control and partial HAUS6-depleted cells. Whole lines show double exponential curve fittings (R^2>0.98), and error bars show 95% confidence interval for each time point. **C**, table showing the calculated microtubule percentages and turnover values for control and partial HAUS6-depleted cells (n=20 Control cells; n=11 siHAUS6 cells). **D**, microtubule flux velocity (n=21 Control cells; n=16 siHAUS6 cells). Each data point represents one measurement; data pooled from at least 3 independent experiments and analyzed using an unpaired t-test (C, D); mean ± S.D.; ns: not significant, *p≤0.05, **p≤0.01, ***p<0.001, ****p≤0.0001. Scale bar: 5 μm.

2.1.2.5. Microtubule growth within k-fibers show a wide angular dispersion and requires Augmin

Comparative fixed-cell super-resolution imaging revealed striking differences in k-fiber structure between control, HAUS6- and Ndc80-depleted cells, whereas depletion of TPX2, HURP, chTOG and CLASP1/2 did not compromise the formation of robust k-fibers, despite an obvious reduction in k-fiber length after chTOG or CLASP1/2 depletion (Figure 2.1.13. A, Figure 2.1.14. C). To directly investigate how Augmin mediates kinetochore-microtubule turnover, we tracked microtubule growth events within a single k-fiber using live-cell CH-STED nanoscopy of EB3 comets in the kinetochore vicinity, now for 1 minute at 750 ms and ~100 nm resolution (Figure 2.1.13. B, Figure 2.1.14. A-B). These imaging conditions did not result in any obvious phototoxicity or relevant photobleaching throughout the recordings (Figure 2.1.14. D). Temporal projections of EB3 comets over consecutive frames in control cells revealed several microtubule growth events within a single k-fiber (Figure 2.1.13. B). Cross-correlation analysis of EB3 comets (see Materials and Methods) in control cells revealed a microtubule growth velocity of ~9 μm/min, with an absolute angular dispersion of 37° ± 13° (mean ± S.D.) relative to the respective k-fiber axis perpendicular to the kinetochore plate (Figure 2.1.13. B-C, Figure 2.1.14. E). Remarkably, detailed inspection of collapsed kymographs within individual k-fibers allowed the direct visualization and discrimination of microtubule growth events that terminate or pass by the kinetochore (Figure 2.1.13. D). We found that HAUS6 or Ndc80 depletion caused a 30-40% reduction in the frequency of microtubule growth events that terminate at the kinetochore (Figure 2.1.13. D-E), with a corresponding reduction in inter-kinetochore distances (Figure 2.1.13. D-F), suggestive of compromised k-fiber formation. However, while HAUS6 depletion did not significantly affect the frequency of microtubule growth events that pass by the kinetochore, this was largely increased after Ndc80 depletion, consistent with a role of Ndc80 in the stabilization of end-on kinetochore-microtubule attachments. Of note, none of these experimental conditions

reduced kinetochore and non-kMT plus-end growth velocity, as determined by measuring the respective slopes from EB3 tracks on the kymographs (Figure 2.1.14. F), in line with our previous cross-correlation analysis (Figure 2.1.14. E). Overall, these data indicate that Augmin and Ndc80 mediate k-fiber formation by distinct mechanisms and directly demonstrates a role for Augmin in microtubule growth events within k-fibers.

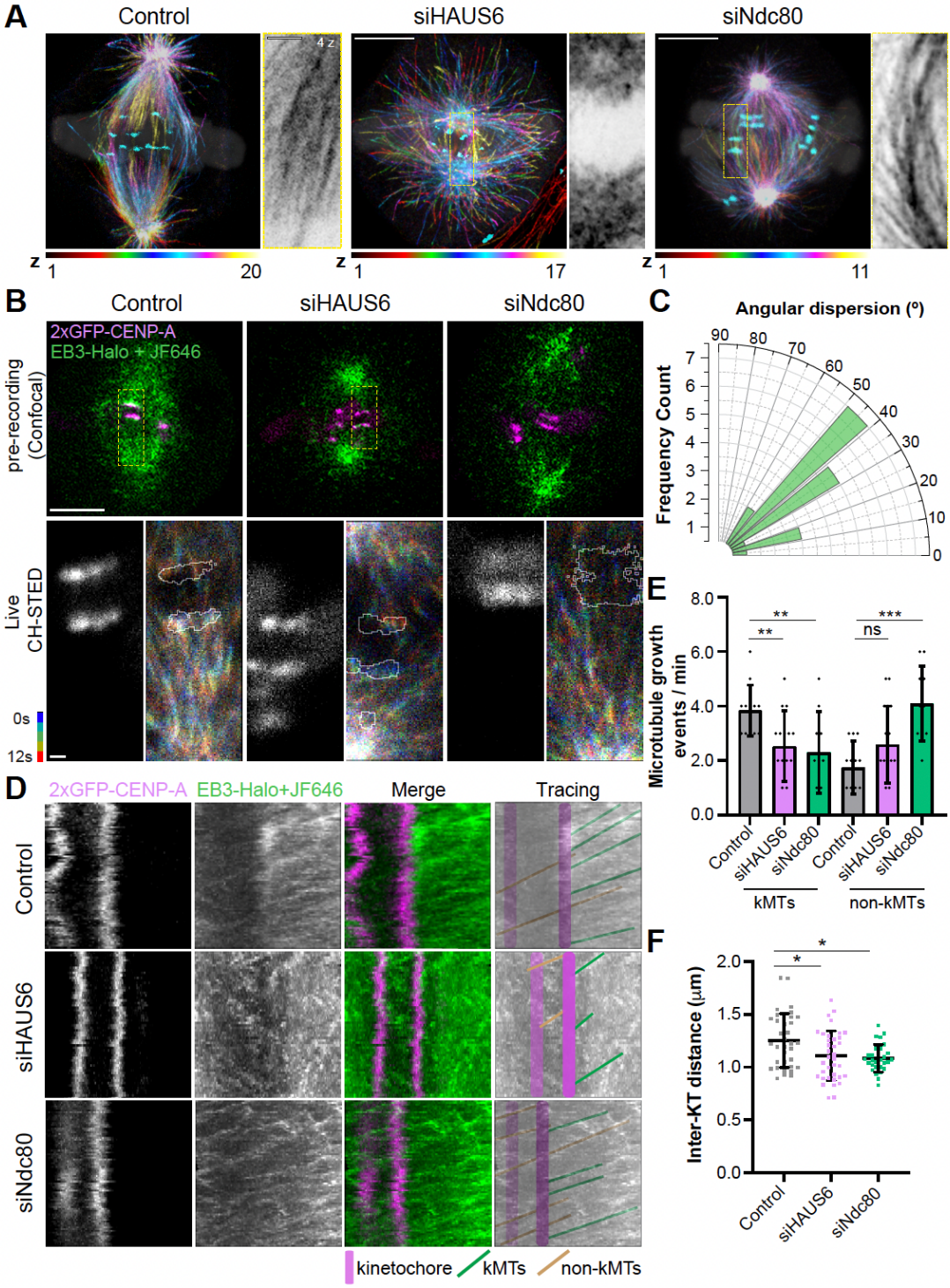

(figure legend on the next page)

Figure 2.1.13. Microtubule growth within individual k-fibers show a wide angular dispersion and requires Augmin.

A, CH-STED images of control, HAUS6- and Ndc80-depleted cells stained with α-tubulin, ACA (cyan) and DAPI (white; opacity 15%). Temporal color code tool on Fiji was used to match each α-tubulin z-plane to a different color. Scale bar: 5 μm. Insets show the maximum-intensity projection of relevant z-planes highlighting the presence/ absence of k-fibers (α-tubulin, inverted grayscale). Scale bar: 1 μm. **B**, Indian muntjac fibroblasts stably expressing GFP-CENP-A (magenta) and EB3-Halo tag conjugated with JF646 (green) were used to track microtubule polymerization events within one k-fiber by live CH-STED microscopy (time-lapse: 750 ms; pixel size: 40 nm). Images on the top show a pre-recording snapshot (confocal) of control, HAUS6- and Ndc80-depleted cells. Images below show chromo-projections of the time-lapse movie of fluorescently labeled EB3 over time and CENP-A contours. A limited time-window of 12 seconds (5 frames) was selected, allowing a fine time-discrimination of microtubule growing events within a k-fiber. Scale bar: 500 nm. **C**, frequency count of EB3 comets' angular dispersion relative to the k-fiber axis in control cells (n=17 cells). **D,** corresponding collapsed kymographs of control, HAUS6- and Ndc80-depleted cells from B. Graphical sketches on the right highlight detected EB3 comets' trajectories; KT- kinetochore (magenta); kMTs - green; non-kMTS - light brown. **E,** number of EB3 growing events per KT (Control: n=46 kMT comets/n=21 non-kMT comets/n=12 cells; siHAUS6: n=38 kMT comets/n=41 non-kMT comets/n=15 cells; siNdc80 n=23 kMT comets/n=41 non-kMT comets/n=10 cells). **F**, distance between KT pairs upon stable expression of 2xGFP-CENP-A (Control n=34 cells; siHAUS6 n=36 cells; siNdc80 n=28 cells). Data pooled from at least 3 independent experiments and analyzed using an unpaired t-test (E, F); mean ± S.D.; ns: not significant, *p≤0.05, **p≤0.01, ***p<0.001. Vertical bar: 10 sec; horizontal bar: 1 μm.

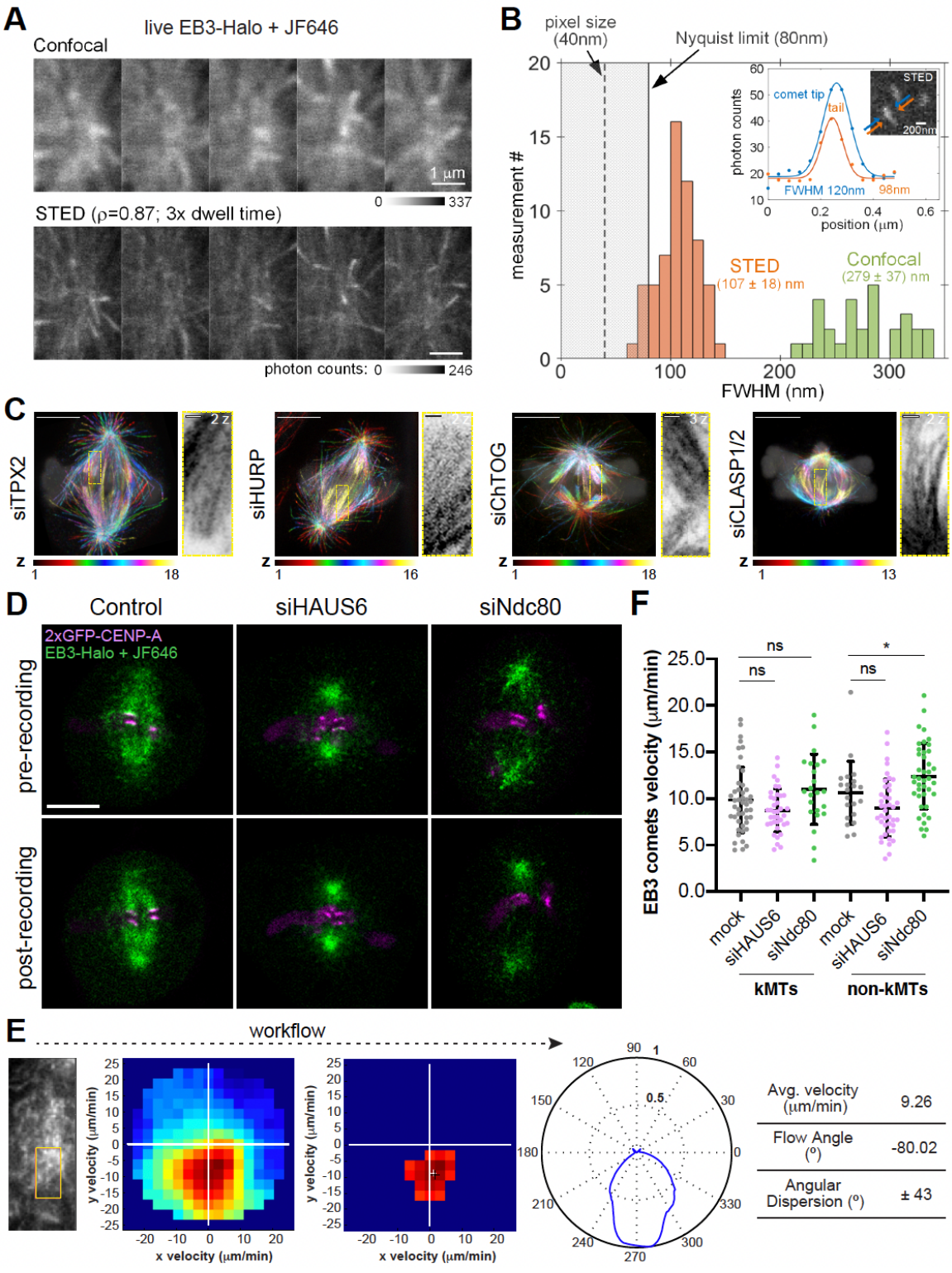

(figure legend on the next page)

Figure 2.1.14. K-fibers in TPX2-, HURP-, chTOG and CLASP1/2-depleted cells were largely indistinguishable from controls.

A, confocal and corresponding STED image frames. Imaging as in Figure 2.1.13., but with a larger ROI and a time-lapse of 2 sec, instead of 750 ms. **B,** resolution measurements based on gaussian fitting of intensity profiles. For reference, the 40 nm (pixel size) and 80 nm (Nyquist limit) vertical lines are shown. **C**, representative super-resolution images of TPX2-, HURP-, chTOG- and CLASP1/2-depleted cells stained with α-tubulin and DAPI (white; opacity 15%). Temporal color code tool on Fiji was used to correspond each α-tubulin z-plane to a different color. Scale bar: 5 μm. Insets show the max-projection (selected z-planes) of a k-fiber (α-tubulin, inverted grayscale). Scale bar: 1 μm. **D,** live CH-STED imaging conditions did not result in any obvious phototoxicity or relevant photobleaching throughout the recordings confirmed by the comparison of pre- and post-recording images of control, siHAUS6 and siNdc80 treated cells. EB3-Halo tag/JF646 (green), 2xGFP-CENP-A (magenta). Scale bar: 5 μm. **E**, cross-correlation analysis of EB3 comets in control cells. Analyzed region of the k-fiber is shown on the right (yellow box). Raw (left) and 2-σ filtered (right) next-neighbor cross-correlation function averaged over time-frame pairs for the ROI shown of the left. Flow angle and average velocity were determined based on the center of mass of the filtered correlation spot. The polar graph (right) shows the semi-infinite domain Radon transform used to estimate the trajectories' angular dispersion (50% level). **F**, EB3 comets velocity was determined from the kymographs shown in Figure 6C. All data were collected from at least 3 independent experiments and analyzed using a Mann-Whitney test; mean ± S.D.; ns: not significant, *$p \leq 0.05$.

2.1.2.6. Augmin is required for microtubule amplification from pre-existing kinetochore microtubules

To directly test whether Augmin is required for microtubule amplification from pre-existing kinetochores, we developed a laser microsurgery-based k-fiber maturation assay (Figure 2.1.15. A). In this assay, we used live Indian muntjac fibroblasts stably expressing GFP-α-tubulin and CENP-A fused with the bright, red-shifted, monomeric fluorescent protein mScarlet, to visualize and discriminate mature k-fibers from other spindle microtubules by spinning-disk confocal microscopy. Then, we used a pulsed laser microbeam to acutely induce partial k-fiber damage and measured the respective kinetics of fluorescence recovery after surgery (FRAS) as a proxy for k-fiber recovery, in controls and after partial HAUS6 depletion by RNAi. While we cannot exclude that a small fraction of non-kMTs is also affected due to the diffraction-limited nature of laser microsurgery, partial k-fiber damage was confirmed by the lack of the typical snap observed immediately after complete k-fiber severing, which results in two independent kinetochore- and pole-proximal microtubule stubs (Figure 2.1.15. B), as well as by correlative live-cell spinning-disk confocal microscopy and super-resolution CH-STED nanoscopy after fixation of the same cell (Figure 2.1.15. C). A 300 nm spacer between the kinetochore-proximal stub and the ablated region was defined to exclude the contribution of microtubule poleward flux for k-fiber recovery (see Materials and Methods). Strikingly, we found that partially-ablated k-fibers in control cells took on average 9 seconds to recover 50% of the fluorescence intensity in the damaged region, corresponding to half the time required in HAUS6-depleted cells (Figure 2.1.15. D). Moreover, while all control cells recovered completely from partial k-fiber ablation within the first 30

seconds after surgery (note that the recovery beyond the initial value is likely due to experimental fluctuations and reflect the possibility that some cells were not yet at steady state when surgery was performed), HAUS6-depleted cells only recovered ~80% in the same period of time (Figure 2.1.15. G). Overall, these data directly demonstrate that Augmin is required for microtubule amplification from pre-existing kinetochore-microtubules, consistent with a critical role in k-fiber maturation.

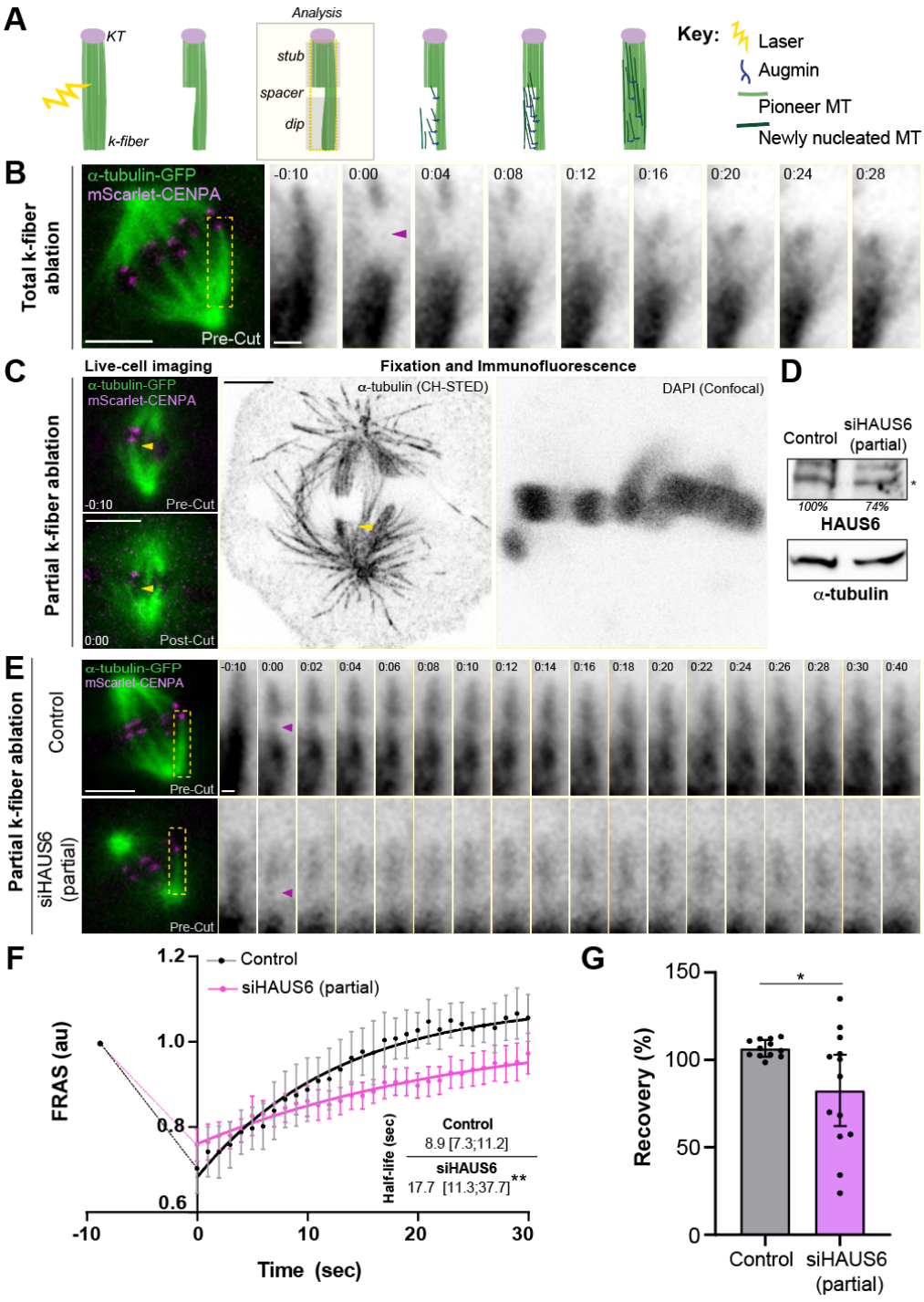

(figure legend on the next page)

Figure 2.1.15. Augmin is required for microtubule amplification from pre-existing kinetochore microtubules.

A, schematic summary of the laser microsurgery-based k-fiber injury/repair assay in control cells (see Materials and Methods for details). **B**, spinning-disk confocal images of total k-fiber severing in control Indian muntjac fibroblasts stably expressing GFP-α-tubulin (green) and mScarlet-CENP-A (magenta). Insets show the analyzed k-fibers (GFP-α-tubulin, inverted grayscale). Scale bar: 5 µm (left); 1 µm (right). C, partial k-fiber damage was confirmed by correlative live-cell spinning disk confocal microscopy (left) and CH-STED nanoscopy (right) upon fixation and immunostaining of the damaged cell (α-tubulin and DAPI shown in inverted grayscale). 0 sec corresponds to the first frame after k-fiber ablation. Scale bar: 5 µm. **D**, immunoblot analysis of cell lysates treated with control or partial HAUS6 RNAi (asterisk indicates the band of interest; ~26% depletion) and α-tubulin was used as loading control (bottom). **E,** control and partial HAUS6-depleted Indian muntjac fibroblasts illustrating microtubule recovery after partial k-fiber laser ablation. Yellow dashed-rectangle indicates the injured k-fiber. Scale bar: 5 µm. Insets show the analyzed k-fibers (GFP-α-tubulin, inverted grayscale). -10 sec represents the maximum time before partial k-fiber ablation. Purple arrowhead points to the ablated k-fiber portion at time zero (first frame after laser ablation). Scale bar: 1 µm, time: min:sec. **F**, kinetics of fluorescence recovery after surgery (FRAS) was determined as a proxy for k-fiber recovery, in controls and after partial HAUS6-depletion by RNAi. Whole lines show a single exponential fitting curve. Each data point represents the mean ± 95% confidence interval. **G**, fluorescence recovery from partial k-fiber ablation within the first 30 seconds after surgery, in control and partial HAUS6-depleted cells (n=12 Control cells; n=13 siHAUS6 cells). Data pooled from at least 3 independent experiments; non-linear fit (F) Mann-Whitney test (G); mean ± S.D.; *p≤0.05, **p≤0.01.

2.1.3. Discussion

The unique cytological features of Indian muntjac cells offer the opportunity to directly address fundamental questions related with kinetochore biology and function that are not possible in any other system, including human cells. This is the case of k-fiber maturation, whose underlying molecular mechanism remained poorly understood. Here we found that Augmin's role in this process is clearly distinct from that of Ndc80 and is consistent with branched microtubule nucleation from pre-existing kMTs. Indeed, Augmin was required to recruit γ-tubulin to the spindle and to sustain, but not to initiate, centrosome-independent microtubule growth from kinetochores. This contrasts with the previous implication of Augmin in the nucleation and/or initial stabilization of chromosome-induced microtubules in *Drosophila* cells (Bucciarelli et al., 2009), but is in agreement with previous works in several mammalian cells, including human, that showed that the vast majority of spindle microtubules do not have a centrosomal origin (Chinen et al., 2020; David et al., 2019; Khodjakov et al., 2000). Importantly, with no prejudice to the role of pioneer centrosomal microtubules that might assist the subsequent microtubule amplification cascade by Augmin (David et al., 2019), our data suggest that Augmin contributes to k-fiber maturation even in the absence of pre-existing centrosomal microtubules. This is consistent with the fact that functional spindles are able to assemble in several animal species, including humans, after perturbation of centrosome function (Basto et al., 2006; Chinen et al., 2020; Debec A., 1982; Khodjakov et al., 2000; Mahoney et al., 2006; Megraw et al., 2001; Moutinho-Pereira et al., 2013; Sir et al., 2013; Watanabe et al., 2020; Wong et al., 2015). In these

cases, short microtubules nucleated in the vicinity of and subsequently oriented and captured by kinetochores (Maiato et al., 2004b; Sikirzhytski et al., 2018) might work as amplification platforms for Augmin-mediated self-organization of k-fibers, while still ensuring the directional bias of microtubule growth towards the kinetochore, independently of centrosomes. When centrosomes are present, Augmin-dependent microtubule amplification of short kMT stubs might promote efficient chromosome bi-orientation through capture of pre-formed k-fibers by astral microtubules (Elting et al., 2014; Khodjakov et al., 2003; Maiato et al., 2004b; Sikirzhytski et al., 2014) or by lateral interactions with an interpolar spindle scaffold that forms soon after nuclear envelope breakdown (Nunes et al., 2020; Renda et al., 2022) and will give rise to bridging fibers (Kajtez et al., 2016) (see scheme below).

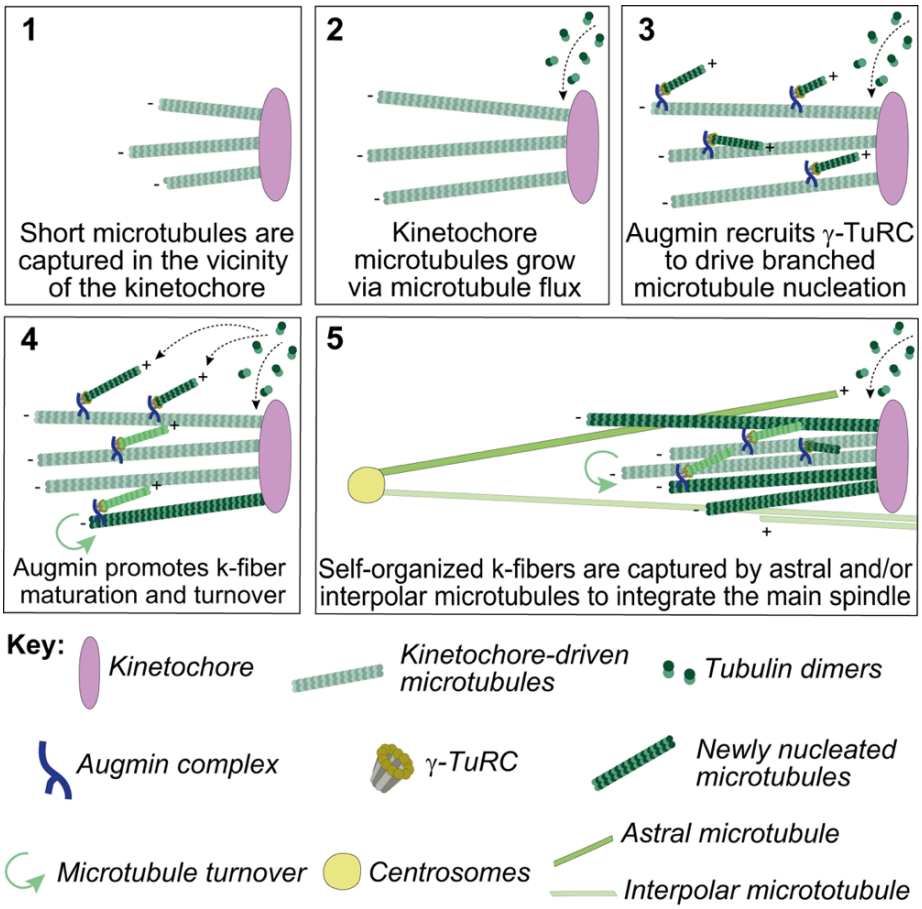

Our findings also reveal that Augmin impacts kMT turnover and poleward flux. While the role of Augmin in promoting microtubule turnover is consistent with *de novo* microtubule nucleation from pre-existing kMTs, how Augmin promotes poleward flux remains less clear. One possibility is that Augmin-mediated microtubule amplification promotes the long-term survival of kMTs that slide poleward, directly, or indirectly facilitating tubulin incorporation at the kinetochores. Alternatively, Augmin might promote flux through its role in the formation/amplification of

interpolar microtubules, which are critical mechanical elements necessary for poleward flux (Barisic et al., 2021b). In support of the second hypothesis, we found that Augmin was also required for interpolar microtubule formation, a property that appears to be conserved in human cells (Manenica et al., 2020). Strikingly, our live-cell super-resolution tracking of EB3-comets in the vicinity of the kinetochore allowed us to follow with unprecedented spatiotemporal resolution microtubule growth events within individual k-fibers and revealed a wide angular dispersion relative to the k-fiber axis. This is somewhat reminiscent of the 'fir-tree' structure observed on k-fibers in *Haemanthus* endosperm spindles (Bajer and Mole-Bajer, 1986) and consistent with Augmin-mediated branched microtubule nucleation from pre-existing microtubules (Alfaro-Aco et al., 2020; Hsia et al., 2014; Kamasaki et al., 2013; Liu et al., 2014; Petry et al., 2013; Tariq et al., 2020; Thawani et al., 2019; Verma and Maresca, 2019). In agreement, Augmin depletion significantly reduced microtubule growth events within individual k-fibers. While the significance of this wide angular dispersion remains unclear, one may speculate that it allows a more efficient microtubule amplification or increases the range of microtubule capture by kinetochores, including neighbour kinetochores, given that Augmin-nucleated microtubules are able to detach from the 'mother' microtubule (Verma and Maresca, 2019). Although this particular structural aspect has been overlooked in previous models of k-fiber formation and maturation in mammals, it implies that additional factors are involved either on bundling or stabilizing newly nucleated kMTs into a cohesive fiber. HURP has been proposed to be such a factor (Silljé et al., 2006; Wong and Fang, 2006), but our phenotypic analysis of k-fibers in HURP-depleted Indian muntjac fibroblasts failed to confirm this hypothesis. In addition, as opposed to critical roles of the chromosomal passenger complex, important players in the Ran-GTP pathway, such as TPX2, previously implicated in branched microtubule nucleation in *Xenopus* egg extracts and *in vitro* reconstitution studies from purified *Xenopus* components (Alfaro-Aco et al., 2020; Petry et al., 2013), as well as in bipolar spindle assembly in human cells (Bird and Hyman 2008), appear to be largely dispensable for robust k-fiber formation and spindle assembly in Indian muntjac fibroblasts, in line with previous findings in *Drosophila* cells (Goshima, 2011; Moutinho-Pereira et al., 2013). While milder effects associated with incomplete knockdown in Indian muntjac cells cannot be excluded, TPX2 has also been shown to be dispensable for microtubule branching in *Drosophila* cells (Verma and Maresca, 2019) and after *in vitro* reconstitution from purified *Drosophila* components (Tariq et al., 2020).

Astral microtubules grew much longer in the absence of Augmin and Ndc80 when compared to controls, which we interpreted as a consequence of an increased soluble pool of tubulin due to compromised k-fiber formation. Although a more direct role of Augmin and Ndc80 in centrosome-dependent microtubule nucleation cannot be excluded, our findings in Indian muntjac cells are consistent with previous observations in *Drosophila* and human cells (Goshima et al.,

2008; Yaguchi et al., 2018), while contrasting with previous reports that suggested that both complexes promote astral microtubule nucleation from purified centrosomes *in vitro* (Wu et al., 2009). It was also surprising that after interference with Augmin function, PRC1 decorated parallel microtubules. This might be explained by a significant reduction of antiparallel interpolar microtubules after Augmin perturbation, which would favour PRC1 association with parallel microtubules that normally have higher off-rates (and equivalent on-rates) compared to antiparallel microtubules (Subramanian et al., 2010).

Lastly, our laser-mediated partial k-fiber injury/repair assay directly demonstrates a role for Augmin in microtubule amplification from pre-existing kMTs. Together with our measurements of kMT turnover and direct observation of microtubule growth events within individual k-fibers, our data provide definitive evidence for a role of Augmin-mediated microtubule amplification in k-fiber maturation, while reconciling this mechanism with growing evidence for centrosome-independent self-organization of kMTs during spindle assembly in animal cells, including human (Conway et al., 2021; Maiato et al., 2004b; Renda et al., 2022; Sikirzhytski et al., 2018).

2.1.4. Materials and Methods

2.1.4.1. Molecular Biology

pLVX-EB3-Halotag, pRRL-2xGFP-CENP-A, pLVX-mScarlet-CENPA and pLVX-PA-GFP-α-tubulin were generated by Gibson assembly. pLVX-GFP-Centrin-1 was a gift from Manuel Thery (Addgene #73331).

2.1.4.2. Cell Culture and Lentiviral Transduction

All Indian muntjac cell lines were grown in Minimum Essential Media (MEM) (Corning), supplemented with 10% FBS (GIBCO, Life Technologies) at 37ºC in humidified conditions with 5% CO_2. Indian muntjac hTERT-immortalized fibroblasts were a gift from Jerry W. Shay (Zou et al., 2002) and Indian muntjac stably expressing H2B-GFP were previously generated in (Drpic et al., 2018). For microtubule plus-ends, centrioles, CENP-A, photoactivatable tubulin and α-tubulin tagging, cells were transduced with pLVx-EB3-Halotag, pLVx-GFP-Centrin-1, pRRL-2xGFP-CENP-A, pLVx-mScarlet-CENPA, pLVx-PA-GFP-α-tubulin and pRRL-EGFP-α-tubulin (Ferreira et al., 2020) lentiviral plasmids, respectively, all under control of a CMV promoter. Lentivirus particles were added to the standard culture media with 1:2000 Polybrene (Sigma) for 12h. Stable lines with uniform level of expression and sufficient fluorescence intensity were selected by FACS. To select pLVx-EB3-Halo tag positive cells, 20 nM of the far-red dye JF646 (Promega®) was added 5-10 minutes before FACS sorting. All Indian muntjac cell lines were authenticated by karyotype analysis.

2.1.4.3. Identification of Indian Muntjac Sequences

The protein sequences of human genes were obtained from NCBI and used as query for tblastn (version 2.2.29 (Morgulis et al., 2008)) using the Indian muntjac genome scaffold sequences and predicted coding sequences (CDC) as targets. Sequence alignments with at least 80% identity, highest coverage of human genes, with matching scaffold and CDS intervals from both tblastn runs were used to identify Indian muntjac orthologs of human gene sequences.

2.1.4.4. Design of siRNAs for RNA Interference (RNAi)

The design of the siRNA sequences was performed using the application BLOCK-ITTM RNAi Designer (Thermo Fisher Scientific). We provided the nucleotide sequence of the genes of interest, selected an ideal CG percentage between 35%–55% and the recommended default motif pattern for the RNAi design. From the 10 designs generated, the one with higher probability of knock-down was selected for each protein of interest.

2.1.4.5. siRNA Experiments

For siRNA experiments, Indian muntjac fibroblasts were plated at 60%–70% confluence in 6-well plates or 22x22 mm no. 1.5 glass coverslips (Corning), previously coated with fibronectin (Sigma-Aldrich) as described in (Almeida et al., 2020) for 24 h in normal medium. Cells were then starved with MEM supplemented with 5% FBS for 30 minutes. siRNA transfection was performed using 5 µL of Lipofectamine RNAi Max (Invitrogen) and 50-100 nM of the respective siRNA, each diluted in 250 µL of serum free-medium (Opti-MEM, Gibco). Untreated and mock transfection (with lipofectamine only) were indistinguishable and therefore referred to as 'Control'. Cells were analyzed 24, 48, 72 or 96 h after depletion, depending on the protein of interest. Depletion efficiency was monitored by western blotting and phenotypic analysis. 64 RNAi sequences were optimized and are available at Table 4 and http://indianmuntjac.i3s.up.pt. 66 conditions were analysed in this study (including double depletion of CLASP1/2 and VASH1/2). Cyclin-B depletion prevented cells' entrance in mitosis, so it was not included in the phenotypical/clustering analyses of this study.

2.1.4.6. Western Blotting

Indian muntjac fibroblasts were collected by scraping the adherent cells or by trypsinization and centrifuged at 200 x g for 5 minutes. The pellet was washed with PBS and centrifuged again. Cells were then resuspended in lysis buffer (*NP-40:* 20 nM HEPES/KOH,pH 7.9; 1 mM EDTA,pH 8; 1 mM EGTA; 150 mM NaCl; 0.5% NP40-IGEPAL; 10% glycerol; 2 mM DTT, supplemented with 1:50 protease inhibitor and 1:100 phenylmethylsulfonyl fluoride (PMSF); OR *for DNA-binding proteins*: 50mM Tris-HCl, pH 7.4; 0,1% digitonin (in EtOH); 0.5% Triton; 400 nM NaCl, supplemented with 30 µg/mL RNAse, 20 µg/mL DNAse, 10 µM $MgCl_2$, with 1:50

protease inhibitor and 1:100 PMSF). The samples were snap-frozen in liquid nitrogen and kept on ice for 30 minutes. After centrifugation at 20 800 x g for 15 minutes at 4ºC, protein concentration was determined by Bradford protein assay (Thermo Fisher Scientific). Protein lysates were run on 7.5/10/15% SDS-PAGE (25-50 µg/lane) according to their molecular weight and transferred to a nitrocellulose Hybond-C membrane using an iBlot Gel Transfer Device (Bio-Rad) or using a wet-transfer system (if protein molecular weight >120kDa). Membranes were then blocked in 5% milk diluted in PBS 0.05% Tween and the primary antibodies were incubated overnight at 4ºC at the dilutions shown in section 2.1.5. (Table 3). After successive washes, the membrane was incubated with the secondary antibodies for 1 hour at RT - 1:5000 α-mouse-HRF; α-rabbit-HRF; α-sheep-HRP (Jackson ImmunoResearch). Detection was performed with Clarity Western ECL Substrate (Bio-Rad). Acquisition of blots was performed with a Bio-Rad ChemiDoc XRS system using the Image Lab software. 'Analyze>Gels' tool in ImageJ was used to quantify the RNAi-mediated depletion efficiency for all screened proteins, except for partial HAUS6 depletion where the calculations were obtained directly from Image Lab. Immunosignals were normalized to GAPDH, α-tubulin or vinculin expression depending on protein molecular weight. All unprocessed western blot data is available at http://indianmuntjac.i3s.up.pt.

2.1.4.7. Immunofluorescence

Indian muntjac fibroblasts were seeded on fibronectin coverslips 24h before the experiment, as shown in (Almeida et al., 2020). Cells were fixed with ice-cold methanol (Sigma) for 4 minutes at -20ºC; or 4% paraformaldehyde (PFA) (Electron Microscopy Sciences); or, for STED microscopy, 4% PFA supplemented with 0.1%-0.2% glutaraldehyde (Electron Microscopy Sciences) for 10 minutes at room temperature (RT). Autofluorescence was quenched by a 0.1% sodium borohydride solution (Sigma-Aldrich) after aldehyde fixation. Extraction after paraformaldehyde fixation was performed using PBS-0.5%Triton (Sigma-Aldrich) for 10 minutes. Cells were incubated for 1 h at RT with blocking solution: 10% FBS diluted in PBS with 0.05% Tween 20 or diluted in cytoskeleton buffer (274 mM NaCl, 10 mM KCl, 2.2 mM Na2HPO4, 0.8 mM KH2PO4, 4 mM EGTA, 4 mM MgCl2, 10 mM Pipes, 10 mM glucose, pH 6.1) with 0.05% Tween 20. Primary antibodies anti α-tubulin (Sigma Aldrich,B-5-1-2) 1:2000/1:200 (STED); anti-centromere antiserum (ACA, Fitzgerald, #90C-CS1058) 1:2000; anti-tyrosinated tubulin (Bio-Rad, MCA77G) 1:2000/1:150 (STED); anti-Mad2 (cMad2, Santa Cruz Biotechnology, sc-65492) 1:250; anti-HURP (gift from Patrick Meraldi) 1:500; anti-γ-tubulin (Sigma-Aldrich, Clone GTU-88 Mab #T6557) 1:5000; anti-PRC1 (C-1, Santa Cruz Biotechnology, sc-3769839) 1:100 (STED); anti-HAUS6 (gift from R. Uehara) 1:50 (STED); anti-detyrosinated tubulin (Gift from Marin Barisic) 1:100 (STED); anti-acetylated tubulin (acetyl K40, Abcam, ab24610) 1:100 (STED); anti-β-tubulin (Sigma-Aldrich, T5201) 1:200 (STED); anti-β-tubulin (Abcam, ab6046) 1:200 (STED) were diluted in the same solution and incubated

over-night at 4ºC. Subsequently, cells were washed 3x with PBS-0.05% Tween and incubated for 1 hour at RT with the corresponding secondary antibody - Alexa 488, 568 and 647 (Thermo Fisher Scientific); or Abberior STAR 580 and Abberior STAR (Abberior Instruments) for STED microscopy. For STED microscopy, secondary antibodies were used at 1:100-150 concentrations. After adding 1 µg/mL 4',6'-diamino-2-fenil-indol (DAPI, Sigma-Aldrich) in PBS-0.05% Tween for 5 minutes, coverslips were washed in PBS and sealed on glass slides mounted with 20 mM Tris pH8, 0.5 N-propyl gallate, 90% glycerol.

2.1.4.8. Drug Treatments

Mitotic arrest at metaphase was obtained using 3-5 µM MG-132 (Merck). Live-cell and fixed cell analysis using MG-132 was performed in the first 2 hours after drug addition to avoid cohesion fatigue. microtubule depolymerization was triggered using 1 µM of nocodazole (Sigma-Aldrich) for 2 hours before fixation or washout. Microtubule re-growth assay was performed by washing out nocodazole with warm medium 2, 5 and 10 minutes before fixation. To induce centriole loss due to Plk4 inhibition, an 8-days treatment with 125 nM centrinone was performed. An equivalent volume of DMSO was used as control for each drug treatment. For the live-CH-STED experiments 75 nM JF646 (Promega) was conjugated with Halo-tag expressing Indian muntjac fibroblasts. SiR-tubulin and SiR-DNA (Spirochrome) (Lukinavicius et al., 2014) were used to visualize microtubules and chromosomes, respectively, at 50 nM concentration incubated for 1 hour prior to live-cell imaging.

2.1.4.9. Cell Viability Assay

Parental Indian muntjac fibroblasts were seeded into a 96-well plate with MEM supplemented with 10% FBS at 37ºC in humidified conditions with 5% CO_2. In the following day, increasing concentrations of Nocodazole (0.5; 1; 2; 20; 200 µM) were added for 2 hours. Cells were then washed with PBS and incubated with 2% v/v Resazurin (stock concentration: 1 mg/mL, Sigma-Aldrich) in normal cell culture medium for 4 h, protected from light. 80 µL of the supernatants were transferred into a new 96-well plate and Resazurin fluorescence was determined in a microplate spectrofluorometer (Synergy MX, Biotek) with the following settings: Ex= 530 ± 9 nm and Em= 590 ± 9 nm.

2.1.4.10. Time-lapse Spinning-disk Confocal Microscopy

Indian muntjac fibroblasts stably expressing human H2B-GFP were plated on fibronectin coated 22x22 mm no. 1.5 glass coverslips 24h before imaging. 1 hour before live-cell imaging, cells were incubated in Leibovitz's L15 medium (GIBCO, Life Technologies) with SiR-tubulin cell-permeable dye. Coverslips were assembled onto 1-well Chamlide CMS imaging chambers (Microsystem AB; Sweden) immediately before imaging. Live-cell imaging was performed on a

temperature-controlled Nikon TE2000 microscope equipped at the camera port with a Yokogawa CSU-X1 spinning-disc head (Solamere Technology), an FW-1000 filter-wheel (ASI) and an iXon+ DU-897 EM-CCD (Andor). The excitation optics are composed of two sapphire lasers at 488 nm and 647 nm (Coherent), which are shuttered by an acousto-optic tunable filter (Gooche&Housego, model R64040-150) and injected into the Yokogawa head via a polarization-maintaining single-mode optical fiber (OZ optics). Sample position was controlled by a motorized SCAN-IM stage (Marzhauser) and a 541.ZSL piezo (Physik Instruments). The objective was an oil-immersion 60x 1.4 NA Plan-Apo DIC CFI (Nikon, VC series), yielding a 190 nm/pixel sampling. All image acquisition was controlled by NIS Elements AR software. An image stack (9 planes separated by 1.5 μm) was acquired every 2 min, spanning a total depth of 12 μm.

2.1.4.11. Power density

Long-term live cell imaging was performed using 488 nm and 647 nm excitation lasers. Power flux was measured as the time-averaged power at the sample plane normalized to the area spanned by the spinning disc pinholes, which is slightly larger than the field of view at the camera plane. We measured a range between 0.2-0.8 $W.cm^{-2}$ for the 488 channel and 0.5-2.5 $W.cm^{-2}$ for the 647 channel. Instantaneous power flux reaches values above ten-fold larger than this estimate.

2.1.4.12. Microtubule Turnover Measurements by Photoactivation

Microtubule turnover was measured in Indian muntjac fibroblasts stably expressing PA-GFP-α-tubulin/GFP-Centrin-1, seeded on fibronectin coated 22x22 mm no. 1.5 glass coverslips. Medium was changed to Leibovitz's L15 medium with SiR-DNA cell-permeable dye (Spirochrome) 1 hour before live-cell imaging. Mitotic cells were identified by Differential Interference Contrast (DIC) microscopy and imaging was performed using a Plan-Apo 100× NA 1.40 DIC objective on a Nikon TE2000U inverted microscope equipped with a Yokogawa CSU-X1 spinning-disc confocal head containing two laser lines (488 nm and 647 nm) and a Mosaic (Andor) photoactivation system (405 nm). Photoactivation was performed in cells with all chromosomes aligned at spindle equator, identified by SiR-DNA signal. Microtubules were locally activated on a thin stripe of ~1 μm width spanning one half-spindle in an area mid-way between the spindle pole and the chromosomes. The 405 nm laser was used at 75% power and cells were pulsed once (500 ms exposure). Seven 1-μm fluorescence image planes were captured using a 100x oil-immersion 1.4 numerical aperture objective every 15 seconds for 4.5 minutes. To determine fluorescence dissipation after photoactivation (FDAPA), whole-spindle sum-projected kymographs were generated and quantified using a custom-written MATLAB script. Intensities were normalized to the first time-point after photoactivation (following background subtraction from the respective non-activated half-spindle). Values were corrected for photobleaching by normalizing to the fluorescence loss of whole cell sum projected images. To calculate microtubule

turnover, the normalized intensity values at each time point were fitted to a double exponential curve $A1 \times e^{-k1 \times t} + A2 \times e^{-k2 \times t}$; t – time, A1 – less stable microtubule population (non-kMTs); A2 – more stable microtubule population (kMTs); k1 and k2 – decay rates of population fractions A1 and A2, respectively (only fittings with R^2>0.98 were retained). From these curves, the rate constants, and the percentage of microtubules for the fast – typically interpreted as the fraction corresponding to non-kMTs; and the slow – typically interpreted as the fraction corresponding kMTs – processes were obtained. The half-life time was calculated as ln(2)/k for each microtubule population.

2.1.4.13. Flux Velocity Measurements

To determine microtubule poleward flux velocity, the whole-spindle sum-projected image sequence was first stabilized using the spindle centrosomes (the coordinates of which were previously determined using a simple centroid-based tracking routine) as references. This procedure generates a guided-kymograph, where a virtual spindle equator remains static (i.e., without translation or rotation) throughout time. The distance between the photoactivated stripe and the virtual equator, as determined by the midpoint between centrosomes, yields the poleward flux velocity.

2.1.4.14. K-fiber Maturation Assay – Laser Microsurgery

Indian muntjac fibroblasts stably expressing human EGFP-α-tubulin and mScarlet-CENP-A were plated on fibronectin coated Ø 25 mm no. 1.5 glass coverslips. Before live-cell imaging, cells were incubated in Leibovitz's L15 medium (GIBCO, Life Technologies). Laser microsurgery was performed on an inverted microscope (TE2000U; Nikon) with a doubled-frequency laser (FQ-500-532; Elforlight), focused by a 100x 1.4 NA plan-apochromatic DIC objective lens (Nikon) equipped with an iXonEM+ EM-CCD camera (Andor Technology). One plane was acquired every 1 second for 2 minutes and subsequently every 1 minute up to 5 minutes. Partial disruption of k-fibers was performed by 2-5 consecutive pulses (0.35 μm step between pulses) conjugated with 3 pulses (0.4 μm Z-step) at each point (12 Hz repetition rate). The pulse width was 10 ns and the pulse energy was 1.5–2 μJ. For the quantification, a straight-line with a specific width (consistent with k-fiber width) was outlined in the ablated k-fiber and monitored during the first 30-40 seconds of movie. All data was normalized to the k-fiber pre-cut intensity values at each time point. The intensity line profiles were then analyzed, and two different regions were defined: 1) stub – corresponding to the region between the kinetochore and the point immediately before the sharp intensity drop; 2) dip – corresponding to a 450 nm region following the stub which contains the ablated k-fiber portion. A region of 300 nm was used as a spacer between the stub and the dip to exclude the contribution of microtubule flux (see scheme Figure 2.1.15. A). To accommodate the focal-plane fluctuations, the average dip intensity was normalized to the

average stub intensity at each time point. Fluorescence Recovery After k-fiber Severing (FRAS) was determined by fitting the ratio at each point to a one phase decay (least squares fit): $y = (y0 - plateau) \times e^{-Kt} + plateau$); *y0*= intensity at time zero; *K*= ln(2)/half-life; *t*= time (sec). Healing recovery percentage was calculated using the following equation: R= ((I_{tf} -I_{ti})/(1 - I*ti*)) ×100, where R= healing recovery; *I*= dip/stub intensity ratio; *tf*= for controls, corresponds to the time were the ratio equals 1; for HAUS6, corresponds to time 30 seconds (4 seconds after all control treated cells reached a ratio of 1); *ti*= time zero/post-cut. The analysis was restricted to cells where stub intensity variation<20% and dip intensity drop>15%. Only a minor fraction of the analyzed k-fibers belonged to the big kinetochore as it rarely localizes on the periphery of the spindle (ideal place to perform k-fiber surgery and track the outcome) and easily gets out of focus (due to its large size). For correlative CH-STED nanoscopy after microsurgery coverslips were assembled onto perfusion imaging chambers (Ske, Research Equipment) before imaging. Immediately after microsurgery, cells were perfused with 5 mL of 4% PFA + 0.2% glutaraldehyde in cytoskeleton and stained as described in methods section 2.1.4.7.. The surgery laser was used to mark a reference frame in the coverslip glass after fixation, thus allowing the cell of interest to be located using a 10x objective on the STED microscope.

2.1.4.15. Stimulated Emission Depletion (STED) Microscopy and Quantification

For Coherent-Hybrid STED (CH-STED) imaging, an Abberior 'Expert Line' gated-STED microscope was used, equipped with a Nikon Lambda Plan-Apo 1.4NA 60x objective lens. CH-STED was implemented as described before (Pereira et al., 2019). All acquisition channels (confocal and CH-STED) were performed using a 0.8 Airy unit pinhole. A time-gate threshold of 500 ps was applied to the STED channel to avoid residual confocal-resolution signal contribution. Fixed-cell images were acquired using excitation wavelengths at 561 nm and 640 nm. Excited volumes were doughnut-depleted with a single laser at 775 nm. Pixel size was set to 40 nm. All images show max-intensity projections. For representation purposes, in Figure 2.1.13. A and Figure 2.1.14. C, a temporal color code tool in Fiji (ImageJ) was used to correspond each z-plane to a different color and DAPI channel was added in Adobe Photoshop CS6 as a separate layer with an opacity of ~15%. Astral microtubule length was measured as the curve length between the spindle pole and the microtubule distal tip in maximum-projection images, using the segmented line tool in Fiji. Microtubule length and number after nocodazole washout in centrinone-treated cells was determined by measuring the distance from a kinetochore to the distal microtubule tip and by counting the number of detected microtubules' foci associated at each kinetochore, respectively. Detyrosinated and acetylated α-tubulin fluorescence intensity after MG-132 treatment for 1 hour was determined by drawing an elliptical ROI around the spindle in sum-projected images (Fiji). Background fluorescence was measured outside the ROI and

subtracted from each cell. All values were normalized to the average levels of control cells. To calculate the fluorescence intensity of polymerized tubulin at each kinetochore, an elliptical ROI was drawn around the microtubule foci in sum-projected images (Fiji) after 2 minutes nocodazole washout. All values were normalized to the average levels of tubulin cytoplasmatic pool in each condition. To determine the proportion of kinetochore-attached microtubules fraction in the spindle, two volumes that are assumed to contain well-defined microtubule populations were defined. *Region 1*, the non-kMTs source, was defined as the volume between two surfaces, each one generated by interpolation of the array of kinetochores in either half-spindle (using a 'thin-plate' spline interpolant). The kinetochores were previously defined manually through identification of microtubule-fiber ends in Fiji. To quantify Region 1 signal, instead of using the whole volume between the two surfaces, we chose a sub-plate of 200 nm width. Eventual microtubules crossing this plate that go on to attach to a kinetochore are assumed to be very rare, particularly in late prometaphase and metaphase. We then assumed that the microtubules accounted for in Region 1 generally extend outside it, even if slightly. An equivalent assumption is that the interpolar microtubules density does not change significantly between Region 1 and its immediate (<500 nm) vicinity. Accordingly, we defined a Region 2 volume lying poleward relative to kinetochores, which contains the sum of two microtubule populations (those that couple the half-spindles and those that attach to kinetochores). Specifically, it is defined as 200 nm-wide and 100 nm poleward-shifted replica of the surfaces defined above (for both half-spindle kinetochores), which enclosed Region 1. The final result for the fraction *f* of kinetochore-attached microtubules is $f = 1-S_{Region1}/S_{Region2}$, where S is the background-subtracted integrated photon count in the corresponding region. Background level was estimated as the average photon count in a metaphase plate region that was visually identified as being devoid of microtubule signal. Total tubulin intensity in HAUS6-depleted cells was normalized to the average levels of control cells. To visualize live microtubule growing events within a single k-fiber, we used Indian muntjac fibroblasts stably expressing EB3-Halotag/GFP-CENP-A imaged by live-CH-STED microscopy with a 1.4NA 60x objective warm-up to 37.5 (set-point), every 750 ms or 8 seconds (to evaluate kinetochore dynamics with or without Augmin and Ndc80). Confocal images of CENP-A were acquired using an excitation wavelength of 488 nm and CH-STED images of EB3 using an excitation wavelength of 640 nm, doughnut-depleted with a single laser of 775 nm. To standardize the quantifications, only chromosomes with a large kinetochore were considered for the analysis. To minimize phototoxicity, the sample was imaged with a 40 nm pixel size, a relatively coarse sampling. According to the Nyquist-Shannon sampling theorem, structuring below 80 nm will not be observed even if the depletion laser is creating such finer structure. To estimate resolution, we excluded 'two-image' statistical measures of the frequency cutoff, such as Fourier ring correlation, due to the dynamics of the object. Additionally, the low SNR and very small dimension of the ROI, do not allow reliable extraction of equivalent one-image statistical

measures, such as power spectral density or Fourier ring 'auto-correlation'. We estimated resolution by gaussian fitting of intensity profiles along manually chosen lines (3 pixel thickness) across EB3 comets. The sometimes-observable anisotropy and one-sided tail of the EB3 comet immediately show that the image is determined by object size, in addition to the point-spread function (PSF) dimension. Whenever possible, and to minimize the object's contribution, we chose the most confined feature of the comet to extract the intensity profile, which in this case is the perpendicular to the comet tail (inset in Figure 2.1.14. B). For the confocal resolution estimate, the above criteria are more ill-defined because the comet-like appearance is much less discernible. Also, the number of comets observed in isolation is much lower at confocal resolution, accounting for the lower number of measurements in this condition in Figure 2.1.14. B). Note that the unavoidable contribution of the object size biases estimated resolutions (both STED and confocal) towards larger values. Fitted curves with an R-squared below 0.8 or with a 'peak' spanning less than 2 datapoints (80 nm) were discarded. Number of measurements was 60 (STED) and 30 (confocal), extracted from a total of 48 images (6 cells, 8 time frames) in each condition. Inter-kinetochore distances were measured using a custom program written in MATLAB, which determines the distance between the vertices of parabolic fits performed on the peaks observed in 3.5 μm length line profiles averaged over a 200 nm width outlined across the pair of kinetochores in Fiji. To prepare the data for local kymograph analysis, we used a custom routine written in MATLAB to compensate for kinetochore movements described by the following steps: (1) 2D tracking of kinetochore tips, (2) region-of-interest (ROI) dimensions definition, and (3) thick-kymograph generation with the ROI being automatically translated and rotated every frame according to the 2D coordinates of the two reference objects in step 1. The direct output is a whole-k-fiber kymograph that can be used to generate a set of aligned images that are the basis for all subsequent analysis. A two-color guided kymograph was represented to facilitate the visualization of EB3 comets that reached and stopped at the kinetochore (classified as k-fiber growing events) or EB3 comets that surpass the kinetochore (named as non-kMTs growing events). By inspection of the kymograph, a first estimate is obtained by manual definition of a kymograph stripe (in x-t), the slope of which is the translation velocity vector projected onto the spindle axis. To control for the sub-estimation of velocity incurred by the said projection, manual estimation of microtubule inclination relative to the spindle axis was used to warrant exclusion of trajectory angles higher than 25º, yielding a real velocity less than 10% higher than calculated. A refined result was obtained by running a custom MATLAB routine where an intensity-based centroid is determined at each timepoint in a preset x-neighborhood from the manual estimate. A linear fit is finally made to the collection of centroids, the slope of which yields a velocity relative to the virtual spindle equator. Chromosome poleward and anti-poleward velocity relative to the equator were measured after each EB3-Halotag track obtained from guided-kymographs aligned to the spindle pole. Velocity was determined measuring the slope of the linear movement within

a half spindle. Chromosome oscillations' amplitude was measured by subtracting the distance to the pole in the starting moment of anti-poleward to poleward movement. The related periodicity was calculated by extracting the time from the start of polymerization cycle until the begging of the next polymerization cycle. The distributions shown in the scattered plots represent each track measured in the total number of cells. Finally, EB3 bursts at kinetochore were calculated dividing the number of time frames with EB3-signal at kinetochores by the total time frames in which a kinetochore was detected. In control cells, the number of EB3 bursts at kinetochores was 0.5, corresponding to the polymerization cycle (half) of 2 minutes movies. To determine the angular dispersion of EB3 comets within a k-fiber we used a custom MATLAB script in which we outlined a ROI with approximately the width of a K-fiber, ~500 nm from the kinetochore during the 1-minute movies. Correlation maps were constructed as an average of the individual spatial cross-correlation functions between time-neighbors (750 ms time-lapse) with the original images masked for photon counts below 1 sigma. A 25 μm/min velocity was preset as a maximal shift. The average correlation map was cleaned at a 2 sigma above average level, which was interpreted as the correlation peak used for further quantification. The peak's center of mass yielded an average flow velocity and direction. To estimate an angular spread attributable to the different orientations of the EB3 comets trajectories, we integrated the correlation map values along radial lines (using a semi-infinite domain version of the Radon transform). The result is a comet-like polar diagram, the angular spread of which was determined as the angle separating the 50% level-crossings around the comet maximum. Finally, angular cropping of the correlation map using the 50% level limits yields the adjusted flow velocity.

2.1.4.16. Wide-field Image Acquisition and Quantification

3D wide-field image acquisition (0.23 μm z-step) was performed on an AxioImager Z1 (60× Plan-Apochromatic oil differential interference contrast objective lens, 1.46 NA, Carl Zeiss Microimaging Inc.) equipped with a CCD camera (ORCA-R2, Hamamatsu) operated by Zen software (Carl Zeiss, Inc.). Blind deconvolution of 3D image datasets was performed using AutoquantX software (Media Cybernetics). All images show maximum intensity projections. Spindle length was determined by measuring the distance between the two spindle poles (labeled with gamma-tubulin) using the straight-line tool in Fiji. γ-tubulin intensity and α-tubulin levels after cold-treatment were determined by drawing an elliptical ROI around the spindle in sum-projected images (Fiji). Background fluorescence was measured outside the ROI and subtracted from each cell. All values were normalized to the average levels of control cells. HURP protein intensity levels were determined by drawing two elliptical selections of different sizes (one containing the other) around the mitotic spindle in sum-projection images. The fluorescence intensity was background subtracted according to the equation: $S_{in,corrected} = S_{in} - ((S_{out}-S_{in})/(A_{out}-A_{in}))\times A_{in}$ S : signal; A: area; and normalized to average fluorescence intensity of control cells.

For quantification of cMad2 protein levels at kinetochores in metaphase arrested cells, ROI manager in Fiji was used. cMad2 fluorescence intensity was background subtracted and normalized for the levels obtained for ACA in the same kinetochore. Adobe Photoshop 2021 and Adobe Illustrator CS5 (Adobe Systems) were used for histogram adjustments and panel assembly for publication.

2.1.4.17. Phenotypical characterization – screening analysis

In preparation for the hierarchical clustering analysis, we set the following eight binary features: A) incomplete congression and faster mitosis (if cells failed chromosome congression and mitotic duration was faster than the average NEBD-AO timing minus two standard deviations of the mean: <23 min); B) incomplete chromosome and normal mitotic duration (if cells failed chromosome congression and mitotic duration was faster than the average NEBD-AO timing plus two standard deviations of the mean: <52 min); C) incomplete congression and prolonged mitosis (if cells didn't congress the chromosomes and mitotic duration was slower than the average NEBD-AO timing plus two standard deviations of the mean: ≥52 min); D) congression delay (if cells congressed all the chromosome to spindle equator and NEBD-Metaphase time was superior to its average minus two standard deviations of the mean: ≥41 min); E) metaphase delay (if cells congressed all the chromosome to spindle equator and NEBD-Metaphase time was superior to its average minus two standard deviations of the mean: ≥28 min); F) anaphase lagging chromosomes; G) mitotic death and H) cytokinesis failure.

2.1.4.18. Hierarchical clustering analysis

The effect of specific genes on mitosis dynamics was characterized using hierarchical clustering analysis. A set of 8 binary features was used to describe the alterations produced by silencing specific genes through siRNA. For each silenced gene, a phenotypical fingerprint was calculated as the mean value of the features vectors for all tested cells. In other words, the calculated fingerprint vector for each gene corresponds to the probabilities of occurrence of the 8 features. The phenotypes fingerprints were compared using a dendrogram representation where the Euclidean distance was used as the distance metric. Ndc80 and Spc24 were used as 'positive controls' for the dendrogram cut-off definition (giving rise to 10 multi-protein clusters). This method provided an unbiased description of how the different fingerprints clustered together. All calculations and graphical representations were carried out using scripts in MATLAB 2018b (The Mathworks Inc, USA).

2.1.4.19. Statistical analysis

Statistical analysis was performed using GraphPad Prism 8. All data represents mean ± S.D., except for Figure 2.1.8. B, Figure 2.1.9. C, Figure 2.1.4, Figure 2.1.6. A', B' and Figure 2.1.10. F where median and interquartile range are shown. D'Agostinho-Pearson omnibus normality test

was used to determine if the data followed a normal distribution. If α=0.05, a statistical significance of differences between the population distributions was determined by Student's t test. If α<0.05, statistical analysis was performed using a Mann-Whitney Rank Sum test. For each graph, ns: not significant, *p≤0.05, **p≤0.01, ***p≤0.001 and ****p≤0.0001. All results presented in this manuscript were obtained from pooling data from at least 3 independent experiments, unless stated otherwise.

2.1.5. Supplemental Material

Table 3. Antibodies used in this screening for immunoblotting.

Protein Name	Source	Catalog Number/Reference	Antibody dilution
Astrin	Gift from D. Compton	(Mack and Compton, 2001)	1:500
Aurora A	Novus Biologicals	NB100-267	1:1000
Aurora B	Rockland (anti-AIM1)	611082	1:1000
Bub1	Gift from S. Taylor	(Taylor et al., 2001)	1:500
BubR1	Abcam	Ab 200062	1:250
Cdc20	Bethyl Laboratories	A301-180A	1:1000
Cdk1	Santa Cruz Biotechnology	anti-cdc2; sc-54	1:500
CENP-C	Gift from W. Earnshaw	(Saitoh et al., 1992)	1.500
CENP-E	Abcam	ab133583	1:250
CENP-F	BD Biosciences	610768	1:250
CENP-I	Gift from P. Meraldi	(McClelland et al., 2007)	1:250
chTOG	Santa Cruz Biotechnology	Anti-Ckap5 (H-4); sc-374394	1:500
Clasp1	N/A	(Pereira et al., 2009)	1:50
Clasp2	N/A	(Pereira et al., 2009)	1:10
Clip-170	Gift from N. Galjart Ab#2360	(Molines et al., 2020)	1:500
Cndg2	Gift from R. Oliveira (Novus Biological)	Citomed #NBP1-88202	1:1000
Cyclin-B1	Cell Signaling	4135	1:250
Dynactin	Gift from R. Gassmann	BD Transduction Lab. 610473	1:1000
Dynein	ThermoFisher Scientific	PA5-49373	1:500
EB1	Abcam	11B11	1:100
EB3	Gift from A. Akhmanova	(Stepanova et al., 2003)	1:3000
GAPDH	Proteintech	60004-1-Ig	1:10000
HAUS6	Gift from R. Uehara	(Uehara et al., 2009b)	1:500
Hec1	Abcam	ab3613	1:500
HURP	Gift from P. Meraldi (R140)	(Silljé et al., 2006)	1:500
INCENP	Santa Cruz Biotechnology	sc-376514	1:250
KIF11	Sigma-Aldrich	HPA010568	1:1000
KIF15	Cytoskeleton Inc.	Cat#AKIN13	1:1000
KIF18A	Gift from AR. Maia	Bethyl Laboratories, A301-079A	1:1000
KIF18B	Gift from J. Welburn	(McHugh et al., 2018)	1:1000
KIF20A	Bethyl Laboratories	A300-879A-M	1:5000
KIF22	Gift from S. Geley	8612	1:500
KIF23	Proteintech	28587-1-AP	1:1000
KIF2A	Gift from D. Compton	(Ganem and Compton, 2004)	1:10000
KIF2C	Gift from D. Compton	(Mack and Compton, 2001)	1:500
KIF4A	Thermo Fisher Scientific	pa5-30492	1:1000
KIFC1	Gift from D. Compton	Santa Cruz Biotechnology sc-100947	1:1000
KNTC1	Gift from Reto Gassman	(Gama et al., 2017)	1:1000
KTNB1	Proteintech	14969	1:1000

Mad1	Millipore	MABE867	1:1000
Mad2	Bethyl Laboratories	A300-300A	1:1000
Mis12	Gift from C. Conde	(Feijão et al., 2013)	1:1000
Mps1	Millipore (clone 3-472-1)	05-682	1:1000
Ndel1	Abnova	H00054820-M01 (anti-NDE1)	1:1000
Ninein	Gift from E. Nigg	(Logarinho et al., 2012)	1:250
NuMa	Gift from D. Compton	(Manning et al., 2007)	1:2000
PICH	Millipore	04-1540	1:250
Plk1	Abcam	ab115763	1:1000
PRC1	Santa Cruz Biotechnology	C-1; sc-376983	1:200
Securin	Thermo Scientific	700791	1:500
Separase	Santa Cruz Biotechnology	sc-390314	1:500
Sgo1	Santa Cruz Biotechnology	sc-393993	1:500
Ska1	Gift from P. Meraldi	clone-680	1:250
Spindly	Gift from A. Desai	(Gassmann et al., 2010)	1:1000
Survivin	Novus Biologicals	NB500-201	1:1000
TPR	Novus Biologicals	NB100-2867	1:1000
Tpx2	Proteintech	11741-1-AP	1:1000
TTL	Proteintech	66076-1-lg	1:1000
VASH1	Proteintech	Cat#12730-1-AP	1:250
Vinculin	ThermoFisher Scientific	700062	1:10000
α-tubulin	Sigma Aldrich	B-5-1-2	1:5000

Table 4. siRNA sequences used in this study.

Protein Name	siRNA sequence (5'-3')
Astrin	GCUAGAGGUCUUCUGUGCA[dT][dT]
Aurora A	GCCAGGGACCUCAUUUCAA[dT][dT]
Aurora B	GGCGAAGGAUCUACUUGAU[dT][dT]
Bub1	CCCAUAUGCAGAGCUACAA[dT][dT]
BubR1	GGAUGCUAUUAUCACAGAU[dT][dT]
Cdc20	GCACGAGUGAUCGACACAU[dT][dT]
Cdk1	GGAAAUAUCUCUAUUAAAA[dT][dT]
CENP-C	GCCACGAGAUACAUACCAA[dT][dT]
CENP-E	GGAGUAAUACCCAGGGCAA[dT][dT]
CENP-F	GCGGACGUCUCUCUGAAUU[dT][dT]
CENP-I	GCUCUCUGCUACUUCACUA[dT][dT]
chTOG	GCAUAUGGCAGACGAGAAA[dT][dT]
Clasp1	GCUGCUGUUGCUGAUGCUU[dT][dT]
Clasp2	GCAUCAGUGUUGGCCACUU[dT][dT]
Clip-170	GCAAAGGAACCUUCAGCUA[dT][dT]
Cnd1	GGUACUGUCCAUCAGACAU[dT][dT]
Cndg2	CCAAAGAGAACAUGGGCAA[dT][dT]
Cyclin-B	CCAAACCUUUGUAGUGAAU[dT][dT]
DHC	GCGAGUACAUCAGGAGAAU[dT][dT]
Dynactin	GCAUCUGGGAACAAAGUUA[dT][dT]
Eb1	GCAGAGGAUCGUGGACAUU[dT][dT]
Eb3	CCCAGAUUCUUGAGCUCAA[dT][dT]
Eg5	GCUGUUGAGGAAGAGCUAA[dT][dT]
HAUS1	GCAGUGACCCUUGAAACAA[dT][dT]
HAUS6	GGUUGGUCCUAAGUUUAUU[dT][dT]
HSET	CCAGCUGCAGGAACUCAAA[dT][dT]
HURP	GCAGCCUCUGUAAUGCCAA[dT][dT]
INCENP	CCAGAAGCUCCUGGAGUUU[dT][dT]
KID	GCCGAGGAAACAUCCUGAU[dT][dT]
KIF15	GCUGAGAUUCUCAGGAUAA[dT][dT]
KIF18A	GGCAAGAAUAUCUGAAGUU[dT][dT]

KIF18B	GGGAGGGAGCCAACAUCAA[dT][dT]
KIF23	CCAUCUAUGAGGAAGAUAA[dT][dT]
KIF2A	GGUGACGUCCGUCCAAUAA[dT][dT]
KIF2C	GCUGGACCUGGAAGUCUAU[dT][dT]
KIF4A	GGAACCGUCAGCAAGACAA[dT][dT]
KTNB1	UCUGGGAUCUGGAGAAAUU[dT][dT]
Mad1	GGAUCUGAACUGGAUGUUU[dT][dT]
Mad2	GCAGAAUGGUUAUACAAGU[dT][dT]
Mis12	GCAGUCCAGAUUCGCAAGU[dT][dT]
Mklp2	CCCACCUGCCAAAGUUCAA[dT][dT]
Mps1	CCAAGCAGUCACCACCAAU[dT][dT]
Ndc80	GCAGACAUUGAGAGAAUAA[dT][dT]
NDEL1	GCCGUCCAAGCUUCACUUU[dT][dT]
Ninein	GCAGUAUGGUUUGCAGAAU[dT][dT]
Nuf2	GCAGAGUUCAAGCAGCUUU[dT][dT]
NuMA	CCAGAUGGAUCGCAGAAUU[dT][dT]
PICH	UGUGCAACUCUGGCCUGCUGCUUUA[dT][dT]
Plk1	CCUCAUCAAGAAGAUGCUU[dT][dT]
Plk4	GGAGGUAUGUGUGGAGCUU[dT][dT]
PRC1	CCUCCUGGAUAUGAUGAUU[dT][dT]
ROD	GCUGGUGAAACAACACCUA[dT][dT]
Securin	UGAAGAUGCCUCCUCCACU[dT][dT]
Separase	GCUCUGCAGCUUCUGGAAU[dT][dT]
Sgo1	GAGAUUAAACGAAAGUCUU[dT][dT]
Ska1	CCCUGAAGAACCGGUUAAA[dT][dT]
Spc24	CCCAGCUCUCUAAGAAGUU[dT][dT]
Spindly	GCUCAAGAGUCGAAUGUUA[dT][dT]
STMN1	CCUAAGAAGAAGGAUCUUU[dT][dT]
Survivin	GCGUCUCCACGUUUAAGAA[dT][dT]
TPR	GCUAGUAUGGAAGAGAAAU[dT][dT]
TPX2	GCCAGAAGCCCAAGUUCAA[dT][dT]
TTL	GCUUUCAGCUCUUCGGCUU[dT][dT]
VASH1	CCACCUGGGAAAGGAUGUGGAAACA[dT][dT]
VASH2	UCUCUUCCUUGACUCAGAUUGUCUU[dT][dT]

CHAPTER 2.2.

‘Chromosome segregation is biased by kinetochore size’

(Published in Current Biology, 2018
https://doi.org/10.1016/j.cub.2018.03.023)

Abstract

Chromosome missegregation during mitosis or meiosis is a hallmark of cancer and the main cause of prenatal death in humans. The gain or loss of specific chromosomes is thought to be random, with cell viability being essentially determined by selection. Several established pathways including centrosome amplification, sister-chromatid cohesion defects, or a compromised spindle assembly checkpoint can lead to chromosome missegregation. However, how specific intrinsic features of the kinetochore - the critical chromosomal interface with spindle microtubules - impact chromosome segregation remains poorly understood. Here we used the unique cytological attributes of female Indian muntjac, the mammal with the lowest known chromosome number (2n = 6), to characterize and track individual chromosomes with distinct kinetochore size throughout mitosis. We show that centromere and kinetochore functional layers scale proportionally with centromere size. Measurement of intra-kinetochore distances, serial-section electron microscopy, and RNAi against key kinetochore proteins confirmed a standard structural and functional organization of the Indian muntjac kinetochores and revealed that microtubule binding capacity scales with kinetochore size. Surprisingly, we found that chromosome segregation in this species is not random. Chromosomes with larger kinetochores bi-oriented more efficiently and showed a 2-fold bias to congress to the equator in a motor-independent manner. Despite robust correction mechanisms during unperturbed mitosis, chromosomes with larger kinetochores were also strongly biased to establish erroneous merotelic attachments and missegregate during anaphase. This bias was impervious to the experimental attenuation of polar ejection forces on chromosome arms by RNAi against the chromokinesin Kif4a. Thus, kinetochore size is an important determinant of chromosome segregation fidelity.

CHAPTER 2.2. Chromosome segregation is biased by kinetochore size

2.2.1. Introduction

Deviation from the normal chromosome number in a given species, also known as aneuploidy, arises through problems in chromosome segregation during mitosis or meiosis. Gain or loss of specific chromosomes can result in stable karyotypes, as in many human trisomies, or represent a permanently unstable condition known as chromosomal instability (CIN), as typically observed in human cancers (Rutledge and Cimini, 2016). The gain/loss of a particular chromosome is believed to be random, with prevalence of particular karyotypes being essentially determined by cell viability and selection. However, we currently do not know whether all chromosomes have the same probability to missegregate.

The kinetochore is a vital component required for chromosome segregation in eukaryotes because it establishes the interface with mitotic spindle microtubules. In mammals, the initial contacts between mitotic spindle microtubules and kinetochores take place during prometaphase, after nuclear envelope breakdown (NEBD). Scattered chromosomes then align at the spindle equator by a process known as chromosome congression (Maiato et al., 2017). When chromosomes are favorably positioned between the spindle poles, they establish end-on kinetochore-microtubule attachments and congress after bi-orientation. More peripheral chromosomes are laterally transported along spindle microtubules toward the equator by the plus-end-directed kinetochore motor CENP-E (kinesin-7) (Barisic et al., 2014; Kapoor et al., 2006). Intriguingly, some metazoans, such as *C. elegans*, congress all their chromosomes in the absence of a CENP-E ortholog, but their kinetochores extend along the entire chromosome length (Maddox et al., 2004). How kinetochore size impacts the mechanisms of chromosome congression and segregation remains unknown.

Kinetochore size varies among different animal and plant species (Comings and Okada, 1971; Maddox et al., 2004; Maiato et al., 2006; Malheiros and De Castro, 1947; McEwen et al., 1998; Neumann et al., 2015; Ribeiro et al., 2009) between different chromosomes within a given species (including humans) (Cherry et al., 1989; Cherry and Johnston, 1987; McEwen et al., 1998; Nixon et al., 2017a; Peretti et al., 1986; Sanchez et al., 1991; Tomkiel et al., 1994), and in response to microtubule attachments throughout mitosis (Hoffman et al., 2001; Magidson et al., 2015). Kinetochore size is primarily determined by the length of α-satellite DNA, the presence of CENP-B boxes, and the extent of incorporation of CENP-A at centromeres (Fachinetti et al., 2015; Irvine et al., 2004; Magidson et al., 2015; Sullivan et al., 2011). Additionally, vertebrate kinetochores have an expandable module formed by proteins involved in spindle assembly checkpoint (SAC) signaling, motor proteins (e.g., CENP-E and cytoplasmic dynein), and microtubule regulating proteins (e.g., CLASPs) located in the fibrous corona (Hoffman et al., 2001; Maiato et al., 2003a;

Tomkiel et al., 1994; Wynne and Funabiki, 2015). How the different centromere and kinetochore functional layers scale with centromere size has not been elucidated.

More recently, computational modeling predicted that adaptive changes in kinetochore size and shape play a critical role in chromosome orientation and error prevention during spindle assembly in human cells (Magidson et al., 2015). However, the physiological relevance of kinetochore size in chromosome segregation has not been experimentally evaluated due to technical limitations, as even the largest human kinetochores are not resolvable by conventional light microscopy in living cells.

To overcome these limitations, here we took advantage of the unique cytological features of the Indian muntjac, a small deer whose females have the lowest known chromosome number (2n = 6) in mammals (Wurster and Benirschke, 1970). Due to centromere-telomere and centromere-centromere tandem fusions during evolution (Chi et al., 2005a), Indian muntjac chromosomes are large and morphologically distinct, with one pair of acrocentric chromosomes (chromosomes 3+X) containing an unusually large compound kinetochore (Brinkley et al., 1984; Comings and Okada, 1971; Wurster and Benirschke, 1970). We show that Indian muntjac cells are amenable for both pharmacological inhibition and genetic manipulation by RNAi. These capacities, combined with high-resolution live-cell and fixed-cell microscopy, allowed us to demonstrate that chromosome congression and segregation in this placental mammal are not random and are strongly biased by kinetochore size. The implications for chromosome segregation fidelity in metazoans are discussed.

2.2.2. Results

2.2.2.1. Indian Muntjac Centromere and Kinetochore Functional Layers Scale Proportionally with Centromere Size

To characterize the Indian muntjac kinetochores we started by measuring their centromere length using chromosome spreads (no microtubules present) from female hTERT-immortalized primary fibroblasts (Zou et al., 2002). In agreement with previous reports (Brinkley et al., 1984; Comings and Okada, 1971), chromosome 3+X contained a distinctively large centromere, measuring 1.87 ± 0.47 μm (mean ± standard deviation (S.D).; n=85 kinetochores, 40 cells) (Figure 2.2.1. A, A'). The centromeres of chromosomes 1 and 2 were significantly smaller, measuring 0.68±0.20 μm (n=90 kinetochores) and 0.45 ± 0.15 μm (n=77 kinetochores), respectively (Figure 2.2.1. A, A'). To determine how different structural and functional centromere/kinetochore proteins scale with linear centromere length we used fluorescence microscopy in chromosome spreads from nocodazole-treated Indian muntjac fibroblasts. Namely, we quantified the total levels of inner and outer kinetochore proteins involved in kinetochore assembly and end-on kinetochore-microtubule attachments (CENP-A and Ndc80/Hec1, respectively), SAC response (Mad2), as well as fibrous

corona motor proteins (CENP-E). Additionally, we have also quantified the levels of active Aurora B on centromeres (Yasui et al., 2004) and of one of its phosphorylated kinetochore substrates (pKNL1; (Welburn et al., 2010)). We found that all these proteins scaled proportionally with centromere size in the absence of microtubules (Figure 2.2.1. B-G and B'-G').

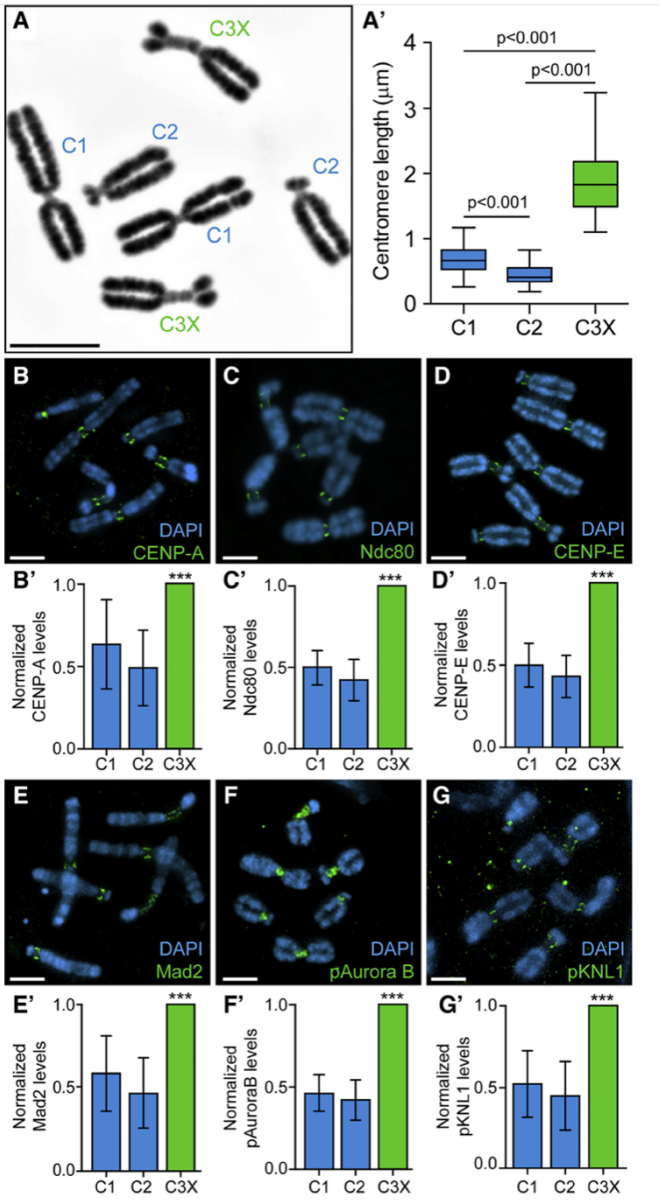

Figure 2.2.1. Centromere and Kinetochore Functional Layers Scale Proportionally with Centromere Size.

A, normal karyotype of female Indian muntjac fibroblasts. **A′**, Centromere length of Indian muntjac chromosomes (box-whisker plots, n = 40 cells, ~80 kinetochores per chromosome type, Mann-Whitney rank-sum test, p<0.001 for all comparisons). B–G, Immunofluorescence of Indian muntjac chromosome spreads (blue) and the centromere and kinetochore proteins (green) CENP-A (**B**), Ndc80 (**C**), CENP-E (**D**), Mad2 (**E**), pAurora B (**F**), and pKNL1 (**G**). Scale bars: 5 µm. B′–G′, Respective quantification of protein levels at Indian muntjac kinetochores, relative to chromosome 3+X (C3X) for CENP-A (**B′**), Ndc80 (**C′**), CENP-E (**D′**), Mad2 (**E′**), pAurora B (**F′**), and pKNL1 (**G′**) (mean ± SD, n ≥ 37 cells per condition, ~100 kinetochores per chromosome type, ***p<0.001 relative to controls, Mann-Whitney rank-sum test).

2.2.2.2. Indian Muntjac Kinetochores Show Standard Structural Organization and Their Microtubule Binding Capacity Scales with Kinetochore Size

To further characterize the structural organization of Indian muntjac kinetochores we compared intra-kinetochore distances (also known as Delta (Wan et al., 2009)) in small and large kinetochores by measuring the corresponding distances between CENP-A and Ndc80/Hec1 on aligned bi-oriented chromosomes (Figure 2.2.2. A). We found that ΔCENP-A-Ndc80 in small and large kinetochores of the Indian muntjac was identical, suggesting similar molecular organization (Figure 2.2.2. A' and A''). Noteworthy, scanning each large kinetochore in three different places resulted in a Delta range that was similar to the one observed in small kinetochores. These findings support the notion that large kinetochores in Indian muntjac result from the tandem organization of a series of repetitive linear sub-units (Zinkowski et al., 1991).

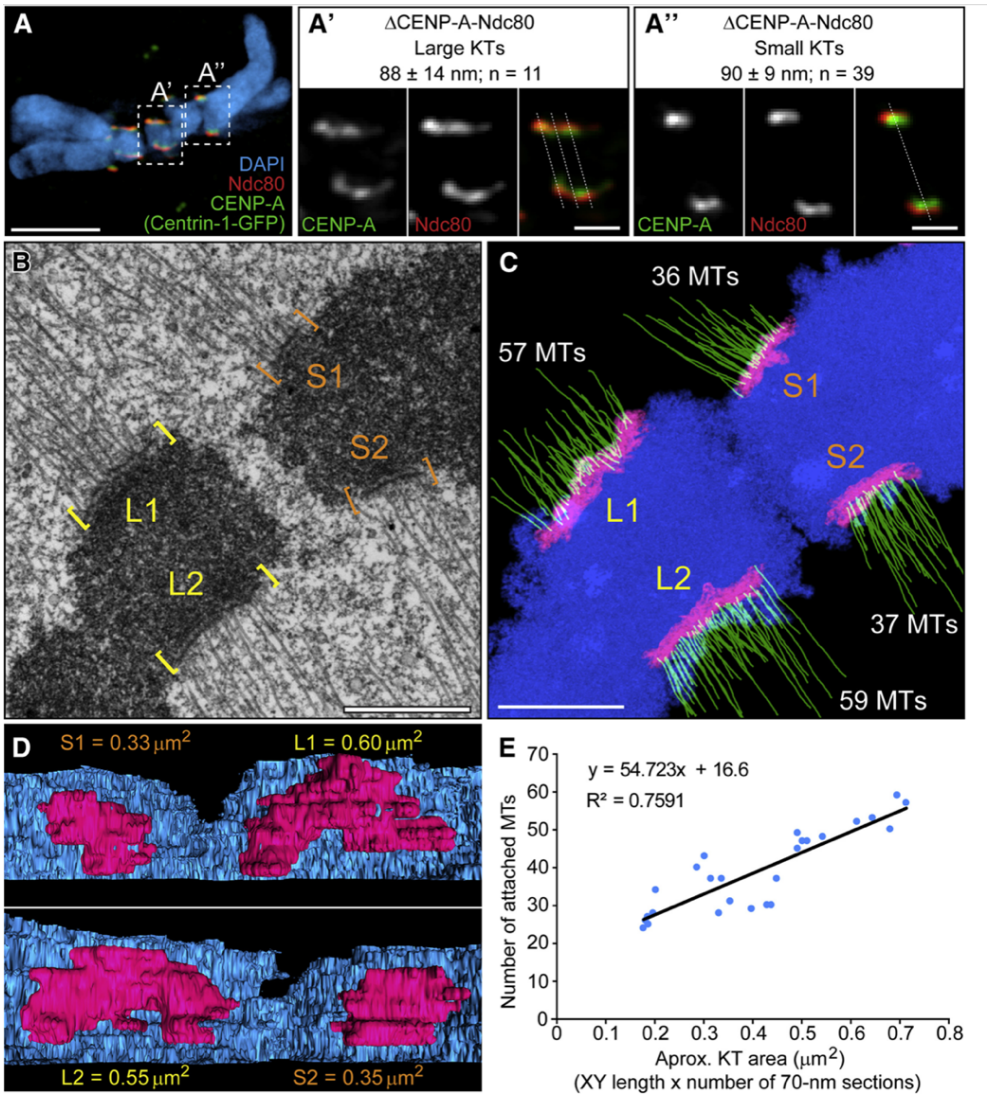

(*figure legend on the next page*)

Figure 2.2.2. Indian Muntjac Kinetochores Show Typical Structural Organization and Their Microtubule Binding Capacity Scales with Kinetochore Size.

A, selected optical planes from an Indian muntjac fibroblast stably expressing Centrin-1-GFP to label the centrioles (green), showing kinetochore pairs for C3X (**A′**) and neighbor chromosome with smaller (**A″**) centromere. The inner and outer parts of the kinetochores were delineated by CENP-A (green) and Ndc80/Hec1 (red). DNA was counterstained with DAPI (blue). A′ and A″, Higher-magnification views of C3X (A′) and smaller kinetochores (A″). Dashed lines denote where intra-kinetochore distances were measured. Scale bars: 5 μm (A) and 1 μm (A′ and A″). Differences between large and small kinetochores were not statistically significant (t test). KT, kinetochore. **B,** single electron microscopy section from consecutive series highlighting the standard organization of the Indian muntjac centromere and kinetochore plates. L1 and L2 correspond to the plates on chromosome C3X; S1 and S2 correspond to the plates on a neighboring chromosome with smaller kinetochores. Scale bar: 2 μm. **C**, Z projection of the entire volume of the corresponding series shown in Figure 2.2.3.. K fibers on the C3X chromosome comprise a larger number of microtubules (green). Kinetochore plates (magenta) and chromosomes (blue) are indicated. Scale bar: 1 μm. microtubule, microtubule. **D**, Surface-rendered model of the volume shown in Figure 2.2.3.. C3X kinetochores are approximately twice as large as in chromosomes with smaller kinetochores. **E**, Quantification of the number of attached microtubules as a function of the approximate kinetochore area. Plot shows serial-section electron microscopy data from 26 kinetochores from 13 chromosomes and 3 cells.

Next, we performed serial-section electron microscopy of metaphase-aligned bi-oriented chromosomes from Indian muntjac fibroblasts and inspected the ultrastructure of the respective kinetochores and centromeric heterochromatin. We found that both small and large kinetochores display expected trilaminar plates adjacent to centromeric heterochromatin, and end-on attached microtubules (Figure 2.2.2. B and Figure 2.2.3.). Manual tracing and projection of all microtubules whose ends terminate at the kinetochores demonstrated that the large kinetochores from chromosome 3+X bind more microtubules than smaller kinetochores in Indian muntjac (Figure 2.2.2. C and Figure 2.2.3). 3-D surface-rendering of entire kinetochore volumes indicated that the size differences among metaphase Indian muntjac chromosomes are maintained upon microtubule attachments (Figure 2.2.2. D). Furthermore, it suggested that the evident differences in kinetochore shape are intrinsically coupled with kinetochore size variability in Indian muntjac, with large attached kinetochores often found slightly bent in response to spindle forces (Figure 2.2.2.D).

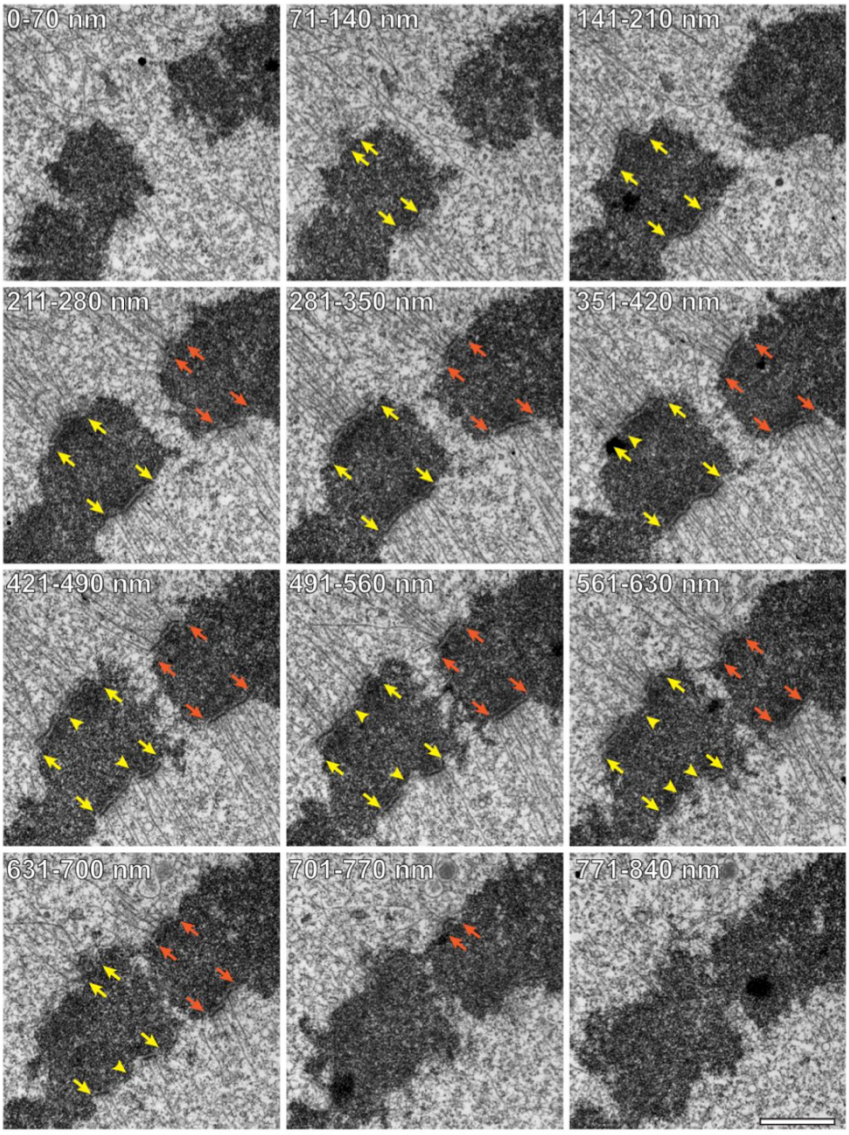

Figure 2.2.3. Serial electron microscope sections spanning two adjacent centromeres in a metaphase Indian muntjac fibroblast.

Plates of C3X kinetochores are marked with yellow arrows. Smaller kinetochores plates on an adjacent non-compound centromere are marked with orange arrows. Notice multiple discontinuities within the plate of C3X kinetochore (arrowheads) likely reflecting their bent state in response to spindle forces and their modular organization. A surface-rendered model of the kinetochore plates and a Z-projection depicting manually-segmented chromatin, kinetochore plates and microtubules are shown in Figure 2.2.2.. Depth occupied by each section within the volume is shown in nanometers. Scale bar: 1 μm.

2.2.2.3. The Molecular Landscape Required to Establish Functional Kinetochore-Microtubule Attachments Is Conserved in Indian Muntjac

To investigate whether Indian muntjac kinetochores are functionally equivalent to other placental mammals, such as humans, we used RNAi to deplete representative centromere and kinetochore components involved in the establishment of end-on kinetochore-microtubule attachments (Ndc80 complex), SAC response (Mad2 and Mps1), the regulation of kinetochore-microtubule

dynamics (CLASP1), and error correction (chromosomal passenger complex). To visualize chromosomes and microtubules in living cells, we stably expressed histone H2B-GFP and used 20–50 nM SiR-tubulin (Lukinavicius et al., 2014), which did not interfere with normal mitotic progression and chromosome segregation (Figures 2.2.4. A-B). Depletion of Ndc80 resulted in massive chromosome missegregation (Figures 2.2.4. A, C). As expected, Mad2 or Mps1 depletion accelerated the onset of anaphase and led to the formation of lagging chromosomes, whereas CLASP1 RNAi resulted in short spindles (Figures 2.2.4. A, C). Finally, depletion of the chromosomal passenger complex protein Survivin caused an overall defect in spindle assembly and incapacity to segregate chromosomes during anaphase, followed by cytokinesis failure and polyploidy (Figures 2.2.4. A, C). Overall, these results suggest that the molecular landscape required to establish functional kinetochore-microtubule attachments is conserved between Indian muntjac and humans.

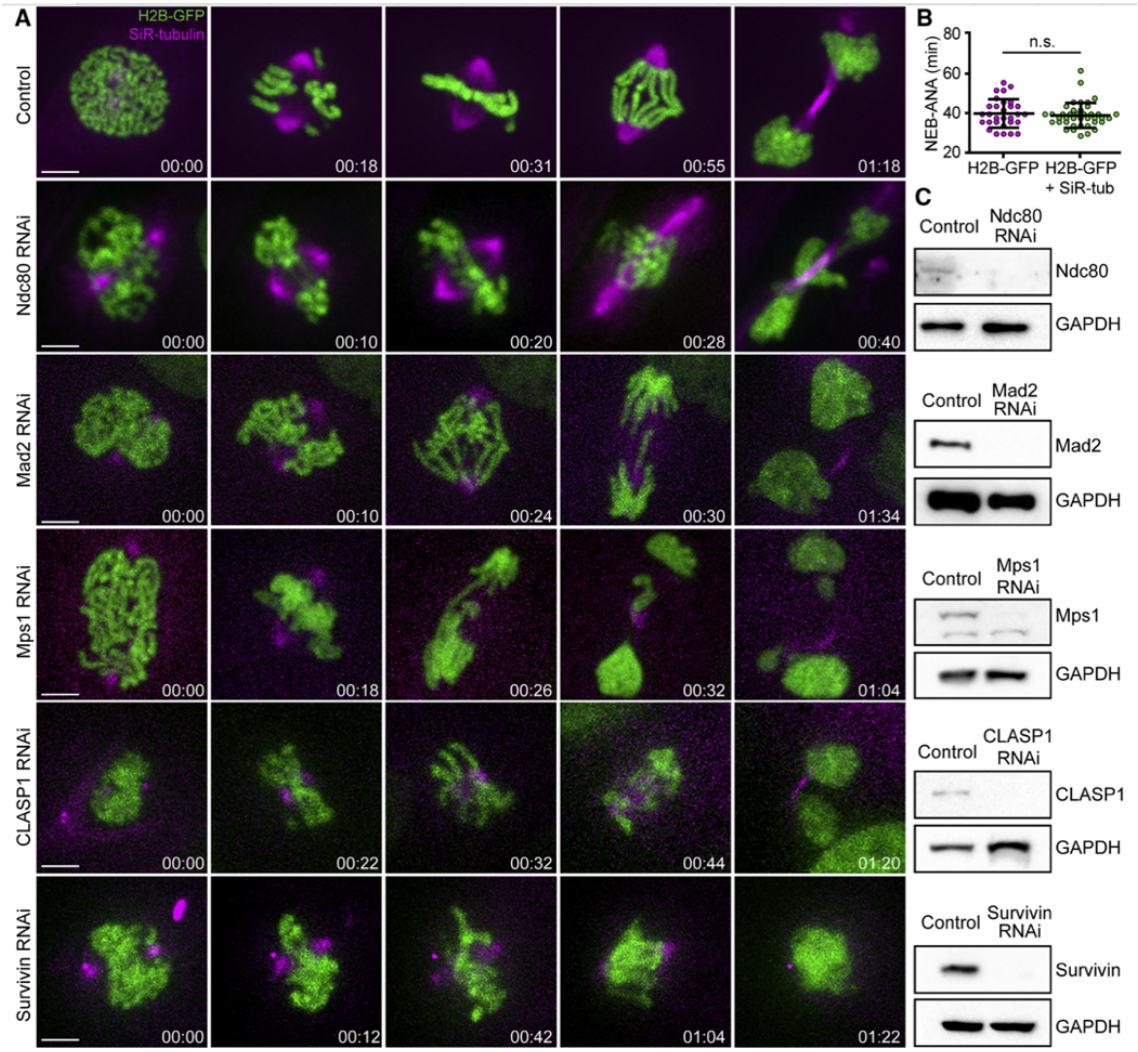

(*figure legend on the next page)*

Figure 2.2.4. The Molecular Landscape Required to Establish Functional Kinetochore-Microtubule Attachments Is Conserved in Indian Muntjac.

A, live-cell imaging of Indian muntjac fibroblasts stably expressing H2B-GFP to visualize the chromosomes (green) and treated with 50 nM SiR-tubulin to label spindle microtubules (magenta). Ndc80, Mad2, Mps1, Clasp1, and Survivin were knocked down by RNAi. Scale bars, 5 μm. Time: h:min. **B**, mitotic timing of Indian muntjac fibroblasts stably expressing H2B-GFP with or without addition of 50 nM SiR-tubulin. There is no statistically significant difference in mitotic timing from NEB to anaphase onset (ANA) in the presence or absence of SiR-tubulin (Mann-Whitney rank-sum test, $p = 0.591$). n.s., not significant. **C**, protein lysates obtained after RNAi were immunoblotted with an antibody specific to each protein of interest. GAPDH was used as loading control.

2.2.2.4. Any Chromosome May Use Either the CENP-E-Dependent or -Independent Pathway to Congress, Regardless of Kinetochore Size

Next, we investigated whether chromosome congression in Indian muntjac fibroblasts also relied on motor-dependent and -independent pathways. To do so, we inhibited the kinetochore motor CENP-E for 1 hour with 20 nM GSK923295 (Wood et al., 2010), which more than doubled the normal frequency of mitotic cells with chromosomes at the poles, consistent with inhibition of CENP-E (Figure 2.2.5. A-B) (Barisic et al., 2014). Importantly, increasing the amount of CENP-E inhibitor by an order of magnitude did not result in further increase of mitotic cells with chromosomes at the poles, suggesting full inhibition of CENP-E motor activity at 20 nM, without displacing endogenous CENP-E from kinetochores (Figure 2.2.5. A-B).

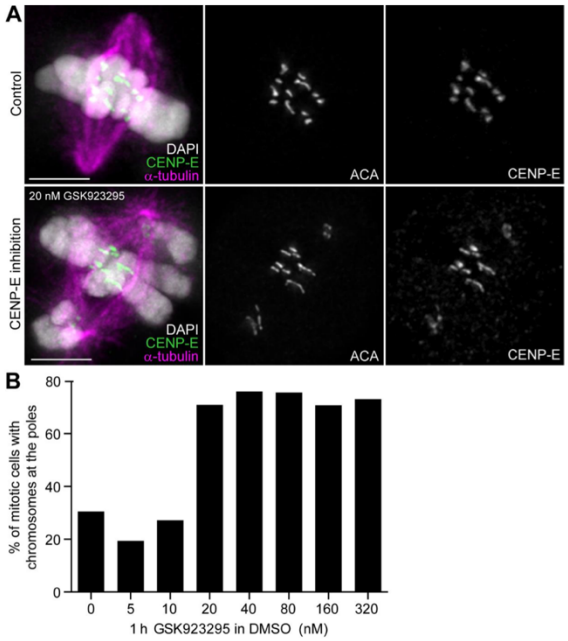

Figure 2.2.5. CENP- E inhibition does not affect its kinetochore localization.

A, immunofluorescence of control Indian muntjac fibroblasts and after CENP-E inhibition, showing chromosomes (DAPI, white in merged image), CENP-E motor protein (green in merged image) and microtubules (α-tubulin, magenta in merged image). Scale bar: 5 μm. **B**, GSK923295 titration. Percentage of mitotic cells with chromosomes at the pole, after 1h incubation with increasing concentrations of CENP-E inhibitor. Control cells (0) were treated with DMSO only.

To directly test the implications of kinetochore size for chromosome congression we treated Indian muntjac fibroblasts stably expressing CENP-A-GFP with 20 nM CENP-E inhibitor for 1 hour and followed cells as they progressed through mitosis (Figure 2.2.6. A-B). We found three different scenarios: 1) very few cells showed all chromosomes at the poles (2/28 cells, 6 independent experiments); 2) some cells aligned all their chromosomes at the metaphase plate soon after NEBD (6/28 cells, 6 independent experiments); and 3) most cells showed at least one chromosome, either with a small or large kinetochore, which remained at the poles (20/28 cells, 6 independent experiments). These data demonstrate that any chromosome may use either the CENP-E-dependent or -independent pathway to congress, regardless of kinetochore size.

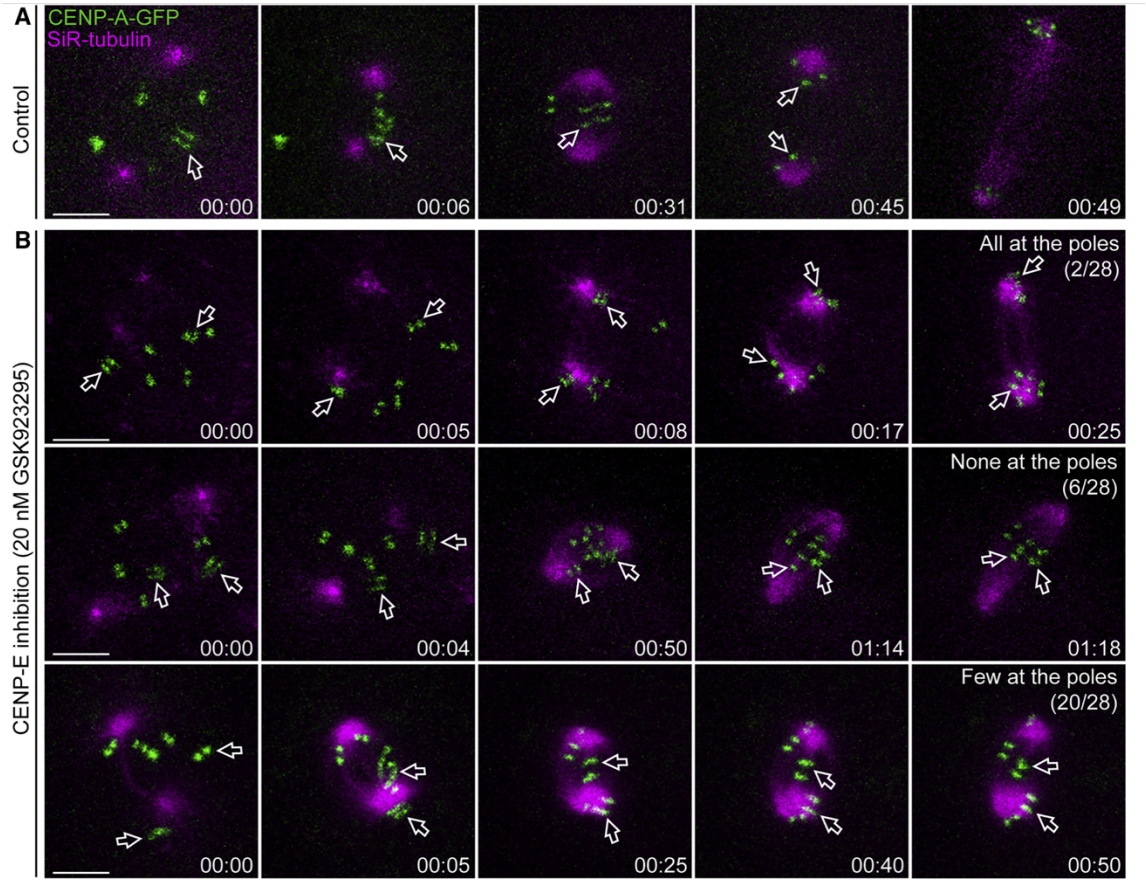

Figure 2.2.6. Any Chromosome May Use Either the CENP-E-Dependent or CENP-E-Independent Pathway to Congress, Regardless of Kinetochore Size.

A, control Indian muntjac fibroblasts stably expressing CENP-A-GFP (green) and treated with 20 nM SiR-tubulin (magenta). Scale bar: 5 µm. Time: h:min. **B,** Indian muntjac fibroblasts stably expressing CENP-A-GFP (green) and treated with 20 nM SiR-tubulin (magenta) after CENP-E inhibition with 20 nM GSK923295. Scale bars, 5 µm. Time: h:min. n = 28 cells, pool of six independent experiments. The arrows indicate the position of large kinetochores from C3X chromosomes.

2.2.2.5. Chromosome Congression and Bi-orientation in Indian Muntjac Are Biased by Kinetochore Size

To determine the number of chromosomes with small or large kinetochores at the pole after CENP-E inhibition we performed immunofluorescence in fixed cells (Figure 2.2.7. A). We found that the number of chromosomes with small and large kinetochores at the pole followed an almost perfect binomial distribution (Figure 2.2.7. B). This indicated that the fate of each individual chromosome was largely independent of the other chromosomes of the same class and that the state of the chromosomes with small kinetochores did not influence the state of the chromosomes with large kinetochores and vice-versa. Most strikingly, the probability of each individual chromosome with small kinetochores to stay at the pole was approximately twice the probability of a chromosome with a large kinetochore: 0.19 ± 0.034 vs. 0.11 ± 0.048, respectively (mean ± S.D.) (Figure 2.2.7. C).

In human cells, >96% of the chromosomes relying on CENP-E for congression are normally excluded from the spindle region and locate closer to one of the spindle poles at NEBD (Barisic et al., 2014). To exclude that the observed bias for Indian muntjac chromosomes with large kinetochores to align independently of CENP-E was due to a tendency to localize in the spindle region and/or equidistantly to the spindle poles at NEBD, we performed four-dimensional (4D, x,y,z,t) tracking of chromosomes with large kinetochores after CENP-E inhibition in living cells ($n = 23$ large kinetochore pairs, 13 cells). We found that 22/23 Indian muntjac chromosomes with large kinetochores were excluded from the spindle ellipsoid region and were nearly randomly positioned along the spindle axis at NEBD (45% of the kinetochores were closer to the poles vs. 55% of the kinetochores that were closer to the spindle equator; Figure 2.2.7. D). Overall, these data indicate that chromosomes with a larger kinetochore rely less on CENP-E motor activity and are biased to congress after bi-orientation, independently of chromosome positioning relative to the spindle region and poles at NEBD.

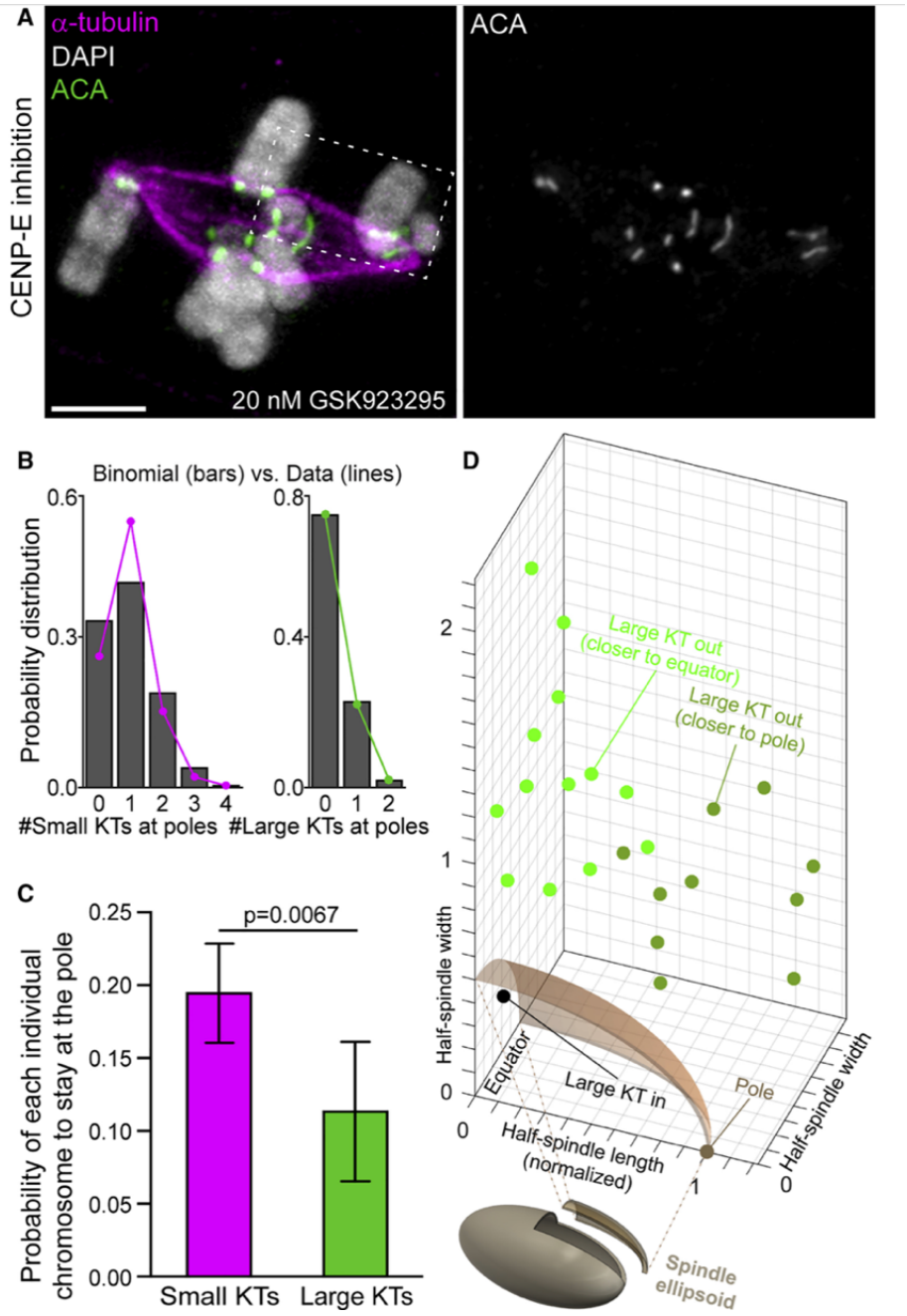

Figure 2.2.7. Chromosome Congression and Bi-orientation in Indian Muntjac Are Biased by Kinetochore Size.

A, immunofluorescence of an Indian muntjac fibroblast after CENP-E inhibition showing chromosomes (DAPI; white in merged image), kinetochores (ACA, white; green in merged image), and microtubules (α-tubulin; magenta in merged image). Scale bar: 5 μm. **B**, quantification of the number of chromosomes with small or large kinetochores at the pole after CENP-E inhibition by immunofluorescence in fixed cells (magenta and green lines) and respective theoretical prediction based on a binomial distribution (gray bars). **C**, probability of each individual chromosome with small or large kinetochores to stay at the pole upon CENP-E inhibition (arbitrary units) (mean ± S.D., n = 621 cells, six independent experiments, p = 0.0067, t test). **D**, 4D (x, y, z, t) tracking of chromosomes with large kinetochores after CENP-E inhibition to determine their position relative to the poles at NEBD and the forming mitotic spindle (see dashed box in A for reference). Note that chromosomes with large kinetochores are randomly distributed relative to the equator and the spindle poles.

2.2.2.6. Chromosomes with Larger Kinetochores Are More Prone to Establish Erroneous Merotelic Attachments that Result in Non-random Missegregation

To directly investigate whether chromosomes with large kinetochores are more prone to establish erroneous attachments with spindle microtubules we set up a monastrol treatment/washout assay in Indian muntjac fibroblasts (Figure 2.2.8. A-B, Figure 2.2.9. A-B). After monastrol washout, cells were released into fresh medium with 1 μM of the Aurora B inhibitor ZM447439 and 2 μM of the proteasome inhibitor MG-132 (to prevent anaphase onset), to partially inhibit error correction without interfering with bipolar spindle assembly, and subsequently fixed (Figure 2.2.8. C, Figure 2.2.9. A-C, Figure 2.2.10.). Calculation of the fraction of each chromosome group (with small or large kinetochores) with merotelic or syntelic (microtubules from the same pole attached to both sister kinetochores) attachments revealed a low frequency of syntelic attachments for chromosomes with either small or large kinetochores (1.9% vs. 1.4%, respectively) (Figure 2.2.8. C). However, the frequency of chromosomes with large kinetochores that established erroneous merotelic attachments was several fold higher when compared with chromosomes with small kinetochores (7.0% vs. 1.6%, respectively) (Figure 2.2.8. C).

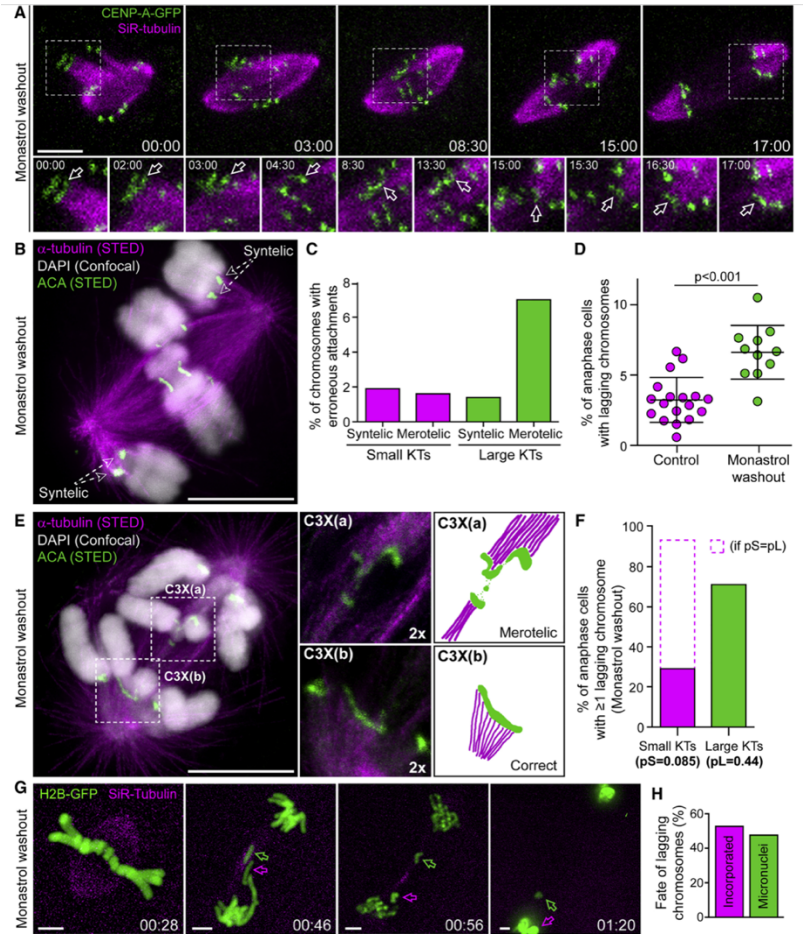

(*figure legend on the next page)*

Figure 2.2.8. Chromosomes with Larger Kinetochores Are More Prone to Establish Erroneous Merotelic Attachments that Result in Non-random Missegregation

A, error correction after monastrol washout in live Indian muntjac fibroblasts stably expressing CENP-A-GFP (green) and treated with 20 nM SiR-tubulin (magenta). Dashed boxes highlight a region with a chromosome with large kinetochores (arrows in lower panels that show 1.5× zoom images, plus additional time frames). Scale bar: 5 μm. Time: min:s. **B**, STED/confocal image of a prometaphase Indian muntjac fibroblast after monastrol washout showing syntelic attachments. Microtubules (α-tubulin, magenta), chromosomes (DAPI, white), and kinetochores (ACA, green) are indicated. Scale bar: 5 μm. **C,** quantification of erroneous attachments on chromosomes with small or large kinetochores (KTs) (n = 207 cells, pool of 3 independent experiments). **D,** frequency of anaphase cells with lagging chromosomes in controls and after monastrol washout (mean ± S.D.; each data point indicates an independent experiment; 2,099 control anaphase cells scored; 3,739 anaphase cells scored after monastrol washout; Mann-Whitney rank-sum test). **E,** STED/confocal image of an Indian muntjac fibroblast in anaphase after monastrol washout. Microtubules (α-tubulin, magenta), chromosomes (DAPI, white), and kinetochores (ACA, green) are indicated. Dashed boxes indicate a lagging chromatid (C3X(a)) containing a large kinetochore with merotelic attachments and the corresponding sister (C3X(b)). Scale bar: 5 μm. The images and graphical sketches on the right highlight the type of attachments in the two sisters (2×zoom). **F,** drequency of anaphase cells with at least 1 lagging chromosome with small or large kinetochores after monastrol washout (n = 32 cells from nine independent experiments). Dashed bar represents theoretical values for the frequency of lagging chromosomes with small kinetochores, if the probability to lag was equal for chromosomes with large or small kinetochores. **G,** Live-cell imaging of an Indian muntjac fibroblast stably expressing H2B-GFP (green) and treated with 50 nM SiR-tubulin (magenta) illustrating missegregation of lagging chromosomes after monastrol washout. Scale bars, 5 μm. Time: h:min. The green and magenta arrows indicate two lagging chromosomes that failed to integrate and reintegrated the main nucleus, respectively. **H,** percentage of cells (from live-cell imaging) with lagging chromosomes incorporating or forming micronuclei after monastrol washout (n = 59 cells, pool of five independent experiments).

To further evaluate the significance of the previous observations and increase our sample size, we promoted the formation of erroneous kinetochore-microtubule attachments by monastrol treatment/washout. As expected, this treatment doubled the frequency of anaphase cells with lagging chromosomes relative to unperturbed controls (6.62 ± 1.91 %, mean ± S.D.) (Figure 2.2.8. D). Stimulated Emission Depletion (STED) super-resolution microscopy indicated that the large kinetochores on anaphase lagging chromosomes were often found stretched and deformed due to the formation of merotelic attachments (Figure 2.2.8. E). Most strikingly, we found that 73% of the anaphase cells after monastrol treatment and washout showed at least one lagging chromosome with a large kinetochore, whereas only 30% of the anaphase cells showed at least one lagging chromosome with small kinetochores (Figure 2.2.8. F), corresponding to a much higher probability of chromosomes with large kinetochores to lag in anaphase, when compared with chromosomes with small kinetochores (pL=0.44; pS=0.085) (see Materials and Methods). In fact, if chromosomes with small or large kinetochores had equal probabilities to lag behind in anaphase, one would predict a much higher frequency of chromosomes with small kinetochores to lag in anaphase, than the one observed experimentally (94% vs. 30%, respectively; Figure

2.2.8. F; see Materials and Methods). Importantly, because chromosome 3+X in female Indian muntjac is smaller than chromosome 1 (which has a smaller kinetochore), but larger than chromosome 2 (also with a smaller kinetochore), these work as internal controls to exclude that the measured bias for chromosome 3+X to lag behind in Indian muntjac was related with chromosome size (Spence et al., 2006). Finally, we tracked the fate of lagging chromosomes after monastrol washout in living fibroblasts and found that ~50% resulted in the formation of micronuclei, a bona fide indicator of chromosome missegregation that has been implicated in chromosome rearrangements in human cancers (Zhang et al., 2015) (Figure 2.2.8. G-H). We concluded that, despite robust error correction mechanisms during a normal mitosis, chromosomes with large kinetochores have a higher tendency to establish persistent merotelic attachments, resulting in a strong bias to lag in anaphase, potentially leading to missegregation.

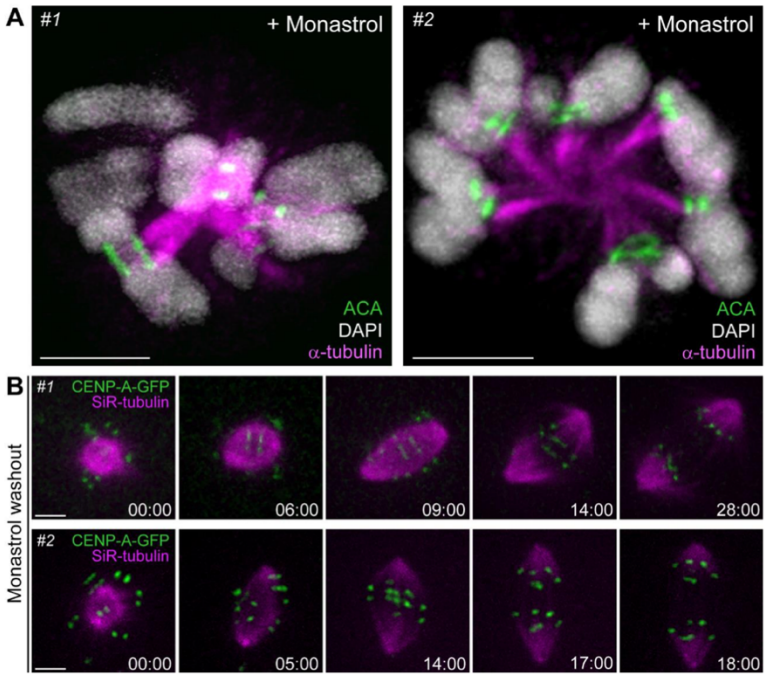

Figure 2.2.9. Monastrol treatment/washout in Indian muntjac fibroblasts.

A, immunofluorescence of two Indian muntjac fibroblasts with monopolar spindles upon monastrol treatment, showing chromosomes (DAPI, white), kinetochores (ACA, green) and microtubules (α-tubulin, magenta). Scale bars, 5 μm. B, Live-cell imaging of two Indian muntjac fibroblasts stably expressing CENP-A-GFP and treated with 20 nM SiR-tubulin (magenta) after monastrol washout. Scale bar: 5 μm. Time: min:sec.

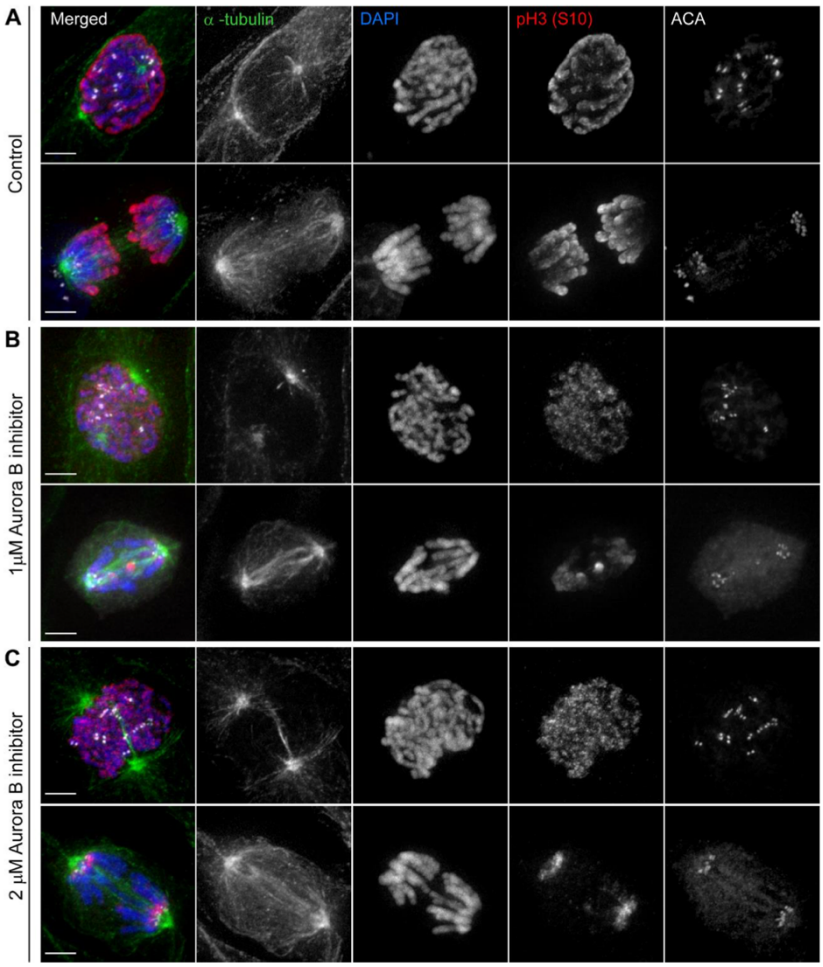

Figure 2.2.10. Titration of the Aurora B inhibitor in Indian muntjac fibroblasts.

A-C, immunofluorescence images of Indian muntjac fibroblasts in control and when treated with 1 or 2 μM of the Aurora-B inhibitor ZM 447439. Cells were incubated for 40 minutes before fixation. Kinetochores are in white, pH3(S10) in red, α-tubulin in green, chromosomes in blue. Scale bar: 5 μm.

2.2.2.7. Preventing error correction also generates a missegregation bias towards chromosomes with large kinetochores

To test whether chromosomes with large kinetochores also missegregate at higher frequency when error correction is prevented, we inhibited SAC activity with the Mps1 inhibitor, Mps1-IN-1 (Kwiatkowski et al., 2010). Similar to its depletion by RNAi (Figure 2.2.4. A, C), Mps1 inhibition with 20 μM Mps1-IN-1 forced cells to prematurely enter anaphase, resulting in a marked increase of cells with lagging chromosomes (10.3%, scored from fixed material) (Figure 2.2.11. A-C). Interestingly, we found that after Mps1 inhibition, 50% of the anaphase cells showed at least one lagging chromosome with a large kinetochore, whereas 56% of the anaphase cells showed at least one lagging chromosome with small kinetochores (Figure 2.2.11. D). This corresponded to a higher probability of chromosomes with large kinetochores to lag in anaphase, when compared with chromosomes with small kinetochores (pL=0.31; pS=0.21) (see Materials

and Methods). In other words, if chromosomes with small or large kinetochores had equal probabilities of lagging behind in anaphase after Mps1 inhibition, one would predict a frequency of 81% of anaphase cells with at least one lagging chromosome with small kinetochores (Figure 2.2.11. D; see Materials and Methods). Thus, preventing error correction also generates a missegregation bias towards chromosomes with large kinetochores.

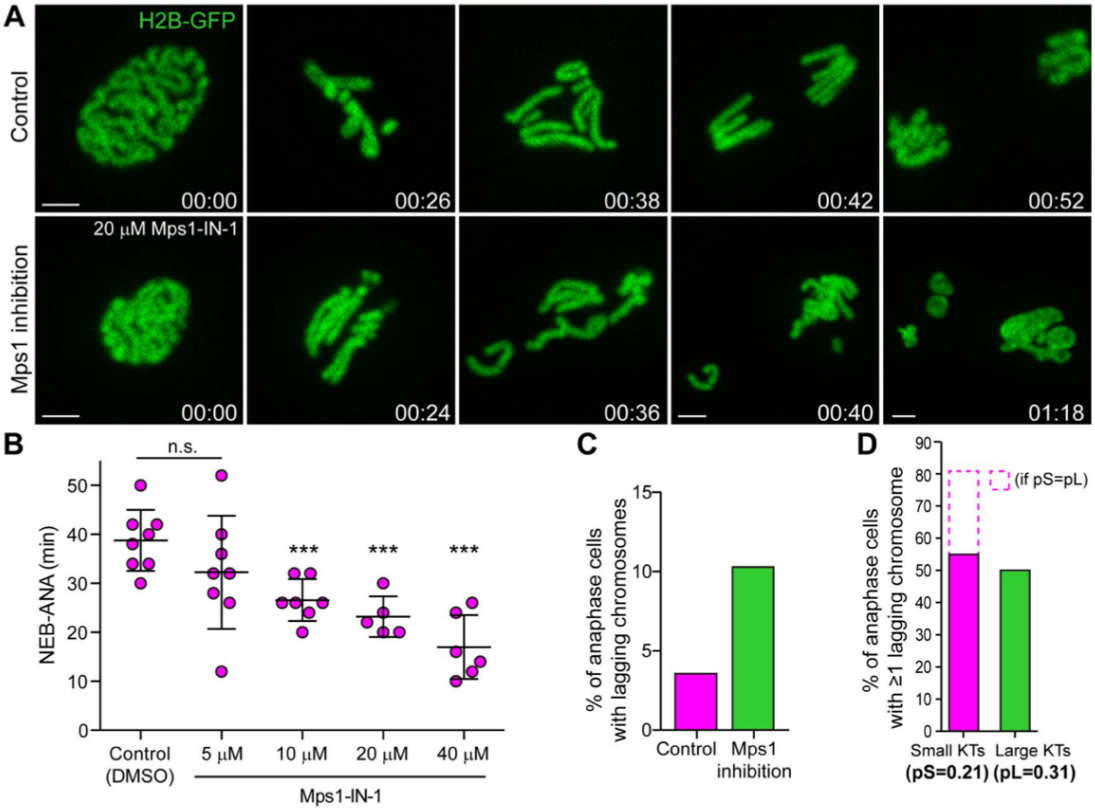

Figure 2.2.9. Preventing error correction also generates a missegregation bias towards chromosomes with large kinetochores.

A, live-cell imaging of Indian muntjac fibroblasts stably expressing H2B-GFP (green) in controls and after treatment with 20 μM Mps1-IN-1. Scale bar: 5 μm. Time: h:min. **B,** quantification of mitotic duration from NEBD to anaphase onset (ANA) in control (DMSO) or Mps1-IN-1-treated Indian muntjac fibroblasts with increasing concentrations. ***p<0.001 relative to controls (t-test, each data point represents one cell). **C,** frequency of anaphase cells with lagging chromosomes in control or Mps1-IN-1-treated (20 μM for 15 minutes prior to fixation) Indian muntjac fibroblasts (n=696 cells, pool of 6 independent experiments). **D,** frequency of anaphase cells with at least 1 lagging chromosome with small or large kinetochores (KTs) after Mps1 inhibition (n=18 cells from 3 independent experiments). Dashed bar represents theoretical values for frequencies of lagging chromosomes with small kinetochores if the probability to lag was equal for chromosomes with small or large kinetochores.

2.2.2.8. Polar Ejection Forces on Chromosome Arms Ensure Mitotic Fidelity but Are Not Implicated in the Observed Missegregation Bias for Chromosomes with Large Kinetochore

Previous reports in *C. elegans* have shown that loss of polar ejection forces after depletion of the Kinesin-4 Klp-19 caused missegregation of holocentric chromosomes (Powers et al., 2004). To test whether polar ejection forces acting on the long chromosome arms of Indian muntjac account for the observed missegregation bias, we have investigated chromosome segregation fidelity in fixed and living cells after RNAi against the chromokinesin Kif4a/kinesin-4 in Indian muntjac fibroblasts (Figure 2.2.12. A-C). We found that experimental attenuation of Kif4a led to a striking increase in the frequency of lagging chromosomes in anaphase (Figure 2.2.12. D-E), consistent with an important role of polar ejection forces in the modulation of kinetochore-microtubule attachments and chromosome segregation fidelity (Cane et al., 2013; Powers et al., 2004; Wandke et al., 2012). However, and most important for our purposes, chromosomes with large kinetochores still showed a strong bias to lag in anaphase after Kif4a RNAi (pL=0.43; pS=0.13) (Figure 2.2.12. C, F). Conversely, if chromosomes with small or large kinetochores had equal probabilities to lag behind in anaphase after Kif4a RNAi, one would predict a frequency of 96% of anaphase cells with at least one lagging chromosome with small kinetochores, and not the experimentally observed value of 44% (Figure 2.2.12. F; see Materials and Methods). These results exclude the role of arm-associated forces in the observed missegregation bias and support that kinetochore size is the critical variable.

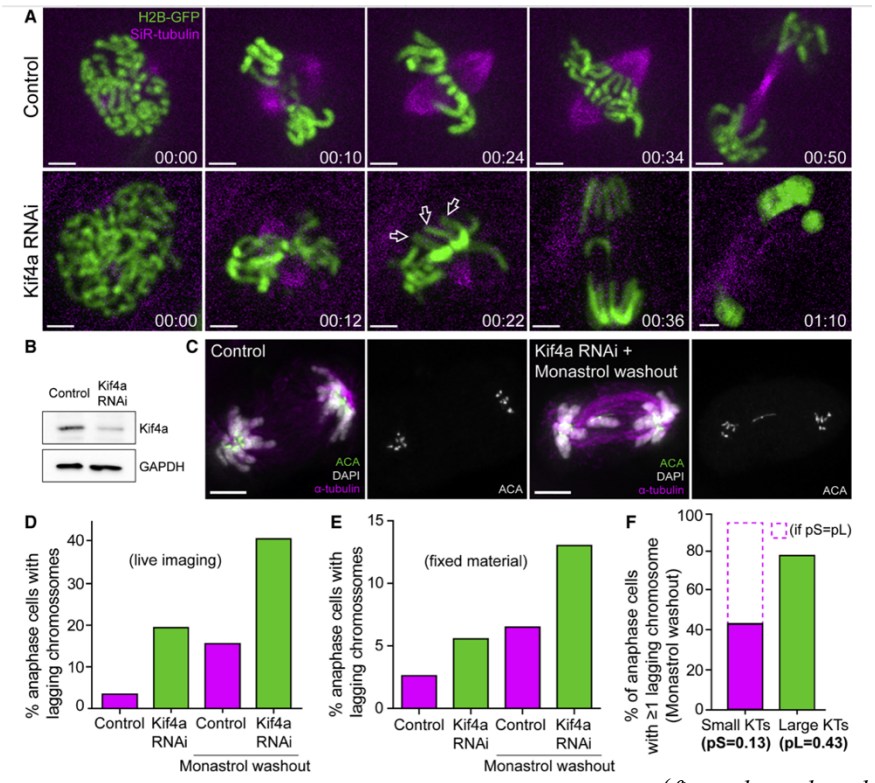

(*figure legend on the next page)*

Figure 2.2.10. Polar Ejection Forces on Chromosome Arms Ensure Mitotic Fidelity but Are Not Implicated in the Observed Missegregation Bias for Chromosomes with Large Kinetochores.

A, live-cell imaging of Indian muntjac fibroblasts stably expressing H2B-GFP to visualize the chromosomes (green) in control (top) and Kif4a RNAi (bottom) cells treated with 50 nM SiR-tubulin to label spindle microtubules (magenta). Scale bar: 5 μm. Time: h:min. White arrows point to the chromosome arms facing the spindle poles. **B**, western blot to monitor Kif4a levels after RNAi. GAPDH was used as loading control. **C**, chromosome missegregation after Kif4a RNAi (fixed cells). Kinetochores (anti-ACA), α-tubulin, and DNA (DAPI) are indicated. Scale bars, 5 μm. **D** and **E**, Comparison of the frequency of anaphase cells with lagging chromosomes in live (D) and fixed (E) material after Kif4a depletion and/or monastrol washout. **F**, frequency of anaphase cells with at least 1 lagging chromosome with small or large kinetochores after monastrol washout in Kif4a-depleted fibroblasts. Dashed bar represents theoretical values for frequencies of lagging chromosomes with small kinetochores if the probability to lag was equal for chromosomes with small or large kinetochores.

2.2.3. Discussion

Here we show how kinetochore size impacts chromosome congression and bi-orientation, error-formation, and correction, as well as chromosome segregation fidelity during mitosis. Accordingly, we found that chromosomes with large kinetochores bi-orient and congress more efficiently, and depend less on the kinetochore motor CENP-E. Because chromosomes with large kinetochores have an increased surface (and possibly a more favorable shape) for potential interaction with microtubules, these results help to explain why certain species with holocentric chromosomes, such as *C. elegans*, can complete congression in the absence of a CENP-E orthologue (Maddox et al., 2004). Noteworthy, this does not seem to be a peculiarity of *C. elegans*, since 9/14 unrelated species with holocentric chromosomes and sequenced genomes also lack a bona fide CENP-E orthologue (our unpublished observations).

Importantly, having a large kinetochore surface that facilitates chromosome bi-orientation comes with a price: chromosomes with large kinetochores have a much higher tendency to establish erroneous merotelic attachments and missegregate during anaphase. This implies that chromosomes that use the CENP-E pathway for congression are less prone to missegregate, offering a plausible explanation for why the CENP-E pathway emerged during evolution. On the other hand, species with holocentric chromosomes would be expected to be highly prone to chromosome missegregation, but in *C. elegans* only ~1% of wild-type anaphases show lagging chromosomes (Stear and Roth, 2002). In agreement, electron microscopy reconstructions of the *C. elegans* spindle failed to reveal merotelic attachments, against what would have been intuitively predicted for a species with the highest possible kinetochore/chromosome ratio (O'Toole et al., 2003; Redemann et al., 2017). Thus, chromosome segregation fidelity might be ensured by a species-specific optimal kinetochore size.

Because chromosomes with large kinetochores also establish more errors, this would work as a negative selective pressure to maintain chromosomes with large kinetochores during evolution, suggesting that the errors resulting from incorrect merotelic attachments are unlikely to be propagated. Indeed, error correction mechanisms during normal mitosis appear to be very robust, in agreement with our findings of very low missegregation rates in unperturbed cells. Moreover, based on direct live-cell imaging, we found that, even when cells were challenged, lagging chromosomes in Indian muntjac fibroblasts were able to re-integrate the main nuclei in ~50% of cases. This likely results from error correction mechanisms that are in place during anaphase and involve mechanical forces that stretch and deform merotelic-attached kinetochores, as shown in other systems (Cimini et al., 2004; Cimini et al., 2003). Noteworthy, any potential loss of a single chromosome in Indian muntjac females would represent the loss of 1/3 of the haploid genome, which would seriously compromise cell viability. In agreement, previous work reported that chromosome missegregation and aneuploidy in Indian muntjac primary fibroblasts was essentially limited to the smallest Y_2 chromosome in males (Vig and Henderson, 1998).

A legitimate question is whether size differences in human kinetochores have any functional implications for chromosome segregation. The length of α-satellite DNA arrays on human centromeres also varies more than 25-fold, ranging from 200 kb in the Y chromosome, to >5 Mb in chromosome 18 (Rudd and Willard, 2004) and this has been proposed to contribute for CENP-A incorporation, at least in some chromosomes (Sullivan et al., 2011). In agreement, the Y chromosome, which carries very little genetic information, was shown to recruit significantly less CENP-A compared with any other chromosome (Bodor et al., 2014; Irvine et al., 2004; Sullivan et al., 2011) and to missegregate at elevated frequencies in human cells (Fachinetti et al., 2015). Moreover, the loss of the Y chromosome is the most common somatic alteration in men and is associated with shorter survival and higher risk of cancer (Forsberg et al., 2014). Thus, in addition to the low genetic pressure to keep the Y chromosome in men, its smaller kinetochore might compromise the establishment of competent microtubule attachments and contribute for the high missegregation rate. On the other extreme, CENP-A domain expansion and overexpression have been linked with chromosome missegregation and genomic instability in human cancer cell models (Shrestha et al., 2017a; Sullivan et al., 2011; Tomonaga et al., 2003). Our finding that all functional centromere/kinetochore layers and respective microtubule binding capacity scale with centromere size suggests that any alterations at the foundations of kinetochore assembly will translate into architectural changes with functional implications for chromosome segregation. Because the level of CENP-A incorporation into human kinetochores also correlates with chromosome size (Irvine et al., 2004), one prediction from our studies is that (with the exception of the Y chromosome) larger human chromosomes might missegregate at higher frequencies.

The microtubule binding capacity of human kinetochores in metaphase has been reported to range between 12-24 microtubules in one study (Wendell et al., 1993) and 13-22 microtubules in another study (McEwen et al., 2001) (both studies from HeLa cells that lack the Y chromosome). This has been interpreted as if all kinetochores on human chromosomes, on average, bind to 17 microtubules. However, this two-fold variability might instead reflect the structural variability in kinetochore size among different human chromosomes (Bodor et al., 2014; Cherry et al., 1989; Cherry and Johnston, 1987; Irvine et al., 2004; Nixon et al., 2017b; Peretti et al., 1986; Sanchez et al., 1991; Tomkiel et al., 1994). The development of correlative light-electron microscopy techniques, combined with labeling techniques (e.g., using CRISPR-Cas9) in which specific human chromosomes could be unequivocally identified and their microtubule binding capacity determined at the ultra-structural level, will be required to clarify this issue. More recently, adaptive changes in kinetochore architecture as cells progress into metaphase were also proposed to play a critical role in chromosome orientation and error prevention during spindle assembly in human cells (Magidson et al., 2015). These conclusions were supported by combining experimental observations of size and morphological changes of human kinetochores in response to microtubule attachments, with predictions derived from computational modelling. In the future, it will be important to define experimental conditions in which kinetochore size and shape could be modulated (e.g., by constitutively maintaining or preventing the expansion of the fibrous corona throughout mitosis), while investigating the respective consequences for chromosome segregation fidelity. A remarkable human condition in which constitutive differences in kinetochore size might bias chromosome missegregation is the occurrence of dicentric chromosomes that remain active during mitosis. As in the Indian muntjac, these chromosomes have a ‘compound’ centromere/kinetochore and were shown to have a much higher tendency to lag behind in anaphase when compared with their normal counterparts, but rarely missegregate or give rise to viable cells (Sullivan and Willard, 1998). Taken together, we believe there is solid ground to generalize our findings about the role of kinetochore size in non-random chromosome (mis)segregation, at least for specific human conditions with strong clinical implications. Our work further highlights the power of Indian muntjac cells to address fundamental biological questions that simply cannot be answered in human cells due to current technical limitations.

2.2.4. Materials and Methods

2.2.4.1. Cell transfection and transduction

Indian muntjac fibroblasts were transfected either with human H2B-GFP (from Geoff Wahl lab, Addgene plasmid #11680) or pSV-IRESneo3-CENP-A-EGFP (kind gift from Patrick Meraldi, University of Geneva) plasmids using Lipofectamine 2000 (Invitrogen) to generate stable cell

lines. For this purpose, at day 1 cells were seeded in 6-well plates at 60-70% confluence in MEM containing 20% FBS. The day after, cells were washed 3x with PBS and incubated with Optimem medium (Gibco, Life Technologies) containing Lipofectamine 2000 (Invitrogen) and the respective DNA for 4 h. Optimem with DNA and Lipofectamine 2000 were previously mixed and incubated for 20 minutes before adding to the cells. After 4 h Optimem medium was exchanged to MEM supplemented with 20% FBS and transfected cells were selected with G418 (Merck Millipore) after 48 h. For centriole labelling, EGFP was fused to the C-terminus of human Centrin-1 and cloned in the Lentilox 3.1 vector. Cells were subsequently infected with the virus, without selection, as previously described (Magidson et al., 2016).

2.2.4.2. Identification of Indian muntjac orthologue sequences for human proteins

The protein sequences of human Ndc80, Mad2, Mps1, CLASP1, Survivin and Kif4a were obtained from NCBI and used as query for tblastn (version 2.2.29; (Morgulis et al., 2008)) using the Indian muntjac genome scaffold sequences and predicted coding sequences as targets (Farré et al., manuscript in preparation). Sequence alignments with at least 80% identity, highest coverage of human genes, and with matching scaffold intervals from both tblastn runs were used to identify Indian muntjac orthologues of gene human sequences.

2.2.4.3. Design of siRNAs for RNA interference (RNAi)

The design of the siRNA sequences was performed using the application *BLOCK-IT™ RNAi Designer* (*ThermoFisher* Scientific). We provided the nucleotide sequence of the genes of interest, selected an ideal CG percentage between 35%-55% and the recommended default motif pattern for the RNAi design. From the 10 designs generated, we selected the one with higher probability of knock-down.

2.2.4.4. RNAi experiments

In day 0, Indian muntjac cells were cultured at 60%-70% confluence in 6-well plate/35 mm dishes. In day 1, the medium was changed to MEM supplemented with 5% FBS. Simultaneously, 5 µL of Lipofectamine RNAi Max (Invitrogen) and 50 nM of the respective siRNAs. The following target sequences were used: 5'-GCAGACAUUGAGAGAAUAA-3' (Ndc80), 5'-GCAGAAUGGUUAUACAAGU-3' (Mad2), 5'-CCAAGCAGUCACCACCAAU-3' (Mps1), 5'-GCUGCUGUUGCUGAUGCUU-3' (CLASP1), 5'-GCGUCUCCACGUUUAAGAA-3' (Survivin), 5'-GGAACCGUCAGCAAGACAA-3' (Kif4a) (Sigma-Aldrich). All siRNAs were diluted in 500 µL of Optimem and added to the cells. Mock transfection was used as control. The cells were analysed 24h, 48h or 72h after depletion. Depletion efficiency was monitored by western blotting and phenotypic analysis.

2.2.4.5. Immunofluorescence

Indian muntjac fibroblasts were seeded on poly-L-lysine-coated coverslips 2 days before the experiment. After fixation with ice-cold methanol (Invitrogen) for 4 minutes at -20ºC or 4% paraformaldehyde (Electron Microscopy Sciences) for 10 minutes at room temperature (RT), cells were washed with PBS-0.05%Tween 20 (Sigma-Aldrich) or cytoskeleton buffer pH 6.1 (274 mM NaCl, 10 mM KCl, 2.2 mM Na2HPO4, 0.8 mM KH2PO4, 4 mM EGTA, 4 mM MgCl2, 10 mM Pipes, 10 mM Glucose). Extraction after paraformaldehyde fixation was performed using PBS-0.1%Triton (Sigma-Aldrich). Cells were incubated with primary antibodies in blocking solution (10% FBS diluted in PBS-0.05%Tween 20 (Sigma-Aldrich) or in cytoskeleton buffer pH 6.1) for 1 hour. The following primary antibodies were used: human anti-centromere antibodies (ACA) (1:2000; Fitzgerald), mouse anti-CENP-A (1:200, kind gift from Lars Jansen, Instituto Gulbenkian de Ciência, Lisbon, Portugal), mouse anti-α-tubulin (1:2000; B-512 clone, Sigma-Aldrich), rabbit anti-pH3(S10) (1:800, Santa Cruz Biotechnology), rabbit anti-pKNL1 58A (32) (1:1000; kind gift from Iain Cheeseman, Whitehead Institute, MIT, Cambridge, MA, USA), sheep anti-CENP-E (1: 1000, kind gift from William C. Earnshaw, Welcome Trust Centre for Cell Biology, The University of Edinburgh, UK), mouse anti-c-Mad2 (1:500; Santa Cruz), rabbit anti-pAuroraB (pT232) (1:1000; Rockland), mouse anti-Hec1/Ndc80 (9G3) (1:500, Abcam). Subsequently, cells were washed 3x with PBS-0.05% Tween or cytoskeleton buffer and incubated 45 minutes with the corresponding secondary antibodies Alexa-488, 568 and 647 (Invitrogen) or Abberior STAR 580 and Abberior STAR 635p (Abberior Instruments) for STED microscopy. For STED microscopy, both primary and secondary antibodies were used at 1:100 concentrations. After adding 1 μg/ml 4'6'-Diamidino-2-phenylindole (DAPI) (Sigma Aldrich) for 5 minutes, coverslips were washed in PBS and sealed on glass slides mounted with 20 mM Tris pH8, 0.5 N-propyl gallate, 90% glycerol.

2.2.4.6. Chromosome spreads

Indian muntjac fibroblasts were incubated with 3.3 μM of nocodazole (Sigma-Aldrich) for 6-7 h, then trypsinized and centrifuged for 5 minutes at 1200 rpm. The pellet was resuspended in 500 μL of the supernatant, and a hypotonic solution (medium:water 1:1 and 3.3 μM nocodazole) was added drop by drop until the final volume of 5 mL. The mixture was incubated at 37ºC for 20 minutes. After centrifugation the supernatant was discarded, and the cells were fixed with Carnoy solution (methanol (AppliChem Panreac): acetic acid (Millipore Corporation) 3:1) overnight at -20ºC. The following day, the Carnoy fixation was repeated, and cells were subsequently spread drop-by-drop onto a glass slide. DNA was counterstained with 1 μg/ml DAPI (Sigma-Aldrich) for 10 minutes and the preparations were mounted on 20 mM Tris pH8, 0.5 N-propyl gallate, 90% glycerol. For chromosome spreads with antibody staining Indian muntjac fibroblasts were incubated with 3.3 μM nocodazole for 6-7 h, then trypsinized and centrifuged for 5 minutes at

1200 rpm. The pellet was resuspended in 500 µL of the hypotonic solution containing sodium citrate (Sigma-Aldrich) and 10% BSA (Sigma-Aldrich) and incubated for 30 minutes at 37ºC. Cells were then placed on glass slides using a Cytospin 4 centrifuge (Thermo Scientific). Glass slides containing chromosome spreads were fixed with 4% paraformaldehyde and immunofluorescence was performed as indicated in section 2.2.4.5..

2.2.4.7. Measurement of intra-kinetochore distances

Selected centromeres with co-planar kinetochores (intensity peaks separated by no more than 1 plane in series recorded at 200-nm Z-steps) were line-scanned. Two Gaussian peaks were detected in the scans via a Matlab function developed by Dr. O'Haver (https://www.mathworks.com/matlabcentral/fileexchange/23611-peakfit--command-line-peak-fitting-function). Delta values were calculated by subtracting the distance between the centers of CENP-A peaks from the distance between the centers of Ndc80/Hec1 peaks and dividing the result by 2. This approach automatically compensates potential chromatic aberrations (Wan et al., 2009). CENP-A was visualized with 3-19 mouse monoclonal antibody (Abcam) and Ndc80/Hec1 with the 9G3 monoclonal antibody (Abcam), both at 1:200 dilution. Although both 3–19 (CENP-A) and 9G3 (Ndc80/Hec1) antibodies were mouse monoclonal, they have different isotypes. 3–19 was followed by a γ1b-specific secondary antibody conjugated to Alexa Fluor 488, and 9G3 was followed by a γ2a-specific secondary antibody conjugated to Alexa Fluor 594, both at 1:100 dilution (Life Technologies).

2.2.4.8. Error formation and prevention of error correction assays

To promote error formation, Indian muntjac fibroblasts were seeded on poly-L-lysine-coated (Sigma-Aldrich) coverslips 2 days before the experiment. Cells were incubated for 12 hours with 100 µM monastrol (Tocris bioscience) and subsequently washed out into MEM medium or MEM containing 1 µM Aurora B inhibitor (Selleckchem) and 2 µM MG-132 (Calbiochem) for the next 50 minutes before fixation, based on previous reports (Lampson et al., 2004). To prevent error correction, cells were incubated with 20 µM Mps1-IN-1 (Kwiatkowski et al., 2010) (kind gift from N. Gray, Dana-Farber Cancer Institute, Boston, MA, USA) for 15 minutes, prior to fixation. This concentration was previously assessed for the formation of lagging chromosomes in Indian muntjac fibroblasts by live cell imaging. When indicated, cells were fixed with ice-cold methanol (Invitrogen) for 4 minutes at -20 °C or 4% paraformaldehyde (Electron Microscopy Sciences) for immunofluorescence analysis.

2.2.4.9. CENP-E inhibitor titration

Indian muntjac fibroblast stably expressing H2B-GFP were seeded in 96 well plates (10.000 cells per well) two days before imaging and kept in culture medium at 37°C in humidified conditions with 5% CO2. On the day of imaging, CENP-E inhibitor, GSK923295 (Selleckchem), was added

in triplicates at the following concentrations: 5 nM, 10 nM, 20 nM, 40 nM, 80 nM, 160 nM and 320 nM. Control cells were treated with DMSO only. Live cell imaging was performed using In Cell Analyzer 2000 (GE Healthcare Life Sciences) 1 hour after addition of the inhibitor. Images were analysed with CellProfiler 2.2.0. and CellProfiler Analyst. In accordance with the results obtained from the CENP-E inhibitor titration, Indian muntjac fibroblasts were treated with 20 nM GSK923295 1 hour before fixation or live-cell imaging.

2.2.4.10. Live-cell imaging

Indian muntjac fibroblasts stably expressing human CENP-A-GFP or H2B-GFP were plated on fibronectin (Sigma-Aldrich) coated 35 mm glass-bottom dishes (14 mm, No 1.5, MatTek Corporation) 2 days before imaging. Before live-cell imaging, cells were cultured in Leibovitz´s-L15 medium (Gibco, Life Technologies). For tubulin staining, we used 20-50 nM SiR-tubulin cell-permeable dye (Lukinavicius et al., 2014) (Spirochrome) and incubated cells for 6-12 hours. Live-cell imaging was performed on a temperature-controlled Nikon TE2000 microscope equipped at the camera port with a modified Yokogawa CSU-X1 spinning-disc head (Solamere Technology), an FW-1000 filter-wheel (ASI) and an iXon+ DU-897 EM-CCD (Andor). The excitation optics are composed of two sapphire lasers at 488 nm and 647 nm (Coherent), which are shuttered by an acousto-optic tuneable filter (Gooche&Housego, model R64040-150) and injected into the Yokogawa head via a polarization-maintaining single-mode optical fiber (OZ optics). Sample position is controlled by a motorized SCAN-IM stage (Marzhauser) and a 541.ZSL piezo (Physik Instrumente). The objective was an oil-immersion 60x 1.4 NA Plan-Apo DIC CFI (Nikon, VC series), yielding an overall (including the pinhole-imaging lens) 190 nm/pixel sampling. A 1.5x tube lens (optivar) was also used (126 nm/pixel sampling). Eleven 1 μm separated z-stacks were acquired every 2 minute while recording Indian muntjac fibroblasts stably expressing H2B-GFP. For 4D kinetochore tracking we used Indian muntjac fibroblasts stably expressing CENP-A-GFP, recorded at 30 seconds or 60 seconds interval and 0.75 μm separated z-stack. The system was controlled by NIS-Elements via a DAC board (National Instruments, PCI-6733).

2.2.4.11. STED super-resolution microscopy

For STED imaging we used a pulsed gated-STED microscope (Abberior Instruments) with excitation wavelengths at 561 nm and 640 nm doughnut-depleted with a single laser at 775 nm. All acquisitions were performed using a 1.4 NA oil-immersion and a pixel size set to 35 nm.

2.2.4.12. Serial section electron microscopy

Cells were fixed with 2.5% glutaraldehyde (Sigma) in PBS, pH 7.4 for 30 minutes, rinsed with PBS (3x5 minutes), and mounted in Rose chambers. Multimode (DIC and 3-color fluorescence) datasets were obtained on a Nikon TE2000 microscope equipped with PlanApo 100x 1.45 NA

objective lens. 3-D LM volumes of metaphase cells selected for EM analyses were recorded on a Zyla 4.2 sCMOS camera (Andor) at 65-nm X-Y pixel size and 200-nm Z-steps. All LM images were deconvolved in SoftWoRx 5.0 software (Applied Precision) with lens specific PSFs. Post-fixation, embedding, and sectioning were done as previously described (Rieder and Cassels, 1999). Thin sections (70-80 nm) were imaged on JEOL 1400 microscope operated at 80 kV using side-mounted 4.0 Megapixel XR401 sCMOS AMT camera (Advanced Microscopy Techniques Corp). Full series of images recorded at 12K magnification were used to reconstruct the volume of the cell and match orientation and superimpose this volume on the corresponding LM dataset. Higher-magnification images (30-40K) were then collected for individual kinetochores. These high-magnification images were subsequently used to trace microtubules end-on attached to the kinetochores. For 3-D models, contours of kinetochores, adjacent chromatin, and end-on attached microtubules were manually traced. Volumes occupied by the kinetochores were visualized as isosurface models in Amira 5.3.3 (Visage Imaging).

2.2.4.13. Western Blotting

Indian muntjac fibroblasts were collected after trypsinization and centrifuged at 1200 rpm for 5 minutes. The pellet was resuspended in PBS and centrifuged, the cells were resuspended in 30-50 µL of Lysis Buffer (NP-40: 20 nM Hepes/KOH pH 7.9; 1 mM EDTA pH 8; 1 mM EGTA; 150 nM NaCl; 0.5% NP40; 10% glycerol, 1:50 protease inhibitor; 1:100 Phenylmethylsulfonyl fluoride). The samples were flash frozen in liquid nitrogen and kept on ice for 30 minutes. After centrifugation at 14000 rpm for 15 minutes at 4 °C, protein concentration was determined by Bradford protein assay *(Bio-Rad*). Protein lysates were run on 7.5/10/15% SDS-PAGE (25-40 µg/lane) and transferred to a nitrocellulose Hybond-C membrane using an iBlot® Gel Transfer Device (*Thermo Scientific*). Membranes were blocked in PBS 0.05% Tween with 5% milk and the primary antibodies were incubated overnight at 4 °C at the following dilutions: anti-Hec1/Ndc80 mouse anti-Hec1/Ndc80 (9G3); anti-Mad2 (rabbit, 1:500, Bethyl Laboratories); anti-CLASP1 (rat, 1:100, (Pereira et al., 2006)), anti-Survivin (rabbit, 1:1000, Novus Biologicals), anti-Aurora A (rabbit, 1:1000, Novus Biologicals); anti-Kif4a (rabbit, 1:1000, Thermo Fisher Scientific); anti-GAPDH (mouse, 1:15000, Proteintech). After successive washes, the membrane was incubated with the secondary antibodies for 1 hour at RT (α-mouse-HRF; α-rabbit-HRF; α-sheep-HRP 1:5000). Detection was performed with Clarity Western ECL Substrate (*Bio-Rad*). Quantification of blots was performed with a Bio-Rad ChemiDoc XRS system using the IMAGELAB software and immunosignals were normalized to GAPDH expression.

2.2.4.14. Fixed image analysis and acquisition

Image acquisition (0.22 µm thick z-stacks) was performed on a Zeiss AxioObserver Z1 wide-field microscope equipped with a plan-apochromatic (1.46 NA 60x) DIC objective and a cooled

CCD (Hamamatsu Orca R2). Autoquant X (Media Cybernetics) was used for blind deconvolution. All images show maximum intensity projections. For classification of kinetochore-microtubule attachments, microtubules were traced through z-stacks and the position of their ends determined relative to the kinetochore signal. In the case of merotelic attachments, kinetochore deformation and/or orientation were also used as a secondary criterion. Protein levels (CENP-A, Ndc80/Hec1, CENP-E, Mad2, pKNL1 and pAuroraB) on chromosome spreads were analysed using ROI manager in Fiji (ImageJ). For quantification of kinetochore protein levels in all chromosomes, fluorescence intensity for each protein was background subtracted and normalized for the levels obtained for chromosome X+3 in the same cell. Adobe Photoshop CS4 and Adobe Illustrator CS5 (Adobe Systems) were used for histogram adjustments and panel assembly for publication.

2.2.4.15. Frequency analysis and joint probability tables

Custom-made scripts were developed in MATLAB 8.1 (The MathWorks Inc.) to perform the frequency analysis for the number of chromosomes with small and large kinetochores staying at the pole upon CENP-E inhibition. Joint probability tables were calculated for six independent sets of mitotic cells, each with at least 100 cells. The tables were used to calculate the marginal and the conditional probabilities of the number of chromosomes with small/large kinetochores found at the pole. The random variables considered for the joint probability table were ‘S’, for the number of chromosomes with small kinetochores that stay at the pole, and ‘L’, for the number of chromosomes with large kinetochores that stay at the pole. Binomial distributions were fitted to both random variables, using information about the number of independent components (2 for large kinetochores, and 4 for small kinetochores) and the respective experimental values. All data are represented as the mean ± S.D. Additional custom-made MATLAB scripts were developed to perform the frequency analysis on the number of lagging chromosomes during anaphase, according to the kinetochore size. Following a similar methodology as above, joint probability tables were calculated and used to obtain the marginal and the conditional probabilities of the number of lagging chromosomes with small and with large kinetochores. Experimental data was used to parameterize the associated probability distributions (binomial). The distributions were used to calculate the probability of having lagging chromosomes of a certain type, given that there was at least a lagging chromosome, under two different conditions: a) imposing equal values for the individual lagging probability, independently of the kinetochore size; and b) estimating the individual lagging probability for each chromosome type, constrained to the mean values of lagging chromosomes (of each type) observed experimentally. For control cells where the total number of chromosomes was not always 6 (4 chromosomes with small kinetochore and 2 with large kinetochore) the frequency analysis for the lagging chromosomes was not performed using joint probability tables. Given that a varying number of total chromosomes imposes important constraints to this approach, the frequency analysis was performed instead in terms of calculation

of mean values for the fraction of chromosomes of each type that become lagging. This way, for each experiment, the total number of chromosomes with small and large kinetochores was accounted to calculate a descriptive measurement, which is independent of the number of chromosomes.

2.2.4.16. Kinetochore tracking

Live-cell imaging of Indian muntjac fibroblasts stably expressing CENP-A-GFP was performed as indicated, every 60 seconds, and analysed after CENP-E inhibition using TrackMate Tool in Fiji (Image J). Initial kinetochore and pole positions at nuclear envelope breakdown were manually tracked in four dimensions (x,y,z,t) using Manual Tracking Tool. Further analyses and plotting were performed using MATLAB to assess the initial position of the chromosomes with large kinetochores relative to the spindle and spindle poles/equator. Data from different cells was pooled together by applying geometric affine transformations (without shear) to generate overlap for the pole's location. Initial positions of the chromosomes with large kinetochores were plotted on a standardized geometrical representation of the mitotic spindle ellipsoid.

2.2.4.17. Statistical analysis

Statistical analysis was performed using SigmaStat 3.5 software. All data represent the mean ± S.D.. Statistical significance of differences between the population distributions was determined by Student t-test. For data that did not follow a normal distribution, statistical analysis was performed using a Mann- Whitney Rank Sum test.

CHAPTER 2.3.

‘Dissecting the relationship between kinetochore size and CENP-E motion dependency for chromosome congression’

Side-project developed in collaboration with the Cell Division Mechanisms group

External supervisor: Reto Gassmann, PhD

External co-supervisor: Helder Rocha, PhD

CHAPTER 2.3. Dissecting the relationship between kinetochore size and CENP-E motion dependency for chromosome congression

2.3.1. Introduction

Efficient chromosome congression to the spindle equator is essential for faithful mitotic progression (Maiato et al., 2017). At the onset of mitosis, DNA is packed into chromosomes, the nuclear envelope breaks down and scattered chromosomes start to interact with spindle microtubules, via proteinaceous structures that localize on the centromeric region of each sister chromatid, called kinetochores (Musacchio and Desai, 2017). When chromosomes are favourably positioned between the spindle poles, they establish end-on kinetochore-microtubule attachments and congress after bi-orientation (Auckland and McAinsh, 2015). In contrast, more peripheral chromosomes are first brought to the vicinity of spindle poles along laterally attached astral microtubules by the microtubule minus-end directed motor protein Dynein at kinetochores (Li et al., 2007; Vorozhko et al., 2008; Yang et al., 2007), and subsequently transported towards the equator by the microtubule plus-end directed kinesin motor CENP-E (kinesin-7) (Barisic et al., 2014; Kapoor et al., 2006). Regulation of kinetochore motors with opposite activities is controlled by tubulin posttranslational modifications (PTMs). Microtubule detyrosination favors CENP-E-mediated chromosome alignment, while inhibiting dynein-driven transport (Barisic and Maiato, 2016; Barisic et al., 2015).

How kinetochore size impacts the mechanisms of chromosome congression remains unclear. Previous work demonstrated that mammalian chromosomes can either congress using CENP-E-dependent or -independent pathways, regardless of their kinetochore size (Drpic et al., 2018; Tovini and McClelland, 2019). However, chromosomes with a larger kinetochore relied less on CENP-E motor activity to congress to the spindle equator. Interestingly, some metazoans, such as *C. elegans*, whose kinetochores extend along the entire chromosome length (holocentric kinetochore), lack a bona fide CENP-E ortholog (Maddox et al., 2004). Proper orientation of sister kinetochores before stable microtubule attachment occurs via ‘direct congression’, a process that is facilitated by the non-kinetochore motor protein Klp-19 (Kinesin-4) that provides polar ejection forces (PEFs) (Powers et al., 2004).

The nematode *C. elegans* is a powerful model for genomic and cell biological studies since a vast array of genetic approaches and live imaging assays are available to study mitotic processes and their key components. During early embryogenesis, mitotic spindle microtubules are vastly composed of 2 of the 9 α-tubulin isoforms, tba-1 and tba-2 (Hurd, 2018). These two isotypes show some degree of redundancy. Depletion of both α-tubulins results in embryonic lethality, while RNAi or deletion of one of them causes only mild effects on embryonic viability (Honda et

al., 2017; Lu and Mains, 2005; Phillips et al., 2004). *In vitro* reconstitution and cell/embryo-based assays showed that tubulin PTMs confer different affinities to motor proteins along microtubules (Barbosa et al., 2017; Barisic et al., 2015), however the physiological relevance of microtubule tyrosination and detyrosination for chromosome congression is still to be investigated.

Here, we generated *C. elegans* embryos stably expressing human CENP-E to determine whether its activity can rescue chromosome congression defects. To do so, we attenuated the contribution of direct congression due to rapid bi-orientation of the holocentric kinetochores by depleting the chromokinesin Klp-19. Interestingly, expression of human CENP-E did not affect the normal course of mitosis and it was sufficient to partially rescue the alignment defects imposed by the loss of PEFs on chromosome arms. In future studies, we propose to confirm the role of CENP-E motor-dependency for chromosome alignment, while investigating whether tubulin detyrosination directly affects chromosome congression *in vivo.*

2.3.2. Results

2.3.2.1. Expression of human CENP-E in *C. elegans*

To directly test this hypothesis, we expressed human CENP-E (hCENP-E) in *C. elegans* embryos. We initially optimized the gene sequence codons to maximize the probability of hCENP-E expression in the worms. This way, the codon frequency probabilities and adaptation index for this species were taken into consideration, while the translated protein remained unaltered (see Materials and Methods). In vertebrates, CENP-E localizes at the kinetochore expandable module throughout mitosis (Craske and Welburn, 2020; Yen et al., 1991). To ensure the correct localization of the motor protein, we isolated the kinetochore protein Kbp-3 (Spc25 orthologue) from *C. elegans* genomic DNA and fused it with hCENP-E. The fragments were assembled into a pRG777 expression backbone tagged with mKate2 fluorescent protein. A construct containing only Kbp-3 was used to rule out any unspecific effect due to its ectopic expression (Figure 2.3.1. A). The correct localization of Kbp-3 (control) and hCENP-E-Kbp-3 (control C-E) at the kinetochores during the first embryonic division was confirmed by live-cell imaging (Figure 2.3.1. B). Interestingly, no phenotype associated with the expression of either construct was detected, thereby validating our approach. Despite the expression levels in the control CENP-E-Kbp-3 worms was reduced to approximately 2/5 of control Kbp-3 levels (Figure 2.3.1. C-D), we further continued our analysis.

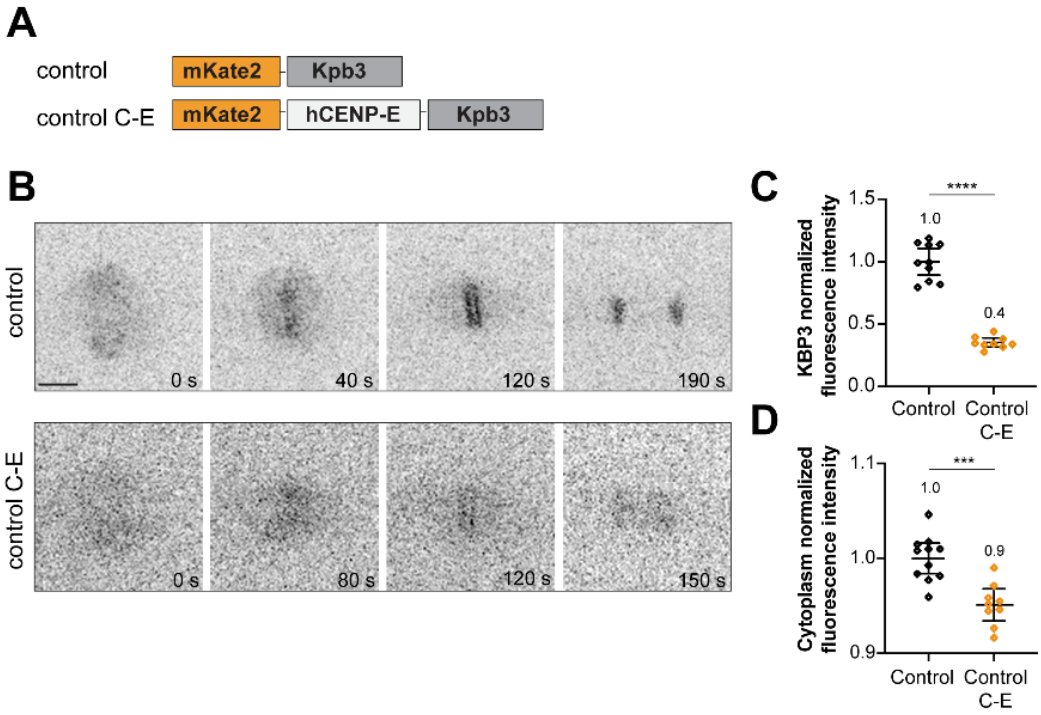

Figure 2.3.1. Expression of human CENP-E (C-E) in C. elegans.

A, schematic representation of the transgenes used in this study: Kbp3 and hCENP-E-Kbp3 were fused with mKate2 fluorescent protein in order to see kinetochores (control and control C-E). **B,** selected stills from time-lapse sequences of the first embryonic division showing the kinetochore localization of the two constructs (kpb3, inverted gray scale). Scale bar: 5 μm. Time-lapse is shown in seconds (s). **C**, normalized fluorescence intensity of Kbp3 at kinetochores. **D**, normalized fluorescence intensity of the cytoplasmic signal. ****p<0.0001; ***p<0.001; unpaired t-test.

Worms stably expressing hCENP-E-Kbp-3 and Kpb-3 were crossed with TH32 worms expressing GFP::histone H2B (to visualize chromosomes) and GFP::γ-tubulin (to visualize spindle poles). Live-cell imaging of the well-established one-cell *C. elegans* embryos unveiled that both hCENP-E-Kbp-3 and Kbp-3 expression did not affect normal mitotic progression (Figure 2.3.2. A). Two different parameters were quantified over time: spindle length/pole separation, defined as the distance between the two spindle poles; and chromosome span, defined as the maximal distance between the outermost chromosomes within the spindle axis (Figure 2.3.2. B, C). These remained unaltered compared with the control embryos (Figure 2.2.2. B, D), thus ruling out unspecific effects associated with transgene expression.

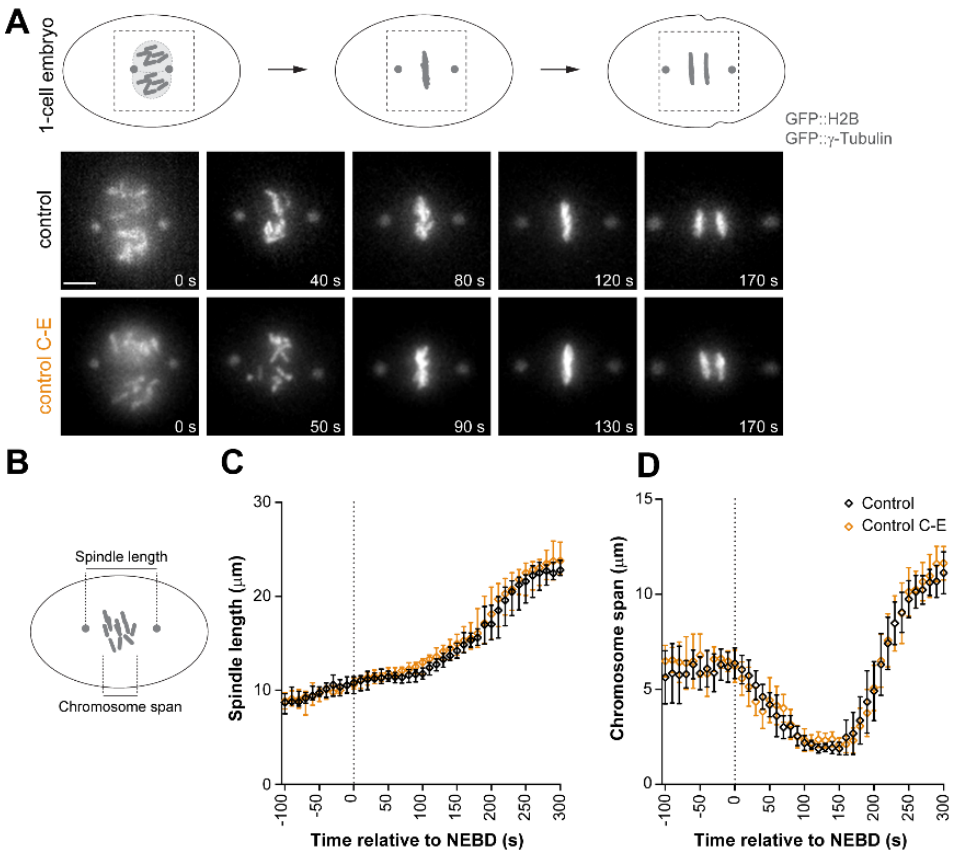

Figure 2.3.2. Expression of hCENP-E did not compromise the normal progression of mitosis.

A, representative live cell-imaging examples of the first embryonic division of control and control C-E embryos stably expressing GFP::H2B to visualize chromosomes, and GFP::γ-tubulin to label spindle poles. Scale bar: 5µm. **B**, schematics of the two quantitative measurements extracted from the live-cell recordings. **C,** spindle pole separation and **D,** chromosome congression kinetics in one-cell embryos, showing the same unperturbed effect in the absence (control) and presence (control C-E) of hCENP-E. Distances were measured in images acquired every 10 s, averaged for the total number of embryos, and plotted against time. Error bars represent the 95 % C.I. Grey dashed line represents NEBD.

2.3.2.2. hCENP-E expression partially rescued congression defects associated with defective kinetochore-microtubule attachments

To generate embryos with defective end-on kinetochore-microtubules attachments and consequently, problems in chromosome congression, we knocked-down the *C. elegans* chromokinesin Klp-19 (Powers et al., 2004). As expected, after nuclear envelope breakdown (NEBD) chromosomes became scattered in the cytoplasm and took longer to congress at the spindle equator (Figure 2.3.3. A). This ultimately led to an increase of lagging chromosomes in anaphase. In the first mitotic division, a premature pole separation prior to anaphase is indicative of an impairment in the formation of load-bearing kinetochore-microtubule attachments capable of sustaining tension (Desai et al., 2003; Gassmann et al., 2008; Oegema et al., 2001). As predicted, Klp-19-depleted embryos displayed premature pole separation starting around 30 s

after NEBD. Pole-to-pole distance (spindle length) started to decrease ~110 s upon NEBD and remained shorter than controls at anaphase onset (Figure 2.3.3. B). Initial pole separation roughly overlapped with the moment when chromosomes scattered along the spindle poles, suggesting that chromosomes had not stablished proper bipolar attachments with the spindle microtubules, capable of resisting the cortical pulling forces exerted on the poles (Figure 2.3.3. C). To test whether hCENP-E rescues the severe alignment defects, we imaged one-cell *C. elegans* embryos stably expressing hCENP-E-Kbp3 (C-E) after depletion of Klp-19 by RNAi (Figure 2.3.3. A). The same quantitative parameters were determined under this condition. The lack of end-on microtubule attachments was still detected by the premature pole separation observed 30 s after NEBD. Strikingly, chromosome span was partially rescued in hCENP-E expressing embryos which resulted in a significantly milder phenotype (chromosomes remained closer to the spindle equator) (Figure 2.3.3 B-C).

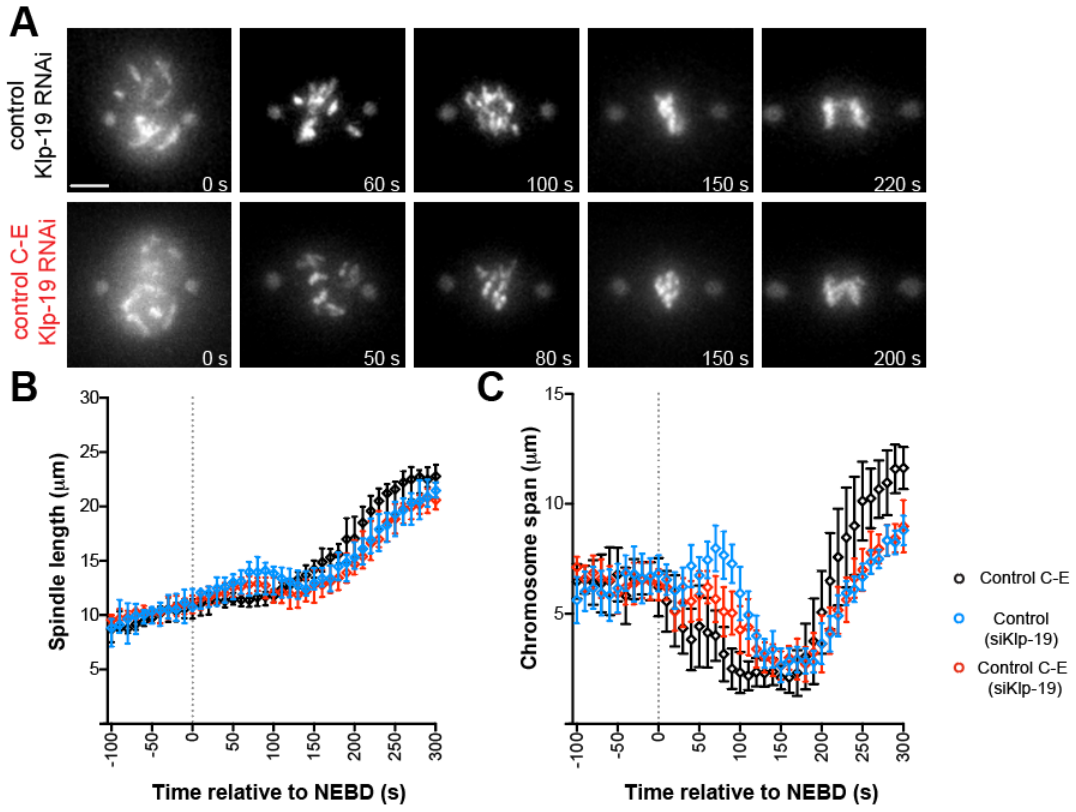

Figure 2.3.3. Expression of hCENP-E partially rescues the congression defects associated with the loss of polar ejection forces

A, representative live cell-imaging stills of the first embryonic division of control and control C-E embryos stably expressing GFP::H2B to visualize chromosomes, and GFP::γ-tubulin to label spindle poles, depleted of chromokinesin Klp-19. Klp-19 RNAi induces (**B)** a premature pole separation at ~120 s after NEBD (time zero on the plots) and (**C**) chromosome scattering on embryos. Phenotypes on embryos expressing hCENP-E (control C-E) were partially rescued. Distances were measured in images acquired every 10 s, averaged for the total number of embryos, and plotted against time. Error bars represent the 95 % C.I. Grey dashed line represents NEBD. Scale bar: 5µm.

2.3.3. Discussion and future perspectives

Most eukaryotic cells use two alternative pathways to congress their chromosomes to the spindle equator. Despite chromosome positioning at NEBD, how chromosomes prioritize one pathway over the other is still poorly understood. This process has been suggested to be biased by kinetochore size (Drpic et al., 2018; Tovini and McClelland, 2019). We speculated that larger kinetochores, which have a higher surface (and possibly a more favorable shape) to interact and to be captured by spindle microtubules, would depend less on CENP-E activity to bi-orient and congress. Accordingly, certain species with holocentric chromosomes, such as *C. elegans* can complete congression in the absence of a CENP-E ortholog (Maddox et al., 2004). This does not seem to be peculiarity of *C. elegans,* since ~65% of the analyzed species with holocentric chromosomes lacked a bona fide CENP-E ortholog (unpublished data). Whether species with holocentric chromosomes lost CENP-E during evolution or if they never had it remains unclear. The fact that CENP-E is present in the branches of all major lineages strongly suggests that it was present in the last eukaryotic common ancestor (LECA) and was selectively lost in certain branches, supporting the first hypothesis. *C. elegans* embryos rapidly bi-orient and congress all chromosomes within approximately 120 s after NEBD, and only ~1% of anaphases show lagging chromosomes (Stear and Roth, 2002). However, when experimentally challenged, they can have high rates of alignment defects and missegregation events. Here, we evaluated the physiological relevance of having a second congression pathway when rapid bi-orientation of chromosomes is compromised. Worms engineered to express human CENP-E fused to the docking kinetochore protein Kbp-3 did not show any problems throughout mitosis. Strikingly, the congression defects associated with the loss of PEFs upon depletion of Klp-19 were significantly rescued by CENP-E expression. This partial-phenotype might be explained by the fact that CENP-E-Kbp3 embryos showed a significantly lower intensity of Kbp-3 at kinetochores, which might translate in a milder expression of CENP-E protein in the worms (Figure 2.3.1. B). Moreover, we cannot exclude that the levels of tubulin detyrosination in one-cell embryos is almost exclusive to the spindle poles region (see supplemental material 2.3.5), which accordantly to previous reports (Barisic et al., 2015), might not be enough to ensure the fully CENP-E function.

In the future we have planned (1) to confirm that the observed rescue is a direct consequence of CENP-E motor domain/activity and (2) to test the hypothesis that CENP-E-mediated transport is enhanced on detyrosinated microtubules. To address the first goal, we generated a motor-dead CENP-E mutant (the last threonine of CENP-E ATP-binding pocket was mutated to an asparagine - it binds to microtubules in a rigor state, which prevents motor activity) (Nakata and Hirokawa, 1995). In parallel, we designed a strategy to increase tubulin detyrosination in *C. elegans* embryos by engineering a CRISPR/Cas9 KO worm for tba-1 and tba-2 C-terminal tyrosine residue. So far, we successfully generated homozygote worms for tba-1.

Overall, this work underscores the physiological relevance of having a kinetochore-motor to assist chromosome congression, while granting the technical tools to test how microtubule detyrosination, as part of the 'tubulin code', works as a navigation system that guides kinetochore motors during cell division, ultimately contributing to faithful chromosome segregation *in vivo*.

2.3.4. Supplemental Material

(*This set of experiments were included for the sake of the PhD thesis but will not be part of the manuscript in preparation).*

Following on previous studies that suggested that CENP-E ability to transport chromosomes is inhibited by tubulin tyrosination (Barisic and Maiato, 2016; Barisic et al., 2015), we took advantage of an engineered animal available in the lab, whose C-terminal tyrosine of tba-1 and tba-2 is mutated to an alanine (YA/YA), thus preventing α-tubulin tyrosination (Barbosa et al., 2017). Although worms with undetectable levels of tyrosinated tubulin and expressing hCENP-E did not show problems during division (data not shown), congression defects derived from Klp-19 depletion were more penetrant (increased chromosome span) (Figure 2.3.4 A).

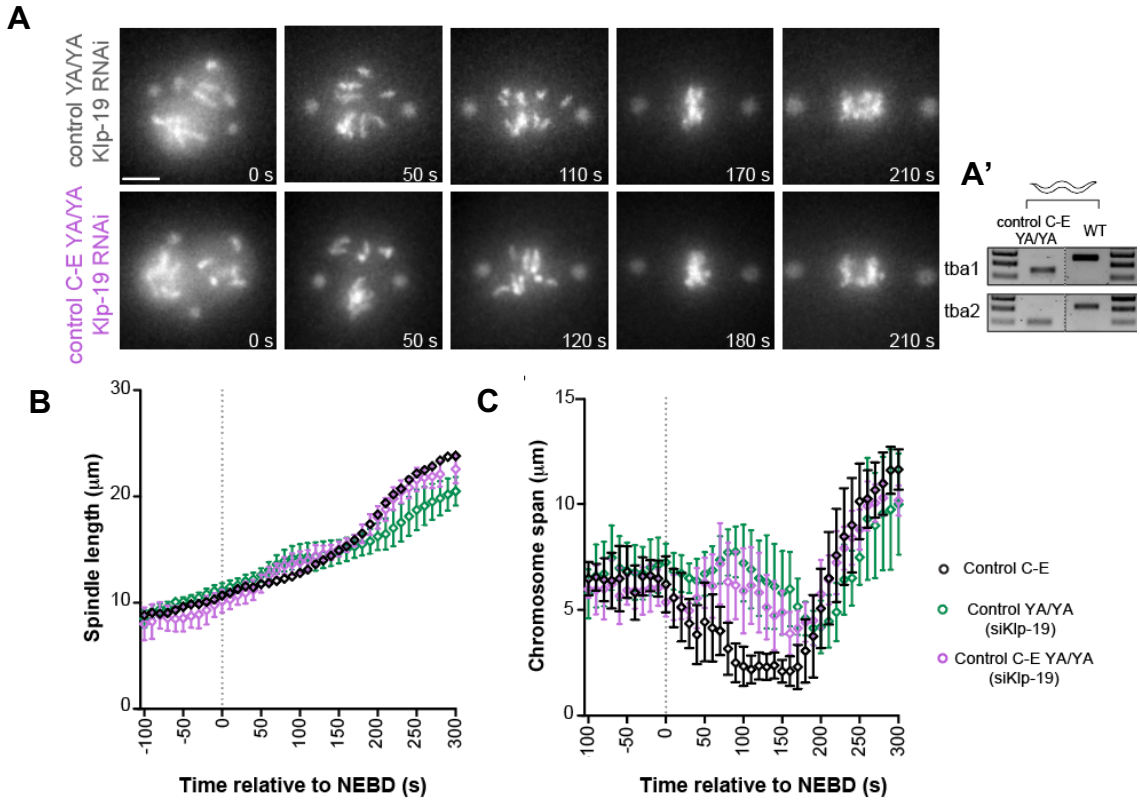

(*figure legend on the next page)*

Figure 2.3.4. Expression of hCENP-E in YA/YA worms does not recue congression defects associated with the loss of polar ejection forces.

A, Time-lapse sequences of one-cell embryos expressing GFP::H2B to visualize chromosomes, and GFP::γ-tubulin to label spindle poles, depleted of chromokinesin Klp-19 on embryos with the C-terminal tyrosine mutated to an alanine (YA/YA). **B,** agarose gel showing the different amplification of tba-1 and tba-2 mutated worms (YA/YA) vs wild-type (WT) worm stain. Plots of spindle pole separation (**C**) and chromosome span profile (**D**) in one-cell embryos showing that depleting klp-19 in C-E YA/YA mutant does not rescue the chromosome scattering phenotype in the same extent. Note that the phenotype after Klp-19 depletion in control YA/YA worms is also more severe. Distances were measured in images acquired every 10 s, averaged for the total number of embryos, and plotted against time. Error bars represent the 95 % C.I. Grey dashed line represents NEBD. Scale bar: 5µm.

Surprisingly, these problems were not significantly rescued by CENP-E expression, suggesting that a certain level of tyrosinated tubulin might be necessary to prioritize CENP-E activity. Another plausible explanation would be that the mutation of α-tubulin last tyrosine residue to an alanine indirectly affected the overall levels of tubulin detyrosination. To test this hypothesis, we processed control and mutated worms (YA/YA) for immunofluorescence and labelled them for detyrosinated-α-tubulin and DAPI, to stain detyrosinated microtubules and chromosomes, respectively. Based on a qualitative analysis of different cell-stage embryos, detyrosinated α-tubulin, which is mostly confined to the spindle poles in control embryos (Figure 2.3.5.), is more dispersed in the mutated strain, arguing that the less-efficient rescue of congression defects may be a result of a lower fraction of detyrosinated-microtubules, and consequently, a reduced CENP-E motion.

The fact that there is no change on the overall levels of detyrosinated tubulin in the embryos after YA/YA mutation, comprehends that this set of experiments is not adequate to tackle the (2) goal. Instead, we will address this question by using a CRISPR/Cas9 KO worm for tba-1 and tba-2 C-terminal tyrosine residue.

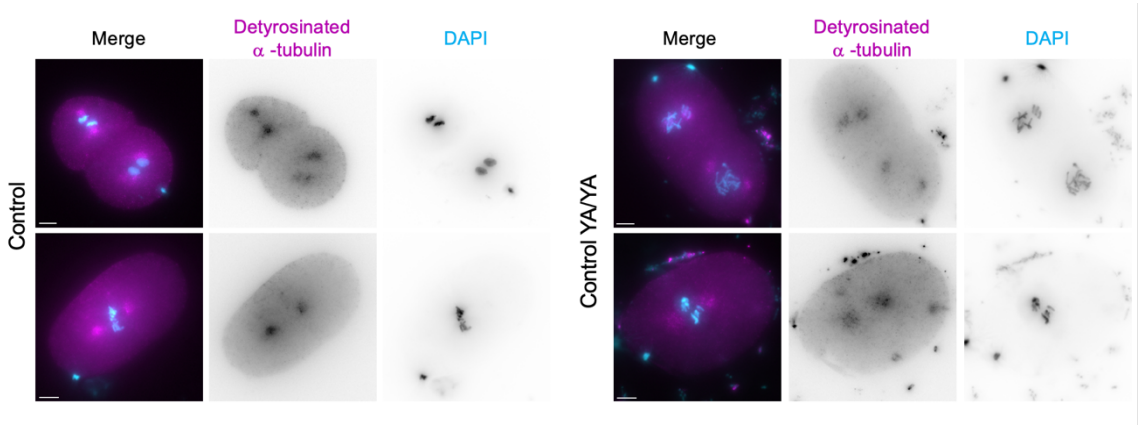

Figure 2.3.5. Detyrosinated microtubules are mostly localized at the spindle poles of C. elegans one-cell embryos.

Representative immunofluorescence images of control and mutated (YA/YA) embryos, labelled for detyrosinated-tubulin (magenta) and DAPI (cyan). Scale bars, 5 µm.

2.3.5. Materials and Methods

2.3.5.1. Codon bias optimization

In order to increase the probability of human gene expression in *C.elegans* we performed a codon bias optimization of CENP-E sequence (isolated from 883-CENP-E 620 plasmid, a gift from Michael Lampson (Zhang et al., 2017)) using the GenScript OptimumGene™ service. Accordantly, the codon adaptation index (CAI) and the frequency of optimal codons (FOP) were calculated to enhance gene expression in this organism (see above the tables provided by GenScript).

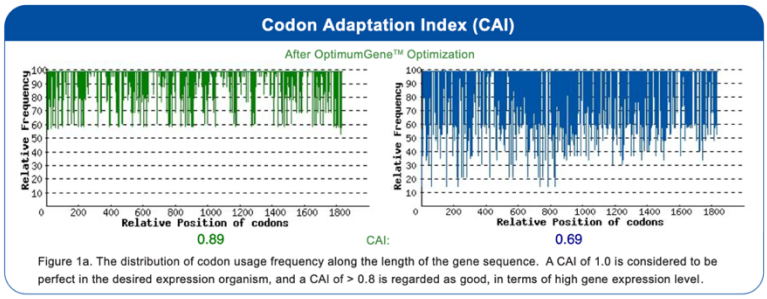

Figure 1a. The distribution of codon usage frequency along the length of the gene sequence. A CAI of 1.0 is considered to be perfect in the desired expression organism, and a CAI of > 0.8 is regarded as good, in terms of high gene expression level.

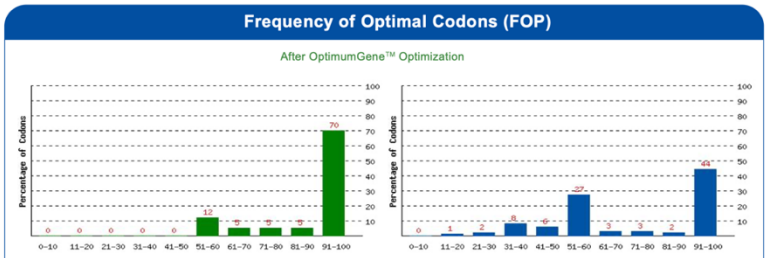

Figure 1b. The percentage distribution of codons in computed codon quality groups. The value of 100 is set for the codon with the highest usage frequency for a given amino acid in the desired expression organism.

The optimized CENP-E sequence used for this study was the following (optimized sequence length:1906, GC %: 36.70):

GGAGCCGTCGCCGTCTGCGTTCGTGTCCGTCCATTGAATAGTCGTGAAGAAAGTCT
GGGAGAAACAGCACAAGTCTACTGGAAAACAGATAACAACGTTATCTACCAAGTT
GATGGATCTAAATCATTCAACTTCGATAGAGTTTTCCATGGAAACGAAACAACTAA
GAACGTTTACGAAGAAATTGCTGCACCAATCATCGATTCTGCTATCCAAGGATACA
ACGGAACTATCTTTGCTTACGGACAAACAGCATCTGGAAAAACATATACTATGATG
GGATCAGAAGATCATTTGGGAGTTATTCCACGAGCAATCCATGATATTTTCCAAAA
GATTAAGAAATTCCCAGATAGAGAATTCCTTTTGCGAGTTTCATACATGGAAATCT
ACAACGAAACAATTACTGATCTTTTGTGTGGAACACAAAAGATGAAGCCACTTATC
ATCAGAGAAGATGTTAACCGAAACGTTTACGTTGCTGATTTGACTGAAGAAGTTGT
TTACACATCTGAAATGGCACTTAAGTGGATCACTAAGGGAGAAAAGTCAAGACATT
ACGGAGAAACAAAGATGAACCAAAGATCATCTCGATCTCATACTATCTTCAGAATG
ATCTTGGAATCTCGAGAAAAAGGAGAACCATCAAATTGTGAAGGATCTGTTAAAGT
TTCACATCTTAACTTGGTTGATTTGGCTGGATCAGAACGAGCTGCACAAACTGGAG
CTGCAGGAGTTAGACTTAAGGAAGGATGCAACATCAACCGATCTCTTTTCATCTTG
GGACAAGTTATTAAGAAACTTTCAGATGGACAAGTTGGAGGATTCATCAACTACAG
AGATTCTAAGCTTACACGAATCTTGCAAAACTCACTTGGAGGAAACGCTAAGACTA

GAATCATCTGCACAATCACTCCAGTTTCTTTCGATGAAACACTTACTGCATTGCAAT
TCGCTTCAACTGCAAAGTACATGAAGAACACACCATACGTTAACGAAGTTTCTACA
GATGAAGCTCTTTTGAAAAGATACCGAAAGGAAATCATGGATTTGAAAAAACAACT
TGAAGAAGTTTCATTGGAAACTAGAGCTCAAGCAATGGAAAAAGATCAACTTGCAC
AACTTTTGGAAGAAAAGGATCTTTTGCAAAAGGTTCAAAACGAAAAGATCGAAAA
CTTGACAAGAATGCTTGTTACTTCATCTTCACTTACATTGCAACAAGAATTGAAAGC
TAAACGAAAAAGACGAGTTACATGGTGTCTTGGAAAGATCAACAAGATGAAGAAC
TCAAACTATGCAGATCAATTCAATATTCCAACTAATATTACAACTAAAACACATAA
ATTGTCTATTAATCTTTTGAGAGAAATTGATGAATCAGTTTGCTCTGAATCAGATGT
TTTCTCAAACACACTTGATACTTTGTCAGAAATCGAATGGAATCCAGCTACTAAGCT
TTTGAACCAAGAAAACATCGAATCTGAACTTAACTCATTGAGAGCAGATTACGATA
ACCTTGTTTTGGATTACGAACAATTGCGAACAGAAAAGGAAGAAATGGAACTTAAG
TTGAAGGAAAAGAATGATTTGGATGAATTCGAAGCTCTTGAAAGAAAGACTAAAA
AAGATCAAGAAATGCAACTTATCCATGAAATTTCAAACCTTAAGAACTTGGTTAAG
CATGCAGAAGTTTACAACCAAGATTTGGAAAACGAACTTTCTTCAAAGGTTGAACT
TTTGCGAGAAAAGGAAGATCAAATTAAGAAACTTCAAGAATACATCGATAGTCAA
AAACTGGAGAACATCAAAATGGATCTGTCCTACTCGCTGGAA

The sequence was cloned into a standard cloning pUC57 flanked by two EcoRV (GATATC) cutting sites.

2.3.5.2. Molecular Cloning

Pmex5_mKate2_KBP-3 and Pmex5_mKate2_CENP-E_KBP-3 plasmids were generated in this study from genomic DNA isolated from C. elegans, pRG777 (kind gift of Reto Gassman) and pUC57-CENP-E (codon optimized). Gibson assembly was used to assemble the two or three DNA fragments, respectively (Gibson, 2009). The primers used for Polymerase Chain Reaction (PCR) amplification and Gibson assembly are described below:

Table 5. Primers used to assemble the plasmids generated in this study.

Template	Primer FW	Primer Rv	Product size (bp)
Plasmid pRG777-hCENP-E (backbone)	AACATCTTGGTCTAAatgcaagatcctttcaagcattcccttcttctctatcac	CGCCCCCTCTTCCGCCATgcttccaccagatccACGGTG	9138
Plasmid pUC57-CENP-E			1894
Genomic DNA from C. elegans	AAGACCCGGGATCTGGTGGAAGCATGGAGTCACTCAACGAGTATATGGACAAGATTATTAATCGTC	gaaaggatcttgcatTTAGACCAAGATGTTGGAGAGGTTCGATctgaaaaaaatacac	806

pRG777-kbp-3 (backbone)	AACATCTTGGTCTAAatg caagatcctttcaagcattcccttcttctc tatcac	GTTGAGTGACTCCATgct tccaccagatccACGGTG	9135
Genomic DNA from C. elegans (mKate2-kbp-3)	ggatctggtggaagcATGGAGT CACTCAACGAGTATATG GACAAGATTATTAATCG TC	gaaaggatcttgcatTTAGACC AAGATGTTGGAGAGGT TCGATctgaaaaaaatacac	798

After isolating the DNA fragments amplified by PCR using Phusion polymerase, they were confirmed by electrophoresis on a 1% agarose gel. Green Safe (NZYtech) was added to the gel before electrophoresis to a final dilution of 1:34.000, followed by separation at 100 V for ~40 minutes. The gel was exposed to UV light and the image acquired with GelDoc system (Bio-Rad). Subsequently, Gisbon Assembly Master Mix (Gibson, 2009) was added to the DNA fragments and incubated at 50ºC for 1 hour. After transforming Top10 competent bacteria with 4-6 uL of the Gibson assembly reaction products, the bacteria were plated in Luria-Bertani (LB) agar plates with Ampicillin (ForMedium AMP25). The following day, colonies were picked to perform a colony PCR. A premixed ready-to-use solution containing DNA polymerase, Green Master Mix (NZYtech), and the specific primers were added to the bacteria. After the initial denaturation at 95ºC for 7 min, the annealing temperature was set to 64ºC. The reaction products were loaded on a 1% agarose gel. The positive colonies were selected, and the DNA extracted using NZYMiniprep kit (NZYtech). After determined the plasmid concentration using a NanoDrop spectrophotometer, a test digestion was performed. The enzymes were selected using *SnapGene* software.

Table 6. Enzymes used to test digest the plasmids used in this study.

Plasmid	Enzymes	Buffer	Expected bands (bp)
Pmex5_mKate2_CENP-E_KBP-3	MluI (NEB) ApaI (NEB)	CutSmart (NEB)	2356 5465 + 3927
Pmex5_mKate2_KBP-3	XmaI (NEB)	CutSmart (NEB)	6933 2940

The Sanger sequencing reaction was performed by GeneCore (i3S) according to manufacturer's instructions with the following components: BigDye ® Terminator v3.1 Cycle Sequencing Kit (Applied Biosystems); BigDye® Terminator v1.1, v3.1 5x Sequencing Buffer (Applied

Biosystems); Primer (10µM); Nuclease-free water (Ambion); Plasmid (~100ng). The results were then analysed in *SnapGene*.

2.3.5.3. Worm Strains

A Mos1 transposon-based strategy (MosSCI) was used to generate a strain stably expressing mKate2::KBP-3 and mKate2::CENP-E_KBP3 under the control of the mex-5 promotor and and tbb-2 3′ UTR for expression in germline cells (Frokjaer-Jensen et al., 2012; Frokjaer-Jensen et al., 2008). Other fluorescent markers were subsequently introduced by mating. GCP and GCP strains created in this study were maintained at 20°C on standard nematode growth medium (NGM) plates seeded with OP50 bacteria.

2.3.5.4. RNA interference

dsRNAs for Klp-19 were delivered by injecting L4 hermaphrodites. After injection, animals were incubated as follows before embryos were isolated for live-cell imaging: 48 h at 20°C for a penetrant depletion.

Table 7. Oligos used for double-stranded RNA production.

Gene ID	Gene Name	Oligonucleotide 1 (T3 promoter)	Oligonucleotide 2 (T7 promoter)	Template
Y43F4B.6	Klp-19	aattaaccctcactaaaggTGAC CCAGAAGAACTCTCGC	taatacgactcactataggTCGGA GATCTTCACACAGCC	gDNA

2.3.5.5. Immunofluorescence

For immunofluorescence of *C. elegans* embryos, 10–12 adult worms were dissected into 3 µL of M9 buffer (86 mM NaCl, 42 mM Na_2HPO_4, 22 mM KH_2PO_4, 1 mM $MgSO_4$) on a poly-*L*-lysine-coated slide. A 18x24 mm coverslip was placed on the 3 µl drop, and slides were plunged into liquid nitrogen. After rapid removal of the coverslip (‘freeze-cracking’), embryos were fixed in −20°C methanol for 20 minutes. Embryos were re-hydrated for 2 x 5 minutes in PBS (137 mM NaCl, 2.7 mM KCl, 8.1 mM Na_2HPO_4, and 1.47 mM KH_2PO_4), blocked with AbDil (PBS with 2% BSA, 0.1% Triton X-100) in a humid chamber at room temperature for 30 min, and incubated with primary antibodies [mouse monoclonal anti-α-tubulin B-5-1-2 (1:1000) and rabbit monoclonal anti-detyrosinated α-tubulin (1:1000)] for 2 hours at room temperature. After washing for 4 x 5 minutes in PBS, embryos were incubated with secondary antibodies conjugated with fluorescent dyes [Alexa Fluor 568 goat anti-mouse IgG (1:1000) and Alexa Fluor 488 goat anti-rabbit IgG (1:1000); Life Technologies—Molecular Probes] for 1h at room temperature. Embryos were washed for 4 x 5 minutes in PBS and mounted in Prolong Gold with DAPI stain (Invitrogen).

Images were recorded on an AxioImager Z1 (100× Plan-Apochromatic oil differential interference contrast objective lens, 1.46 NA, Carl Zeiss Microimaging Inc.) equipped with a CCD camera (ORCA-R2, Hamamatsu) operated by Zen software (Carl Zeiss, Inc.). Image files were imported into Fiji for further processing.

2.3.5.6. Live-cell imaging of embryos

Adult gravid hermaphrodite worms were dissected in a watch glass filled with Egg Salts medium (118 mM KCl, 3.4 mM $MgCl_2$, 3.4 mM $CaCl_2$ and 5 mM HEPES pH 7.4), and embryos were mounted on a fresh 2% agarose pad and covered with an 18 mm×18 mm coverslip (No. 1.5H, Marienfeld). Embryos co-expressing GFP::histone-H2B, GFP::γ-tubulin and mKate2::KBP3/CENP-E_KBP3 for tracking of nuclei, centrosomes and kinetochores were imaged on Axio Observer microscope (Zeiss) equipped with an Orca Flash 4.0 camera (Hamamatsu), a Colibri.2 light source, and controlled by ZEN software (Zeiss). All other imaging was performed on a Nikon Eclipse Ti microscope coupled to an Andor Revolution XD spinning disk confocal system composed of an iXon Ultra 897 CCD camera (Andor Technology), a solid-state laser combiner (ALC-UVP 350i, Andor Technology), and a CSU-X1 confocal scanner (Yokogawa Electric Corporation), controlled by Andor IQ3 software (Andor Technology). All imaging was performed in temperature-controlled rooms kept at 20°C. Time-lapse sequences were processed and analyzed with Fiji software (Image J version 2.0.0-rc-56/1.51 h).

2.3.5.7. Pole to Pole Distance and Chromosome Span Measurements

Embryos expressing GFP::histone-H2B, GFP::γ-tubulin and mKate2::KBP3/CENP-E_KBP3 were imaged at 10 s intervals, with 9 z-slices spaced 1.5 μm apart for the fluorescence channel, and a single central slice per time point for the DIC channel, at 2x2 binning with a 63x NA 1.4 oil immersion objective (Zeiss) from just prior to NEBD in the one-cell embryo until the onset of cytokinesis. Embryo length was defined as the distance between the outermost points of the eggshell visible in the DIC image. After maximum intensity projection of GFP z-stacks, the x and y coordinates of the centrosomes and of the chromosomes closer to each centrosome were recorded over time using the MtrackJ plugin by manually clicking in the center of centrosomes and on the outer edge of the chromosomes.

2.3.5.8. Statistical Analysis

Statistical analysis was performed with GraphPad Prism 8.1.2 software. The type of statistical analysis (t-test or oneway ANOVA/Bonferroni's multiple comparison test) is indicated in the figure legends. Differences were considered significant at $p \leq 0.05$.

CHAPTER 3.

CONCLUDING REMARKS

CHAPTER 3. CONCLUDING REMARKS

During cell division in eukaryotes, a microtubule-based network undergoes drastic changes and remodeling to assemble a mitotic spindle competent to segregate chromosomes. Several model systems have been widely used to dissect the molecular and structural mechanisms behind mitotic spindle assembly and function. These include budding and fission yeasts, which are ideal for genetic and molecular approaches, but show limitations in high-resolution live-cell imaging, while being evolutionarily distant from humans. On the other hand, systems that were historically used for their exceptional properties for live-cell imaging of mitosis (e.g., newt lung cells and Haemanthus endosperm cells) lack the necessary genomic tools for molecular studies. In a CRISPR/Cas9 era, human cultured cells have conquered the privilege to be positioned among the most powerful genetically manipulatable systems, but their high chromosome number and the sub-diffraction size of human cellular structures can represent a significant bottleneck for the molecular dissection of mitosis in mammals. We believe that we significantly broaden this scenario by establishing a unique placental mammal model system that combines the powerful genetic tools and low chromosome number of fission yeast and *Drosophila melanogaster*, with the exceptional cytological features of a rat kangaroo cell. This system is based on hTERT-immortalized fibroblasts from a female Indian muntjac, a mammal with only six chromosomes. The present thesis comprehends a series of methodologies established in our laboratory for the study of mitosis in Indian muntjac cells. These include standard techniques such as immunofluorescence, western blotting, but also several state-of-the-art methodologies, including super-resolution STED microscopy (fixed- and live-cell imaging), laser microsurgery and photoactivation (Almeida et al., 2020). By combining Indian muntjac fibroblasts (Zou et al., 2002) and a draft genome sequence, we obtained proof-of-principle that the Indian muntjac is a valuable system to study different molecular and physiological aspects of mitosis. We show that Indian muntjac cells are amenable for both pharmacological inhibition and genetic manipulation by RNAi. Most live-cell screenings lack the specific knock-down conditions for every protein of interest, and the spatial-temporal resolution of the imaging is not adequate for short processes within the cell cycle, such as mitosis. We overcame this caveat by providing optimized conditions for the depletion of more than 60 mitotic genes, imaged with high temporal resolution. The results indicated a large conservation degree between Indian muntjac and other mammals, including humans, thus validating Indian muntjac as a powerful model system. Depletion of Eg5 or the Augmin complex subunit HAUS6 exhibited the most dramatic changes in mitosis of Indian muntjac fibroblasts. We then focused on the in-depth characterization of Augmin functions. By assessing γ-tubulin localization, spindle length, HURP fluorescence intensity and localization, and overall tubulin levels after a cold-treatment, in control and HAUS6-depleted cells, we

validated Augmin's conserved roles in the muntjac system. Next, we provided experimental data that demonstrates that Augmin is required for both interpolar and kinetochore microtubule formation. The former was further validated by the direct demonstration that Augmin is required to sustain centrosome-independent microtubule growth from kinetochores, while promoting microtubule turnover and assisting poleward flux in metaphase cells. Live-cell CH-STED microscopy and laser microsurgery offered definitive proof that Augmin plays a key role in kinetochore microtubule self-organization and maturation. The fact that we observed microtubule growth events with a wide angular dispersion relative to the k-fiber axis is somewhat reminiscent of the first drawings of 'fir-tree'/'tree-like' microtubule patterns observed in Haemanthus endosperm, onion roots spindles, and green plants (Bajer and Mole-Bajer, 1986; Palevitz, 1988; Wasteneys and Williamson, 1989). Likewise, Augmin-mediated branched microtubule nucleation is well documented in Drosophila S2 cells and by *in vitro* reconstitution of microtubule nucleation (Tariq et al., 2020; Verma and Maresca, 2019). These observations pose the question of what are the physiological advantages of having branched-microtubule nucleation within single k-fibers? Does that provide wider range for microtubule 'exploration'? Or otherwise, can this contribute to a more rapid microtubule amplification cascade, where daughter microtubules can work as new platforms for further microtubule amplification? Importantly, these hypotheses are not incompatible with the potential role of motor proteins and microtubules cross-linkers that can drive the incorporation of recent-nucleated microtubules in a k-fiber bundle.

We propose a model where Augmin is required to amplify microtubules from pre-existing kinetochore microtubules, regardless of pioneer centrosomal microtubules (Almeida et al., 2022). This is consistent with the observation that functional spindles are assembled in several animal species, including humans, after perturbation of centrosomes function (Basto et al., 2006; Chinen et al., 2020; Debec A., 1982; Khodjakov et al., 2000; Mahoney et al., 2006; Megraw et al., 2001; Moutinho-Pereira et al., 2013; Sir et al., 2013). Augmin-dependent microtubule nucleation is compatible with the 'thickening' of short kinetochore microtubule stubs, that might facilitate the interaction of pre-formed k-fibers with astral microtubules (Elting et al., 2014; Khodjakov et al., 2003; Maiato et al., 2004b; Sikirzhytski et al., 2014) or with an interpolar spindle scaffold (Kajtez et al., 2016; Nunes et al., 2020; Renda et al., 2022), thus promoting chromosome bi-orientation.

Overall, this work provides live-cell evidence of a Augmin-dependent model for k-fiber formation and maturation, that had not been fully built upon experimental data before. Nonetheless, there are outstanding questions in the field: when does Augmin-dependent pathway becomes activated during spindle assembly in animal cells? Does Augmin bind directly to microtubules or via other proteins? Where does the Augmin complex bind: to specific predefined sites or randomly along the microtubule lattice? Do tubulin PTMs regulate Augmin-microtubule binding and affinity? These questions will require further investigation in the future.

Interestingly, in non-mitotic cells, Augmin and γ-TuRC were also shown to be crucial for microtubule organization, specifically for the generation of highly bundled neuronal microtubule networks and to ensure a uniform microtubule polarity in axons (Sanchez-Huertas et al., 2016; Sanchez-Huertas and Luders, 2015). Moreover, recent findings showed that disruption of Augmin in neural stem cells induces a p53-dependent apoptosis and aborts brain development, suggesting that Augmin-mediated microtubule nucleation is essential for neuronal development (Viais et al., 2021). In a different cellular context, Augmin subunit HAUS3 was identified as a potential prognostic marker for hepatocellular carcinoma (HCC). High levels of HAUS3 in HCC tissues significantly correlated with poor prognosis of patients (larger tumor size and greater number of cancer lesions) (Zhang et al., 2019). These works underscore the importance of bridging fundamental research with pre-clinical research, thus broadening the current knowledge underlying human diseases.

The morphological differences between Indian muntjac chromosomes and kinetochores allowed us to track individual chromosomes throughout mitosis. Measurement of intra-kinetochore distances, serial-section EM, and RNAi against key kinetochore proteins confirmed a standard structural and functional organization of the Indian muntjac kinetochores and revealed that microtubule binding capacity scales with kinetochore size. Besides, we found that chromosome segregation in mammals is biased by kinetochore size (Drpic et al., 2018). Remarkably, our findings were later supported by evidence in human cells. The authors demonstrated that inherent properties of individual chromosomes and centromeres, including kinetochore size, can bias chromosome missegregation and consequently aneuploidy rates (Dumont et al., 2020; Worrall et al., 2018).

Interestingly, a parallel between cancer evolution and speciation/evolutionary theory has been suggested (MacDonald and McClelland, 2021). Although chromosome aneuploidy is rarely observed in speciation, chromosome breakage during cytokinesis can lead to genomic rearrangements and contribute to karyotypic evolution indirectly. Understanding the underlying drivers of CIN in cancer, including the bias in chromosome (mis)segregation and loss, can represent an important piece to perceive evolutionary karyotype changes, and vice-versa. Some species may be more or less vulnerable to develop cancer-linked karyotypic changes, which can be dependent on their chromosomal and centromere structure. Recent analysis identified centromere-related genes (CENP-Q and CENP-V) associated with rapid evolutionary rearrangements in the Indian muntjac genome (Mudd et al., 2020). However, the driver of the increased rate of chromosome fusions in the genus *Muntiacus* is still unclear. Extending similar analyses to major karyotypic events during speciation may provide insights into the genetic factors that give rise to and maintain karyotype rearrangements (MacDonald and McClelland, 2021). From a different perspective, others believe that chromosome fusions on the muntjac

lineage differs from those that have been described in cancer. Observation that these events did not occur in a single catastrophic event (Huang et al., 2006a; Huang et al., 2006b) and occurred without disrupting gene order, is largely distinct from the extensive rearrangements found in cancer due to chromothripsis (Stephens et al., 2011).

Our work also unveiled that chromosome congression to spindle equator is biased by kinetochore size. Chromosomes with large kinetochores relied less on CENP-E motor activity to congress to the spindle equator. This data, together with the observation that ~65% of species with large holocentric kinetochores lack a kinesin-7 orthologue (unpublished data), raised the need to dissect if CENP-E-dependent chromosome motion confers any evolutionary advantage. During unperturbed mitosis, nematodes *C. elegans* efficiently congress all chromosomes in a matter of seconds due to rapid chromosome 'direct congression'. However, when kinetochore microtubule attachments are challenged, embryos take longer to orient their chromosomes and show high rates of lagging chromosomes in anaphase (Powers et al., 2004). We showed that this phenotype can be partially rescued when human CENP-E is ectopically expressed. This underlines the physiological relevance of having a kinetochore motor to assist chromosome congression when kinetochore microtubule end-on attachments are compromised. As a future perspective we aim to directly test the prevailing model that suggests that CENP-E-dependent chromosome motion towards the cell equator is enhanced by microtubule detyrosination *in vivo.*

LIST OF REFERENCES

LIST OF REFERENCES

Afonso, O., I. Matos, A.J. Pereira, P. Aguiar, M.A. Lampson, and H. Maiato. 2014. Feedback control of chromosome separation by a midzone Aurora B gradient. *Science*. 345:332-336.

Aillaud, C., C. Bosc, L. Peris, A. Bosson, P. Heemeryck, J. Van Dijk, J. Le Friec, B. Boulan, F. Vossier, L.E. Sanman, S. Syed, N. Amara, Y. Coute, L. Lafanechere, E. Denarier, C. Delphin, L. Pelletier, S. Humbert, M. Bogyo, A. Andrieux, K. Rogowski, and M.J. Moutin. 2017. Vasohibins/SVBP are tubulin carboxypeptidases (TCPs) that regulate neuron differentiation. *Science (New York, N.Y.*. 358:1448-1453.

Akhmanova, A., C.C. Hoogenraad, K. Drabek, T. Stepanova, B. Dortland, T. Verkerk, W. Vermeulen, B.M. Burgering, C.I. De Zeeuw, F. Grosveld, and N. Galjart. 2001. Clasps are CLIP-115 and -170 associating proteins involved in the regional regulation of microtubule dynamics in motile fibroblasts. *Cell*. 104:923-935.

Al-Bassam, J., and F. Chang. 2011. Regulation of microtubule dynamics by TOG-domain proteins XMAP215/Dis1 and CLASP. *Trends in cell biology*. 21:604-614.

Al-Bassam, J., H. Kim, G. Brouhard, A. van Oijen, S.C. Harrison, and F. Chang. 2010. CLASP promotes microtubule rescue by recruiting tubulin dimers to the microtubule. *Dev Cell*. 19:245-258.

Alberts, B., A. Johnson, J. Lewis, D. Morgan, M. Raff, K. Roberts, P. Walter, J. Wilson, and T. Hunt. 2017. Molecular biology of the cell. WW Norton & Company.

Alfaro-Aco, R., A. Thawani, and S. Petry. 2020. Biochemical reconstitution of branching microtubule nucleation. *Elife*. 9.

Alfieri, C., L. Chang, Z. Zhang, J. Yang, S. Maslen, M. Skehel, and D. Barford. 2016. Molecular basis of APC/C regulation by the spindle assembly checkpoint. *Nature*. 536:431-436.

Allan, V.J. 2011. Cytoplasmic dynein. *Biochem Soc Trans*. 39:1169-1178.

Almeida, A.C., D. Drpic, N. Okada, J. Bravo, M. Madureira, and H. Maiato. 2020. Functional Dissection of Mitosis Using Immortalized Fibroblasts from the Indian Muntjac, a Placental Mammal with Only Three Chromosomes. *Methods Mol Biol*. 2101:247-266.

Almeida, A.C., and H. Maiato. 2018. Chromokinesins. *Curr Biol*. 28:R1131-R1135.

Almeida, A.C., J. Soares-de-Oliveira, D. Drpic, L.P. Cheeseman, J. Damas, H.A. Lewin, D.M. Larkin, P. Aguiar, A.J. Pereira, and H. Maiato. 2022. Augmin-dependent microtubule self-organization drives kinetochore fiber maturation in mammals. *Cell Reports*. 39.

Alvarez-Fernandez, M., and M. Malumbres. 2014. Preparing a cell for nuclear envelope breakdown: Spatio-temporal control of phosphorylation during mitotic entry. *Bioessays*. 36:757-765.

Antonio, C., I. Ferby, H. Wilhelm, M. Jones, E. Karsenti, A.R. Nebreda, and I. Vernos. 2000. Xkid, a chromokinesin required for chromosome alignment on the metaphase plate. *Cell*. 102:425-435.

Arnal, I., C. Heichette, G.S. Diamantopoulos, and D. Chretien. 2004. CLIP-170/tubulin-curved oligomers coassemble at microtubule ends and promote rescues. *Curr Biol*. 14:2086-2095.

Auckland, P., and A.D. McAinsh. 2015. Building an integrated model of chromosome congression. *J Cell Sci*. 128:3363-3374.

Bajer, A. 1957. Cine-micrographic studies on mitosis in endosperm. III. The origin of the mitotic spindle. *Exp Cell Res*. 13:493-502.

Bajer, A.S., and J. Mole-Bajer. 1986. Reorganization of microtubules in endosperm cells and cell fragments of the higher plant Haemanthus in vivo. *J Cell Biol*. 102:263-281.

Bakhoum, S.F., and D.A. Compton. 2012. Kinetochores and disease: keeping microtubule dynamics in check! *Curr Opin Cell Biol*. 24:64-70.

Bakhoum, S.F., G. Genovese, and D.A. Compton. 2009a. Deviant kinetochore microtubule dynamics underlie chromosomal instability. *Curr Biol*. 19:1937-1942.

Bakhoum, S.F., S.L. Thompson, A.L. Manning, and D.A. Compton. 2009b. Genome stability is ensured by temporal control of kinetochore-microtubule dynamics. *Nat Cell Biol*. 11:27-35.

Barbosa, D.J., J. Duro, B. Prevo, D.K. Cheerambathur, A.X. Carvalho, and R. Gassmann. 2017. Dynactin binding to tyrosinated microtubules promotes centrosome centration in C. elegans by enhancing dynein-mediated organelle transport. *PLoS Genet*. 13:e1006941.

Barisic, M., P. Aguiar, S. Geley, and H. Maiato. 2014. Kinetochore motors drive congression of peripheral polar chromosomes by overcoming random arm-ejection forces. *Nat Cell Biol*. 16:1249-1256.

Barisic, M., and S. Geley. 2011. Spindly switch controls anaphase: spindly and RZZ functions in chromosome attachment and mitotic checkpoint control. *Cell Cycle*. 10:449-456.

Barisic, M., and H. Maiato. 2016. The Tubulin Code: A Navigation System for Chromosomes during Mitosis. *Trends Cell Biol*. 26:766-775.

Barisic, M., A.J. Pereira, and H. Maiato. 2012. Fluorescent speckle microscopy in cultured cells. *Methods Enzymol*. 504:147-161.

Barisic, M., and G. Rajendraprasad. 2021. Mitotic poleward flux: Finding balance between microtubule dynamics and sliding. *Bioessays*. 43:e2100079.

Barisic, M., G. Rajendraprasad, and Y. Steblyanko. 2021a. The metaphase spindle at steady state - Mechanism and functions of microtubule poleward flux. *Semin Cell Dev Biol*. 117:99-117.

Barisic, M., G. Rajendraprasad, and Y. Steblyanko. 2021b. The metaphase spindle at steady state - Mechanism and functions of microtubule poleward flux. *Semin Cell Dev Biol*.

Barisic, M., R. Silva e Sousa, S.K. Tripathy, M.M. Magiera, A.V. Zaytsev, A.L. Pereira, C. Janke, E.L. Grishchuk, and H. Maiato. 2015. Mitosis. Microtubule detyrosination guides chromosomes during mitosis. *Science*. 348:799-803.

Barisic, M., B. Sohm, P. Mikolcevic, C. Wandke, V. Rauch, T. Ringer, M. Hess, G. Bonn, and S. Geley. 2010. Spindly/CCDC99 is required for efficient chromosome congression and mitotic checkpoint regulation. *Molecular biology of the cell*. 21:1968-1981.

Barnum, K.J., and M.J. O'Connell. 2014. Cell cycle regulation by checkpoints. *Methods Mol Biol*. 1170:29-40.

Barr, A.R., and F. Gergely. 2008. MCAK-independent functions of ch-Tog/XMAP215 in microtubule plus-end dynamics. *Mol Cell Biol*. 28:7199-7211.

Barroso-Vilares, M., J.C. Macedo, M. Reis, J.D. Warren, D. Compton, and E. Logarinho. 2020. Small-molecule inhibition of aging-associated chromosomal instability delays cellular senescence. *EMBO Rep*. 21:e49248.

Basto, R., J. Lau, T. Vinogradova, A. Gardiol, C.G. Woods, A. Khodjakov, and J.W. Raff. 2006. Flies without centrioles. *Cell*. 125:1375-1386.

Bazzi, H., and K.V. Anderson. 2014. Acentriolar mitosis activates a p53-dependent apoptosis pathway in the mouse embryo. *Proc Natl Acad Sci U S A*. 111:E1491-1500.

Begley, M.A., A.L. Solon, E.M. Davis, M.G. Sherrill, R. Ohi, and M.W. Elting. 2021. K-fiber bundles in the mitotic spindle are mechanically reinforced by Kif15. *Mol Biol Cell*:mbcE20060426.

Ben-David, U., and A. Amon. 2020. Context is everything: aneuploidy in cancer. *Nat Rev Genet*. 21:44-62.

Beneden, P.J. 1876. Animal parasites and messmates. Henry S. King.

Bettencourt-Dias, M., and D.M. Glover. 2007. Centrosome biogenesis and function: centrosomics brings new understanding. *Nat Rev Mol Cell Biol*. 8:451-463.

Bielek, E. 1978. [Ultrastructure of kinetochores]. *Verh Anat Ges*:193-198.

Biggins, S., and A.W. Murray. 2001. The budding yeast protein kinase Ipl1/Aurora allows the absence of tension to activate the spindle checkpoint. *Genes Dev*. 15:3118-3129.

Bird , A.W., and A.A. Hyman 2008. Building a spindle of the correct length in human cells requires the interaction between TPX2 and Aurora A. *Journal of Cell Biology*. 182:289-300.

Bird, A.W., and A.A. Hyman. 2008. Building a spindle of the correct length in human cells requires the interaction between TPX2 and Aurora A. *J Cell Biol*. 182:289-300.

Bodakuntla, S., A.S. Jijumon, C. Villablanca, C. Gonzalez-Billault, and C. Janke. 2019. Microtubule-Associated Proteins: Structuring the Cytoskeleton. *Trends Cell Biol*. 29:804-819.

Bodor, D.L., J.F. Mata, M. Sergeev, A.F. David, K.J. Salimian, T. Panchenko, D.W. Cleveland, B.E. Black, J.V. Shah, and L.E. Jansen. 2014. The quantitative architecture of centromeric chromatin. *Elife*. 3:e02137.

Bogenberger, J.M., H. Neitzel, and F. Fittler. 1987. A highly repetitive DNA component common to all Cervidae: its organization and chromosomal distribution during evolution. *Chromosoma*. 95:154-161.

Bonaccorsi, S., M.G. Giansanti, and M. Gatti. 1998. Spindle self-organization and cytokinesis during male meiosis in asterless mutants of Drosophila melanogaster. *J Cell Biol*. 142:751-761.

Bonner, M.K., D.S. Poole, T. Xu, A. Sarkeshik, J.R. Yates, 3rd, and A.R. Skop. 2011. Mitotic spindle proteomics in Chinese hamster ovary cells. *PLoS One*. 6:e20489.

Booth, D.G., F.E. Hood, I.A. Prior, and S.J. Royle. 2011. A TACC3/ch-TOG/clathrin complex stabilises kinetochore fibres by inter-microtubule bridging. *EMBO J*. 30:906-919.

Borisy, G.G., and E.W. Taylor. 1967. The mechanism of action of colchicine. Binding of colchincine-3H to cellular protein. *J Cell Biol*. 34:525-533.

Boveri, T. 1900. Ueber die Natur der Centrosomen. Fischer.

Brenner, S., D. Pepper, M.W. Berns, E. Tan, and B.R. Brinkley. 1981. Kinetochore structure, duplication, and distribution in mammalian cells: analysis by human autoantibodies from scleroderma patients. *J Cell Biol*. 91:95-102.

Brinkley, B.R., and J. Cartwright, Jr. 1971. Ultrastructural analysis of mitotic spindle elongation in mammalian cells in vitro. Direct microtubule counts. *J Cell Biol*. 50:416-431.

Brinkley, B.R., and J. Cartwright, Jr. 1975. Cold-labile and cold-stable microtubules in the mitotic spindle of mammalian cells. *Ann N Y Acad Sci*. 253:428-439.

Brinkley, B.R., and E. Stubblefield. 1966. The fine structure of the kinetochore of a mammalian cell in vitro. *Chromosoma*. 19:28-43.

Brinkley, B.R., M.M. Valdivia, A. Tousson, and S.L. Brenner. 1984. Compound kinetochores of the Indian muntjac. Evolution by linear fusion of unit kinetochores. *Chromosoma*. 91:1-11.

Brinkley, B.R., R.P. Zinkowski, W.L. Mollon, F.M. Davis, M.A. Pisegna, M. Pershouse, and P.N. Rao. 1988. Movement and segregation of kinetochores experimentally detached from mammalian chromosomes. *Nature*. 336:251-254.

Britten, R.J., and D.E. Kohne. 1968. Repeated sequences in DNA. Hundreds of thousands of copies of DNA sequences have been incorporated into the genomes of higher organisms. *Science*. 161:529-540.

Brouhard, G.J., and A.J. Hunt. 2005. Microtubule movements on the arms of mitotic chromosomes: polar ejection forces quantified in vitro. *Proc Natl Acad Sci U S A*. 102:13903-13908.

Brouhard, G.J., J.H. Stear, T.L. Noetzel, J. Al-Bassam, K. Kinoshita, S.C. Harrison, J. Howard, and A.A. Hyman. 2008. XMAP215 is a processive microtubule polymerase. *Cell*. 132:79-88.

Brown, P., and W. Loughman. 1980. Visible light observations on the kinetochore of the Indian muntjac, Muntiacus muntjac, Z. *Cytogenetic and Genome Research*. 27:123-128.

Bruinsma, W., J.A. Raaijmakers, and R.H. Medema. 2012. Switching Polo-like kinase-1 on and off in time and space. *Trends Biochem Sci*. 37:534-542.

Brust-Mascher, I., and J.M. Scholey. 2002. Microtubule flux and sliding in mitotic spindles of Drosophila embryos. *Mol Biol Cell*. 13:3967-3975.

Bucciarelli, E., C. Pellacani, V. Naim, A. Palena, M. Gatti, and M.P. Somma. 2009. Drosophila Dgt6 interacts with Ndc80, Msps/XMAP215, and gamma-tubulin to promote kinetochore-driven MT formation. *Curr Biol*. 19:1839-1845.

Bullough, W.S., and M. Johnson. 1951. The energy relations of mitotic activity in adult mouse epidermis. *Proc R Soc Lond B Biol Sci*. 138:562-575.

Cai, S., C.B. O'Connell, A. Khodjakov, and C.E. Walczak. 2009. Chromosome congression in the absence of kinetochore fibres. *Nat Cell Biol*. 11:832-838.

Campbell, S., M.A. Amin, D. Varma, and T.C. Bidone. 2019. Computational model demonstrates that Ndc80-associated proteins strengthen kinetochore-microtubule attachments in metaphase. *Cytoskeleton (Hoboken)*. 76:549-561.

Cane, S., A.A. Ye, S.J. Luks-Morgan, and T.J. Maresca. 2013. Elevated polar ejection forces stabilize kinetochore-microtubule attachments. *J Cell Biol*. 200:203-218.

Carazo-Salas, R.E., O.J. Gruss, I.W. Mattaj, and E. Karsenti. 2001. Ran-GTP coordinates regulation of microtubule nucleation and dynamics during mitotic-spindle assembly. *Nat Cell Biol*. 3:228-234.

Carazo-Salas, R.E., G. Guarguaglini, O.J. Gruss, A. Segref, E. Karsenti, and I.W. Mattaj. 1999. Generation of GTP-bound Ran by RCC1 is required for chromatin-induced mitotic spindle formation. *Nature*. 400:178-181.

Casanova, C.M., S. Rybina, H. Yokoyama, E. Karsenti, and I.W. Mattaj. 2008. Hepatoma up-regulated protein is required for chromatin-induced microtubule assembly independently of TPX2. *Mol Biol Cell*. 19:4900-4908.

Cassimeris, L., C.L. Rieder, and E.D. Salmon. 1994. Microtubule assembly and kinetochore directional instability in vertebrate monopolar spindles: implications for the mechanism of chromosome congression. *J Cell Sci*. 107 (Pt 1):285-297.

Cheerambathur, D.K., R. Gassmann, B. Cook, K. Oegema, and A. Desai. 2013. Crosstalk between microtubule attachment complexes ensures accurate chromosome segregation. *Science*. 342:1239-1242.

Cheeseman, I.M., J.S. Chappie, E.M. Wilson-Kubalek, and A. Desai. 2006. The conserved KMN network constitutes the core microtubule-binding site of the kinetochore. *Cell*. 127:983-997.

Cheeseman, I.M., and A. Desai. 2008. Molecular architecture of the kinetochore-microtubule interface. *Nat Rev Mol Cell Biol*. 9:33-46.

Cheeseman, L.P., E.F. Harry, A.D. McAinsh, I.A. Prior, and S.J. Royle. 2013. Specific removal of TACC3-ch-TOG-clathrin at metaphase deregulates kinetochore fiber tension. *J Cell Sci*. 126:2102-2113.

Chen, J.W.C., Z.A. Chen, K.B. Rogala, J. Metz, C.M. Deane, J. Rappsilber, and J.G. Wakefield. 2017. Cross-linking mass spectrometry identifies new interfaces of Augmin required to localise the gamma-tubulin ring complex to the mitotic spindle. *Biol Open*. 6:654-663.

Chen, L., Q. Qiu, Y. Jiang, K. Wang, Z. Lin, Z. Li, F. Bibi, Y. Yang, J. Wang, W. Nie, W. Su, G. Liu, Q. Li, W. Fu, X. Pan, C. Liu, J. Yang, C. Zhang, Y. Yin, Y. Wang, Y. Zhao, C. Zhang, Z. Wang, Y. Qin, W. Liu, B. Wang, Y. Ren, R. Zhang, Y. Zeng, R.R. da Fonseca, B. Wei, R. Li, W. Wan, R. Zhao, W. Zhu, Y. Wang, S. Duan, Y. Gao, Y.E. Zhang, C. Chen, C. Hvilsom, C.W. Epps, L.G. Chemnick, Y. Dong, S. Mirarab, H.R. Siegismund, O.A. Ryder, M.T.P. Gilbert, H.A. Lewin, G. Zhang, R. Heller, and W. Wang. 2019a. Large-scale ruminant genome sequencing provides insights into their evolution and distinct traits. *Science (New York, N.Y.* 364:eaav6202.

Chen, L., Q. Qiu, Y. Jiang, K. Wang, Z. Lin, Z. Li, F. Bibi, Y. Yang, J. Wang, W. Nie, W. Su, G. Liu, Q. Li, W. Fu, X. Pan, C. Liu, J. Yang, C. Zhang, Y. Yin, Y. Wang, Y. Zhao, C. Zhang, Z. Wang, Y. Qin, W. Liu, B. Wang, Y. Ren, R. Zhang, Y. Zeng, R.R. da Fonseca, B. Wei, R. Li, W. Wan, R. Zhao, W. Zhu, Y. Wang, S. Duan, Y. Gao, Y.E. Zhang, C. Chen, C. Hvilsom, C.W. Epps, L.G. Chemnick, Y. Dong, S. Mirarab, H.R. Siegismund, O.A. Ryder, M.T.P. Gilbert, H.A. Lewin, G. Zhang, R. Heller, and W. Wang. 2019b. Large-scale ruminant genome sequencing provides insights into their evolution and distinct traits. *Science*. 364.

Chen, R.H., J.C. Waters, E.D. Salmon, and A.W. Murray. 1996. Association of spindle assembly checkpoint component XMAD2 with unattached kinetochores. *Science (New York, N.Y.* 274:242-246.

Cherry, L.M., A.J. Faulkner, L.A. Grossberg, and R. Balczon. 1989. Kinetochore size variation in mammalian chromosomes: an image analysis study with evolutionary implications. *J Cell Sci*. 92 (Pt 2):281-289.

Cherry, L.M., and D.A. Johnston. 1987. Size variation in kinetochores of human chromosomes. *Hum Genet*. 75:155-158.

Chi, J., B. Fu, W. Nie, J. Wang, A.S. Graphodatsky, and F. Yang. 2005a. New insights into the karyotypic relationships of Chinese muntjac (Muntiacus reevesi), forest musk

deer (Moschus berezovskii) and gayal (Bos frontalis). *Cytogenet Genome Res*. 108:310-316.

Chi, J.X., L. Huang, W. Nie, J. Wang, B. Su, and F. Yang. 2005b. Defining the orientation of the tandem fusions that occurred during the evolution of Indian muntjac chromosomes by BAC mapping. *Chromosoma*. 114:167-172.

Chinen, T., S. Yamamoto, Y. Takeda, K. Watanabe, K. Kuroki, K. Hashimoto, D. Takao, and D. Kitagawa. 2020. NuMA assemblies organize microtubule asters to establish spindle bipolarity in acentrosomal human cells. *The EMBO journal*. 39:e102378.

Chretien, D., S.D. Fuller, and E. Karsenti. 1995. Structure of growing microtubule ends: two-dimensional sheets close into tubes at variable rates. *J Cell Biol*. 129:1311-1328.

Cimini, D., L.A. Cameron, and E.D. Salmon. 2004. Anaphase spindle mechanics prevent mis-segregation of merotelically oriented chromosomes. *Curr Biol*. 14:2149-2155.

Cimini, D., B. Moree, J.C. Canman, and E.D. Salmon. 2003. Merotelic kinetochore orientation occurs frequently during early mitosis in mammalian tissue cells and error correction is achieved by two different mechanisms. *J Cell Sci*. 116:4213-4225.

Cleveland, D.W., Y. Mao, and K.F. Sullivan. 2003. Centromeres and kinetochores: from epigenetics to mitotic checkpoint signaling. *Cell*. 112:407-421.

Cole, D.G., W.M. Saxton, K.B. Sheehan, and J.M. Scholey. 1994. A "slow" homotetrameric kinesin-related motor protein purified from Drosophila embryos. *J Biol Chem*. 269:22913-22916.

Colicino, E.G., and H. Hehnly. 2018. Regulating a key mitotic regulator, polo-like kinase 1 (PLK1). *Cytoskeleton (Hoboken)*. 75:481-494.

Comings, D.E., and T.A. Okada. 1971. Fine structure of kinetochore in Indian muntjac. *Exp Cell Res*. 67:97-110.

Conduit, P.T., A. Wainman, and J.W. Raff. 2015. Centrosome function and assembly in animal cells. *Nat Rev Mol Cell Biol*. 16:611-624.

Contreras, L.C., J.C. Torres-Mura, and A.E. Spotorno. 1990. The largest known chromosome number for a mammal, in a South American desert rodent. *Experientia*. 46:506-508.

Conway, W., R. Kiewisz, G. Fabig, C.P. Kelleher, H.-Y. Wu, M. Anjur-Dietrich, T. Müller-Reichert, and D. Needleman. 2021. Self-organization of kinetochore-fibers in human mitotic spindles. *bioRxiv*:2021.2011.2011.468239.

Craske, B., and J.P.I. Welburn. 2020. Leaving no-one behind: how CENP-E facilitates chromosome alignment. *Essays Biochem*. 64:313-324.

D'Avino, P.P., M.S. Savoian, and D.M. Glover. 2005. Cleavage furrow formation and ingression during animal cytokinesis: a microtubule legacy. *Journal of Cell Science*. 118:1549-1558.

David, A.F., P. Roudot, W.R. Legant, E. Betzig, G. Danuser, and D.W. Gerlich. 2019. Augmin accumulation on long-lived microtubules drives amplification and kinetochore-directed growth. *J Cell Biol*. 218:2150-2168.

De Brabander, M., G. Geuens, J. De Mey, and M. Joniau. 1981. Nucleated assembly of mitotic microtubules in living PTK2 cells after release from nocodazole treatment. *Cell Motil*. 1:469-483.

Debec A., S.A., Szöllösi D. . 1982. A Drosophila melanogaster cell line lacking centriole. *Biol Cell* 44 133–138.

DeLuca, J.G., W.E. Gall, C. Ciferri, D. Cimini, A. Musacchio, and E.D. Salmon. 2006. Kinetochore microtubule dynamics and attachment stability are regulated by Hec1. *Cell*. 127:969-982.

DeLuca, K.F., S.M. Lens, and J.G. DeLuca. 2011. Temporal changes in Hec1 phosphorylation control kinetochore-microtubule attachment stability during mitosis. *J Cell Sci*. 124:622-634.

den Elzen, N., and J. Pines. 2001. Cyclin A is destroyed in prometaphase and can delay chromosome alignment and anaphase. *J Cell Biol*. 153:121-136.

Desai, A., and T.J. Mitchison. 1997. Microtubule polymerization dynamics. *Annu Rev Cell Dev Biol*. 13:83-117.

Desai, A., S. Rybina, T. Muller-Reichert, A. Shevchenko, A. Shevchenko, A. Hyman, and K. Oegema. 2003. KNL-1 directs assembly of the microtubule-binding interface of the kinetochore in C. elegans. *Genes Dev*. 17:2421-2435.

Desai, A., S. Verma, T.J. Mitchison, and C.E. Walczak. 1999. Kin I kinesins are microtubule-destabilizing enzymes. *Cell*. 96:69-78.

Dick, A.E., and D.W. Gerlich. 2013. Kinetic framework of spindle assembly checkpoint signalling. *Nat Cell Biol*. 15:1370-1377.

Ding, R., K.L. McDonald, and J.R. McIntosh. 1993. Three-dimensional reconstruction and analysis of mitotic spindles from the yeast, Schizosaccharomyces pombe. *J Cell Biol*. 120:141-151.

Drpic, D., A.C. Almeida, P. Aguiar, F. Renda, J. Damas, H.A. Lewin, D.M. Larkin, A. Khodjakov, and H. Maiato. 2018. Chromosome Segregation Is Biased by Kinetochore Size. *Curr Biol*. 28:1344-1356 e1345.

Drpic, D., A.J. Pereira, M. Barisic, T.J. Maresca, and H. Maiato. 2015. Polar Ejection Forces Promote the Conversion from Lateral to End-on Kinetochore-Microtubule Attachments on Mono-oriented Chromosomes. *Cell Rep*. 13:460-468.

Dudka, D., C. Castrogiovanni, N. Liaudet, H. Vassal, and P. Meraldi. 2019. Spindle-Length-Dependent HURP Localization Allows Centrosomes to Control Kinetochore-Fiber Plus-End Dynamics. *Curr Biol*. 29:3563-3578 e3566.

Dumont, M., R. Gamba, P. Gestraud, S. Klaasen, J.T. Worrall, S.G. De Vries, V. Boudreau, C. Salinas-Luypaert, P.S. Maddox, S.M. Lens, G.J. Kops, S.E. McClelland, K.H. Miga, and D. Fachinetti. 2020. Human chromosome-specific aneuploidy is influenced by DNA-dependent centromeric features. *EMBO J*. 39:e102924.

Dumont, S., and T.J. Mitchison. 2009. Force and length in the mitotic spindle. *Curr Biol*. 19:R749-761.

Eggert, U.S., T.J. Mitchison, and C.M. Field. 2006. Animal cytokinesis: from parts list to mechanisms. *Annu. Rev. Biochem.* 75:543-566.

Elting, M.W., C.L. Hueschen, D.B. Udy, and S. Dumont. 2014. Force on spindle microtubule minus ends moves chromosomes. *J Cell Biol*. 206:245-256.

Elting, M.W., P. Suresh, and S. Dumont. 2018. The Spindle: Integrating Architecture and Mechanics across Scales. *Trends Cell Biol*. 28:896-910.

Ems-McClung, S.C., and C.E. Walczak. 2010. Kinesin-13s in mitosis: Key players in the spatial and temporal organization of spindle microtubules. *Semin Cell Dev Biol*. 21:276-282.

Erdmann, R.S., S.W. Baguley, J.H. Richens, R.F. Wissner, Z. Xi, E.S. Allgeyer, S. Zhong, A.D. Thompson, N. Lowe, R. Butler, J. Bewersdorf, J.E. Rothman, D. St Johnston, A. Schepartz, and D. Toomre. 2019. Labeling Strategies Matter for Super-Resolution Microscopy: A Comparison between HaloTags and SNAP-tags. *Cell Chem Biol*. 26:584-592.e586.

Euteneuer, U., and J.R. McIntosh. 1980. Polarity of midbody and phragmoplast microtubules. *J Cell Biol*. 87:509-515.

Fachinetti, D., J.S. Han, M.A. McMahon, P. Ly, A. Abdullah, A.J. Wong, and D.W. Cleveland. 2015. DNA Sequence-Specific Binding of CENP-B Enhances the Fidelity of Human Centromere Function. *Dev Cell*. 33:314-327.

Feijão, T., O. Afonso, A.F. Maia, and C.E. Sunkel. 2013. Stability of kinetochore-microtubule attachment and the role of different KMN network components in Drosophila. *Cytoskeleton (Hoboken)*. 70:661-675.

Ferenz, N.P., R. Paul, C. Fagerstrom, A. Mogilner, and P. Wadsworth. 2009. Dynein antagonizes eg5 by crosslinking and sliding antiparallel microtubules. *Curr Biol*. 19:1833-1838.

Feringa, F.M., L. Krenning, A. Koch, J. van den Berg, B. van den Broek, K. Jalink, and R.H. Medema. 2016. Hypersensitivity to DNA damage in antephase as a safeguard for genome stability. *Nat Commun*. 7:12618.

Ferreira, J.G., A.L. Pereira, and H. Maiato. 2014. Microtubule plus-end tracking proteins and their roles in cell division. *Int Rev Cell Mol Biol*. 309:59-140.

Ferreira, L.T., and H. Maiato. 2021. Prometaphase. *Semin Cell Dev Biol*. 117:52-61.

Ferreira, L.T., B. Orr, G. Rajendraprasad, A.J. Pereira, C. Lemos, J.T. Lima, C. Guasch Boldu, J.G. Ferreira, M. Barisic, and H. Maiato. 2020. alpha-Tubulin detyrosination impairs mitotic error correction by suppressing MCAK centromeric activity. *J Cell Biol*. 219.

Fink, G., L. Hajdo, K.J. Skowronek, C. Reuther, A.A. Kasprzak, and S. Diez. 2009. The mitotic kinesin-14 Ncd drives directional microtubule-microtubule sliding. *Nat Cell Biol*. 11:717-723.

Flemming, W. 1882. Zellsubstanz, kern und zelltheilung. Vogel.

Forsberg, L.A., C. Rasi, N. Malmqvist, H. Davies, S. Pasupulati, G. Pakalapati, J. Sandgren, T. Diaz de Stahl, A. Zaghlool, V. Giedraitis, L. Lannfelt, J. Score, N.C. Cross, D. Absher, E.T. Janson, C.M. Lindgren, A.P. Morris, E. Ingelsson, L. Lind, and J.P. Dumanski. 2014. Mosaic loss of chromosome Y in peripheral blood is associated with shorter survival and higher risk of cancer. *Nat Genet*. 46:624-628.

Frokjaer-Jensen, C., M.W. Davis, M. Ailion, and E.M. Jorgensen. 2012. Improved Mos1-mediated transgenesis in C. elegans. *Nat Methods*. 9:117-118.

Frokjaer-Jensen, C., M.W. Davis, C.E. Hopkins, B.J. Newman, J.M. Thummel, S.P. Olesen, M. Grunnet, and E.M. Jorgensen. 2008. Single-copy insertion of transgenes in Caenorhabditis elegans. *Nat Genet*. 40:1375-1383.

Fronicke, L., B.P. Chowdhary, and H. Scherthan. 1997. Segmental homology among cattle (Bos taurus), Indian muntjac (Muntiacus muntjak vaginalis), and Chinese muntjac (M. reevesi) karyotypes. *Cytogenet Cell Genet*. 77:223-227.

Fronicke, L., and H. Scherthan. 1997. Zoo-fluorescence in situ hybridization analysis of human and Indian muntjac karyotypes (Muntiacus muntjak vaginalis) reveals satellite DNA clusters at the margins of conserved syntenic segments. *Chromosome Res*. 5:254-261.

Funabiki, H., and A.W. Murray. 2000. The Xenopus chromokinesin Xkid is essential for metaphase chromosome alignment and must be degraded to allow anaphase chromosome movement. *Cell*. 102:411-424.

Gache, V., P. Waridel, C. Winter, A. Juhem, M. Schroeder, A. Shevchenko, and A.V. Popov. 2010. Xenopus meiotic microtubule-associated interactome. *PLoS One*. 5:e9248.

Gaglio, T., A. Saredi, J.B. Bingham, M.J. Hasbani, S.R. Gill, T.A. Schroer, and D.A. Compton. 1996. Opposing motor activities are required for the organization of the mammalian mitotic spindle pole. *J Cell Biol*. 135:399-414.

Gama, J.B., C. Pereira, P.A. Simoes, R. Celestino, R.M. Reis, D.J. Barbosa, H.R. Pires, C. Carvalho, J. Amorim, A.X. Carvalho, D.K. Cheerambathur, and R. Gassmann. 2017. Molecular mechanism of dynein recruitment to kinetochores by the Rod-Zw10-Zwilch complex and Spindly. *The Journal of cell biology*. 216:943-960.

Ganem, N.J., and D.A. Compton. 2004. The KinI kinesin Kif2a is required for bipolar spindle assembly through a functional relationship with MCAK. *J Cell Biol*. 166:473-478.

Ganem, N.J., K. Upton, and D.A. Compton. 2005. Efficient mitosis in human cells lacking poleward microtubule flux. *Curr Biol*. 15:1827-1832.

Gard, D.L., and M.W. Kirschner. 1987. A microtubule-associated protein from Xenopus eggs that specifically promotes assembly at the plus-end. *J Cell Biol*. 105:2203-2215.

Gassmann, R., A. Essex, J.S. Hu, P.S. Maddox, F. Motegi, A. Sugimoto, S.M. O'Rourke, B. Bowerman, I. McLeod, J.R. Yates, 3rd, K. Oegema, I.M. Cheeseman, and A. Desai. 2008. A new mechanism controlling kinetochore-microtubule interactions revealed by comparison of two dynein-targeting components: SPDL-1 and the Rod/Zwilch/Zw10 complex. *Genes Dev*. 22:2385-2399.

Gassmann, R., A.J. Holland, D. Varma, X. Wan, F. Civril, D.W. Cleveland, K. Oegema, E.D. Salmon, and A. Desai. 2010. Removal of Spindly from microtubule-attached kinetochores controls spindle checkpoint silencing in human cells. *Genes & development*. 24:957-971.

Geley, S., E. Kramer, C. Gieffers, J. Gannon, J.M. Peters, and T. Hunt. 2001. Anaphase-promoting complex/cyclosome-dependent proteolysis of human cyclin A starts at the beginning of mitosis and is not subject to the spindle assembly checkpoint. *J Cell Biol*. 153:137-148.

Gergely, F., V.M. Draviam, and J.W. Raff. 2003. The ch-TOG/XMAP215 protein is essential for spindle pole organization in human somatic cells. *Genes Dev*. 17:336-341.

Gibson, D.G. 2009. Synthesis of DNA fragments in yeast by one-step assembly of overlapping oligonucleotides. *Nucleic Acids Res*. 37:6984-6990.

Giet, R., and D.M. Glover. 2001. Drosophila aurora B kinase is required for histone H3 phosphorylation and condensin recruitment during chromosome condensation and to organize the central spindle during cytokinesis. *J Cell Biol*. 152:669-682.

Girao, H., and H. Maiato. 2020. Measurement of Microtubule Half-Life and Poleward Flux in the Mitotic Spindle by Photoactivation of Fluorescent Tubulin. *Methods Mol Biol*. 2101:235-246.

Girao, H., N. Okada, T.A. Rodrigues, A.O. Silva, A.C. Figueiredo, Z. Garcia, T. Moutinho-Santos, I. Hayashi, J.E. Azevedo, S. Macedo-Ribeiro, and H. Maiato. 2020. CLASP2 binding to curved microtubule tips promotes flux and stabilizes kinetochore attachments. *J Cell Biol*. 219.

Godek, K.M., L. Kabeche, and D.A. Compton. 2015. Regulation of kinetochore-microtubule attachments through homeostatic control during mitosis. *Nat Rev Mol Cell Biol*. 16:57-64.

Godinho, S.A., and D. Pellman. 2014. Causes and consequences of centrosome abnormalities in cancer. *Philos Trans R Soc Lond B Biol Sci*. 369.

Gorbsky, G.J., and G.G. Borisy. 1989. Microtubules of the kinetochore fiber turn over in metaphase but not in anaphase. *The Journal of cell biology*. 109:653-662.

Goshima, G. 2011. Identification of a TPX2-like microtubule-associated protein in Drosophila. *PLoS One*. 6:e28120.

Goshima, G., M. Mayer, N. Zhang, N. Stuurman, and R.D. Vale. 2008. Augmin: a protein complex required for centrosome-independent microtubule generation within the spindle. *J Cell Biol*. 181:421-429.

Goshima, G., F. Nedelec, and R.D. Vale. 2005. Mechanisms for focusing mitotic spindle poles by minus end-directed motor proteins. *J Cell Biol*. 171:229-240.

Goshima, G., and R.D. Vale. 2003. The roles of microtubule-based motor proteins in mitosis: comprehensive RNAi analysis in the Drosophila S2 cell line. *J Cell Biol*. 162:1003-1016.

Goshima, G., R. Wollman, S.S. Goodwin, N. Zhang, J.M. Scholey, R.D. Vale, and N. Stuurman. 2007. Genes required for mitotic spindle assembly in Drosophila S2 cells. *Science*. 316:417-421.

Grimm, J.B., B.P. English, J. Chen, J.P. Slaughter, Z. Zhang, A. Revyakin, R. Patel, J.J. Macklin, D. Normanno, R.H. Singer, T. Lionnet, and L.D. Lavis. 2015. A general method to improve fluorophores for live-cell and single-molecule microscopy. *Nat Methods*. 12:244-250, 243 p following 250.

Guimaraes, G.J., Y. Dong, B.F. McEwen, and J.G. Deluca. 2008. Kinetochore-microtubule attachment relies on the disordered N-terminal tail domain of Hec1. *Curr Biol*. 18:1778-1784.

Haren, L., M.H. Remy, I. Bazin, I. Callebaut, M. Wright, and A. Merdes. 2006. NEDD1-dependent recruitment of the gamma-tubulin ring complex to the centrosome is necessary for centriole duplication and spindle assembly. *J Cell Biol*. 172:505-515.

Hartmann, N., and H. Scherthan. 2004. Characterization of ancestral chromosome fusion points in the Indian muntjac deer. *Chromosoma*. 112:213-220.

Hartwell, L.H., and T.A. Weinert. 1989. Checkpoints: controls that ensure the order of cell cycle events. *Science*. 246:629-634.

Hayward, D., J. Metz, C. Pellacani, and J.G. Wakefield. 2014. Synergy between multiple microtubule-generating pathways confers robustness to centrosome-driven mitotic spindle formation. *Dev Cell*. 28:81-93.

Heald, R., R. Tournebize, T. Blank, R. Sandaltzopoulos, P. Becker, A. Hyman, and E. Karsenti. 1996. Self-organization of microtubules into bipolar spindles around artificial chromosomes in Xenopus egg extracts. *Nature*. 382:420-425.

Hepperla, A.J., P.T. Willey, C.E. Coombes, B.M. Schuster, M. Gerami-Nejad, M. McClellan, S. Mukherjee, J. Fox, M. Winey, D.J. Odde, E. O'Toole, and M.K. Gardner. 2014. Minus-end-directed Kinesin-14 motors align antiparallel microtubules to control metaphase spindle length. *Dev Cell*. 31:61-72.

Herman, J.A., M.P. Miller, and S. Biggins. 2020. chTOG is a conserved mitotic error correction factor. *Elife*. 9.

Hinchcliffe, E.H. 2011. The centrosome and bipolar spindle assembly: does one have anything to do with the other? *Cell Cycle*. 10:3841-3848.

Hinchcliffe, E.H., F.J. Miller, M. Cham, A. Khodjakov, and G. Sluder. 2001. Requirement of a centrosomal activity for cell cycle progression through G1 into S phase. *Science*. 291:1547-1550.

Hoffman, D.B., C.G. Pearson, T.J. Yen, B.J. Howell, and E.D. Salmon. 2001. Microtubule-dependent changes in assembly of microtubule motor proteins and mitotic spindle checkpoint proteins at PtK1 kinetochores. *Mol Biol Cell*. 12:1995-2009.

Hofmann, N.R. 2012. Augmin's Role in Microtubule Generation in Plants. Am Soc Plant Biol.

Holder, J., E. Poser, and F.A. Barr. 2019. Getting out of mitosis: spatial and temporal control of mitotic exit and cytokinesis by PP1 and PP2A. *FEBS Lett*. 593:2908-2924.

Honda, Y., K. Tsuchiya, E. Sumiyoshi, N. Haruta, and A. Sugimoto. 2017. Tubulin isotype substitution revealed that isotype combination modulates microtubule dynamics in C. elegans embryos. *J Cell Sci*. 130:1652-1661.

Hornsveld, M., F.M. Feringa, L. Krenning, J. van den Berg, L.M.M. Smits, N.B.T. Nguyen, M.J. Rodriguez-Colman, T.B. Dansen, R.H. Medema, and B.M.T. Burgering. 2021. A FOXO-dependent replication checkpoint restricts proliferation of damaged cells. *Cell Rep*. 34:108675.

Hotta, T., Z. Kong, C.M. Ho, C.J. Zeng, T. Horio, S. Fong, T. Vuong, Y.R. Lee, and B. Liu. 2012. Characterization of the Arabidopsis augmin complex uncovers its critical function in the assembly of the acentrosomal spindle and phragmoplast microtubule arrays. *Plant Cell*. 24:1494-1509.

Howard, J., and A.A. Hyman. 2009. Growth, fluctuation and switching at microtubule plus ends. *Nat Rev Mol Cell Biol*. 10:569-574.

Hoyt, M.A., L. Totis, and B.T. Roberts. 1991. S. cerevisiae genes required for cell cycle arrest in response to loss of microtubule function. *Cell*. 66:507-517.

Hsia, K.C., E.M. Wilson-Kubalek, A. Dottore, Q. Hao, K.L. Tsai, S. Forth, Y. Shimamoto, R.A. Milligan, and T.M. Kapoor. 2014. Reconstitution of the augmin complex provides insights into its architecture and function. *Nat Cell Biol*. 16:852-863.

Hsu, T.C., S. Pathak, and T.R. Chen. 1975. The possibility of latent centromeres and a proposed nomenclature system for total chromosome and whole arm translocations. *Cytogenet Cell Genet*. 15:41-49.

Hu, C.K., N. Ozlu, M. Coughlin, J.J. Steen, and T.J. Mitchison. 2012. Plk1 negatively regulates PRC1 to prevent premature midzone formation before cytokinesis. *Molecular biology of the cell*. 23:2702-2711.

Huang, L., J. Chi, J. Wang, W. Nie, W. Su, and F. Yang. 2006a. High-density comparative BAC mapping in the black muntjac (Muntiacus crinifrons): molecular cytogenetic dissection of the origin of MCR 1p+4 in the X1X2Y1Y2Y3 sex chromosome system. *Genomics*. 87:608-615.

Huang, L., J. Wang, W. Nie, W. Su, and F. Yang. 2006b. Tandem chromosome fusions in karyotypic evolution of Muntiacus: evidence from M. feae and M. gongshanensis. *Chromosome Res*. 14:637-647.

Hueschen, C.L., S.J. Kenny, K. Xu, and S. Dumont. 2017. NuMA recruits dynein activity to microtubule minus-ends at mitosis. *Elife*. 6.

Hughes, A. 1952. The mitotic cycle. The cytoplasm and nucleus during interphase and mitosis. *The mitotic cycle. The cytoplasm and nucleus during interphase and mitosis.*

Hurd, D.D. 2018. Tubulins in C. elegans. *WormBook*. 2018:1-32.

Inoue, S. 1953. [Polarization optical studies of the mitotic spindle. I. The demonstration of spindle fibers in living cells]. *Chromosoma*. 5:487-500.

Inoue, S. 2008. Microtubule dynamics in cell division: exploring living cells with polarized light microscopy. *Annu Rev Cell Dev Biol*. 24:1-28.

Inoue, S., and A. Bajer. 1961. Birefringence in endosperm mitosis. *Chromosoma*. 12:48-63.

Irvine, D.V., D.J. Amor, J. Perry, N. Sirvent, F. Pedeutour, K.H. Choo, and R. Saffery. 2004. Chromosome size and origin as determinants of the level of CENP-A incorporation into human centromeres. *Chromosome Res*. 12:805-815.

Itabashi, T., J. Takagi, Y. Shimamoto, H. Onoe, K. Kuwana, I. Shimoyama, J. Gaetz, T.M. Kapoor, and S. Ishiwata. 2009. Probing the mechanical architecture of the vertebrate meiotic spindle. *Nat Methods*. 6:167-172.

Jagric, M., P. Risteski, J. Martincic, A. Milas, and I.M. Tolic. 2021. Optogenetic control of PRC1 reveals its role in chromosome alignment on the spindle by overlap length-dependent forces. *Elife*. 10.

Jang, C.Y., J.A. Coppinger, A. Seki, J.R. Yates, 3rd, and G. Fang. 2009. Plk1 and Aurora A regulate the depolymerase activity and the cellular localization of Kif2a. *J Cell Sci*. 122:1334-1341.

Janke, C., and J.C. Bulinski. 2011. Post-translational regulation of the microtubule cytoskeleton: mechanisms and functions. *Nat Rev Mol Cell Biol*. 12:773-786.

Janke, C., and M.M. Magiera. 2020. The tubulin code and its role in controlling microtubule properties and functions. *Nat Rev Mol Cell Biol*. 21:307-326.

Johmura, Y., N.K. Soung, J.E. Park, L.R. Yu, M. Zhou, J.K. Bang, B.Y. Kim, T.D. Veenstra, R.L. Erikson, and K.S. Lee. 2011. Regulation of microtubule-based microtubule nucleation by mammalian polo-like kinase 1. *Proc Natl Acad Sci U S A*. 108:11446-11451.

Johnston, F.P., R.B. Church, and C.C. Lin. 1982. Chromosome rearrangement between the Indian muntjac and Chinese muntjac is accompanied by a delection of middle repetitive DNA. *Can J Biochem*. 60:497-506.

Kabeche, L., and D.A. Compton. 2013. Cyclin A regulates kinetochore microtubules to promote faithful chromosome segregation. *Nature*. 502:110-113.

Kajtez, J., A. Solomatina, M. Novak, B. Polak, K. Vukusic, J. Rudiger, G. Cojoc, A. Milas, I. Sumanovac Sestak, P. Risteski, F. Tavano, A.H. Klemm, E. Roscioli, J. Welburn, D. Cimini, M. Gluncic, N. Pavin, and I.M. Tolic. 2016. Overlap microtubules link sister k-fibres and balance the forces on bi-oriented kinetochores. *Nat Commun*. 7:10298.

Kalab, P., and R. Heald. 2008. The RanGTP gradient - a GPS for the mitotic spindle. *J Cell Sci*. 121:1577-1586.

Kamasaki, T., E. O'Toole, S. Kita, M. Osumi, J. Usukura, J.R. McIntosh, and G. Goshima. 2013. Augmin-dependent microtubule nucleation at microtubule walls in the spindle. *J Cell Biol*. 202:25-33.

Kapoor, T.M. 2017. Metaphase Spindle Assembly. *Biology (Basel)*. 6.

Kapoor, T.M., M.A. Lampson, P. Hergert, L. Cameron, D. Cimini, E.D. Salmon, B.F. McEwen, and A. Khodjakov. 2006. Chromosomes can congress to the metaphase plate before biorientation. *Science*. 311:388-391.

Katayama, H., K. Sasai, M. Kloc, B.R. Brinkley, and S. Sen. 2008. Aurora kinase-A regulates kinetochore/chromatin associated microtubule assembly in human cells. *Cell Cycle*. 7:2691-2704.

Ke, K., J. Cheng, and A.J. Hunt. 2009. The distribution of polar ejection forces determines the amplitude of chromosome directional instability. *Curr Biol*. 19:807-815.

Khawaja, S., G.G. Gundersen, and J.C. Bulinski. 1988. Enhanced stability of microtubules enriched in detyrosinated tubulin is not a direct function of detyrosination level. *The Journal of cell biology*. 106:141-149.

Khodjakov, A., R.W. Cole, B.F. McEwen, K.F. Buttle, and C.L. Rieder. 1997. Chromosome fragments possessing only one kinetochore can congress to the spindle equator. *J Cell Biol*. 136:229-240.

Khodjakov, A., R.W. Cole, B.R. Oakley, and C.L. Rieder. 2000. Centrosome-independent mitotic spindle formation in vertebrates. *Curr Biol*. 10:59-67.

Khodjakov, A., L. Copenagle, M.B. Gordon, D.A. Compton, and T.M. Kapoor. 2003. Minus-end capture of preformed kinetochore fibers contributes to spindle morphogenesis. *J Cell Biol*. 160:671-683.

Khodjakov, A., and J. Pines. 2010. Centromere tension: a divisive issue. *Nat Cell Biol*. 12:919-923.

Khodjakov, A., and C.L. Rieder. 2001. Centrosomes enhance the fidelity of cytokinesis in vertebrates and are required for cell cycle progression. *J Cell Biol*. 153:237-242.

Kiewisz, R., G. Fabig, W. Conway, D. Needleman, and T. Müller-Reichert. 2021. Three-dimensional structure of the kinetochore-fibers in human mitotic spindles. *bioRxiv*:2021.2011.2013.468347.

King, J.M., and R.B. Nicklas. 2000. Tension on chromosomes increases the number of kinetochore microtubules but only within limits. *J Cell Sci*. 113 Pt 21:3815-3823.

Kirschner, M., and T. Mitchison. 1986. Beyond self-assembly: from microtubules to morphogenesis. *Cell*. 45:329-342.

Kollman, J.M., A. Merdes, L. Mourey, and D.A. Agard. 2011. Microtubule nucleation by gamma-tubulin complexes. *Nat Rev Mol Cell Biol*. 12:709-721.

Komarova, Y.A., A.S. Akhmanova, S. Kojima, N. Galjart, and G.G. Borisy. 2002. Cytoplasmic linker proteins promote microtubule rescue in vivo. *J Cell Biol*. 159:589-599.

Kops, G., and R. Gassmann. 2020. Crowning the Kinetochore: The Fibrous Corona in Chromosome Segregation. *Trends Cell Biol*. 30:653-667.

Krenn, V., and A. Musacchio. 2015. The Aurora B Kinase in Chromosome Bi-Orientation and Spindle Checkpoint Signaling. *Front Oncol*. 5:225.

Kuo, Y.W., and J. Howard. 2021. Cutting, Amplifying, and Aligning Microtubules with Severing Enzymes. *Trends Cell Biol*. 31:50-61.

Kurasawa, Y., W.C. Earnshaw, Y. Mochizuki, N. Dohmae, and K. Todokoro. 2004. Essential roles of KIF4 and its binding partner PRC1 in organized central spindle midzone formation. *EMBO J*. 23:3237-3248.

Kwiatkowski, N., N. Jelluma, P. Filippakopoulos, M. Soundararajan, M.S. Manak, M. Kwon, H.G. Choi, T. Sim, Q.L. Deveraux, S. Rottmann, D. Pellman, J.V. Shah, G.J. Kops, S. Knapp, and N.S. Gray. 2010. Small-molecule kinase inhibitors provide insight into Mps1 cell cycle function. *Nat Chem Biol*. 6:359-368.

LaFountain, J.R., Jr., C.S. Cohan, A.J. Siegel, and D.J. LaFountain. 2004. Direct visualization of microtubule flux during metaphase and anaphase in crane-fly spermatocytes. *Molecular biology of the cell*. 15:5724-5732.

Lampson, M.A., and I.M. Cheeseman. 2011. Sensing centromere tension: Aurora B and the regulation of kinetochore function. *Trends Cell Biol*. 21:133-140.

Lampson, M.A., K. Renduchitala, A. Khodjakov, and T.M. Kapoor. 2004. Correcting improper chromosome-spindle attachments during cell division. *Nat Cell Biol*. 6:232-237.

Lara-Gonzalez, P., J. Pines, and A. Desai. 2021. Spindle assembly checkpoint activation and silencing at kinetochores. *Semin Cell Dev Biol*. 117:86-98.

Lara-Gonzalez, P., F.G. Westhorpe, and S.S. Taylor. 2012. The spindle assembly checkpoint. *Curr Biol*. 22:R966-980.

Lawo, S., M. Bashkurov, M. Mullin, M.G. Ferreria, R. Kittler, B. Habermann, A. Tagliaferro, I. Poser, J.R. Hutchins, B. Hegemann, D. Pinchev, F. Buchholz, J.M. Peters, A.A. Hyman, A.C. Gingras, and L. Pelletier. 2009. HAUS, the 8-subunit human Augmin complex, regulates centrosome and spindle integrity. *Curr Biol*. 19:816-826.

Lee, C., R. Sasi, and C.C. Lin. 1993. Interstitial localization of telomeric DNA sequences in the Indian muntjac chromosomes: further evidence for tandem chromosome fusions in the karyotypic evolution of the Asian muntjacs. *Cytogenet Cell Genet*. 63:156-159.

Leite, J., D.S. Osorio, A.F. Sobral, A.M. Silva, and A.X. Carvalho. 2019. Network Contractility During Cytokinesis-from Molecular to Global Views. *Biomolecules*. 9.

Levesque, A.A., and D.A. Compton. 2001. The chromokinesin Kid is necessary for chromosome arm orientation and oscillation, but not congression, on mitotic spindles. *J Cell Biol*. 154:1135-1146.

Li, R., and A.W. Murray. 1991. Feedback control of mitosis in budding yeast. *Cell*. 66:519-531.

Li, Y., W. Yu, Y. Liang, and X. Zhu. 2007. Kinetochore dynein generates a poleward pulling force to facilitate congression and full chromosome alignment. *Cell Res*. 17:701-712.

Liming, S., and S. Pathak. 1981. Gametogenesis in a male Indian muntjac x Chinese muntjac hybrid. *Cytogenet Cell Genet*. 30:152-156.

Liming, S., Y. Yingying, and D. Xingsheng. 1980. Comparative cytogenetic studies on the red muntjac, Chinese muntjac, and their F1 hybrids. *Cytogenet Cell Genet*. 26:22-27.

Lin, C.C., R. Sasi, Y.S. Fan, and Z.Q. Chen. 1991. New evidence for tandem chromosome fusions in the karyotypic evolution of Asian muntjacs. *Chromosoma*. 101:19-24.

Linse, K., and E.M. Mandelkow. 1988. The GTP-binding peptide of beta-tubulin. Localization by direct photoaffinity labeling and comparison with nucleotide-binding proteins. *J Biol Chem*. 263:15205-15210.

Liu, D., G. Vader, M.J. Vromans, M.A. Lampson, and S.M. Lens. 2009. Sensing chromosome bi-orientation by spatial separation of aurora B kinase from kinetochore substrates. *Science*. 323:1350-1353.

Liu, D., M. Vleugel, C.B. Backer, T. Hori, T. Fukagawa, I.M. Cheeseman, and M.A. Lampson. 2010. Regulated targeting of protein phosphatase 1 to the outer kinetochore by KNL1 opposes Aurora B kinase. *J Cell Biol*. 188:809-820.

Liu, T., J. Tian, G. Wang, Y. Yu, C. Wang, Y. Ma, X. Zhang, G. Xia, B. Liu, and Z. Kong. 2014. Augmin triggers microtubule-dependent microtubule nucleation in interphase plant cells. *Curr Biol*. 24:2708-2713.

Logarinho, E., S. Maffini, M. Barisic, A. Marques, A. Toso, P. Meraldi, and H. Maiato. 2012. CLASPs prevent irreversible multipolarity by ensuring spindle-pole resistance to traction forces during chromosome alignment. *Nat Cell Biol*. 14:295-303.

Lopes, D., and H. Maiato. 2020. The Tubulin Code in Mitosis and Cancer. *Cells*. 9.

Lu, C., and P.E. Mains. 2005. Mutations of a redundant alpha-tubulin gene affect Caenorhabditis elegans early embryonic cleavage via MEI-1/katanin-dependent and -independent pathways. *Genetics*. 170:115-126.

Luders, J., U.K. Patel, and T. Stearns. 2006. GCP-WD is a gamma-tubulin targeting factor required for centrosomal and chromatin-mediated microtubule nucleation. *Nat Cell Biol*. 8:137-147.

Lukinavicius, G., L. Reymond, E. D'Este, A. Masharina, F. Gottfert, H. Ta, A. Guther, M. Fournier, S. Rizzo, H. Waldmann, C. Blaukopf, C. Sommer, D.W. Gerlich, H.D. Arndt, S.W. Hell, and K. Johnsson. 2014. Fluorogenic probes for live-cell imaging of the cytoskeleton. *Nat Methods*. 11:731-733.

Ma, S.L., Wang, Y. X., and Shi, L. M. 1990. A new species of the genus Muntiacus from Yunnan, China. *Chinese Zool.* Res. 1147.

MacDonald, C., and S.E. McClelland. 2021. Chromosome Instability through the Ages: Parallels between Speciation and Somatic (Cancer) Evolution. *Trends Genet*. 37:691-694.

Mack, G.J., and D.A. Compton. 2001. Analysis of mitotic microtubule-associated proteins using mass spectrometry identifies astrin, a spindle-associated protein. *Proc Natl Acad Sci U S A*. 98:14434-14439.

Maddox, P., A. Straight, P. Coughlin, T.J. Mitchison, and E.D. Salmon. 2003. Direct observation of microtubule dynamics at kinetochores in Xenopus extract spindles: implications for spindle mechanics. *The Journal of cell biology*. 162:377-382.

Maddox, P.S., K. Oegema, A. Desai, and I.M. Cheeseman. 2004. "Holo"er than thou: chromosome segregation and kinetochore function in C. elegans. *Chromosome Res*. 12:641-653.

Magidson, V., J. He, J.G. Ault, C.B. O'Connell, N. Yang, I. Tikhonenko, B.F. McEwen, H. Sui, and A. Khodjakov. 2016. Unattached kinetochores rather than intrakinetochore tension arrest mitosis in taxol-treated cells. *The Journal of cell biology*. 212:307-319.

Magidson, V., C.B. O'Connell, J. Loncarek, R. Paul, A. Mogilner, and A. Khodjakov. 2011. The spatial arrangement of chromosomes during prometaphase facilitates spindle assembly. *Cell*. 146:555-567.

Magidson, V., R. Paul, N. Yang, J.G. Ault, C.B. O'Connell, I. Tikhonenko, B.F. McEwen, A. Mogilner, and A. Khodjakov. 2015. Adaptive changes in the kinetochore architecture facilitate proper spindle assembly. *Nat Cell Biol*. 17:1134-1144.

Mahoney, N.M., G. Goshima, A.D. Douglass, and R.D. Vale. 2006. Making microtubules and mitotic spindles in cells without functional centrosomes. *Curr Biol*. 16:564-569.

Maiato, H., O. Afonso, and I. Matos. 2015. A chromosome separation checkpoint: A midzone Aurora B gradient mediates a chromosome separation checkpoint that regulates the anaphase-telophase transition. *Bioessays*. 37:257-266.

Maiato, H., J. DeLuca, E.D. Salmon, and W.C. Earnshaw. 2004a. The dynamic kinetochore-microtubule interface. *J Cell Sci*. 117:5461-5477.

Maiato, H., E.A. Fairley, C.L. Rieder, J.R. Swedlow, C.E. Sunkel, and W.C. Earnshaw. 2003a. Human CLASP1 is an outer kinetochore component that regulates spindle microtubule dynamics. *Cell*. 113:891-904.

Maiato, H., A.M. Gomes, F. Sousa, and M. Barisic. 2017. Mechanisms of Chromosome Congression during Mitosis. *Biology (Basel)*. 6.

Maiato, H., P.J. Hergert, S. Moutinho-Pereira, Y. Dong, K.J. Vandenbeldt, C.L. Rieder, and B.F. McEwen. 2006. The ultrastructure of the kinetochore and kinetochore fiber in Drosophila somatic cells. *Chromosoma*. 115:469-480.

Maiato, H., A. Khodjakov, and C.L. Rieder. 2005. Drosophila CLASP is required for the incorporation of microtubule subunits into fluxing kinetochore fibres. *Nat Cell Biol*. 7:42-47.

Maiato, H., C.L. Rieder, W.C. Earnshaw, and C.E. Sunkel. 2003b. How do kinetochores CLASP dynamic microtubules? *Cell Cycle*. 2:511-514.

Maiato, H., C.L. Rieder, and A. Khodjakov. 2004b. Kinetochore-driven formation of kinetochore fibers contributes to spindle assembly during animal mitosis. *J Cell Biol*. 167:831-840.

Maiato, H., P. Sampaio, and C.E. Sunkel. 2004c. Microtubule-associated proteins and their essential roles during mitosis. *International review of cytology*. 241:53-153.

Malheiros, N., and D. De Castro. 1947. Chromosome number and behaviour in Luzula purpurea Link. *Nature*. 159:156.

Mandelkow, E.M., E. Mandelkow, and R.A. Milligan. 1991. Microtubule dynamics and microtubule caps: a time-resolved cryo-electron microscopy study. *J Cell Biol*. 114:977-991.

Manenica, M., V. Štimac, I. Koprivec, J. Simunić, and I.M. Tolić. 2020. Augmin regulates kinetochore tension and spatial arrangement of spindle microtubules by nucleating bridging fibers. *bioRxiv*:2020.2009.2010.291740.

Maney, T., M. Wagenbach, and L. Wordeman. 2001. Molecular dissection of the microtubule depolymerizing activity of mitotic centromere-associated kinesin. *J Biol Chem*. 276:34753-34758.

Mann, B.J., S.K. Balchand, and P. Wadsworth. 2017. Regulation of Kif15 localization and motility by the C-terminus of TPX2 and microtubule dynamics. *Mol Biol Cell*. 28:65-75.

Mann, B.J., and P. Wadsworth. 2019. Kinesin-5 Regulation and Function in Mitosis. *Trends Cell Biol*. 29:66-79.

Manning, A.L., S.F. Bakhoum, S. Maffini, C. Correia-Melo, H. Maiato, and D.A. Compton. 2010. CLASP1, astrin and Kif2b form a molecular switch that regulates kinetochore-microtubule dynamics to promote mitotic progression and fidelity. *EMBO J*. 29:3531-3543.

Manning, A.L., N.J. Ganem, S.F. Bakhoum, M. Wagenbach, L. Wordeman, and D.A. Compton. 2007. The kinesin-13 proteins Kif2a, Kif2b, and Kif2c/MCAK have distinct roles during mitosis in human cells. *Mol Biol Cell*. 18:2970-2979.

Maresca, T.J., A.C. Groen, J.C. Gatlin, R. Ohi, T.J. Mitchison, and E.D. Salmon. 2009. Spindle assembly in the absence of a RanGTP gradient requires localized CPC activity. *Curr Biol*. 19:1210-1215.

Maresca, T.J., and E.D. Salmon. 2010. Welcome to a new kind of tension: translating kinetochore mechanics into a wait-anaphase signal. *Journal of cell science*. 123:825-835.

Marshall, W.F., J.F. Marko, D.A. Agard, and J.W. Sedat. 2001. Chromosome elasticity and mitotic polar ejection force measured in living Drosophila embryos by four-dimensional microscopy-based motion analysis. *Curr Biol*. 11:569-578.

Martinez-Alonso, D., and M. Malumbres. 2020. Mammalian cell cycle cyclins. *Semin Cell Dev Biol*. 107:28-35.

Matos, I., A.J. Pereira, M. Lince-Faria, L.A. Cameron, E.D. Salmon, and H. Maiato. 2009. Synchronizing chromosome segregation by flux-dependent force equalization at kinetochores. *J Cell Biol*. 186:11-26.

Matthey, R. 1973. The chromosome formulae of eutherian mammals. *Chiarelli AB, Capanna E (eds) Cytotaxonomy and vertebrate evolution* Academic Press, London: pp 531-553.

Mayr, M.I., S. Hummer, J. Bormann, T. Gruner, S. Adio, G. Woehlke, and T.U. Mayer. 2007. The human kinesin Kif18A is a motile microtubule depolymerase essential for chromosome congression. *Curr Biol*. 17:488-498.

McClelland, S.E., S. Borusu, A.C. Amaro, J.R. Winter, M. Belwal, A.D. McAinsh, and P. Meraldi. 2007. The CENP-A NAC/CAD kinetochore complex controls chromosome congression and spindle bipolarity. *The EMBO journal*. 26:5033-5047.

McDonald, K.L., E.T. O'Toole, D.N. Mastronarde, and J.R. McIntosh. 1992. Kinetochore microtubules in PTK cells. *J Cell Biol*. 118:369-383.

McEwen, B.F., G.K. Chan, B. Zubrowski, M.S. Savoian, M.T. Sauer, and T.J. Yen. 2001. CENP-E is essential for reliable bioriented spindle attachment, but chromosome alignment can be achieved via redundant mechanisms in mammalian cells. *Mol Biol Cell*. 12:2776-2789.

McEwen, B.F., Y. Ding, and A.B. Heagle. 1998. Relevance of kinetochore size and microtubule-binding capacity for stable chromosome attachment during mitosis in PtK1 cells. *Chromosome Res*. 6:123-132.

McEwen, B.F., A.B. Heagle, G.O. Cassels, K.F. Buttle, and C.L. Rieder. 1997. Kinetochore fiber maturation in PtK1 cells and its implications for the mechanisms of chromosome congression and anaphase onset. *J Cell Biol*. 137:1567-1580.

McHugh, T., A.A. Gluszek, and J.P.I. Welburn. 2018. Microtubule end tethering of a processive kinesin-8 motor Kif18b is required for spindle positioning. *J Cell Biol*. 217:2403-2416.

McIntosh, J.R. 2021. Anaphase A. *Semin Cell Dev Biol*. 117:118-126.

McIntosh, J.R., W.Z. Cande, and J.A. Snyder. 1975. Structure and physiology of the mammalian mitotic spindle. *Soc Gen Physiol Ser*. 30:31-76.

McIntosh, J.R., and T. Hays. 2016. A Brief History of Research on Mitotic Mechanisms. *Biology (Basel)*. 5.

McIntosh, J.R., and S.C. Landis. 1971. The distribution of spindle microtubules during mitosis in cultured human cells. *J Cell Biol*. 49:468-497.

McIntosh, J.R., M.I. Molodtsov, and F.I. Ataullakhanov. 2012. Biophysics of mitosis. *Q Rev Biophys*. 45:147-207.

McKinley, K.L., and I.M. Cheeseman. 2016. The molecular basis for centromere identity and function. *Nat Rev Mol Cell Biol*. 17:16-29.

McNally, F.J., and A. Roll-Mecak. 2018. Microtubule-severing enzymes: From cellular functions to molecular mechanism. *J Cell Biol*. 217:4057-4069.

Megraw, T.L., L.R. Kao, and T.C. Kaufman. 2001. Zygotic development without functional mitotic centrosomes. *Curr Biol*. 11:116-120.

Meireles, A.M., K.H. Fisher, N. Colombie, J.G. Wakefield, and H. Ohkura. 2009. Wac: a new Augmin subunit required for chromosome alignment but not for acentrosomal microtubule assembly in female meiosis. *J Cell Biol*. 184:777-784.

Meunier, S., and I. Vernos. 2016. Acentrosomal Microtubule Assembly in Mitosis: The Where, When, and How. *Trends Cell Biol*. 26:80-87.

Mikhailov, A., M. Shinohara, and C.L. Rieder. 2005. The p38-mediated stress-activated checkpoint. A rapid response system for delaying progression through antephase and entry into mitosis. *Cell Cycle*. 4:57-62.

Mimori-Kiyosue, Y., I. Grigoriev, H. Sasaki, C. Matsui, A. Akhmanova, S. Tsukita, and I. Vorobjev. 2006. Mammalian CLASPs are required for mitotic spindle organization and kinetochore alignment. *Genes Cells*. 11:845-857.

Minshull, J., R. Golsteyn, C.S. Hill, and T. Hunt. 1990. The A- and B-type cyclin associated cdc2 kinases in Xenopus turn on and off at different times in the cell cycle. *EMBO J*. 9:2865-2875.

Mitchison, T., L. Evans, E. Schulze, and M. Kirschner. 1986. Sites of microtubule assembly and disassembly in the mitotic spindle. *Cell*. 45:515-527.

Mitchison, T., and M. Kirschner. 1984. Dynamic instability of microtubule growth. *Nature*. 312:237-242.

Mitchison, T.J. 1989. Polewards microtubule flux in the mitotic spindle: evidence from photoactivation of fluorescence. *J Cell Biol*. 109:637-652.

Mohri, H. 1968. Amino-acid composition of "Tubulin" constituting microtubules of sperm flagella. *Nature*. 217:1053-1054.

Molines, A.T., V. Stoppin-Mellet, I. Arnal, and F.M. Coquelle. 2020. Plant and mouse EB1 proteins have opposite intrinsic properties on the dynamic instability of microtubules. *BMC Res Notes*. 13:296.

Monda, J.K., and I.M. Cheeseman. 2018. The kinetochore-microtubule interface at a glance. *J Cell Sci*. 131.

Morgulis, A., G. Coulouris, Y. Raytselis, T.L. Madden, R. Agarwala, and A.A. Schaffer. 2008. Database indexing for production MegaBLAST searches. *Bioinformatics*. 24:1757-1764.

Mountain, V., C. Simerly, L. Howard, A. Ando, G. Schatten, and D.A. Compton. 1999. The kinesin-related protein, HSET, opposes the activity of Eg5 and cross-links microtubules in the mammalian mitotic spindle. *J Cell Biol*. 147:351-366.

Moutinho-Pereira, S., N. Stuurman, O. Afonso, M. Hornsveld, P. Aguiar, G. Goshima, R.D. Vale, and H. Maiato. 2013. Genes involved in centrosome-independent mitotic spindle assembly in Drosophila S2 cells. *Proc Natl Acad Sci U S A*. 110:19808-19813.

Mudd, A.B., J.V. Bredeson, R. Baum, D. Hockemeyer, and D.S. Rokhsar. 2020. Analysis of muntjac deer genome and chromatin architecture reveals rapid karyotype evolution. *Commun Biol*. 3:480.

Murata, T., and M. Hasebe. 2007. Microtubule-dependent microtubule nucleation in plant cells. *J Plant Res*. 120:73-78.

Murata, T., S. Sonobe, T.I. Baskin, S. Hyodo, S. Hasezawa, T. Nagata, T. Horio, and M. Hasebe. 2005. Microtubule-dependent microtubule nucleation based on recruitment of gamma-tubulin in higher plants. *Nat Cell Biol*. 7:961-968.

Murmann, A.E., A. Mincheva, M.O. Scheuermann, M. Gautier, F. Yang, J. Buitkamp, P.L. Strissel, R. Strick, J.D. Rowley, and P. Lichter. 2008. Comparative gene mapping in cattle, Indian muntjac, and Chinese muntjac by fluorescence in situ hybridization. *Genetica*. 134:345-351.

Musacchio, A. 2011. Spindle assembly checkpoint: the third decade. *Philosophical transactions of the Royal Society of London*. 366:3595-3604.

Musacchio, A. 2015. The Molecular Biology of Spindle Assembly Checkpoint Signaling Dynamics. *Curr Biol*. 25:R1002-1018.

Musacchio, A., and A. Desai. 2017. A Molecular View of Kinetochore Assembly and Function. *Biology*. 6.

Nakaoka, Y., T. Miki, R. Fujioka, R. Uehara, A. Tomioka, C. Obuse, M. Kubo, Y. Hiwatashi, and G. Goshima. 2012. An inducible RNA interference system in Physcomitrella patens reveals a dominant role of augmin in phragmoplast microtubule generation. *Plant Cell*. 24:1478-1493.

Nakata, T., and N. Hirokawa. 1995. Point mutation of adenosine triphosphate-binding motif generated rigor kinesin that selectively blocks anterograde lysosome membrane transport. *J Cell Biol*. 131:1039-1053.

Neumann, P., Z. Pavlikova, A. Koblizkova, I. Fukova, V. Jedlickova, P. Novak, and J. Macas. 2015. Centromeres Off the Hook: Massive Changes in Centromere Size and Structure Following Duplication of CenH3 Gene in Fabeae Species. *Mol Biol Evol*. 32:1862-1879.

Nicklas, R.B., and G.W. Gordon. 1985. The total length of spindle microtubules depends on the number of chromosomes present. *J Cell Biol*. 100:1-7.

Nicklas, R.B., and C.A. Koch. 1969. Chromosome micromanipulation. 3. Spindle fiber tension and the reorientation of mal-oriented chromosomes. *J Cell Biol*. 43:40-50.

Nicklas, R.B., D.F. Kubai, and T.S. Hays. 1982. Spindle microtubules and their mechanical associations after micromanipulation in anaphase. *J Cell Biol*. 95:91-104.

Nieuwenhuis, J., A. Adamopoulos, O.B. Bleijerveld, A. Mazouzi, E. Stickel, P. Celie, M. Altelaar, P. Knipscheer, A. Perrakis, V.A. Blomen, and T.R. Brummelkamp. 2017. Vasohibins encode tubulin detyrosinating activity. *Science (New York, N.Y.*. 358:1453-1456.

Nigg, E.A., and A.J. Holland. 2018. Once and only once: mechanisms of centriole duplication and their deregulation in disease. *Nat Rev Mol Cell Biol*. 19:297-312.

Nixon, F.M., C. Gutierrez-Caballero, F.E. Hood, D.G. Booth, I.A. Prior, and S.J. Royle. 2015. The mesh is a network of microtubule connectors that stabilizes individual kinetochore fibers of the mitotic spindle. *Elife*. 4.

Nixon, F.M., T.R. Honnor, N.I. Clarke, G.P. Starling, A.J. Beckett, A.M. Johansen, J.A. Brettschneider, I.A. Prior, and S.J. Royle. 2017a. Microtubule organization within mitotic spindles revealed by serial block face scanning electron microscopy and image analysis. *J Cell Sci*. 130:1845-1855.

Nixon, F.M., T.R. Honnor, N.I. Clarke, G.P. Starling, A.J. Beckett, A.M. Johansen, J.A. Brettschneider, I.A. Prior, and S.J. Royle. 2017b. Microtubule organization within mitotic spindles revealed by serial block face scanning EM and image analysis. *Journal of cell science*.

Nogales, E. 2001. Structural insight into microtubule function. *Annu Rev Biophys Biomol Struct*. 30:397-420.

Nunes Bastos, R., S.R. Gandhi, R.D. Baron, U. Gruneberg, E.A. Nigg, and F.A. Barr. 2013. Aurora B suppresses microtubule dynamics and limits central spindle size by locally activating KIF4A. *J Cell Biol*. 202:605-621.

Nunes, V., M. Dantas, D. Castro, E. Vitiello, I. Wang, N. Carpi, M. Balland, M. Piel, P. Aguiar, H. Maiato, and J.G. Ferreira. 2020. Centrosome-nuclear axis repositioning drives the assembly of a bipolar spindle scaffold to ensure mitotic fidelity. *Molecular biology of the cell*. 31:1675-1690.

Nurse, P. 1975. Genetic control of cell size at cell division in yeast. *Nature*. 256:547-551.

Nurse, P. 1990. Universal control mechanism regulating onset of M-phase. *Nature*. 344:503-508.

Nurse, P. 2000. A long twentieth century of the cell cycle and beyond. *Cell*. 100:71-78.

O'Connell, C.B., J. Loncarek, P. Kalab, and A. Khodjakov. 2009. Relative contributions of chromatin and kinetochores to mitotic spindle assembly. *J Cell Biol*. 187:43-51.

O'Toole, E., M. Morphew, and J.R. McIntosh. 2020. Electron tomography reveals aspects of spindle structure important for mechanical stability at metaphase. *Mol Biol Cell*. 31:184-195.

O'Toole, E.T., K.L. McDonald, J. Mantler, J.R. McIntosh, A.A. Hyman, and T. Muller-Reichert. 2003. Morphologically distinct microtubule ends in the mitotic centrosome of Caenorhabditis elegans. *The Journal of cell biology*. 163:451-456.

Oegema, K., A. Desai, S. Rybina, M. Kirkham, and A.A. Hyman. 2001. Functional analysis of kinetochore assembly in Caenorhabditis elegans. *J Cell Biol*. 153:1209-1226.

Orr, B., F. De Sousa, A.M. Gomes, O. Afonso, L.T. Ferreira, A.C. Figueiredo, and H. Maiato. 2021. An anaphase surveillance mechanism prevents micronuclei formation from frequent chromosome segregation errors. *Cell Rep*. 37:109783.

Orr, B., L. Talje, Z. Liu, B.H. Kwok, and D.A. Compton. 2016. Adaptive Resistance to an Inhibitor of Chromosomal Instability in Human Cancer Cells. *Cell Rep*. 17:1755-1763.

Pagano, M., R. Pepperkok, F. Verde, W. Ansorge, and G. Draetta. 1992. Cyclin A is required at two points in the human cell cycle. *EMBO J*. 11:961-971.

Palevitz, B. 1988. Microtubular fir-trees in mitotic spindles of onion roots. *Protoplasma*. 142:74-78.

Paul, R., R. Wollman, W.T. Silkworth, I.K. Nardi, D. Cimini, and A. Mogilner. 2009. Computer simulations predict that chromosome movements and rotations accelerate mitotic spindle assembly without compromising accuracy. *Proc Natl Acad Sci U S A*. 106:15708-15713.

Paweletz, N. 2001. Walther Flemming: pioneer of mitosis research. *Nature reviews Molecular cell biology*. 2:72-75.

Pereira, A., M. Sousa, A.C. Almeida, L.T. Ferreira, A.R. Costa, M. Novais-Cruz, C. Ferras, M.M. Sousa, P. Sampaio, M. Belsley, and H. Maiato. 2019. Coherent-hybrid STED: high contrast sub-diffraction imaging using a bi-vortex depletion beam. *Opt Express*. 27:8092-8111.

Pereira, A.J., and H. Maiato. 2012. Maturation of the kinetochore-microtubule interface and the meaning of metaphase. *Chromosome Res*. 20:563-577.

Pereira, A.J., I. Matos, M. Lince-Faria, and H. Maiato. 2009. Dissecting mitosis with laser microsurgery and RNAi in Drosophila cells. *Methods Mol Biol*. 545:145-164.

Pereira, A.L., A.J. Pereira, A.R. Maia, K. Drabek, C.L. Sayas, P.J. Hergert, M. Lince-Faria, I. Matos, C. Duque, T. Stepanova, C.L. Rieder, W.C. Earnshaw, N. Galjart, and H. Maiato. 2006. Mammalian CLASP1 and CLASP2 cooperate to ensure mitotic fidelity by regulating spindle and kinetochore function. *Mol Biol Cell*. 17:4526-4542.

Peretti, D., P. Maraschio, S. Lambiase, F. Lo Curto, and O. Zuffardi. 1986. Indirect immunofluorescence of inactive centromeres as indicator of centromeric function. *Hum Genet*. 73:12-16.

Peterson, J.B., and H. Ris. 1976. Electron-microscopic study of the spindle and chromosome movement in the yeast Saccharomyces cerevisiae. *J Cell Sci*. 22:219-242.

Petry, S., A.C. Groen, K. Ishihara, T.J. Mitchison, and R.D. Vale. 2013. Branching microtubule nucleation in Xenopus egg extracts mediated by augmin and TPX2. *Cell*. 152:768-777.

Petry, S., C. Pugieux, F.J. Nedelec, and R.D. Vale. 2011. Augmin promotes meiotic spindle formation and bipolarity in Xenopus egg extracts. *Proc Natl Acad Sci U S A*. 108:14473-14478.

Petry, S., and R.D. Vale. 2015. Microtubule nucleation at the centrosome and beyond. *Nat Cell Biol*. 17:1089-1093.

Phillips, J.B., R. Lyczak, G.C. Ellis, and B. Bowerman. 2004. Roles for two partially redundant alpha-tubulins during mitosis in early Caenorhabditis elegans embryos. *Cell Motil Cytoskeleton*. 58:112-126.

Pines, J. 2011. Cubism and the cell cycle: the many faces of the APC/C. *Nat Rev Mol Cell Biol*. 12:427-438.

Piperno, G., M. LeDizet, and X.J. Chang. 1987. Microtubules containing acetylated alpha-tubulin in mammalian cells in culture. *The Journal of cell biology*. 104:289-302.

Powers, J., D.J. Rose, A. Saunders, S. Dunkelbarger, S. Strome, and W.M. Saxton. 2004. Loss of KLP-19 polar ejection force causes misorientation and missegregation of holocentric chromosomes. *J Cell Biol*. 166:991-1001.

Prosser, S.L., and L. Pelletier. 2017. Mitotic spindle assembly in animal cells: a fine balancing act. *Nat Rev Mol Cell Biol*. 18:187-201.

Puklowski, A., Y. Homsi, D. Keller, M. May, S. Chauhan, U. Kossatz, V. Grunwald, S. Kubicka, A. Pich, M.P. Manns, I. Hoffmann, P. Gonczy, and N.P. Malek. 2011. The SCF-FBXW5 E3-ubiquitin ligase is regulated by PLK4 and targets HsSAS-6 to control centrosome duplication. *Nat Cell Biol*. 13:1004-1009.

Rattner, J.B., and D.P. Bazett-Jones. 1989. Kinetochore structure: electron spectroscopic imaging of the kinetochore. *J Cell Biol*. 108:1209-1219.

Redemann, S., J. Baumgart, N. Lindow, M. Shelley, E. Nazockdast, A. Kratz, S. Prohaska, J. Brugues, S. Furthauer, and T. Muller-Reichert. 2017. C. elegans chromosomes connect to centrosomes by anchoring into the spindle network. *Nat Commun*. 8:15288.

Remak, R. 1855. Untersuchungen über die Entwicklung der Wirbelthiere. Verlag von G. Reimer.

Renda, F., C. Miles, I. Tikhonenko, R. Fisher, L. Carlini, T.M. Kapoor, A. Mogilner, and A. Khodjakov. 2022. Non-centrosomal microtubules at kinetochores promote rapid chromosome biorientation during mitosis in human cells. *Curr Biol*.

Ribeiro, S.A., J.C. Gatlin, Y. Dong, A. Joglekar, L. Cameron, D.F. Hudson, C.J. Farr, B.F. McEwen, E.D. Salmon, W.C. Earnshaw, and P. Vagnarelli. 2009. Condensin regulates the stiffness of vertebrate centromeres. *Mol Biol Cell*. 20:2371-2380.

Rieder, C.L. 1981. The structure of the cold-stable kinetochore fiber in metaphase PtK1 cells. *Chromosoma*. 84:145-158.

Rieder, C.L. 1982. The formation, structure, and composition of the mammalian kinetochore and kinetochore fiber. *Int Rev Cytol*. 79:1-58.

Rieder, C.L., and S.P. Alexander. 1990. Kinetochores are transported poleward along a single astral microtubule during chromosome attachment to the spindle in newt lung cells. *J Cell Biol*. 110:81-95.

Rieder, C.L., and G. Cassels. 1999. Correlative light and electron microscopy of mitotic cells in monolayer cultures. *Methods Cell Biol*. 61:297-315.

Rieder, C.L., and R.W. Cole. 1998. Entry into mitosis in vertebrate somatic cells is guarded by a chromosome damage checkpoint that reverses the cell cycle when triggered during early but not late prophase. *J Cell Biol*. 142:1013-1022.

Rieder, C.L., E.A. Davison, L.C. Jensen, L. Cassimeris, and E.D. Salmon. 1986. Oscillatory movements of monooriented chromosomes and their position relative to the spindle pole result from the ejection properties of the aster and half-spindle. *J Cell Biol*. 103:581-591.

Rieder, C.L., and E.D. Salmon. 1994. Motile kinetochores and polar ejection forces dictate chromosome position on the vertebrate mitotic spindle. *J Cell Biol*. 124:223-233.

Roll-Mecak, A. 2020. The Tubulin Code in Microtubule Dynamics and Information Encoding. *Dev Cell*. 54:7-20.

Roos, U.P. 1973. Light and electron microscopy of rat kangaroo cells in mitosis. II. Kinetochore structure and function. *Chromosoma*. 41:195-220.

Roy, L.M., K.I. Swenson, D.H. Walker, B.G. Gabrielli, R.S. Li, H. Piwnica-Worms, and J.L. Maller. 1991. Activation of p34cdc2 kinase by cyclin A. *J Cell Biol*. 113:507-514.

Royle, S.J., N.A. Bright, and L. Lagnado. 2005. Clathrin is required for the function of the mitotic spindle. *Nature*. 434:1152-1157.

Rudd, M.K., and H.F. Willard. 2004. Analysis of the centromeric regions of the human genome assembly. *Trends Genet*. 20:529-533.

Rutledge, S.D., and D. Cimini. 2016. Consequences of aneuploidy in sickness and in health. *Curr Opin Cell Biol*. 40:41-46.

Saitoh, H., J. Tomkiel, C.A. Cooke, H. Ratrie, 3rd, M. Maurer, N.F. Rothfield, and W.C. Earnshaw. 1992. CENP-C, an autoantigen in scleroderma, is a component of the human inner kinetochore plate. *Cell*. 70:115-125.

Salmon, E.D., D. Goode, T.K. Maugel, and D.B. Bonar. 1976. Pressure-induced depolymerization of spindle microtubules. III. Differential stability in HeLa cells. *J Cell Biol*. 69:443-454.

Sampath, S.C., R. Ohi, O. Leismann, A. Salic, A. Pozniakovski, and H. Funabiki. 2004. The chromosomal passenger complex is required for chromatin-induced microtubule stabilization and spindle assembly. *Cell*. 118:187-202.

Sanchez, L., P. Martinez, and V. Goyanes. 1991. Analysis of centromere size in human chromosomes 1, 9, 15, and 16 by electron microscopy. *Genome*. 34:710-713.

Sanchez-Huertas, C., F. Freixo, R. Viais, C. Lacasa, E. Soriano, and J. Luders. 2016. Non-centrosomal nucleation mediated by augmin organizes microtubules in post-mitotic neurons and controls axonal microtubule polarity. *Nat Commun*. 7:12187.

Sanchez-Huertas, C., and J. Luders. 2015. The augmin connection in the geometry of microtubule networks. *Curr Biol*. 25:R294-299.

Santaguida, S., and A. Musacchio. 2009. The life and miracles of kinetochores. *EMBO J*. 28:2511-2531.

Scherthan, H. 1990. Localization of the repetitive telomeric sequence (TTAGGG)n in two muntjac species and implications for their karyotypic evolution. *Cytogenet Cell Genet*. 53:115-117.

Scherthan, H., T. Cremer, U. Arnason, H.U. Weier, A. Lima-de-Faria, and L. Fronicke. 1994. Comparative chromosome painting discloses homologous segments in distantly related mammals. *Nat Genet*. 6:342-347.

Schmidt, W.J. 1937. Die Doppelbrechung von Karyoplasma, Metaplasma und Zytoplasma. Gebrüder Borntraeger, Berlin.

Schmidtke, J., H. Brennecke, M. Schmid, H. Neitzel, and K. Sperling. 1981. Evolution of muntjac DNA. *Chromosoma*. 84:187-193.

Schmitt, F.O. 1939. The ultrastructure of protoplasmic constituents. *Physiological Reviews*. 19:270-302.

Schweizer, N., L. Haren, I. Dutto, R. Viais, C. Lacasa, A. Merdes, and J. Luders. 2021. Sub-centrosomal mapping identifies augmin-gammaTuRC as part of a centriole-stabilizing scaffold. *Nat Commun*. 12:6042.

Sekine, Y., Y. Okada, Y. Noda, S. Kondo, H. Aizawa, R. Takemura, and N. Hirokawa. 1994. A novel microtubule-based motor protein (KIF4) for organelle transports, whose expression is regulated developmentally. *J Cell Biol*. 127:187-201.

Sen, O., J.U. Harrison, N.J. Burroughs, and A.D. McAinsh. 2021. Kinetochore life histories reveal an Aurora-B-dependent error correction mechanism in anaphase. *Dev Cell*. 56:3082-3099.e3085.

Sharp, L. 1934. An Introduction to Cytology. McGrav-Hill Book Co. *Inc., New York.*

Shimamoto, Y., Y.T. Maeda, S. Ishiwata, A.J. Libchaber, and T.M. Kapoor. 2011. Insights into the micromechanical properties of the metaphase spindle. *Cell*. 145:1062-1074.

Shrestha, R.L., G.S. Ahn, M.I. Staples, K.M. Sathyan, T.S. Karpova, D.R. Foltz, and M.A. Basrai. 2017a. Mislocalization of centromeric histone H3 variant CENP-A contributes to chromosomal instability (CIN) in human cells. *Oncotarget*.

Shrestha, R.L., D. Conti, N. Tamura, D. Braun, R.A. Ramalingam, K. Cieslinski, J. Ries, and V.M. Draviam. 2017b. Aurora-B kinase pathway controls the lateral to end-on conversion of kinetochore-microtubule attachments in human cells. *Nat Commun*. 8:150.

Shrestha, R.L., and V.M. Draviam. 2013. Lateral to end-on conversion of chromosome-microtubule attachment requires kinesins CENP-E and MCAK. *Curr Biol*. 23:1514-1526.

Shrestha, S., M. Hazelbaker, A.L. Yount, and C.E. Walczak. 2018. Emerging Insights into the Function of Kinesin-8 Proteins in Microtubule Length Regulation. *Biomolecules*. 9.

Sikirzhytski, V., V. Magidson, J.B. Steinman, J. He, M. Le Berre, I. Tikhonenko, J.G. Ault, B.F. McEwen, J.K. Chen, H. Sui, M. Piel, T.M. Kapoor, and A. Khodjakov. 2014. Direct kinetochore-spindle pole connections are not required for chromosome segregation. *J Cell Biol*. 206:231-243.

Sikirzhytski, V., F. Renda, I. Tikhonenko, V. Magidson, B.F. McEwen, and A. Khodjakov. 2018. Microtubules assemble near most kinetochores during early prometaphase in human cells. *J Cell Biol*. 217:2647-2659.

Sillje, H.H., S. Nagel, R. Korner, and E.A. Nigg. 2006. HURP is a Ran-importin beta-regulated protein that stabilizes kinetochore microtubules in the vicinity of chromosomes. *Curr Biol*. 16:731-742.

Silljé, H.H., S. Nagel, R. Körner, and E.A. Nigg. 2006. HURP is a Ran-importin beta-regulated protein that stabilizes kinetochore microtubules in the vicinity of chromosomes. *Curr Biol*. 16:731-742.

Sir, J.H., M. Putz, O. Daly, C.G. Morrison, M. Dunning, J.V. Kilmartin, and F. Gergely. 2013. Loss of centrioles causes chromosomal instability in vertebrate somatic cells. *The Journal of cell biology*. 203:747-756.

Snyder, J.A., and J.R. McIntosh. 1975. Initiation and growth of microtubules from mitotic centers in lysed mammalian cells. *J Cell Biol*. 67:744-760.

Soma, H., H. Kada, K. Mtayoshi, Y. Suzuki, C. Meckvichal, A. Mahannop, and B. Vatanaromya. 1983. The chromosomes of Muntiacus feae. *Cytogenet Cell Genet*. 35:156-158.

Song, J.G., M.R. King, R. Zhang, R.S. Kadzik, A. Thawani, and S. Petry. 2018. Mechanism of how augmin directly targets the gamma-tubulin ring complex to microtubules. *J Cell Biol*. 217:2417-2428.

Spence, J.M., W. Mills, K. Mann, C. Huxley, and C.J. Farr. 2006. Increased missegregation and chromosome loss with decreasing chromosome size in vertebrate cells. *Chromosoma*. 115:60-74.

Stear, J.H., and M.B. Roth. 2002. Characterization of HCP-6, a C. elegans protein required to prevent chromosome twisting and merotelic attachment. *Genes & development*. 16:1498-1508.

Steblyanko, Y., G. Rajendraprasad, M. Osswald, S. Eibes, A. Jacome, S. Geley, A.J. Pereira, H. Maiato, and M. Barisic. 2020. Microtubule poleward flux in human cells is driven by the coordinated action of four kinesins. *EMBO J*. 39:e105432.

Stepanova, T., J. Slemmer, C.C. Hoogenraad, G. Lansbergen, B. Dortland, C.I. De Zeeuw, F. Grosveld, G. van Cappellen, A. Akhmanova, and N. Galjart. 2003. Visualization of microtubule growth in cultured neurons via the use of EB3-GFP (end-binding protein 3-green fluorescent protein). *J Neurosci*. 23:2655-2664.

Stephens, P.J., C.D. Greenman, B. Fu, F. Yang, G.R. Bignell, L.J. Mudie, E.D. Pleasance, K.W. Lau, D. Beare, L.A. Stebbings, S. McLaren, M.L. Lin, D.J. McBride, I. Varela, S. Nik-Zainal, C. Leroy, M. Jia, A. Menzies, A.P. Butler, J.W. Teague, M.A. Quail, J. Burton, H. Swerdlow, N.P. Carter, L.A. Morsberger, C. Iacobuzio-Donahue, G.A. Follows, A.R. Green, A.M. Flanagan, M.R. Stratton, P.A. Futreal, and P.J. Campbell. 2011. Massive genomic rearrangement acquired in a single catastrophic event during cancer development. *Cell*. 144:27-40.

Strnad, P., S. Leidel, T. Vinogradova, U. Euteneuer, A. Khodjakov, and P. Gonczy. 2007. Regulated HsSAS-6 levels ensure formation of a single procentriole per centriole during the centrosome duplication cycle. *Dev Cell*. 13:203-213.

Sturgill, E.G., D.K. Das, Y. Takizawa, Y. Shin, S.E. Collier, M.D. Ohi, W. Hwang, M.J. Lang, and R. Ohi. 2014. Kinesin-12 Kif15 targets kinetochore fibers through an intrinsic two-step mechanism. *Curr Biol*. 24:2307-2313.

Subramanian, R., E.M. Wilson-Kubalek, C.P. Arthur, M.J. Bick, E.A. Campbell, S.A. Darst, R.A. Milligan, and T.M. Kapoor. 2010. Insights into antiparallel microtubule crosslinking by PRC1, a conserved nonmotor microtubule binding protein. *Cell*. 142:433-443.

Sullivan, B.A., and H.F. Willard. 1998. Stable dicentric X chromosomes with two functional centromeres. *Nat Genet*. 20:227-228.

Sullivan, L.L., C.D. Boivin, B. Mravinac, I.Y. Song, and B.A. Sullivan. 2011. Genomic size of CENP-A domain is proportional to total alpha satellite array size at human centromeres and expands in cancer cells. *Chromosome Res*. 19:457-470.

Suresh, P., A.F. Long, and S. Dumont. 2020. Microneedle manipulation of the mammalian spindle reveals specialized, short-lived reinforcement near chromosomes. *Elife*. 9.

Suzuki, A., B.L. Badger, X. Wan, J.G. DeLuca, and E.D. Salmon. 2014. The architecture of CCAN proteins creates a structural integrity to resist spindle forces and achieve proper Intrakinetochore stretch. *Dev Cell*. 30:717-730.

Tanenbaum, M.E., L. Macurek, N. Galjart, and R.H. Medema. 2008. Dynein, Lis1 and CLIP-170 counteract Eg5-dependent centrosome separation during bipolar spindle assembly. *EMBO J*. 27:3235-3245.

Tanenbaum, M.E., L. Macurek, A. Janssen, E.F. Geers, M. Alvarez-Fernandez, and R.H. Medema. 2009. Kif15 cooperates with eg5 to promote bipolar spindle assembly. *Curr Biol*. 19:1703-1711.

Tanenbaum, M.E., R.D. Vale, and R.J. McKenney. 2013. Cytoplasmic dynein crosslinks and slides anti-parallel microtubules using its two motor domains. *Elife*. 2:e00943.

Tariq, A., L. Green, J.C.G. Jeynes, C. Soeller, and J.G. Wakefield. 2020. In vitro reconstitution of branching microtubule nucleation. *Elife*. 9.

Taylor, S.S., D. Hussein, Y. Wang, S. Elderkin, and C.J. Morrow. 2001. Kinetochore localisation and phosphorylation of the mitotic checkpoint components Bub1 and BubR1 are differentially regulated by spindle events in human cells. *J Cell Sci*. 114:4385-4395.

Thawani, A., H.A. Stone, J.W. Shaevitz, and S. Petry. 2019. Spatiotemporal organization of branched microtubule networks. *Elife*. 8.

Theurkauf, W.E., and R.S. Hawley. 1992. Meiotic spindle assembly in Drosophila females: behavior of nonexchange chromosomes and the effects of mutations in the nod kinesin-like protein. *J Cell Biol*. 116:1167-1180.

Tilney, L.G., J. Bryan, D.J. Bush, K. Fujiwara, M.S. Mooseker, D.B. Murphy, and D.H. Snyder. 1973. Microtubules: evidence for 13 protofilaments. *J Cell Biol*. 59:267-275.

Tokai-Nishizumi, N., M. Ohsugi, E. Suzuki, and T. Yamamoto. 2005. The chromokinesin Kid is required for maintenance of proper metaphase spindle size. *Mol Biol Cell*. 16:5455-5463.

Tomkiel, J., C.A. Cooke, H. Saitoh, R.L. Bernat, and W.C. Earnshaw. 1994. CENP-C is required for maintaining proper kinetochore size and for a timely transition to anaphase. *J Cell Biol*. 125:531-545.

Tomonaga, T., K. Matsushita, S. Yamaguchi, T. Oohashi, H. Shimada, T. Ochiai, K. Yoda, and F. Nomura. 2003. Overexpression and mistargeting of centromere protein-A in human primary colorectal cancer. *Cancer Res*. 63:3511-3516.

Torosantucci, L., M. De Luca, G. Guarguaglini, P. Lavia, and F. Degrassi. 2008. Localized RanGTP accumulation promotes microtubule nucleation at kinetochores in somatic mammalian cells. *Molecular biology of the cell*. 19:1873-1882.

Tournebize, R., A. Popov, K. Kinoshita, A.J. Ashford, S. Rybina, A. Pozniakovsky, T.U. Mayer, C.E. Walczak, E. Karsenti, and A.A. Hyman. 2000. Control of microtubule dynamics by the antagonistic activities of XMAP215 and XKCM1 in Xenopus egg extracts. *Nat Cell Biol*. 2:13-19.

Tovini, L., and S.E. McClelland. 2019. Impaired CENP-E Function Renders Large Chromosomes More Vulnerable to Congression Failure. *Biomolecules*. 9.

Tsipouri, V., M.G. Schueler, S. Hu, N.C.S. Program, A. Dutra, E. Pak, H. Riethman, and E.D. Green. 2008. Comparative sequence analyses reveal sites of ancestral chromosomal fusions in the Indian muntjac genome. *Genome Biol*. 9:R155.

Tsuchiya, K., H. Hayashi, M. Nishina, M. Okumura, Y. Sato, M.T. Kanemaki, G. Goshima, and T. Kiyomitsu. 2021. Ran-GTP Is Non-essential to Activate NuMA for Mitotic Spindle-Pole Focusing but Dynamically Polarizes HURP Near Chromosomes. *Curr Biol*. 31:115-127 e113.

Tulu, U.S., C. Fagerstrom, N.P. Ferenz, and P. Wadsworth. 2006. Molecular requirements for kinetochore-associated microtubule formation in mammalian cells. *Curr Biol*. 16:536-541.

Uehara, R., and G. Goshima. 2010. Functional central spindle assembly requires de novo microtubule generation in the interchromosomal region during anaphase. *J Cell Biol*. 191:259-267.

Uehara, R., T. Kamasaki, S. Hiruma, I. Poser, K. Yoda, J. Yajima, D.W. Gerlich, and G. Goshima. 2016. Augmin shapes the anaphase spindle for efficient cytokinetic furrow ingression and abscission. *Molecular biology of the cell*. 27:812-827.

Uehara, R., R.-s. Nozawa, A. Tomioka, S. Petry, R.D. Vale, C. Obuse, and G. Goshima. 2009a. The augmin complex plays a critical role in spindle microtubule generation for mitotic progression and cytokinesis in human cells. *Proceedings of the National Academy of Sciences*. 106:6998-7003.

Uehara, R., R.S. Nozawa, A. Tomioka, S. Petry, R.D. Vale, C. Obuse, and G. Goshima. 2009b. The augmin complex plays a critical role in spindle microtubule generation for mitotic progression and cytokinesis in human cells. *Proc Natl Acad Sci U S A*. 106:6998-7003.

van den Wildenberg, S.M., L. Tao, L.C. Kapitein, C.F. Schmidt, J.M. Scholey, and E.J. Peterman. 2008. The homotetrameric kinesin-5 KLP61F preferentially crosslinks microtubules into antiparallel orientations. *Curr Biol*. 18:1860-1864.

van der Horst, A., and S.M. Lens. 2014. Cell division: control of the chromosomal passenger complex in time and space. *Chromosoma*. 123:25-42.

Vanneste, D., V. Ferreira, and I. Vernos. 2011. Chromokinesins: localization-dependent functions and regulation during cell division. *Biochem Soc Trans*. 39:1154-1160.

Vanneste, D., M. Takagi, N. Imamoto, and I. Vernos. 2009. The role of Hklp2 in the stabilization and maintenance of spindle bipolarity. *Curr Biol*. 19:1712-1717.

Verde, F., J.M. Berrez, C. Antony, and E. Karsenti. 1991. Taxol-induced microtubule asters in mitotic extracts of Xenopus eggs: requirement for phosphorylated factors and cytoplasmic dynein. *J Cell Biol*. 112:1177-1187.

Verhey, K.J., and J. Gaertig. 2007. The tubulin code. *Cell Cycle*. 6:2152-2160.

Verma, V., and T.J. Maresca. 2019. Direct observation of branching MT nucleation in living animal cells. *J Cell Biol*. 218:2829-2840.

Vernos, I., J. Raats, T. Hirano, J. Heasman, E. Karsenti, and C. Wylie. 1995. Xklp1, a chromosomal Xenopus kinesin-like protein essential for spindle organization and chromosome positioning. *Cell*. 81:117-127.

Viais, R., M. Farina-Mosquera, M. Villamor-Paya, S. Watanabe, L. Palenzuela, C. Lacasa, and J. Luders. 2021. Augmin deficiency in neural stem cells causes p53-dependent apoptosis and aborts brain development. *Elife*. 10.

Vig, B.K., and A. Henderson. 1998. Aneuploidy in male Indian muntjac cells is limited to the Y2 chromosome. *Mutagenesis*. 13:33-37.

Vorozhko, V.V., M.J. Emanuele, M.J. Kallio, P.T. Stukenberg, and G.J. Gorbsky. 2008. Multiple mechanisms of chromosome movement in vertebrate cells mediated through the Ndc80 complex and dynein/dynactin. *Chromosoma*. 117:169-179.

Vukusic, K., R. Buda, A. Bosilj, A. Milas, N. Pavin, and I.M. Tolic. 2017. Microtubule Sliding within the Bridging Fiber Pushes Kinetochore Fibers Apart to Segregate Chromosomes. *Dev Cell*. 43:11-23 e16.

Vukusic, K., I. Ponjavic, R. Buda, P. Risteski, and I.M. Tolic. 2021. Microtubule-sliding modules based on kinesins EG5 and PRC1-dependent KIF4A drive human spindle elongation. *Developmental cell*. 56:1253-1267 e1210.

Vukusic, K., and I.M. Tolic. 2021. Anaphase B: Long-standing models meet new concepts. *Semin Cell Dev Biol*. 117:127-139.

Wadsworth, P., and A. Khodjakov. 2004. E pluribus unum: towards a universal mechanism for spindle assembly. *Trends Cell Biol*. 14:413-419.

Wainman, A., D.W. Buster, T. Duncan, J. Metz, A. Ma, D. Sharp, and J.G. Wakefield. 2009. A new Augmin subunit, Msd1, demonstrates the importance of mitotic spindle-templated microtubule nucleation in the absence of functioning centrosomes. *Genes Dev*. 23:1876-1881.

Walczak, C.E., S. Gayek, and R. Ohi. 2013. Microtubule-depolymerizing kinesins. *Annu Rev Cell Dev Biol*. 29:417-441.

Walczak, C.E., T.J. Mitchison, and A. Desai. 1996. XKCM1: a Xenopus kinesin-related protein that regulates microtubule dynamics during mitotic spindle assembly. *Cell*. 84:37-47.

Walczak, C.E., I. Vernos, T.J. Mitchison, E. Karsenti, and R. Heald. 1998. A model for the proposed roles of different microtubule-based motor proteins in establishing spindle bipolarity. *Curr Biol*. 8:903-913.

Wan, X., R.P. O'Quinn, H.L. Pierce, A.P. Joglekar, W.E. Gall, J.G. DeLuca, C.W. Carroll, S.T. Liu, T.J. Yen, B.F. McEwen, P.T. Stukenberg, A. Desai, and E.D. Salmon. 2009. Protein architecture of the human kinetochore microtubule attachment site. *Cell*. 137:672-684.

Wandke, C., M. Barisic, R. Sigl, V. Rauch, F. Wolf, A.C. Amaro, C.H. Tan, A.J. Pereira, U. Kutay, H. Maiato, P. Meraldi, and S. Geley. 2012. Human chromokinesins promote chromosome congression and spindle microtubule dynamics during mitosis. *J Cell Biol*. 198:847-863.

Wang, S.Z., and R. Adler. 1995. Chromokinesin: a DNA-binding, kinesin-like nuclear protein. *J Cell Biol*. 128:761-768.

Wang, W., and H. Lan. 2000. Rapid and parallel chromosomal number reductions in muntjac deer inferred from mitochondrial DNA phylogeny. *Mol Biol Evol*. 17:1326-1333.

Warren, J.D., B. Orr, and D.A. Compton. 2020. A comparative analysis of methods to measure kinetochore-microtubule attachment stability. *Methods Cell Biol*. 158:91-116.

Wasteneys, G., and R. Williamson. 1989. Microtubule reassembly in internodal cell of Nitella tasmanica: assembly of cortical microtubules in branching clusters and its relevance to steady state microtubule assembly. *J Cell Sci*. 93:705-714.

Watanabe, S., F. Meitinger, A.K. Shiau, K. Oegema, and A. Desai. 2020. Centriole-independent mitotic spindle assembly relies on the PCNT-CDK5RAP2 pericentriolar matrix. *The Journal of cell biology*. 219.

Webster, D.R., J. Wehland, K. Weber, and G.G. Borisy. 1990. Detyrosination of alpha tubulin does not stabilize microtubules in vivo. *The Journal of cell biology*. 111:113-122.

Welburn, J.P., M. Vleugel, D. Liu, J.R. Yates, 3rd, M.A. Lampson, T. Fukagawa, and I.M. Cheeseman. 2010. Aurora B phosphorylates spatially distinct targets to differentially regulate the kinetochore-microtubule interface. *Mol Cell*. 38:383-392.

Wendell, K.L., L. Wilson, and M.A. Jordan. 1993. Mitotic block in HeLa cells by vinblastine: ultrastructural changes in kinetochore-microtubule attachment and in centrosomes. *J Cell Sci*. 104 (Pt 2):261-274.

Wilhelm, T., A.M. Olziersky, D. Harry, F. De Sousa, H. Vassal, A. Eskat, and P. Meraldi. 2019. Mild replication stress causes chromosome mis-segregation via premature centriole disengagement. *Nat Commun*. 10:3585.

Williams, B.C., M.F. Riedy, E.V. Williams, M. Gatti, and M.L. Goldberg. 1995. The Drosophila kinesin-like protein KLP3A is a midbody component required for central spindle assembly and initiation of cytokinesis. *J Cell Biol*. 129:709-723.

Wilson, E.B. 1925. The cell in development and heredity. Macmillan.

Wimbish, R.T., and J.G. DeLuca. 2020. Hec1/Ndc80 Tail Domain Function at the Kinetochore-Microtubule Interface. *Front Cell Dev Biol*. 8:43.

Witt, P.L., H. Ris, and G.G. Borisy. 1980. Origin of kinetochore microtubules in Chinese hamster ovary cells. *Chromosoma*. 81:483-505.

Witt, P.L., H. Ris, and G.G. Borisy. 1981. Structure of kinetochore fibers: microtubule continuity and inter-microtubule bridges. *Chromosoma*. 83:523-540.

Wollman, R., E.N. Cytrynbaum, J.T. Jones, T. Meyer, J.M. Scholey, and A. Mogilner. 2005. Efficient chromosome capture requires a bias in the 'search-and-capture' process during mitotic-spindle assembly. *Curr Biol*. 15:828-832.

Wong, J., and G. Fang. 2006. HURP controls spindle dynamics to promote proper interkinetochore tension and efficient kinetochore capture. *J Cell Biol*. 173:879-891.

Wong, Y.L., J.V. Anzola, R.L. Davis, M. Yoon, A. Motamedi, A. Kroll, C.P. Seo, J.E. Hsia, S.K. Kim, J.W. Mitchell, B.J. Mitchell, A. Desai, T.C. Gahman, A.K. Shiau, and K. Oegema. 2015. Cell biology. Reversible centriole depletion with an inhibitor of Polo-like kinase 4. *Science (New York, N.Y.* 348:1155-1160.

Wood, K.W., L. Lad, L. Luo, X. Qian, S.D. Knight, N. Nevins, K. Brejc, D. Sutton, A.G. Gilmartin, P.R. Chua, R. Desai, S.P. Schauer, D.E. McNulty, R.S. Annan, L.D. Belmont, C. Garcia, Y. Lee, M.A. Diamond, L.F. Faucette, M. Giardiniere, S. Zhang, C.M. Sun, J.D. Vidal, S. Lichtsteiner, W.D. Cornwell, J.D. Greshock, R.F. Wooster, J.T. Finer, R.A. Copeland, P.S. Huang, D.J. Morgans, Jr., D. Dhanak, G. Bergnes, R. Sakowicz, and J.R. Jackson. 2010. Antitumor activity of an allosteric inhibitor of centromere-associated protein-E. *Proceedings of the National Academy of Sciences of the United States of America*. 107:5839-5844.

Wordeman, L., and T.J. Mitchison. 1995. Identification and partial characterization of mitotic centromere-associated kinesin, a kinesin-related protein that associates with centromeres during mitosis. *J Cell Biol*. 128:95-104.

Worrall, J.T., N. Tamura, A. Mazzagatti, N. Shaikh, T. van Lingen, B. Bakker, D.C.J. Spierings, E. Vladimirou, F. Foijer, and S.E. McClelland. 2018. Non-random Mis-segregation of Human Chromosomes. *Cell Rep*. 23:3366-3380.

Wu, G., R. Wei, E. Cheng, B. Ngo, and W.H. Lee. 2009. Hec1 contributes to mitotic centrosomal microtubule growth for proper spindle assembly through interaction with Hice1. *Mol Biol Cell*. 20:4686-4695.

Wurster, D.H., and K. Benirschke. 1967. Chromosome studies in some deer, the springbok, and the pronghorn, with notes on placentation in deer. *Cytologia (Tokyo)*. 32:273-285.

Wurster, D.H., and K. Benirschke. 1970. Indian muntjac, Muntiacus muntjak: a deer with a low diploid chromosome number. *Science*. 168:1364-1366.

Wynne, D.J., and H. Funabiki. 2015. Kinetochore function is controlled by a phospho-dependent coexpansion of inner and outer components. *J Cell Biol*. 210:899-916.

Yaguchi, K., T. Yamamoto, R. Matsui, Y. Tsukada, A. Shibanuma, K. Kamimura, T. Koda, and R. Uehara. 2018. Uncoordinated centrosome cycle underlies the instability of non-diploid somatic cells in mammals. *The Journal of cell biology*. 217:2463-2483.

Yang, F., N.P. Carter, L. Shi, and M.A. Ferguson-Smith. 1995. A comparative study of karyotypes of muntjacs by chromosome painting. *Chromosoma*. 103:642-652.

Yang, F., P.C. O'Brien, J. Wienberg, H. Neitzel, C.C. Lin, and M.A. Ferguson-Smith. 1997. Chromosomal evolution of the Chinese muntjac (Muntiacus reevesi). *Chromosoma*. 106:37-43.

Yang, Z., U.S. Tulu, P. Wadsworth, and C.L. Rieder. 2007. Kinetochore dynein is required for chromosome motion and congression independent of the spindle checkpoint. *Curr Biol*. 17:973-980.

Yasui, Y., T. Urano, A. Kawajiri, K. Nagata, M. Tatsuka, H. Saya, K. Furukawa, T. Takahashi, I. Izawa, and M. Inagaki. 2004. Autophosphorylation of a newly identified site of Aurora-B is indispensable for cytokinesis. *The Journal of biological chemistry*. 279:12997-13003.

Ye, F., L. Tan, Q. Yang, Y. Xia, L.W. Deng, M. Murata-Hori, and Y.C. Liou. 2011. HURP regulates chromosome congression by modulating kinesin Kif18A function. *Curr Biol*. 21:1584-1591.

Yen, T.J., D.A. Compton, D. Wise, R.P. Zinkowski, B.R. Brinkley, W.C. Earnshaw, and D.W. Cleveland. 1991. CENP-E, a novel human centromere-associated protein required for progression from metaphase to anaphase. *EMBO J*. 10:1245-1254.

Yingxiang, M.S.W., and X. Longhui. 1986. TAXONOMIC AND PHYLOGENETIC STUDIES ON THE GENUS MUNTIACUS. *Acta Theriologica Sinica*:03.

Yu, I., C.P. Garnham, and A. Roll-Mecak. 2015. Writing and Reading the Tubulin Code. *J Biol Chem*. 290:17163-17172.

Zaytsev, A.V., L.J. Sundin, K.F. DeLuca, E.L. Grishchuk, and J.G. DeLuca. 2014. Accurate phosphoregulation of kinetochore-microtubule affinity requires unconstrained molecular interactions. *J Cell Biol*. 206:45-59.

Zernike, F. 1955. How I discovered phase contrast. *Science*. 121:345-349.

Zhai, Y., P.J. Kronebusch, and G.G. Borisy. 1995. Kinetochore microtubule dynamics and the metaphase-anaphase transition. *J Cell Biol*. 131:721-734.

Zhang, C.Z., A. Spektor, H. Cornils, J.M. Francis, E.K. Jackson, S. Liu, M. Meyerson, and D. Pellman. 2015. Chromothripsis from DNA damage in micronuclei. *Nature*. 522:179-184.

Zhang, D., G.C. Rogers, D.W. Buster, and D.J. Sharp. 2007. Three microtubule severing enzymes contribute to the "Pacman-flux" machinery that moves chromosomes. *J Cell Biol*. 177:231-242.

Zhang, H., C. Aonbangkhen, E.V. Tarasovetc, E.R. Ballister, D.M. Chenoweth, and M.A. Lampson. 2017. Optogenetic control of kinetochore function. *Nat Chem Biol*. 13:1096-1101.

Zhang, L., H. Shao, Y. Huang, F. Yan, Y. Chu, H. Hou, M. Zhu, C. Fu, F. Aikhionbare, G. Fang, X. Ding, and X. Yao. 2011. PLK1 phosphorylates mitotic centromere-associated kinesin and promotes its depolymerase activity. *J Biol Chem*. 286:3033-3046.

Zhang, X., R. Zhuang, Q. Ye, J. Zhuo, K. Chen, D. Lu, X. Wei, H. Xie, X. Xu, and S. Zheng. 2019. High Expression of Human AugminComplex Submit 3 Indicates Poor Prognosis and Associates with Tumor Progression in Hepatocellular Carcinoma. *Journal of Cancer*. 10:1434-1443.

Zhou, Q., L. Huang, J. Zhang, X. Zhao, Q. Zhang, F. Song, J. Chi, F. Yang, and W. Wang. 2006. Comparative genomic analysis links karyotypic evolution with genomic evolution in the Indian muntjac (Muntiacus muntjak vaginalis). *Chromosoma*. 115:427-436.

Zhu, C., and W. Jiang. 2005. Cell cycle-dependent translocation of PRC1 on the spindle by Kif4 is essential for midzone formation and cytokinesis. *Proc Natl Acad Sci U S A*. 102:343-348.

Zhu, C., E. Lau, R. Schwarzenbacher, E. Bossy-Wetzel, and W. Jiang. 2006. Spatiotemporal control of spindle midzone formation by PRC1 in human cells. *Proc Natl Acad Sci U S A*. 103:6196-6201.

Zhu , H., J.A. Coppinger , C.-Y. Jang , J.R. Yates , III, and G. Fang 2008. FAM29A promotes microtubule amplification via recruitment of the NEDD1–γ-tubulin complex to the mitotic spindle. *Journal of Cell Biology*. 183:835-848.

Zhu, H., J.A. Coppinger, C.Y. Jang, J.R. Yates, 3rd, and G. Fang. 2008. FAM29A promotes microtubule amplification via recruitment of the NEDD1-gamma-tubulin complex to the mitotic spindle. *J Cell Biol*. 183:835-848.

Zinkowski, R.P., J. Meyne, and B.R. Brinkley. 1991. The centromere-kinetochore complex: a repeat subunit model. *J Cell Biol*. 113:1091-1110.

Zou, Y., X. Yi, W.E. Wright, and J.W. Shay. 2002. Human telomerase can immortalize Indian muntjac cells. *Exp Cell Res*. 281:63-76.